Shaping of light beams with photonic crystals: spatial filtering, beam collimation and focusing

---

A thesis submitted for the degree of Doctor of Philosophy in Physical Science of

Lina Maigyte

Directors

Dr. Kestutis Staliunas

Dr. Crina Maria Cojocaru

Departament de Física i Enginyeria Nuclear

Terrassa, May 2014

UNIVERSITAT POLITÈCNICA DE CATALUNYA
BARCELONATECH

Preface

Lenses were used to focus rays of the sun-light to start fires many centuries BC, if not more, and they were called “burning glasses”. Pieces of transparent minerals found in nature, and polished in a proper way, were used for this purpose. In the XI century, lenses (or the so-called “reading stones”) started to be utilized to magnify characters of manuscripts, while in XIII century they would be widely used with the invention of the eyeglass. The principles of light focusing by lenses have been investigated already since the Greek times, yielding to the knowledge of refraction, such as the Snell’s law, and the concept of refractive index. Scientists kept on improving lenses through the hundreds of years, but to their disappointment, they could not correct chromatic aberration, which they believed was caused by the imperfection of lens surface. This was until it was found that refractive index varies with the wavelength of light, determined by the dispersion relation. Dispersion causes chromatic aberrations in lenses, as well as, the splitting of light into its constituent colors in prisms or rainbows. Knowing that, compounds of lenses were arranged to correct chromatic aberrations. Lenses, and other optical components (i.e. mirrors, plates, prisms, waveguides, polarizers, filters, etc.) were advancing through centuries to help to control light in the way it was needed. It can be claimed that more than ever the precise control of light was required in the last and the

present century, as the invention of the laser specially fostered the study of the control of propagation and shape of light beams. While the technology continues to evolve, more sophisticated control over light is required.

To give an example, nowadays, a good camera objective consists of a compound of lenses, which can image, magnify, filter, correct the aberrations, etc. With compounds of lenses, one can have a precise control of light, however the size of such devices can reach ten or more centimeters (Fig. 1).

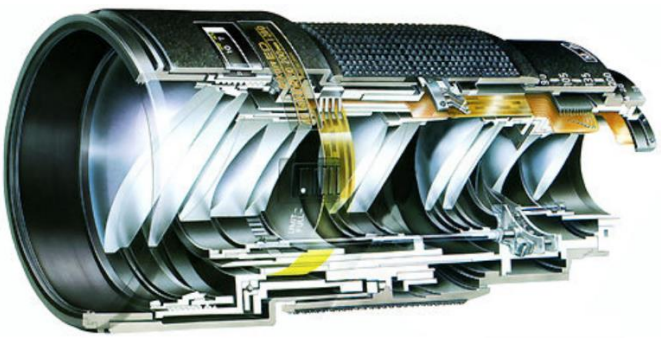

Figure 1. A cross-section of a camera objective, including compound of lenses to image, magnify, filter, correct the aberrations, etc. The usual size of high quality camera objective reach 10-15cm.

With the fast technological evolution appeared the need of small, tiny photonic integrated circuits. In the last decades electronic integrated circuits have shrunk to the micro-meter scale and are predicted to shrink even more in the near future. However, this rate of miniaturization is slowing down since smaller electronic components result in an increasing resistance and power dissipation in circuits. Optical devices, which would use light rather than electrons to perform a wide variety of optical functionalities, could help to avoid this problem, in addition, enabling faster and better quality transmission of information compared to electronic circuits. Recent development in nano-structures, photonic crystals, metamaterials and silicon technologies have expanded the possibilities to implement the photonic chips. However, to broaden and address the functionalities of photonic circuits, the fundamental

and technological research of optical structures and components at micro-nano scale must advance.

At the end of the 1980's, the concept of photonic crystal was introduced for the first time by E. Yablonovich and S. John in their pioneering works [Yab87, Joh87]. Since then, a huge amount of studies appeared, trying to understand the physics involved in photonic crystals, as they were promising candidates for a better control over propagation and the shape of light beams compared to lenses and other optical components. Additionally, due to the smallness of photonic crystals, they could be used in micro-optical devices, as well as, photonic integrated circuits. Just think about the possibility of replacing the objective in Fig. 1 by a 100 µm (or less) thickness slice of PhC (Fig. 2) to achieve the same functionality!

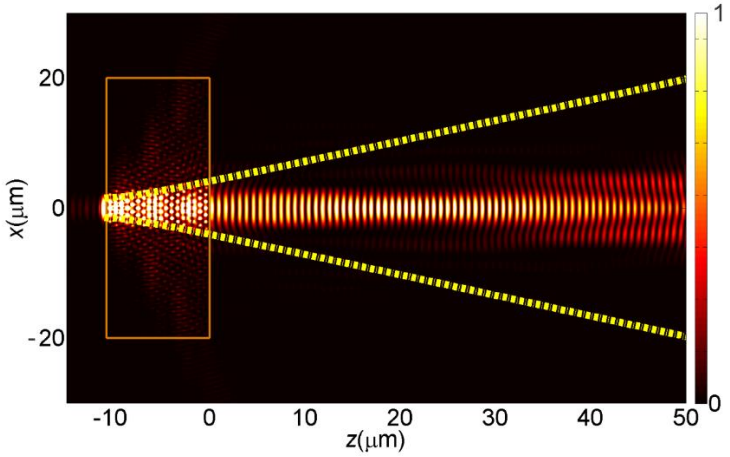

Figure 2. An example of numerical simulation showing the focusing of light beam behind of 10 µm length photonic crystal (marked by the orange rectangle). The dashed lines correspond to a spreading of the beam without photonic crystal (free space propagation).

Indeed, photonic crystals have many interesting properties and functionalities: band-gaps, slow light, localization in defects, wave guiding (e.g. photonic crystal fibers), negative refraction, etc. Rapidly developing technologies allow to enable these peculiarities from theories to experiments

and practice. At approximately the time when I started my Masters & PhD work, the idea to apply photonic crystals for spatial filtering of light beams [Sta09a] was proposed by my PhD directors. The development of the idea, bringing it closer to applications, become the main objective of my PhD work.

High spatial quality of laser beams are of great importance as they are vastly used in technologies, communications, micro-circuits, science, etc. However laser beams are not always coherent and very usually they have to be "cleaned". Therefore, building very compact spatial filters to solve this problem would be a real dream for many technologies. The work presented in this thesis helped to bring it closer to reality.

My work thus consisted of the first experimental demonstration of the spatial filtering by photonic crystals, and its further development and improvement: introducing chirp (the variation of longitudinal period of the structure along it) to extend the angular filtering range, considering different geometries (of three-dimensional crystals), and considering different materials. The main part of my original PhD work is based on the research along these lines, and resulted in 3 publications [Mai10, Pur13, Pur14]. The work is described in the second chapter of the thesis.

Spatial filtering is based on the appearance of angular band-gaps, i.e. the angular regions where the waves can not propagate. The appearance of angular band gaps is fundamentally related with the distortion of dispersion curves. This can be seen as the (somewhat unusual) representation of the so-called Kramers-Kroning relation, and extends to all physical systems, starting from the oscillator driven around its resonance. In this way, the Kramers-Kroning relation also affects our system: the spatial filtering relates to another effect – the focusing of a beam behind the structure of the photonic crystal (the so-called flat lensing). Therefore, another part of my PhD studies has been devoted to flat lensing, which resulted in 3 articles [Trull11, Mai13, Kum14] and in another original chapter of my PhD thesis. Most of the studies were done in conservative systems, i.e. in photonic crystals made of transparent materials, like glass or polymers. However, the ideas developed in my PhD seem to work

also in lossy systems, in particular in metallic PhCs. Both effects, spatial filtering and beam focusing, were predicted also in metallic materials [Kum14].

The PhD thesis is organized as follows. Chapter 1 is devoted to overview the general properties of photonic crystals. We introduce basic concepts such as dimensionality, lattice, band gap, etc. The chapter is significantly dedicated to explain and distinguish the concepts of temporal and spatial dispersion.

In the first part of Chapter 2 we define spatial filtering, we describe usual techniques to obtain it, as well as, alternative ones. One of the alternative techniques is spatial filtering by photonic crystals. We describe the working principle of spatial filtering by photonic crystals, and we overview the state of the art of the field. After a brief introduction, we show the original work. Firstly, we present the experimental demonstration of spatial filtering effect by three-dimensional low contrast photonic crystals, together with theoretical-numerical predictions. Moreover, we analyze possible ways to enhance spatial filtering by photonic structures. One of the possibilities is to introduce chirp into photonic crystal structure, therefore we have studied this case and proved it experimentally. Additionally, we have investigated three-dimensional photonic crystals with axisymmetric geometry, which led to axisymmetric spatial filtering effect. The effect was predicted numerically and proved experimentally. With three-dimensional axisymmetric photonic crystals also, but with slightly different parameters, we have numerically and experimentally proved super-collimation effect based on diffusion of angular components of the beam.

Chapter 3 is devoted to negative diffraction effects, due to anomalous spatial dispersion. Mainly we study flat lensing effects by photonic crystals. In the first part of the chapter, we discuss the state of the art in the field, and then we present our numerical simulations showing lensing and double focusing effects behind a two-dimensional rhombic photonic crystal (in low order bands). Furthermore, in the next section of the chapter we present the first experimental results, to the best of our knowledge, of flat lensing in visible frequency range. The experiment was done using three-dimensional polymer

based photonic crystal, with longitudinal periods ~10 times larger than the wavelength and, therefore, we were working in high order bands. For this experimentally studied case, the analytical predictions and numerical simulations are provided. Additionally, we present experimental results, as well as theoretical-numerical analysis of the beam collimation effect behind the three-dimensional polymer based woodpile PhC at visible wavelengths. In the last part of the chapter, we numerically study light beam propagation in metallic photonic crystals, where we demonstrate and analyse flat lensing and spatial filtering effects.

Finally, Chapter 4 summarizes the results and presents the conclusions of the thesis, as well as, a discussion on future perspectives.

In this way my PhD is based on 6 published papers (in 2 I am first author, in 4 second one), on one accepted paper and several to be sent to peer-review journals. The list of the articles is provided at the end of the thesis.

Contents

Chapter 1
Introduction

Since the pioneering works of E. Yablonovitch [Yab87] and S. John [Joh87] in late eighties, where the concept of photonic crystals (PhCs) was introduced, the science of PhCs has thrived, and lots of efforts have been devoted to the study of extraordinary wave propagation phenomena in PhCs. One of the most studied effects is the appearance of photonic band gaps (BG), i.e. forbidden frequency ranges where waves cannot propagate through the structure. The photonic BG is a temporal (chromatic) effect. However, in the last decade, spatial effects such as self-collimation, negative refraction, etc. were also discovered. To understand all the phenomena appearing in PhCs, firstly the wave propagation properties of these periodic structures have to be understood.

In the first part of the chapter, we will present a general overview of the general properties of PhCs. We will briefly discuss the similarities between the PhCs and crystalline solids and we will present different geometries of PhCs. We will also present the Maxwell's equations for the electromagnetic wave

propagation in periodic materials, followed by the explanation of plane-wave expansion method, broadly used to calculate chromatic and spatial dispersion relation in PhCs. In addition, PhCs found in nature will be described.

One-dimensional (1D) PhCs give a good theoretical framework to study and understand the effects due to periodicity in a simpler manner, therefore the second part of the chapter is dedicated to 1D PhCs. It will overview the frequency filtering due to BG for 1D PhCs. The coupled mode and multiple scattering methods for calculating transmission and reflection spectra of electromagnetic field will be described. Furthermore, 1D PhCs with a defect and also with chirp (variation of the period along the structure) will be introduced. In analogy to frequency filtering, angular filtering is also possible in PhCs, and will be described for the 1D case.

In the final part of the chapter, the concept of spatial dispersion and effects related to the modification of spatial dispersion (negative refraction, super-prism, flat lensing, super-lensing, negative diffraction, self-collimation, spatial filtering, etc.) appearing in two-dimensional (2D) and three-dimensional (3D) PhCs will be presented.

1.1. General properties of photonic crystals

1.1.1. Photonic crystals: definition, dimensionality and geometry

Photonic crystals are materials with a periodic variation of the macroscopic dielectric constant (or equivalently the refractive index). The variation can be in 1D, 2D or 3D as shown schematically in Fig. 1.1. The different colours of the structures represent different refractive indices of the material. Some SEM images of real structures for 1D, 2D and 3D PhCs are shown (Fig. 1.1(g)-(l), respectively).

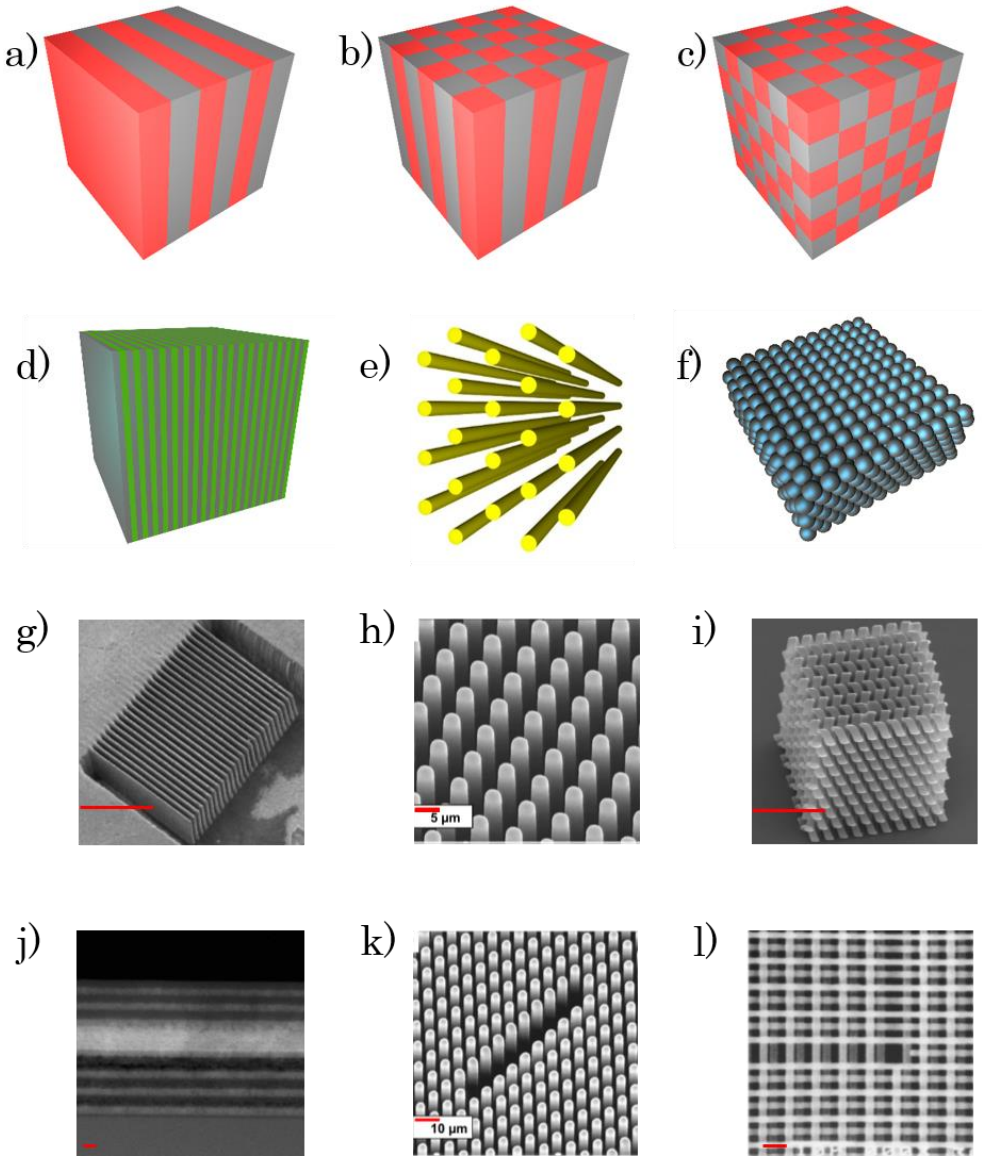

Figure 1.1. Schematic representations of: (a),(d) – 1D PhCs, (b),(e) – 2D PhCs, (c),(f) – 3D PhCs. SEM images of: (g) 1D comb-shaped periodic structure, the scale marked in red is of 500 µm [Yan04a]; (h) 2D PhC consisting of periodically distributed tube arrays, the scale marked in red is of 5 µm [Kra14]; (i) 3D PhC fabricated by two-photon polymerization technique, the scale marked in red is of 16 µm [Ovs08]; fabricated PhCs with introduced defects: (j) 1D PhC (scale 500 µm) [Li13], (k) 2D PhC (scale 10 µm) [Kra14], (l) 3D PhC (scale 4 µm) [Nod00].

Some optical properties of PhCs are analogous to the electronic properties of crystalline solids such as semiconductors. The analogy is based on the periodicity of both types of crystals.

A crystalline solid is a material where atoms or molecules are distributed in space in periodic arrangement. If an electron, which can behave as wave, propagates through such a crystal, it experiences a periodic potential originated from the periodically distributed atoms or molecules of the crystalline solid. The periodic potential and the geometry of the solid determine most of the conduction properties of the crystal. Perhaps, one of the most important properties is the appearance of energy BGs separating the conduction and valence bands, which is due to a coherent scattering of electron waves from the layers or rows of atoms/molecules, with a spacing similar to the wavelength of the electron wave. This means that electrons with certain energies (velocities) are forbidden to propagate in the crystal in certain directions. Fulfilling some conditions (i.e strong enough periodic modulation of the potential), these electrons of particular energies can be forbidden to propagate in all the directions and the so called complete BG can be obtained.

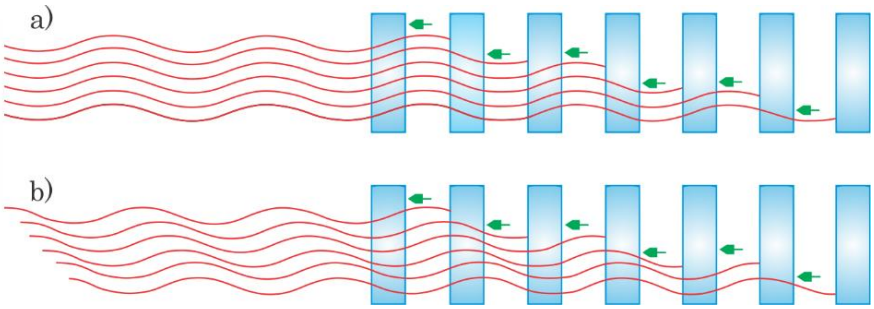

Figure 1.2. (a) Coherent and (b) incoherent scattering of a wave in 1D periodic structure.

For PhCs, the periodic variation of the macroscopic dielectric constant plays the role of an "optical periodic potential" that affects the propagation of photons or electromagnetic waves inside the structure. Therefore, the coherent scattering of electromagnetic waves in this case is obtained due to the variation of the

macroscopic dielectric constant, which has a periodicity similar to the wavelength of the electromagnetic wave (an example of coherent and incoherent scattering for 1D periodic distribution is shown in Fig. 1.2). Analogously to the crystalline solid case, the photonic BG will occur for certain frequencies for certain directions, consequently inhibiting the propagation of photons at these frequencies for those directions inside the structure [Yab01].

The geometry of PhCs in real space is characterized by the so-called direct (or Bravais) lattice. By definition, a lattice is an infinite array of discrete points with an arrangement and orientation that appears exactly the same from whichever of the points the array is viewed [Ash76]. 1D PhCs have a unique type of lattice, while 2D PhCs have five, and 3D PhCs have fourteen distinct types of lattices. If we consider that a crystal is infinite in real space, the position of the elements of the d-dimensional direct lattice can be described by the position vectors of the lattice $\overrightarrow{R_l}$:

$$\overrightarrow{R_l} = \sum_{j=1}^{d} n_{i_j} \overrightarrow{a_j}, \tag{1.1}$$

with integer-numbers n_{i_j} and basis (or elementary lattice) vectors $\overrightarrow{a_j}$, j=1,…,d.

To describe the whole periodically repeated space, the concept of primitive cell is introduced. A primitive cell is defined by the smallest volume/area of space which, when translated by all vectors of a direct lattice, fills all the space without overlapping. However, such a primitive cell is not unique and to obtain a unique one, the ***Wigner-Seitz*** cell is introduced. The Wigner-Seitz cell around a lattice point is the region of space that is closer to that point than to any other lattice point [Ash76]. The Wigner-Seitz cell can be constructed by drawing the perpendicular bisector planes of the translation vectors from one lattice point to its neighbors. The translation of the Wigner-Seitz cell spanning the vectors $\overrightarrow{a_j}$ in the space produces the lattice of the system. Some of the direct lattices in real space are shown in Figs. 1.3(a), (d), (g).

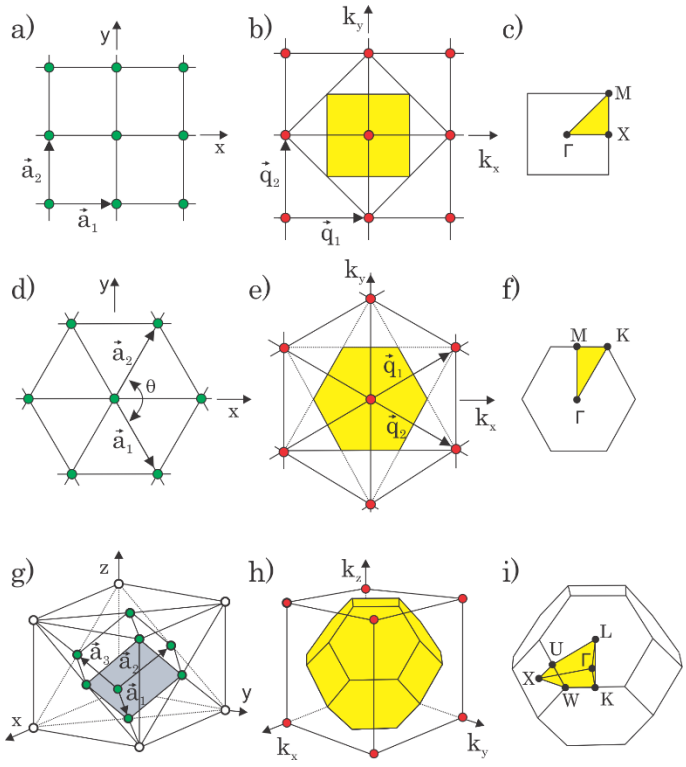

Figure 1.3. (a) A square lattice in direct space, with lattice constants $|\vec{a}_1| = |\vec{a}_b|$, (b) a reciprocal lattice of the square lattice in (a) with periods $q_1 = 2\pi/a_1$, $q_2 = 2\pi/a_2$, $q_1 = q_2$; the area coloured in yellow is a Brillouin zone, (c) the area between Γ-M-X points shaded in yellow, illustrates irreducible Brillouin zone; (d) A triangular lattice in direct space, where lattice constants are equal to $|\vec{a}_1| = |\vec{a}_b|$ and $\theta = 120°$. (e) the reciprocal lattice of triangular lattice in (d), where yellow hexagon marks a Brillouin zone and (f) illustrates irreducible Brillouin zone for the area between Γ-M-K; (g) Face-centered cubic lattice; (h) The reciprocal lattice of (g) where yellow volume illustrates a Brillouin zone and in (i) the irreducible Brillouin zone with the corner points Γ-X-U-L-K-W is demonstrated.

One more important parameter of the PhC is the ***lattice constant***. The lattice constant is a physical dimension, which defines the size of the primitive cell and is equal to the modulus of the basis vector of the direct space $a_j = |\overrightarrow{a_j}|$, where j=1,…,d. A 2D lattice would have two lattice constants a_1 and a_2. For both cases of square and triangular (as well called rhombic) lattices of 2D PhC (shown in Fig. 3(a) and (d) respectively), $a = a_1 = a_2$, therefore it is sufficient to relate it only with one of the basis vectors. The same happens for 3D cubic PhC, where lattice constant is $a = a_1 = a_2 = a_3$.

When the lattice constant and the size of scatterers (the material in the position of lattice points with the dielectric constant different from the host material) are known, the ***filling factor*** f of the structure (percentage of area or volume occupied by the constituent objects in the total area or volume of the PhC) can be calculated. As an example, the filling factor for a square lattice when the scatterrers are rods with radius r is:

$$f = \frac{2\pi r^2}{a^2}, \tag{1.2}$$

and for a triangular lattice

$$f = \frac{2\pi r^2}{\sqrt{3}a^2}. \tag{1.3}$$

To understand basic concepts of the periodic systems, the ***reciprocal lattice*** is introduced. The relation between the reciprocal and the direct lattice is given by the Fourier transform of the original (direct) lattice. Let us consider a 3D direct lattice consisting of a set of primitive vectors $\{\vec{a}_1, \vec{a}_2, \vec{a}_3\}$. The reciprocal lattice can be defined by the three primitive vectors $\{\vec{b}_1, \vec{b}_2, \vec{b}_3\}$:

$$\begin{aligned} \overrightarrow{b_1} &= (2\pi/\Omega)\, \overrightarrow{a_2} \times \overrightarrow{a_3}, \\ \overrightarrow{b_2} &= (2\pi/\Omega)\, \overrightarrow{a_3} \times \overrightarrow{a_1}, \\ \overrightarrow{b_3} &= (2\pi/\Omega)\, \overrightarrow{a_1} \times \overrightarrow{a_2}, \end{aligned} \tag{1.4}$$

where $\Omega = \overrightarrow{a_1} \cdot (\overrightarrow{a_2} \times \overrightarrow{a_3})$ is the volume of the elementary cell. For the general case, the reciprocal primitive vector can be expressed as:

$$b_i^{\alpha} = (2\pi/\Omega)\varepsilon_{ijk}\varepsilon^{\alpha\beta\gamma}\overrightarrow{a_j^{\beta}} \times \overrightarrow{a_k^{\gamma}} \begin{cases} i,j,k = 1,2,3 \\ \alpha,\beta,\gamma = x,y,z \end{cases} \tag{1.5}$$

where ε_{ijk} and $\varepsilon^{\alpha\beta\gamma}$are called Levi-Civita symbols and they are totally antisymmetric tensors. The vectors of the direct and the reciprocal lattice satisfy the orthogonality condition $\overrightarrow{a_j} \cdot \overrightarrow{b_\iota} = 2\pi\delta_{ji}$, where δ_{ij} is a Kronecker delta with the

property $\delta_{ij} = 1$, when $i = j$ and $\delta_{ij} = 0$, when $i \neq j$. Some of the reciprocal lattices are shown in Fig. 1.3.

An important concept in the reciprocal lattice is the so-called ***Brillouin zone***, which in fact is the Wigner-Seitz cell for the reciprocal space (In Fig 3. some examples of Brillouin zones are shown). The Brillouin zone can be minimized to irreducible Brillouin zone, Fig. 1.3(c), (f), (i), which contains the information required to deduce the PhC dispersion relation.

A very useful property of PhCs is scaling. The scaling law tells that PhCs with the same lattice geometry, but different size of the lattice constant, will have the same band structure. The only difference will be simply the scales of frequency and the wave vector. Fabrication of structures with small lattice constants is usually a difficult technological task. Therefore, the scaling law helps to simplify experimental studies fabricating larger lattice constants PhCs, which can confirm theoretical predictions for smaller scale crystals [Sak04]. The scalability property of PhCs allows to apply them to a wide frequency range.

The periodicity of the PhC structure is often described by periods rather than the lattice constant and usually they can differ in magnitude. To avoid any confusion, we present several examples in Fig 1.4.

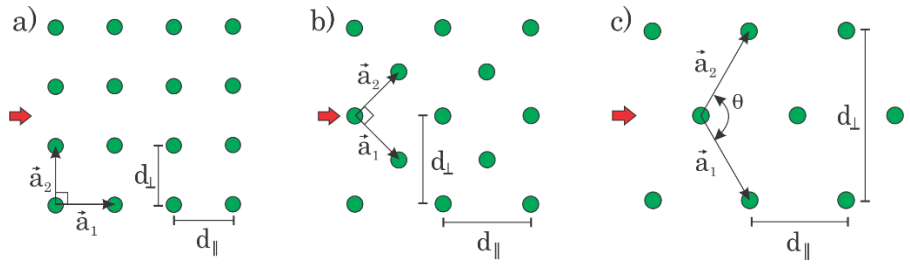

Figure 1.4. (a) A square lattice, where transverse ($d_\perp$) and longitudinal ($d_\parallel$) periods are equal to the lattice constant $d_\perp = d_\parallel = a$ (according to the beam propagation direction). (b) The same lattice as in (a), but rotated by 45° degrees and therefore $d_\perp = d_\parallel = a\sqrt{2}$. (c) A triangular lattice where relation between transverse/longitudinal periods and lattice constant is $d_\perp = 2a\,sin(\theta/2)$, $d_\parallel = 2a\,cos(\theta/2)$. The red arrows in the figure indicate the beam propagation direction.

A 2D PhC according to the direction of light propagation has a transverse period $d_\perp$(transverse to the incoming beam) and longitudinal period $d_\parallel$ (parallel

to the incoming beam). If we have a square lattice and the light is propagating along the ΓX direction (Fig. 1.4(a)), then both transverse and longitudinal periods will be equal to the lattice constant ($d_\perp = d_\parallel = a$). However, if we rotate the same square lattice by 45° degrees, then the beam will propagate along the ΓM direction (Fig. 1.4(b)) and the periods are going to differ from the lattice constant $d_\perp = d_\parallel \neq a$, but they can be related with the it by $d_\perp = d_\parallel = a\sqrt{2}$. Fig. 1.4(c) shows an example of a triangular lattice. In this case, periods are not equal to the lattice constant, but knowing the magnitude of the lattice constant and the angle between the lattice vectors, the transverse and longitudinal periods can be found. In the latter case, the transverse period can be expressed as $d_\perp = 2a\sin(\theta/2)$, while the longitudinal as $d_\parallel = 2a\cos(\theta/2)$. For 1D structures, the period is always equal to the lattice constant $d = a$.

1.1.2. **Chromatic dispersion**

Knowing the dimensionality, the geometry, the lattice constant and the refractive index contrast of the PhC, the photonic BGs can be calculated. The BGs are angle-dependent due to the different periodicities experienced by light propagating at different incidence angles, which results in the fact that the reflected color depends sharply on the angle. If for some frequency range, the BG occurs at all incidence angles, as well as, for both polarizations of light, we call it a ***complete photonic BG***. In such a crystal, light with frequency within the complete BG cannot propagate. For 2D PhC the complete BG can be obtained for in-plane propagation, while for 3D PhCs the complete BG can be obtained in all three dimensions. When the gap appears only in some, but not all the propagation directions, it is called a ***pseudo gap***. In Fig. 1.5 are shown chromatic band diagrams with a complete BG (a) and a pseudo-gap (b).

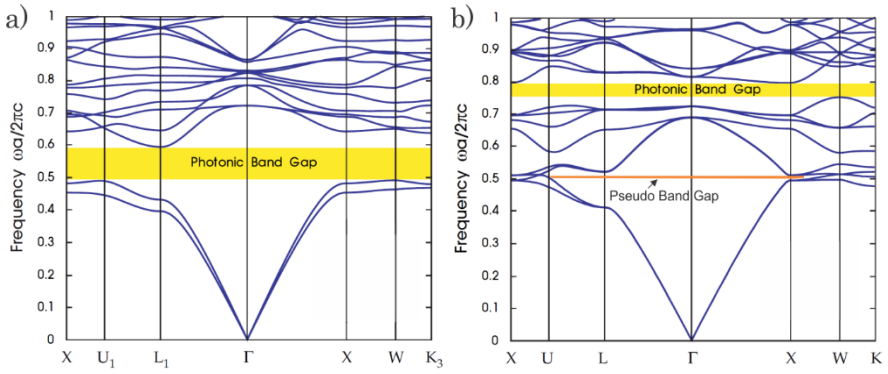

Figure 1.5. Photonic band structures: (a) for the lowest bands of a Yablonovite ("diamond like") structure, producing a full photonic BG [Joa08]; (b) for the lowest bands of an "inverse opal" structure (air sphares in dielectric ($\varepsilon = 13$)), which produce a narrower full BG, as well as pseudo BG marked in orange [Joa08].

After E. Yablonovitch and S. John pioneering publications in the PhC field, there were lots of skepticism from the scientific community about the possibilities to construct PhCs with full 3D BG. Only three years later, the first theoretical prediction in which a 3D PhC with the diamond lattice has complete photonic BG was shown by Ho, Chan and Soukoulis [Ho90]. In 1991, an experimental work of Yablonovitch [Yab91a] demonstrated that 3D PhCs can have complete BG in the microwave regime. The PhC was a modification of a diamond structure (now called "Yablonovite") and it was mechanically constructed by periodically drilling air holes in a dielectric material. Since PhCs are scalable, that means that full BG in the visible regime can be also obtained. After this experiment the science of PhCs has thrived [Yab01]. The full BG in-plane for 2D PhCs was suggested with PhC consisting of square [Pli91a], triangular [Pli91b], and hexagonal [Vil92] lattices of holes and pillars, etc., which was followed by experiments in the microwave regime [McC91, Rob92, Mea92]. A vast number of theoretical proposals to model 1D, 2D and 3D PhCs in order to obtain complete or pseudo-gaps continued through years [Sou96, Qiu99, Koe03, Juo11]. However, experimental demonstration in visible range of full BGs was a huge technological challenge for a long time. Nevertheless, with continuous advances in the synthesis, fabrication and self-assembly of photonic nano-materials through the last decades, the first full 2D BG in the visible regime was demonstrated at the

end of twentieth century in PhC fibers [Kni98, Cre99]. At the same time, a full BG for IR [Gru96, Yam98] and near-IR in 3D PhC was obtained [Nod99, Nod00]. However, even for nowadays technology it remains a challenging task to fabricate a 3D structure with periodicity twice smaller than the wavelength of the visible light. Only very recently (2013) Frolich *et. al.* presented an experimental work, where for the first time a 3D full BG was demonstrated for the visible regime with a titania woodpile structure [Fro13].

Another very important property of PhCs is the emergence of highly localized defect modes within the BG region, which can be obtained, when the periodicity of the PhC is violated, i.e., by introducing a defect. This effect is analogous to the localized impurity states in semiconductor crystals, which is obtained by adding dopants into the crystalline structure. In 1991, Yablonovich experimentally demonstrated that introducing a defect into a 3D PhC creates a localized mode within the BG [Yab91b]. Just as the type (donor or acceptor) of localized mode in a semiconductor depends on the impurity introduced in the crystal, the localized states in PhCs can be as well called donor or acceptor depending on the types of defects introduced. In the work of [Yab91b], a part of dielectric material was removed from the periodic structure, and an acceptor type of mode was created. Depending on the width of the defect layer the frequency of the defect mode could be tuned from low frequency edge, to the center of BG. When an extra dielectric material was added to one of the primitive cells, the donor type localized mode emerged close to the high frequency edge of the BG.

The possibility to create localized modes in PhCs by introducing defects in 1D, 2D or 3D structures is very important as it can be utilized for many applications. Just to give a few examples, a 1D PhC with a defect in one layer can be used as a dielectric Fabry-Perot filter [Wu10a, Son13], a 2D PhC with a line defect can be used as a waveguide for the defect mode [Bro99, Vla05, Cas14], a 3D PhC with the point defects can form optical cavities to trap light [Rin08, Tan11]. Up to now, lots of research has been performed on localized states in PhCs as this phenomenon opens many possibilities to control the flow of light.

1.1.3. **Spatial (angular) dispersion**

Electromagnetic waves propagation can be dramatically modified due to photonic BGs of PhCs, which are presented in photonic band diagrams (chromatic dispersion) (Fig. 1.5). In 1998, H. Kosaka proposed an alternative approach to control the photon flow based on the use of the "allowed" photonic bands, by representing ***spatial dispersion diagrams*** for PhCs (Fig. 1.6(a)). In these diagrams we plot $\omega a/2\pi c$ as a function of k_x and k_y, which represents the dispersion surfaces. Spatial dispersion surfaces can be projected to a plane of k_x, k_y to represent the spatial dispersion curves (in literature also called iso-frequency/equi-frequency contours) (Fig. 1.6(b)). The richness of spatial dispersion curves allows to shape the beam in diverse manners, i.e. by managing spatial dispersion, one can control the diffraction properties of narrow beams. This idea led to the demonstration of novel optical effects such as the superprism effect (here broad beams are used), the self-collimation effect, negative refraction, flat lensing, etc. [Van14].

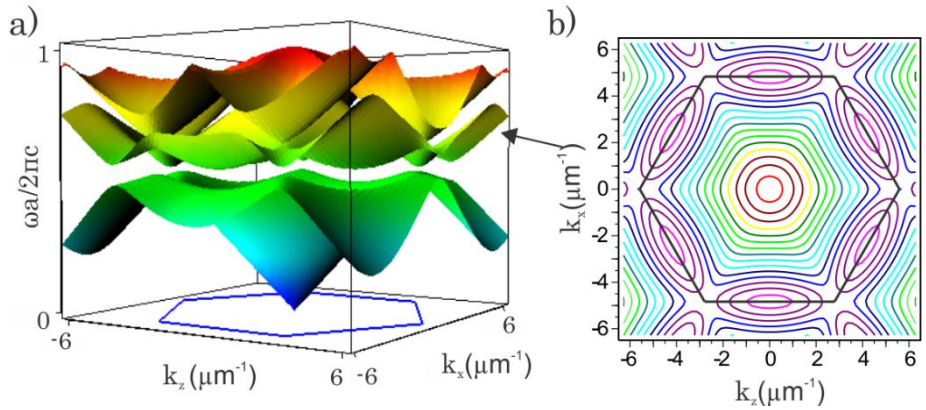

Figure 1.6. (a) An example of a dispersion surface for a 2D PhC of a rhombic symmetry, where three dispersion surfaces for the lowest three bands are shown; (b) The plot of the equi-frequency contour for the second band. An arrow indicates the dispersion surface corresponding to the equi-frequency contour.

To explain the physical principles of light propagation in PhCs, as well as, the engineering of chromatic and spatial dispersion diagrams, the basic concepts

of electromagnetic waves propagation in periodic structures are introduced in the following sections.

1.1.4. **Wave propagation theory in periodic media**

Propagation of waves in periodic media was firstly studied in the field of solid-state physics. In 1928, Felix Bloch, extending the work of Gaston Floquet, proved that electrons in a crystalline (periodic) solid propagate without scattering and can be described by a plane wave multiplying a periodic envelope function, which forms the so-called Bloch wave [Ash76]. Moreover, the energy of the propagating electrons takes discrete values depending on the crystal wave vector, which is given by the plane wave of the Bloch wave. If the energy of the electron in the crystalline solid is represented as a function of the crystal wave vector, an energy band diagram is obtained. Since the PhCs are analogous to crystalline solids, the theory developed by Bloch can be extended to PhCs.

One of the most widely used methods to calculate band diagrams of PhCs is the plane-wave expansion (PWE) method [Sak04]. The PWE method consists in representing the periodic material parameters (ε, μ) and the field amplitude by their Fourier expansions on the basis of the reciprocal lattice vectors, which makes possible to convert the partial differential equations describing light propagation into an infinite matrix eigenvalue problem. The matrix is truncated and numerically solved, finding the frequencies corresponding to each Bloch wave, which allows to obtain the band diagram of the periodic medium. In the following, we will describe the path from the Maxwell's equations to the infinite eigenvalue problem.

If we consider an electromagnetic wave propagating in a media in the absence of charges and currents (which is the case for PhCs), the Maxwell's equations can be written as:

$$\nabla \cdot \vec{D}(\vec{r},t) = 0, \tag{1.6}$$

$$\nabla \cdot \vec{B}(\vec{r},t) = 0, \tag{1.7}$$

$$\nabla \times \vec{E}(\vec{r},t) = -\frac{\partial}{\partial t}\vec{B}(\vec{r},t), \tag{1.8}$$

$$\nabla \times \vec{H}(\vec{r},t) = \frac{\partial}{\partial t}\vec{D}(\vec{r},t), \tag{1.9}$$

where $\vec{D}$ is the electric displacement field, $\vec{B}$ is the magnetic induction field, $\vec{E}$ is the electric field, and $\vec{H}$ is the magnetic field.

If we consider a non-magnetic material ($\mu = \mu_0$) and that the permittivity $\varepsilon(\vec{r})$ is real-valued, isotropic, and perfectly periodic with respect to the spatial coordinate $\vec{r}$, we can write:

$$\vec{\mathrm{B}}(\vec{r},t) = \mu_0 \vec{\mathrm{H}}(\vec{r},t), \tag{1.10}$$

and:

$$\vec{\mathrm{D}}(\vec{r},t) = \varepsilon_0 \varepsilon(\vec{r}) \vec{\mathrm{E}}(\vec{r},t). \tag{1.11}$$

The resulting Maxwell's equations are:

$$\nabla \cdot \{\varepsilon(\vec{r})\vec{\mathrm{E}}(\vec{r},t)\} = 0, \tag{1.12}$$

$$\nabla \cdot \vec{H}(\vec{r},t) = 0, \tag{1.13}$$

$$\nabla \times \vec{E}(\vec{r},t) = -\mu_0 \frac{\partial}{\partial t}\vec{H}(\vec{r},t), \tag{1.14}$$

$$\nabla \times \vec{H}(\vec{r},t) = \varepsilon_0 \varepsilon(\vec{r}) \frac{\partial}{\partial t}\vec{E}(\vec{r},t). \tag{1.15}$$

If we calculate the time derivative of Eqs. (1.14) and (1.15) we obtain

$$\nabla \times \frac{\partial \vec{\mathrm{E}}(\vec{r},t)}{\partial \mathrm{t}} = -\mu_0 \frac{\partial^2 \vec{\mathrm{H}}(\vec{r},t)}{\partial \mathrm{t}^2}, \tag{1.16}$$

$$\nabla \times \frac{\partial \vec{\mathrm{H}}(\vec{r},t)}{\partial \mathrm{t}} = \varepsilon_0 \varepsilon(\vec{r}) \frac{\partial^2 \mathrm{E}(\vec{r},t)}{\partial \mathrm{t}^2}. \tag{1.17}$$

Introducing Eqs. (1.14) and (1.15) into (Eq 1.16) and (Eq 1.17), we obtain two alternative forms of wave equations:

$$\frac{1}{\varepsilon(\vec{r})}\nabla\times\{\nabla\times\vec{\mathrm{E}}(\vec{r},t)\}=-\frac{1}{c^2}\frac{\partial^2\vec{\mathrm{E}}(\vec{r},t)}{\partial \mathrm{t}^2}, \tag{1.18}$$

$$\nabla\times\left\{\frac{1}{\varepsilon(\vec{r})}\nabla\times\vec{\mathrm{H}}(\vec{r},t)\right\}=-\frac{1}{c^2}\frac{\partial^2\vec{\mathrm{H}}(\vec{r},t)}{\partial \mathrm{t}^2}, \tag{1.19}$$

where c is the speed of light in free space given by

$$c=\frac{1}{\sqrt{\varepsilon_0\mu_0}}. \tag{1.20}$$

In order to obtain the dispersion relation as shown in the frequency diagrams, harmonic electromagnetic waves will be considered:

$$\vec{\mathrm{E}}(\vec{r},t)=\vec{\mathrm{E}}(\vec{r})e^{-i\omega t}, \tag{1.21}$$

$$\vec{\mathrm{H}}(\vec{r},t)=\vec{\mathrm{H}}(\vec{r})e^{-i\omega t}. \tag{1.22}$$

Introducing them into the wave equations, they become:

$$\frac{1}{\varepsilon(\vec{r})}\nabla\times\{\nabla\times\vec{\mathrm{E}}(\vec{r})\}=\frac{\omega^2}{c^2}\vec{\mathrm{E}}(\vec{r}), \tag{1.23}$$

$$\nabla\times\left\{\frac{1}{\varepsilon(\vec{r})}\nabla\times\vec{\mathrm{H}}(\vec{r})\right\}=\frac{\omega^2}{c^2}\vec{\mathrm{H}}(\vec{r}). \tag{1.24}$$

In the case of a PhC, the material is periodic in space, so the permittivity $\varepsilon(\vec{r})$ fulfills:

$$\varepsilon\left(\vec{r}+\vec{R}\right)=\varepsilon(\vec{r}), \tag{1.25}$$

where $\vec{R}=m_1\vec{a}_1+m_2\vec{a}_2+m_3\vec{a}_3$ is a 3D direct lattice vector, $\{\vec{a}_i\}$ are the primitive lattice vectors of the PhC, and m_i are integers, with $i=1,2,3$ (for each dimension). The relation between the primitive vectors of the direct lattice and the reciprocal lattice vectors, $\{\vec{b}_i;\ \mathrm{i}=1,2,3\}$, is given in Eqs. (1.2), and a vector of the 3D reciprocal lattice can be expressed as $\vec{G}=l_1\vec{b}_1+l_2\vec{b}_2+l_3\vec{b}_3$. Thus, the periodic permittivity, or more conveniently its inverse, can be Fourier expanded in the vectors of the reciprocal lattice as:

$$\frac{1}{\varepsilon(\vec{r})}=\sum_{\vec{G}}\epsilon_{\vec{G}}^{-1}\,e^{i\vec{G}\cdot\vec{r}}, \tag{1.26}$$

where $\epsilon_{\vec{G}}^{-1}$ is the Fourier coefficient the of function $1/\varepsilon(\vec{r})$, which fullfils $\epsilon_{-\vec{G}}^{-1} = \epsilon_{\vec{G}}^{-1^*}$ as the permittivity is a real function. On the other hand, the electric and magnetic fields in the PhC must fulfill the Bloch theorem:

$$\vec{\mathrm{E}}(\vec{r}) = \vec{u}_{\vec{k}n}(\vec{r})e^{i\vec{k}\cdot\vec{r}}, \tag{1.27}$$

$$\vec{\mathrm{H}}(\vec{r}) = \vec{v}_{\vec{k}n}(\vec{r})e^{i\vec{k}\cdot\vec{r}}, \tag{1.28}$$

where the electric and magnetic fields are characterized by a wave vector $\vec{k}$ in the first Brillouin zone and a band index n, and $\vec{u}_{\vec{k}n}(\vec{r})$ and $\vec{v}_{\vec{k}n}(\vec{r})$ are periodic functions with the periodicity of the lattice and satisfy $\vec{u}_{\vec{k}n}(\vec{r}+\vec{R}) = \vec{u}_{\vec{k}n}(\vec{r})$ and $\vec{v}_{\vec{k}n}(\vec{r}+\vec{R}) = \vec{v}_{\vec{k}n}(\vec{r})$. These periodic functions can be Fourier expanded in the vectors of the reciprocal lattice, and Eqs. (1.27) and (1.28) can be rewritten as

$$\vec{\mathrm{E}}(\vec{r}) = \sum_{\vec{G}} \vec{E}_{\vec{k}n,\vec{G}}\, e^{i(\vec{G}+\vec{k})\cdot\vec{r}}, \tag{1.29}$$

$$\vec{\mathrm{H}}(\vec{r}) = \sum_{\vec{G}} \vec{H}_{\vec{k}n,\vec{G}}\, e^{i(\vec{G}+\vec{k})\cdot\vec{r}}, \tag{1.30}$$

where $\vec{E}_{\vec{k}n,\vec{G}}$ and $\vec{H}_{\vec{k}n,\vec{G}}$ are the expansion coefficients in reciprocal space of the electric and the magnetic field, respectively.

Substituting Eqs. (1.26), (1.29), and (1.30) into (1.23) and (1.24) we obtain

$$\sum_{\vec{G}''} \epsilon_{\vec{G}''}^{-1} e^{i\vec{G}''\cdot\vec{r}} \nabla \times \left\{ \nabla \times \sum_{\vec{G}'} \vec{E}_{\vec{k}n,\vec{G}'}\, e^{i(\vec{G}'+\vec{k})\cdot\vec{r}} \right\} = \frac{\omega^2}{c^2} \sum_{\vec{G}} \vec{E}_{\vec{k}n,\vec{G}}\, e^{i(\vec{G}+\vec{k})\cdot\vec{r}}, \tag{1.31}$$

$$\nabla \times \left\{ \sum_{\vec{G}''} \epsilon_{\vec{G}''}^{-1} e^{i\vec{G}''\cdot\vec{r}} \nabla \times \sum_{\vec{G}'} \vec{H}_{\vec{k}n,\vec{G}'}\, e^{i(\vec{G}'+\vec{k})\cdot\vec{r}} \right\} = \frac{\omega^2}{c^2} \sum_{\vec{G}} \vec{H}_{\vec{k}n,\vec{G}}\, e^{i(\vec{G}+\vec{k})\cdot\vec{r}}. \tag{1.32}$$

Using the mathematical property $\nabla \times (\varphi\vec{F}) = \nabla\varphi \times \vec{F} + \varphi\nabla \times \vec{F}$, taking into account that $\nabla \times \vec{E}_{\vec{k}n,\vec{G}'} = 0$ and $\nabla \times \vec{H}_{\vec{k}n,\vec{G}'} = 0$, considering that $\vec{G}'' = \vec{G} - \vec{G}'$ and that plane waves $e^{i\vec{G}\cdot\vec{r}}$ form an orthogonal set, Eqs. (1.31) and (1.32) become:

$$-\sum_{\vec{G}'}\epsilon^{-1}_{\vec{G}-\vec{G}'}\left(\vec{k}+\vec{G}'\right)\times\left\{\left(\vec{k}+\vec{G}'\right)\times\vec{E}_{\vec{k}n,\vec{G}'}\right\}=\frac{\omega^2}{c^2}\vec{E}_{\vec{k}n,\vec{G}} \tag{1.33}$$

$$-\sum_{\vec{G}'}\epsilon^{-1}_{\vec{G}-\vec{G}'}\left(\vec{k}+\vec{G}\right)\times\left\{\left(\vec{k}+\vec{G}'\right)\times\vec{H}_{\vec{k}n,\vec{G}'}\right\}=\frac{\omega^2}{c^2}\vec{H}_{\vec{k}n,\vec{G}} \tag{1.34}$$

Eqs. (1.33) and (1.34) represent an eigenvalue problem in which, for every $\vec{k}$, the eigenvalue is ω^2/c^2. Thus, the solutions of either Eq. (1.33) or Eq. (1.34) allow to plot the band diagram of the PhC. The left hand-hand side of Eq. (1.33) or Eq. (1.34) is a matrix of infinite size, therefore, it must be truncated in order to numerically solve the eigenvalue problem. In general, the larger the matrix is taken, the more accurate are the solutions for the band diagrams and higher bands can be obtained. Matrices of the order of 10^3 elements can be used to numerically solve the eigenvalue problem. Furthermore, if the eigenvectors are calculated, by using Eqs. (1.29) and (1.30), it is possible to find the electric and magnetic fields in real space, respectively. These are the eigenfunctions of the differential equations, the so-called Bloch functions.

1.1.5. **Natural photonic crystals**

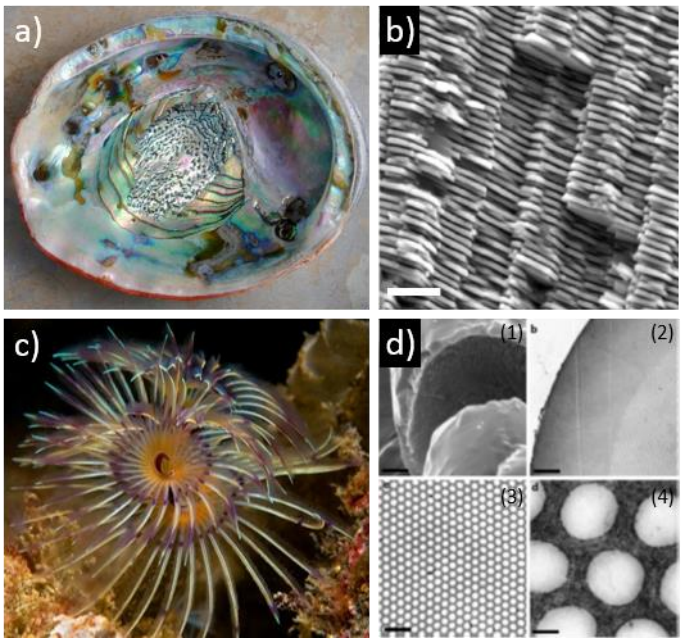

Figure 1.7. (a) Abalone shell. (b) The cross-section of the abalone shell showing a layered microstructure (the scale shown in the image is of 10 μm) [Tan04]. (c) Polychaete worm. (d) (1) Scanning electron micrograph (SEM) and (2-4) transmission electron micrograph (TEM) images of transverse sections of hair-like setae from polychaete worms. Bars: (1) 2 mm; (2) 5 mm; (3) 1 mm; (4) 120 nm [Vuk03].

After the pioneering publications of E. Yablonovich and S. John, when the scientists were struggling to fabricate different kinds of PhCs to demonstrate BGs, it was realized that a variety of fauna, flora and natural materials possess multilayer and crystal like structures. For example, silver reflections in many fishes [Den71] and cephalopods [Mat07], iridescence reflections in scarabs [Brad10], abalone shells [Tan04], some fruits [Lee91] and plant leaves [Lee97] are due to the crystal multilayer structures (1D PhCs) (Figs. 1.7(a) and (b) show an abalone shell and its multilayer structure), while the hairs of sea worm

polychaete (Figs. 1.7(c) and (d)) [Vuk03], the feathers of birds such as peacock [Zi03] and magpie [Vig06] are 2D PhCs.

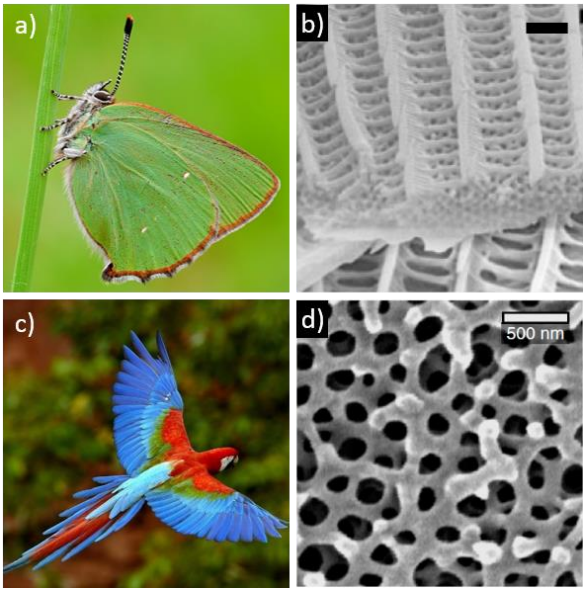

Figure 1.8. (a) *Callophrys ruby* butterfly (b) SEM images of *Callophrys ruby* wing. The scale bar is 1 μm [Sab11] (c) *Scarlet macow* (d) Cross-sectional SEM image of the structure of scarlet macow feathers[Yin12]

Many different beetle and butterfly species have wings, which include structures from 1D, 2D to 3D PhCs [Gal10] (Fig. 1.8(b) shows 3D butterfly structure [Sab11]). 3D PhCs are found in natural opals [Col01] (synthetically fabricated PhCs which mimic natural opals structure are called colloidal crystals). Quasi-ordered (amorphous) 3D PhCs, periodic in all three dimensions, although with imperfections, were found in feathers of scarlet macow (Figs. 1.8(c),(d)) [Yin12]. Each of these natural PhCs has a photonic BG structure, however it is always only a partial (pseudo) BG, which means that the waves of different colours are strongly Bragg-scattered in different directions and, therefore, strong iridescence is observed [Yab01].

1.2. One-dimensional photonic crystals

1.2.1. Chromatic dispersion and frequency band gaps

It is known that 1D periodic structures reflect efficiently the waves with wavelength equal to $\lambda \approx 2d$ (d stands for the period). This is the condition of Bragg reflection: the reflected waves are in phase with one another (Fig. 1.9) and result in a constructive interference.

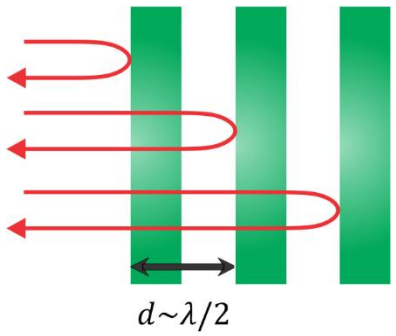

Figure 1.9. Reflections from the periodic interfaces which create constructive interference.

The BGs appear where no real $\vec{k}$ solutions are possible and a forbidden window for particular frequencies occurs [Yab87, Joh87, Joa08, Ho90, Yab91a, Yab93]. The waves at those particular frequencies cannot propagate in the structure and are simply reflected. The central frequency of the BG or mid-gap frequency ω_m is equal to $\omega_m = \frac{\pi c}{d} m$ (or wavelength $\lambda_m = 2d/m$) where m is the order of the BG (m =1,2,3…), so ω_m it is directly related to the period of the structure. The width of the photonic BG ($\Delta\omega_m$) is different for different values of m and depends on the refractive index profile. Very roughly, the width for the first band gap is: $\Delta\omega_1 = c\frac{\pi}{\lambda}\Delta n$ [Joa08], therefore the higher the refractive index contrast Δn between the two materials of the layered structure, the broader is the width of the band-gap [Joa08].

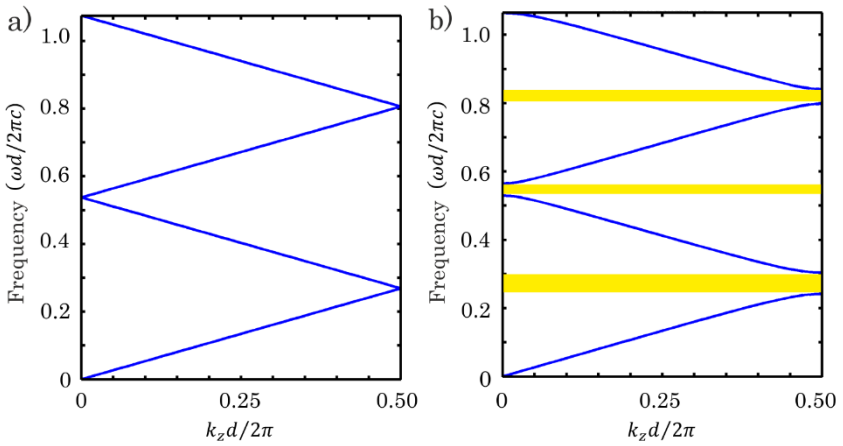

Figure 1.10. (a) Dispersion relation of the material with refractive index $n = 1.86$. (b) Dispersion relation of the periodic structure with the period $d = 0.16\ \mu m$ ($d_1 = d_2 = 0.08\ \mu m$) and refractive indices $n_1 = 2.17$, $n_2 = 1.49$. Yellow areas correspond to BGs.

Photonic band diagrams (chromatic dispersion relation) can be calculated by the PWE method described previously. Fig. 1.10 shows two examples of such diagrams calculated by the PWE method. The case (a) shows the dispersion relation of a homogeneous material, where the refractive index of the material is chosen to be $n = 1.86$, with the refractive index contrast $\Delta n \to 0$; (for exactly $\Delta n = 0$ the folding of dispersion is shown only for the illustration purposes, but it does not have any physical meaning). Fig. 1.10(b) shows the dispersion relation for the periodic structure consisting of two materials with different refractive indices: one with $n_1 = 2.17$ and the other one with $n_2 = 1.49$. In this particular case, the period of the structure is taken as $\lambda/2$ at $\lambda = 0.328$ μm (inside material), therefore $d = 0.164\mu m$. In the example $d_{l_1} = d_{l_2} = 0.082\mu m$ (d_{l_1}– thickness of the layer of the first material, d_{l_2}– thickness of the layer of the second material). The effective refractive index n_{eff}, which represents the refractive index of the system if it was made only of one material, can be calculated as $n_{eff} = \sqrt{(d_1 n_1^2 + d_2 n_2^2)/(d_1 + d_2)}$, and for this particular 1D PhC, as $d_{l_1} = d_{l_2}$ it can be calculated with expression $n_{eff} = \sqrt{(n_1^2 + n_2^2)/2}$, therefore $n_{eff} = 1.86$.

1.2.2. **Coupled-mode method**

For the most simple calculation of the transmission and reflection of a 1D PhC around the BG it is possible to use a coupled-mode model for forward-backward propagating waves (the infinite number of harmonics is truncated to only two).

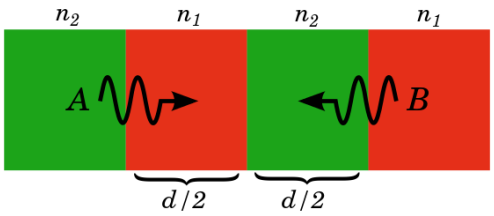

Figure 1.11. Schematic representation of amplitudes of the forward and backwards propagating fields along 1D PhC.

Let's consider a periodic medium along the z propagation direction consisting of two different materials of the same thickness $d/2$, and refractive indices n_1 and n_2 (Fig. 1.11), so that the dielectric constant fulfills $\varepsilon(z) = \varepsilon(z + d)$ and

$$\varepsilon(z) = \begin{cases} \varepsilon_0 n_2^2 & 0 < z < d/2, \\ \varepsilon_0 n_1^2 & d/2 < z < d. \end{cases} \tag{1.35}$$

Considering only two modes, forward and backward waves, with the same transverse profile $\vec{E}(x, y)$, the electric field in such medium can be described by the following expression:

$$\vec{E} = A(z)\vec{E}(x, y)e^{i(\omega t - kz)} + B(z)\vec{E}(x, y)e^{i(\omega t + kz)}, \tag{1.36}$$

where $A(z)$ and $B(z)$ are the amplitudes of the forward and backwards propagating modes, respectively. The evolution of these amplitudes is governed by the following coupled-mode equations [Yar03]:

$$\frac{dA}{dz} = -i\Delta kA - i\Omega B, \tag{1.37}$$

$$\frac{dB}{dz} = i\Delta kB + i\Omega^* A. \tag{1.38}$$

Here, $\Delta k = k - \pi/d$ corresponds to the wavevector from the edge of the first Brillouine zone, and the coupling Ω between the two counterpropagating waves can be calculated as [Yar03]:

$$\Omega = \frac{\mathrm{i}}{\lambda}\frac{2(n_2^2 - n_1^2)}{n_1^2 + n_2^2}, \tag{1.39}$$

where the effective refractive index of the 1D PhC has been taken as $\sqrt{\frac{n_1^2+n_2^2}{2}}$. Since we are interested in finding the transmission and reflection spectrum around the BG, to calculate the value of the coupling we consider the wavelength corresponding to the edge of the Brillouin zone, λ = 2d.

By diagonalizing the coupled-mode equations (1.37) and (1.38), and considering as contour conditions that the amplitude of forward propagating field at the input is $A(z = 0) = 1$, while the backwards propagating field at the output is $B(z = L) = 0$, it is easy to calculate the transmission spectrum, $T = |A(z = L)|^2$, and the reflection spectrum, $R = |B(z = 0)|^2$, as a function of Δk:

$$T = \left|\frac{2\xi}{e^{\xi L}(\lambda + i\Delta k) + e^{-\xi L}(\lambda - i\Delta k)}\right|^2, \tag{1.40}$$

$$R = 1 - T, \tag{1.41}$$

where L is the length of the 1D PhC, and $\xi = \xi_1 = -\xi_2 = \pm\sqrt{-\Delta k^2 + |\Omega|^2}$ are the eigenvalues resulting from the diagonalization of the coupled-mode equations. We can also express the transmission and reflection spectra as a function of the angular frequency $\Delta\omega = \omega - \omega_0$, by multiplying Δk by the speed of light in vacuum and dividing by the effective refractive index, i.e., $\Delta\omega = c\sqrt{2/(n_1^2 + n_2^2)}\Delta k$, being $\omega_0 = c\sqrt{2/(n_1^2 + n_2^2)}\pi/d$ the central frequency of the bandgap. Furthermore, the width of the BG can be estimated as [Yar03]:

$$\Delta\omega_{BG} = \omega_0\frac{d}{\pi}2|\Omega| = \omega_0\frac{2}{\pi}\frac{(n_2^2 - n_1^2)}{n_1^2 + n_2^2}. \tag{1.42}$$

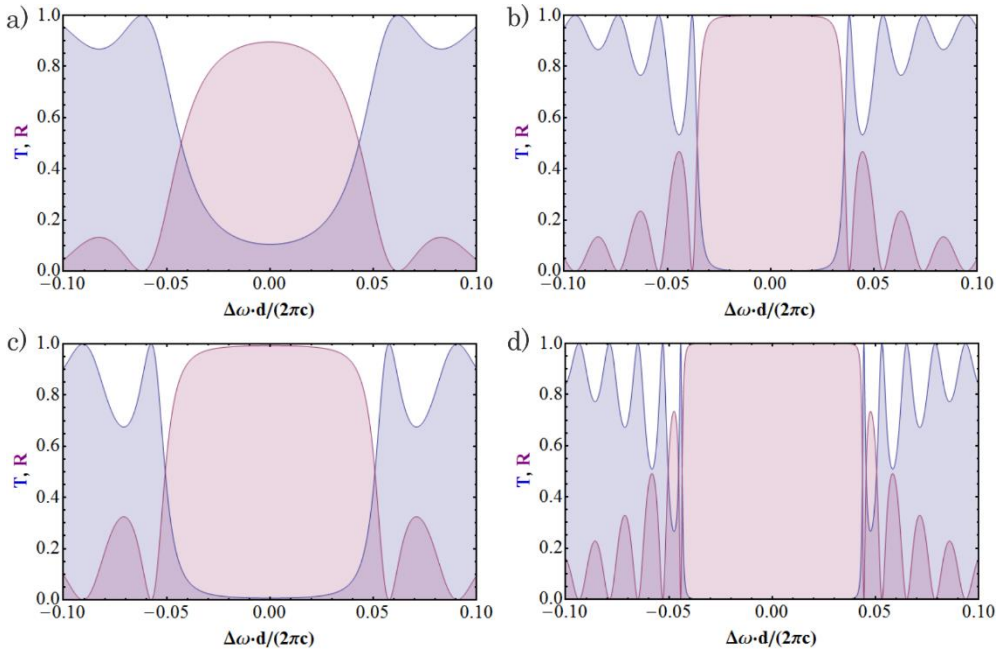

Figure 1.12. Transmission-reflection spectra for 1D PhC of a finite length, calculated from coupled mode model for the PhC with parameters $n_1 = 2.17$, $n_2 = 1.49$, $d_{l_1} = d_{l_2} = 0.082\mu m$; (a) with $N = 5$. (b) with $N = 12$; for the PhC with parameters $n_1 = 3.17$, $n_2 = 1.49$, $d_{l_1} = d_{l_2} = 0.082\mu m$; (c) with $N = 5$. (d) with $N = 12$. Blue line corresponds to transmission, purple line corresponds to reflection.

Fig. 1.12 shows the transmission-reflection spectra calculated from the coupled mode model, where transmission is marked with blue colour while reflection with purple. Fig. 1.12 demonstrates that the reflectivity of the structure within the BG increases with the number of periods, and that the width of the gap, $\Delta\omega$, depends on the refractive index contrast.

The structural parameters of the 1D PhC in Fig. 1.12(a) and (b) are the same as previously described in Fig. 1.10 ($n_1 = 2.17, n_2 = 1.49$ and $d_{l_1} = d_{l_2} = 0.082\mu m$), the only difference between the figures is the number of periods N (in (a) $N = 5$, while in (b) $N = 12$). To completely block the transmission, a minimum number of periods in the structure must be present. If that threshold is not reached, frequencies belonging to the forbidden BG will be partially transmitted (Fig 1.12(a)). In Fig. 1.12(b) full reflection and no transmission can be seen, where, with $N = 12$, the threshold is reached. Using Eq. (1.42) we can also estimate the

width of the BG obtaining a value of $\Delta\omega_{BG} \cdot d/(2\pi c) \approx 0.06$, which is very similar to the one calculated with the PWE method.

Additionally, we have increased the refractive index contrast of the structure to demonstrate that the width of the BG $\Delta\omega$ depends on it (we have set $n_1 = 3.17$, while all other parameters were kept the same). Fig. 1.11(c) ($N = 5$) and Fig. 1.12(d) ($N = 12$), show broader width of BG compared to Figs. 11(a) and (b).

1.2.3. Scattering (transfer) matrix method

Coupled mode theory for forward-backward propagating waves is convenient and allows analytical results. However, it gives only one of the m BG orders. To obtain higher order BGs, full multiple scattering theory can be used [Sal07].

In this case, we also consider two fields, one propagating forward and one backwards, and the same periodic medium as before consisting of two different materials of the same thickness $d/2$, and refractive indices n_1 and n_2. The full electric field in this medium is given by Eq. (1.36). Let's focus on one period of the 1D PhC, see Fig. 1.13.

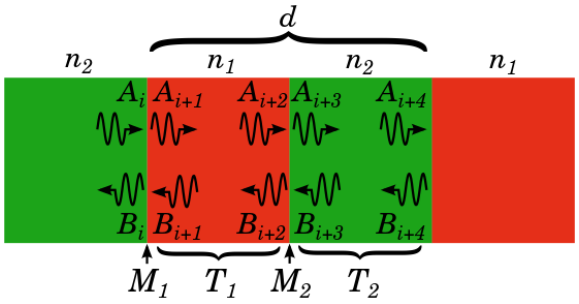

Figure 1.13. Schematic representation of amplitudes of the forward and backwards propagating fields in different positions along one period of the 1D PhC.

We consider first an interface between the layer with refractive index n_2 and with n_1. At that interface, part of the incident field from the left, we will call it

A_i, is reflected back and another part is transmitted. Similarly, the backwards field coming from the other side of the interface B_{i+1} is partially reflected and transmitted. Therefore, the forward field after the interface A_{i+1} will consist of the transmitted part of A_i and the reflected part of B_{i+1}, whereas the backwards propagating field before the interface B_i will be the sum of the reflected A_i and the transmitted B_{i+1} field. This is summarized by the following equations:

$$\begin{pmatrix} A_{i+1} \\ B_i \end{pmatrix} = \begin{pmatrix} t_{21} & r_{12} \\ r_{21} & t_{12} \end{pmatrix} \begin{pmatrix} A_i \\ B_{i+1} \end{pmatrix}, \tag{1.43}$$

where r_{jk} and t_{jk} are the reflection and transmission coefficients, respectively, from a layer with n_j to a layer with n_k refractive index. The values of r_{jk} and t_{jk} are:

$$r_{jk} = \frac{n_j - n_k}{n_j + n_k}, \tag{1.44}$$

$$t_{jk} = \frac{2n_j}{n_j + n_k}. \tag{1.45}$$

In particular, $r_{jk} = -r_{kj}$, so we define $r = r_{12} = -r_{21}$. The matrix in Eq. (1.43) is called scattering matrix. In Eq. (1.43) the vector on the left hand side of the equality includes fields corresponding to two different positions in space. Eq. (1.43) must be rewritten in a way that on the left hand side the vector includes the fields behind the interface, whereas on the right hand side appears the vector corresponds to the fields in front the interface:

$$\begin{pmatrix} A_{i+1} \\ B_{i+1} \end{pmatrix} = \frac{1}{t_{21}} \begin{pmatrix} 1 & r \\ r & 1 \end{pmatrix} \begin{pmatrix} A_i \\ B_i \end{pmatrix} = M_1 \begin{pmatrix} A_i \\ B_i \end{pmatrix}. \tag{1.46}$$

Therefore, by applying the matrix in Eq. (1.46) to the amplitudes of the fields in front of the interface, we get the amplitudes behind the interface. The type of matrix in Eq. (1.46) is called wave-transfer matrix. The fields behind the interface will propagate through the first layer of thickness $d/2$ and refractive index n_1, changing their phase as

$$\begin{pmatrix} A_{i+2} \\ B_{i+2} \end{pmatrix} = \begin{pmatrix} e^{ik_0 n_1 d/2} & 0 \\ 0 & e^{-ik_0 n_1 d/2} \end{pmatrix} \begin{pmatrix} A_{i+1} \\ B_{i+1} \end{pmatrix} = T_1 \begin{pmatrix} A_{i+1} \\ B_{i+1} \end{pmatrix}, \tag{1.47}$$

where $k_0 = 2\pi/\lambda_0$ is the wavenumber in vacuum. At $d/2$ we arrive at the next interface, where there is a refractive index change from n_1 to n_2. Similarly as for the first interface, the amplitudes of the fields behind the interface are:

$$\begin{pmatrix} A_{i+3} \\ B_{i+3} \end{pmatrix} = \frac{1}{t_{12}} \begin{pmatrix} 1 & -r \\ -r & 1 \end{pmatrix} \begin{pmatrix} A_{i+2} \\ B_{i+2} \end{pmatrix} = M_2 \begin{pmatrix} A_{i+2} \\ B_{i+2} \end{pmatrix}. \tag{1.48}$$

Finally, light will travel along the distance $d/2$ of the second layer of refractive index n_2 before making a full period, leading to a change of phase given by:

$$\begin{pmatrix} A_{i+4} \\ B_{i+4} \end{pmatrix} = \begin{pmatrix} e^{ik_0 n_2 d/2} & 0 \\ 0 & e^{-ik_0 n_2 d/2} \end{pmatrix} \begin{pmatrix} A_{i+3} \\ B_{i+3} \end{pmatrix} = T_2 \begin{pmatrix} A_{i+3} \\ B_{i+3} \end{pmatrix}. \tag{1.49}$$

Thus, the change of the field amplitudes propagating one period of the 1D PhC is given by

$$\begin{pmatrix} A_{i+4} \\ B_{i+4} \end{pmatrix} = T_2 M_2 T_1 M_1 \begin{pmatrix} A_i \\ B_i \end{pmatrix}. \tag{1.50}$$

Defining the matrix $P = T_2 M_2 T_1 M_1$, and considering that we started in the period I and evolved the field until the next period $I + 1$ so we can rewrite the amplitudes as $\begin{pmatrix} A_{I+1} \\ B_{I+1} \end{pmatrix} = \begin{pmatrix} A_{i+4} \\ B_{i+4} \end{pmatrix}$ and $\begin{pmatrix} A_I \\ B_I \end{pmatrix} = \begin{pmatrix} A_i \\ B_i \end{pmatrix}$, the previous equation can be reexpressed as:

$$\begin{pmatrix} A_{I+1} \\ B_{I+1} \end{pmatrix} = P \begin{pmatrix} A_I \\ B_I \end{pmatrix}. \tag{1.51}$$

Similarly, if we consider light traveling K periods of a 1D PhC, the amplitude of the forward and backward propagating fields will be given by applying K times the wave-transfer matrix for one period:

$$\begin{pmatrix} A_{I+K} \\ B_{I+K} \end{pmatrix} = P^K \begin{pmatrix} A_I \\ B_I \end{pmatrix}. \tag{1.52}$$

The values of the transmission and reflection can be found from the elements of the matrix P^N (N is the number of periods of finite PhC). Behind the PhC, there cannot be field propagating backwards, therefore $B_{NP} = 0$ and we have

$$\begin{pmatrix} A_N \\ 0 \end{pmatrix} = P^N \begin{pmatrix} A_0 \\ B_0 \end{pmatrix}. \tag{1.53}$$

The transmission and the reflection coefficients for the amplitude will be equal to A_N/A_0 and B_0/A_0, respectively, which can be found from Eqs. (1.53), in which

$$P^N = \begin{pmatrix} P_{11}^N & P_{12}^N \\ P_{21}^N & P_{22}^N \end{pmatrix}. \tag{1.54}$$

The transmission and the reflection for the intensity read:

$$T = \left|\frac{A_N}{A_0}\right|^2 = \left|\frac{P_{11}^N P_{22}^N - P_{21}^N P_{12}^N}{P_{22}^N}\right|^2, \tag{1.55}$$

$$R = \left|\frac{B_0}{A_0}\right|^2 = \left|-\frac{P_{21}^N}{P_{22}^N}\right|^2. \tag{1.56}$$

The values of T and R can be expressed as a function of the wavelength in vacuum λ_0.

In Fig. 14 the calculation of BGs calculated by multiple scattering theory is shown, where higher order BGs also appear. The structure used for this simulations is the same as previously, with a period of $d = 0.164\mu m$, where $d_{l_1} = d_{l_2} = 0.082\ \mu m$ and refractive indices $n_1 = 2.17$ and $n_2 = 1.49$, number of periods N=20.

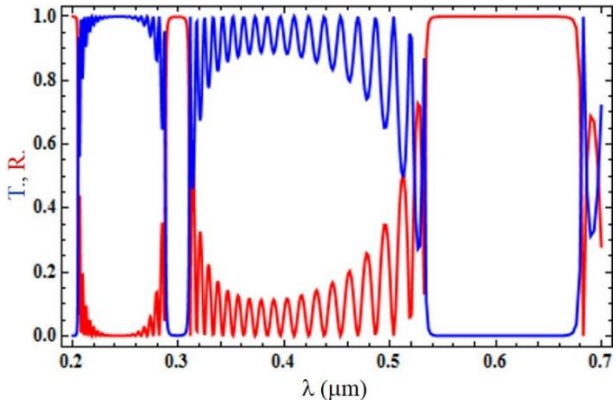

Figure 1.14. Transmission-reflection spectra calculated by scattering matrix method as a function of λ in vacuum, where three first BGs of the structure (described in a text) are visible.

1.2.4. **1D photonic crystals with defects**

The periodicity of the PhC can be broken by introducing a ***defect*** into the structure [Joa08]. This defect can create a highly localized transmission mode in the BG frequency range [Liu11, San04, Zhu09, Wan97, Smi93]. There are several possibilities to include a defect in a PhC. One can either change the width of one layer of one material (Fig. 1.15(a)), or change the material of one layer (change the refractive index) keeping the same width (Fig. 1.15(c)).

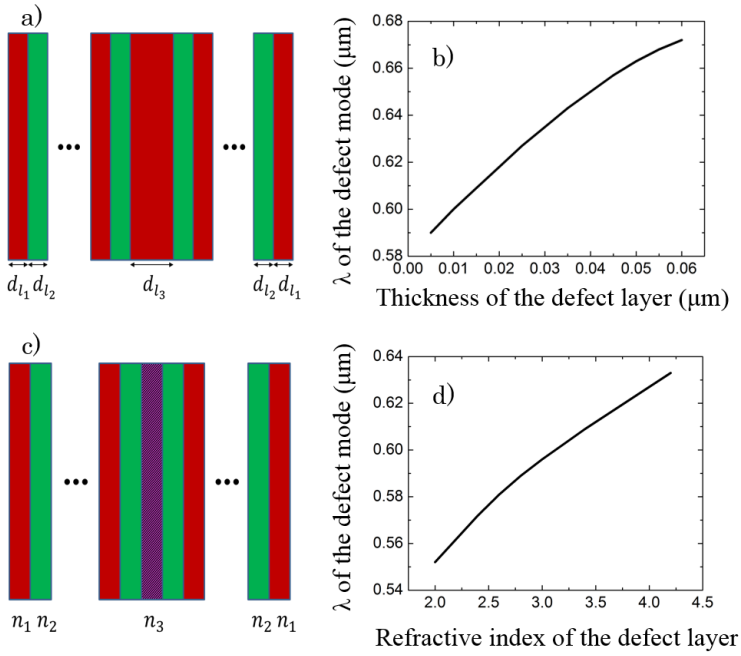

Figure 1.15. (a), (c) PhC structures containing defect by: (a) different size of the layer, (c) different refractive index of the layer; (b), (d) Numerical simulations with scattering matrix method. The parameters of the structure are: $d_{l_1} = d_{l_2} = 0.082\ \mu m$, $n_1 = 2.17$, $n_2 = 1.49$ and N=14, and the defect is introduced in the middle of the PhC. In (b) and (d) the variation of the wavelenght of the defect mode (in vacuum) is presented: (b) increasing the thickness of defect layer, (d) increasing the refractive index of the defect layer.

If the thickness of the defect layer is increased, the wavelength of the defect mode increases (frequency decreases) (Fig. 1.15(b)). If the refractive index of the

defect is increased the same effect as mentioned before is obtained, i.e. the wavelength of the defect mode would increase (Fig 1.15.d) [Wan97].

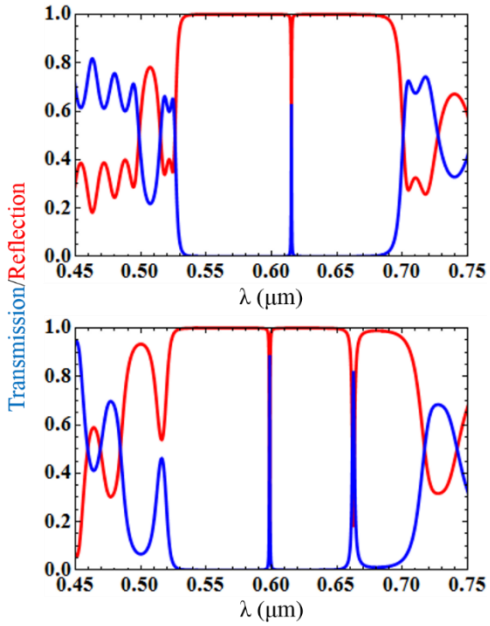

Figure 1.16. Reflection spectra with introduced defects of different layer sizes for the same structure parameters as in Fig.14; (a) One defect with the layer size of $d_{l_3} = 0.02\ \mu m$ introduced in the middle of the structure with N=14, (b) two defects, where one of defect layers is $d_{l_3} = 0.02\ \mu m$ and another one of $d_{l_4} = 0.03\ \mu m$. d_{l_3} is introduced in the 9th period of the structure, while d_{l_4} is introduced in 12th period d_{l_4}, where total number of periods is N=20. λ is represented in vacuum.

The position of the defect layer is important. If the position for the defect is in the middle of the structure the transmission for the defect modes is maximized (Fig. 1.16(a)) [Wan97]. Single defect PhCs are interesting because they can be applied in light-emitting diodes, lasers, and filters [Zho01, Fei05, Son05]. More defects could be introduced into the periodic structure, which would lead to an increased number of defect modes in the band-gap (Fig 1.16(b)), which is, among others, interesting for narrow band filters [Liu11].

1.2.5. **1D photonic crystals with chirp**

Another technique to engineer the BGs in 1D PhCs is the use of ***chirped (or graded) structures***. These are structures with gradually increasing or decreasing period (Fig. 1.17) [Oue87, Wu10b, Hil94, Fer95]. Chirping can also be achieved by a slowly-varying the refractive index gradient [Lou05].

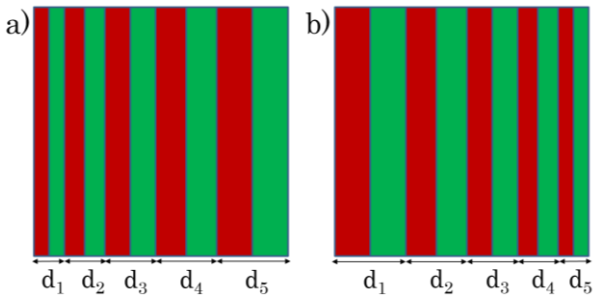

Figure 1.17. Chirped 1D PhCs: (a) gradual increase of the period from left to the right; (b) gradual decrease of the period from left to right.

Since the BG frequency depends on the period of the structure, in a chirped PhC, where the period is gradually increasing, the BG frequency range moves along the structure, thus the total BG can increase. In Fig. 1.18(a) the profile of the refractive index for a gradually increasing period is schematically illustrated. In Fig. 1.18(b) we see the BGs for a structure of period d=0.164 μm (all parameters are the same as used in simulation for Fig. 1.14), where one of the BGs appears around $\lambda = 600$ nm. In Fig. 1.18(c) a longer period of $d = 0.2$ μm ($d_{l_1} = d_{l_2} = 0.1$ μm, $\mathrm{N} = 20$) was chosen, for which the BG appears around $\lambda =$ 750 nm. In Fig. 1.18(a) arrows indicate how the period of the structure is related with the BG diagram discussed above: a shorter period gives a BG for shorter wavelengths, a longer period gives a BG for longer wavelengths. Therefore, introducing chirp into the structure, which gradually changes from $d_1 =$ 0.164 μm, to $d_2 = 0.2$ μm, we extend the BG, as shown in Fig. 1.18(d). The larger

is the difference between the first and last periods, the broader will be the bandwidth of the BG. Obviously, the length of such crystal must be increased too, until the reflection in the BG reaches approximately 100% (here N=40). A too fast variation of the period along the structure (too strong chirp) can result in a "jump" through the BG – a non-adiabatic effect called Landau – Zener transition [Nak12].

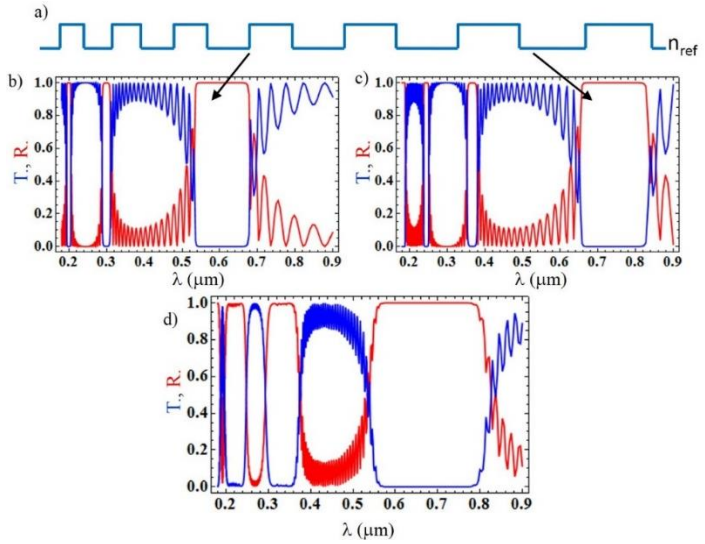

Figure 1.18. (a) Refractive index profile of a chirped 1D PhC with linearly increasing period. Calculations with scattering matrix method: (b), (c) transmission-reflection spectra for unchirped crystals of different parameters (descrption in text) and (c) transmission-reflection spectra of a chirped PhC. λ is represented in vacuum.

Very similar physical principles work for engineering of angular BGs for spatial filtering. Angular BGs correspond to Bloch waves with the undefined spatial dispersion relation. Bloch modes in the forward direction for these particular angular components do not exist and plane wave components inside the angular BG cannot propagate. Consequently, they are back reflected and filtered out from the angular distribution of transmitted field.

1.2.6. **Spatial filtering by 1D photonic crystals**

The principle of frequency filtering in 1D PhC can be applied to spatial filtering of a light beam. Consider that the frequency BGs occur at different frequencies for different propagation directions (Fig 1.19).

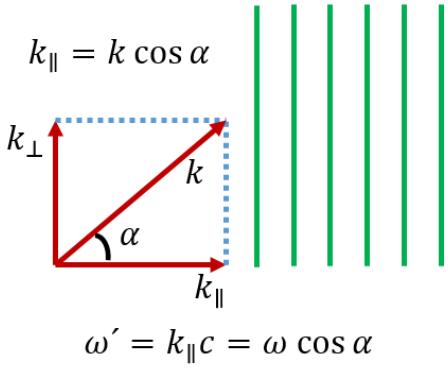

Figure 1.19. Schematic representation of conditions for angular BG in 1D PhC structure.

The Bragg condition for the central wavelength of the band gap λ_{BG} for oblique incidence (inserting reciprocal magnitudes into relation $\lambda = 2d$) reads:

$$2k_{\parallel} = q,\ \ 2\frac{2\pi}{\lambda_{BG}}\cos\alpha = \frac{2\pi}{d},$$

$$\lambda_{BG} = 2d\cos\alpha. \qquad (1.57)$$

Where $k_{\parallel}$ is the longitudinal component of an incident wave-vector $\vec{k}$ ($k = 2\pi/\lambda$), $q = 2\pi/d$ is the reciprocal period of the 1D structure and α is the incidence angle of $\vec{k}$. In this way, propagation and reflection of waves at an incident angle α are equivalent to those of waves of smaller frequency ω' without oblique incidence:

$$\omega' = k_{\parallel}c = \omega_0\cos\alpha, \qquad (1.58)$$

which can be expressed as:

$$k_{\parallel} = k\cos\alpha. \qquad (1.59)$$

If we launch a monochromatic Gaussian beam (which can be Fourier decomposed into a set of $\vec{k}$ vectors with different α values) into a 1D PhC, the Bragg condition for waves at oblique incidence Eq. (1.59) and the scattering matrix method, will lead to the transmission spectrum of the beam (for its constituent angular components).

For clarity, in Fig. 1.20 we plot the BG in a 2D map in terms of the angle and the wavelength (calculated with the Bragg condition for oblique incidence, Eq. (1.59) and scattering matrix method). The structure is a 1D PhC with the same parameters as in Fig. 1.14 ($d = 0.164\mu m$, where $d_{l_1} = d_{l_2} = 0.082\ \mu m$ and refractive indices $n_1 = 2.17$ and $n_2 = 1.49$, number of periods $N = 20$).

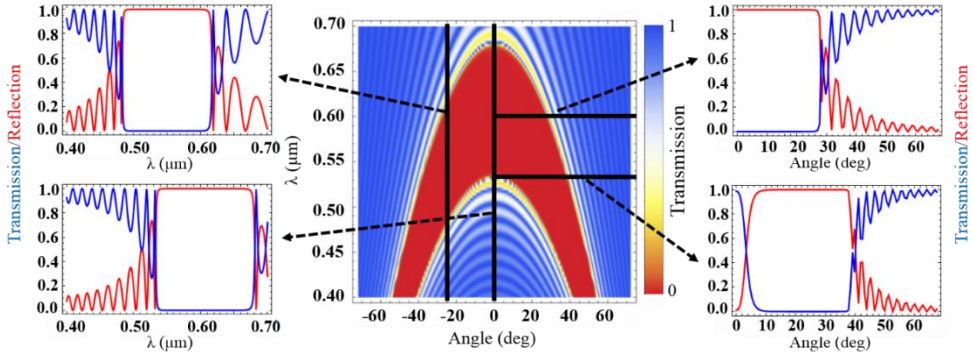

Figure 1.20. Center – 2D map of transmission spectra depending both on angle of incidence α and on the wavelength λ (in vacuum), where BG is clearly observed (red area); left: (top) vertical cut at $\alpha = 25°$; (bottom) vertical cut at $\alpha = 0°$, right: (top) horizontal cut at $\lambda = 600\ nm$; (bottom) horizontal cut at $\lambda = 532\ nm$.

On the left side of Fig. 1.20, the chromatic transmission-reflection spectrum at incidence angles $\alpha = 0°$ and $\alpha = 25°$ are shown (the plots are the vertical cuts of the 2D map as illustrated by arrows). It is seen that the central wavelength of the BG λ_{BG} is shifted. The plots on the right side are horizontal cuts of the 2D map at the wavelengths of $\lambda = 600$ nm (top) and $\lambda = 532$ nm (bottom), which show transmission-reflection spectra for different angular components for these particular wavelengths. For the case of $\lambda = 600$ nm, in the central part of the angular distribution there is an angular BG of the width of 56°. For the wavelength of $\lambda = 532$ nm, a transmission window in the central part of the distribution is obtained with the angular width of 10°. Thus, the considered 1D

PhC could be used as a low-pass spatial filter for this wavelength. Such filter however, can hardly be of practical use, as the transmission band in the central part is very broad.

1D PhCs with defect layers could be used as spatial filters for oblique incident angles ($\alpha \neq 0$). It was demonstrated that they can work as a 2D low-pass spatial filter [Jia05, Jia06, Luo09, Son13]. To illustrate that, using the scattering matrix method (applying Bragg condition for oblique incidence) we have calculated the angle dependent transmittance by a 1D PhC with a defect layer (Fig. 1.22). The parameters of the 1D PhC are identical to the ones described for Fig. 1.21, except that the defect of $d_{l_3} = 0.023$ μm is inserted in the middle of the structure which in total contains 14 periods (N = 14).

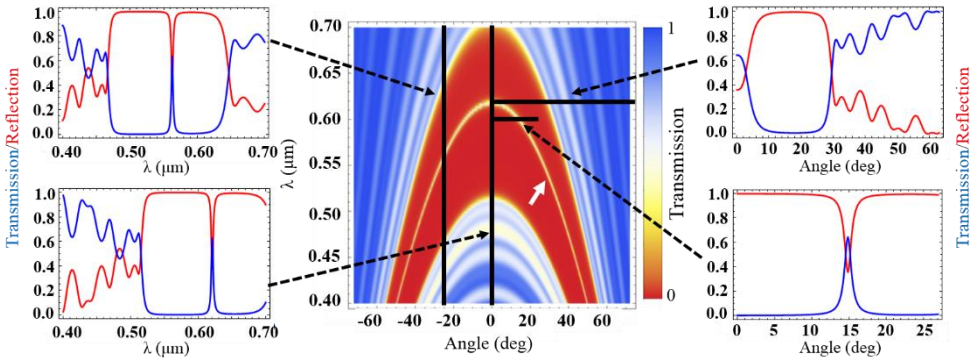

Figure 1.21. Center - 2D map of transmission spectra (depending on α and λ in vacuum) with the defect mode within the BG; left: (top) vertical cut at $\alpha = 25°$; (bottom) vertical cut at $\alpha = 0°$, right: (top) horizontal cut at $\lambda = 621\,nm$; (bottom) horizontal cut at $\lambda = 600\,nm$.

Due to the defect layer, a defect mode (marked by a white arrow) appears within the BG, which can also be seen for the vertical cuts of the 2D map at angles of $\alpha = 0°$ (bottom) and $\alpha = 25°$ (top) (left side). For the case of $\alpha = 25°$, the defect mode appears at $\lambda = 565$ nm, while for the case of $\alpha = 0°$, the defect mode is at $\lambda = 620$ nm. On the right side of the Fig. 1.21, the horizontal cuts of the 2D map at wavelengths of $\lambda = 621$ nm (top) and $\lambda = 600$ nm (bottom) are shown. Similarly, as in the case of 1D PhC without the defect (Fig. 1.20 right (bottom)), at $\lambda = 621$ nm there is a transmission window at $\alpha = 0°$, with an angular width of 10°. In addition to this, from the 2D map with the defect it can be observed that, for

various wavelengths, appears a relatively narrow transmission window with the central angle $\alpha \neq 0°$ within the angular BG region. In the considered example it appears for $\lambda = 600$ nm, at $\alpha = 15°$ (Fig. 1.21 right (bottom)), with an angular width narrower as compared to the previous cases (when the transmission window is located at $\alpha = 0°$).

However, the practical use of 1D PhCs with defects for spatial filtering is very limited. As it was shown in [Son13], the experimentally measured central transmitted angular width of the defect mode is 3 times larger as compared to numerical calculations. This disagreement is due to the influence of the random errors in layer thickness. The problem is that, in fabrication, even a small imprecision of the width of the defect moves the angular characteristics very strongly. Nowadays, technologies allow to fabricate angular filters with an angular width of ~10° for 1D PhCs.

1.3. Two- and three- dimensional photonic crystals

As already discussed in the previous section, chromatic dispersion diagrams of 1D PhCs have frequency BGs. The interesting observation is that the dispersion line close to the area of BGs, i.e., near the corner of the Brillouin zone, is highly nonlinear, and the flattening of the dispersion lines is always present (Fig. 1.22(a), around red ellipsoids). Here, the strong nonlinearity in dispersion is implied by a large effective refractive index n_{eff} variation near the Brillouin zone edge (Fig. 1.22(b), where the effective refractive index was calculated with $n_{eff} = k(\omega)c/\omega$ and the PWE method). This variation can be explained by the general Kramers-Kronings relation, where the distortion of dispersion appears due to particular resonant conditions of the system. This nonlinearity in dispersion, or flattening of the dispersion line, primarily causes a change of the group velocity, $\vec{v}_g = \partial\omega/\partial\vec{k}$ [Bab08]. An especially noticeable change of group

velocity appears at the edges of the bands (marked in red in Fig. 1.22), where the light slows down.

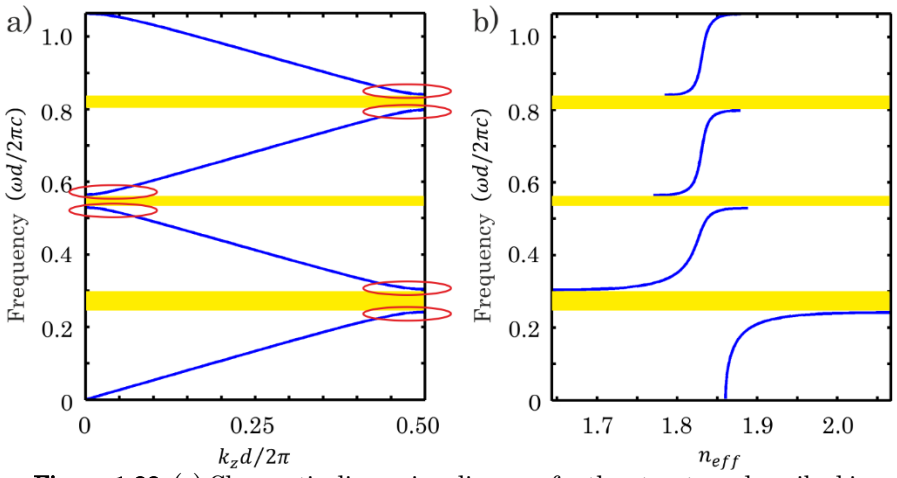

Figure 1.22. (a) Chromatic dispersion diagram for the structure described in Fig 10. Red ellipsoids mark highly nonlinear dispersion locations (near the BGs), where the slowing down of group velocity appears. (b) Frequency propagating mode as a function of the effective refractive index n_{eff}, where the highly nonlinear behavior of n_{eff} close to the area of BGs is visible.

For the case of PhCs with line defects, slowing down of light also appears around the defect lines at the regions where the dispersion curve becomes flat. The slowing down of light is very useful for the enhancement of linear and nonlinear optical effects, as well as, for the control of optical signal in the time domain [Bab08], and, it has been extensively investigated [Not01, Let01, Ino02, Asa04, Bab04, Vla05, Ger05, Fin06, Kra07]. Slowing-down-like effects also occur for the spatial dispersion case with iso-frequency surfaces, for which drastic changes in the group velocity direction can appear.

1.3.1. Spatial (angular) dispersion

Temporal dispersion determines the phase velocity, the group velocity, and the frequency band gaps in PhCs. In order to define the spatial propagation of a beam at a particular frequency, one should explore the spatial dispersion

relation. Dispersion surfaces $\omega(k_x, k_y)$ represent all the allowed wave vectors that can exist in the material for all orientations throughout the Brillouin zone at a particular frequency. Dispersion surfaces can be calculated by the PWE method (explained in the first part of the chapter). An example of dispersion surface for a square lattice 2D PhC for the TE polarization (electric field is parallel to the rods) of electromagnetic wave is shown in Fig. 1.23(a) (the calculation was done using the commercial RSoft software which applies the PWE method). However, in many cases it is more convenient to represent spatial dispersion as iso-frequency contours (Fig. 1.23(b)) which are the intersection of a constant frequency ω plane to a dispersion surface, rather than dispersion surfaces. These contours simplify the observation of sharp bending, flat parts or unusual shapes in the spatial dispersion, which determine many interesting propagation effects in PhCs, like negative refraction, the super-prism effect, etc. If we take an isotropic, homogeneous media (e.g. free space), equi-frequency contours are perfect circles, which means that light propagate isotropically, while for PhCs, equi-frequency contours exhibit various shapes, so light travels anisotropically in the structure [Van14].

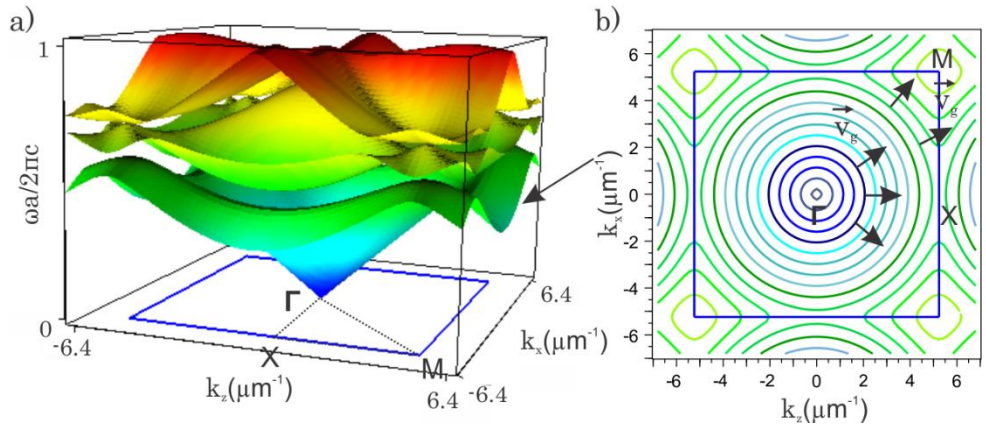

Figure 1.23. (a) Dispersion surfaces for the first three bands of the square lattice 2D PhC, where circular rods with the radius $r = 0.2a$ and refractive index $n = 1.5$ are set at the lattice points. The host medium is air. The lattice constant is equal to $a = 0.6\ \mu m$ The Brillouin zone is marked by a blue square. (b) The iso-frequency contour for the first band of the structure. The black arrows indicate the direction of grup velocity. The Brillouin zone is marked by a blue square.

As we mentioned previously, the spatial dispersion in PhCs can modify the group velocity. Before entering into a detailed explanation, we would like to specify the term of group velocity in a more rigorous manner. The group velocity is defined as the gradient of the optical frequency with respect to $\vec{k}$:

$$\overrightarrow{v_g} = \frac{\partial \omega}{\partial \vec{k}} = \vec{\nabla}_k \omega \tag{1.60}$$

Where $\vec{\nabla}_k = \frac{\partial}{\partial k_x}\vec{e}_x + \frac{\partial}{\partial k_x}\vec{e}_z$, here $\vec{e}_x$ and $\vec{e}_z$ are unit vectors in directions of k_x and k_z. The group velocity gives the direction and the velocity of the energy transport of the wave. Its value is given by the slope of the chromatic dispersion curve. As it can be seen from Eq. (1.60), the group velocity is always perpendicular to the iso-frequency contours $\omega(\vec{k}) = const.$ and it points to the direction of increasing frequency (Fig. 1.22(b)).

1.3.2. Negative refraction, super-prism and flat-lensing effects

The propagation direction (the energy transport) of the wave is parallel to the group velocity vector $\overrightarrow{v_g}$. Consequently, the propagation direction of the wave in a PhC is along the normal vector with respect to the dispersion curve. A strong deviation of the iso-frequency contour from a spherical shape (for example, sharp corners and bends) can lead to large changes in the direction of the wave for small changes of the wavevector of the incoming beam [Joa08]. Fig. 1.24 schematically shows spatial dispersion curves for a homogeneous material and for a square lattice 2D PhC at a particular frequency ω (a square lattice 2D PhC and its irreducible Brillouin zone are schematically depicted). The dashed circle marked in thick blue colour stands for the spatial dispersion contour for the homogeneous material, while the solid thick blue curve stands for a spatial dispersion contour at the same frequency in the periodic material. For a simpler representation, only a part of the dispersion contour for the PhC around the M symmetry point of the

Brillouin zone is depicted. The dashed circle in black colour illustrates how the spatial dispersion would look like for a homogeneous material with the refractive index equal to the effective refractive index of the considered PhC.

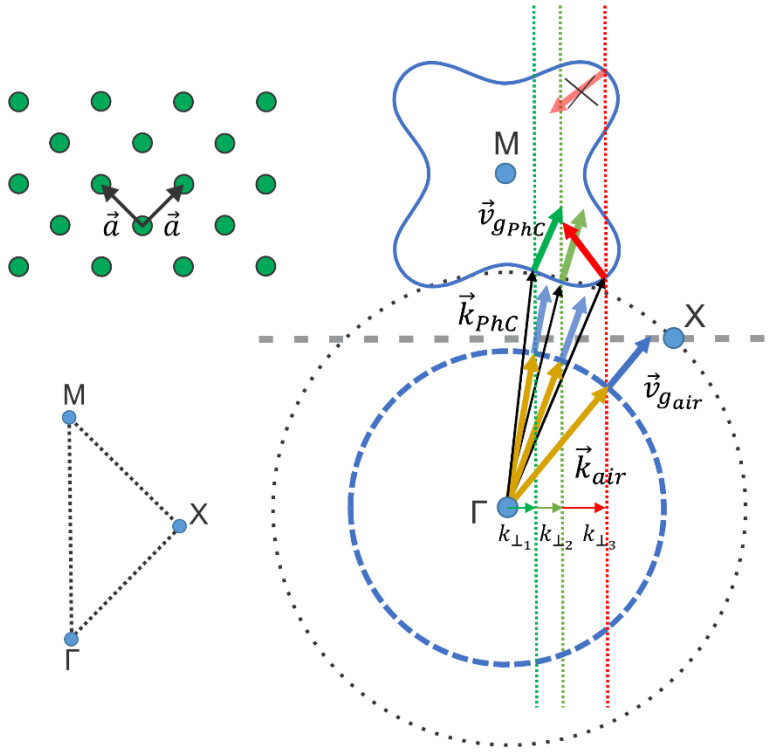

Figure 1.24. The schematic illustration. Left: (top) the square lattice 2D PhC, (bottom) the irreducible Brillouin zone for the PhC. Right: solid blue line marks a part of iso-frequency contour inside the PhC for a monochromatic source (the contour is shown only around M symmetry point, to simplify the illustration), (bottom) dashed blue circle marks an iso-frequency contour for the same monochromatic frequency as (top) in homogeneous material. Dotted thick grey lines indicates the orientation of the interface between air and the PhC.

In this example several wave vectors $\vec{k}$ at particular directions in the homogeneous material are marked in yellow colour. The group velocities for those wave-vectors are marked in thick blue arrows. Consider that these wave-vectors with particular angles are incident into the PhC. To see the direction of the wave inside the crystal after crossing the interface between air and PhC, we have to

use the construction line method [Van14]. This method is based on the fact that the component of the incident wave vector, which is parallel to the interface between different refractive index materials, is conserved while crossing the boundary. The latter can be proved using the Snell-Descartes law (continuity of the tangential components of the electric filed) [Van14].

The conserved wave vector components are marked in our example by thin coloured arrows ($\vec{k}_{\perp 1}, \vec{k}_{\perp 2}, \vec{k}_{\perp 3}$). The construction lines (dashed coloured bars) are drawn for the described geometry of wave-vectors. It is clear from the definition that construction lines must be perpendicular to the interface (or parallel to the normal direction of the interface) and drawn at the distance of wave-vector component fulfilling the condition (parallel to the interface). We see that for every wave vector, two intersection points for the spatial dispersion curve inside the PhC are obtained. We can eliminate the points for which the group velocity is directed towards the PhC interface, due to the conservation of the energy flow [Van14] and, therefore, only one crossing point for every wave-vector is left. At those crossing points, the wave-vectors inside the PhC corresponding to the ones in the air, can be identified (in figure marked by black arrows) and, moreover, the direction of the group velocities for those wave vectors can be found (marked in thick coloured (red, green, dark green) arrows). As mentioned before, the direction of the group velocity defines the direction of wave propagation, therefore, the refraction behavior of the wave inside the PhC can be obtained. Let's focus on the group velocity direction marked by a red arrow. It is anomalous as it lies on the same side of the normal as the incident wave, and it is opposite of the usual Snell's law of refraction. This peculiar effect is called negative refraction and due to its anomalous origin it attracted lots of attention [Dow94, Not00, She01, Not02, Cub03, Fot03, Par04, Ber04]. Fig. 1.25 shows how negative refraction affects wave propagation inside the PhC and how it continues propagating in free space.

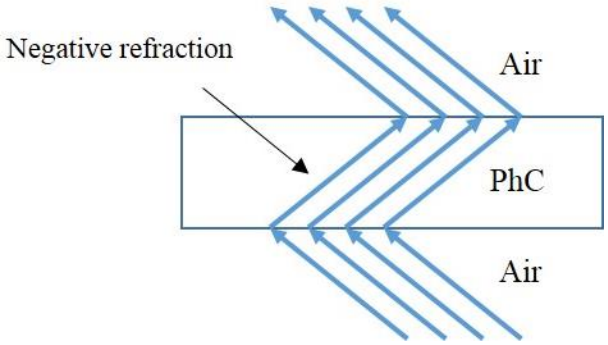

Figure 1.25. Illustration of light incident with particular angle into PhC and undergoing negative refraction effect inside the PhC.

Another related effect is the so-called super-prism effect, i. e. an enormous change in the refracted angle is obtained for a small change in incident angle or frequency, due to sharp corner regions of the dispersion surfaces of PhCs [Par04, Lin96, Kos98, Kos99a, Ser06]. Fig. 1.24 schematically demonstrated this example of sharp dispersion corner in a PhC, where, due to the slight change in incidence angle of a monochromatic wave, the refracted angle changed drastically (i.e. completely different group velocity directions for arrows marked in green and in red). It is well known that an ordinary prism, with small material dispersion, refracts waves of different wavelengths into different angles. With the superprism effect inside a PhC, a much smaller range of wavelengths can be split over a much wider range of angles, which can be used, for example, for frequency demultiplexing [Joa08]. The superprism effect was experimentally proved by H. Kosaka, *et. al.* and Fig. 1.26 demonstrates their experimental results (Fig 1.26(a) shows the refracted angle change due to the change of incidence angle for a monochromatic wave, while Fig. 1.26(b), demonstrates the refracted angle change for different frequencies with a fixed incident angle).

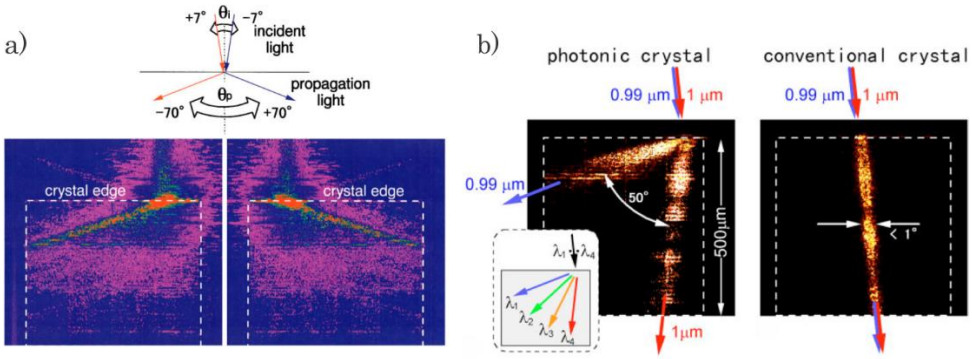

Figure 1.26. Photographs (experimental) demonstrating the superprism phenomenon: (a) Angle sensitive propagation: the tilting angle of the incident light is changing form +7° (left) to −7° (right), resulting in a huge swing of propagating light inside the PhC from −70°(left) to +70°(right). Both paths show negative bending [Kos98]. (b) Frequency sensitive propagation: (left) light paths inside PhC with incident wavelength of 0.99 μm and 1.0 μm and tilt angle 15°. A large swing reaching 50° is achieved with this slight change in a wavelength; (right) light propagation in a silicon wafer under the same conditions as (left). Both beams of different wavelenghts track almost the same path [Kos99a]

The effect of negative refraction can be used to build flat PhC lenses. Such a lens has a main advantage versus usual lenses, as it does not have an optical axis and consequently, it does not require precise alignment. Lots of research has been done in order to demonstrate flat lensing with PhCs [Luo02a, Luo02b, Li03, Lu05a, Fab06, Sun06, Ren07]. In addition, sub-wavelength imaging (the so-called super-lensing), overcoming diffraction limit, has been studied and demonstrated [Luo03, Wan04, Mou05]. This effect is based on the amplification of evanescent waves within the PhC. Moreover, flat lensing has been investigated in Sonic [Che04, Qiu05] and Phononic Crystals [Yan04b, Ke05, Suk08, Suk08] for acoustic waves, where the physical principle is the same as for PhCs.

The original idea of using materials with negative refraction to obtain a flat lens was proposed by Veselago in 1968 [Ves68]. However, the working principle of a "Veselago lens" is different from a PhCs lens. His suggestion was a homogeneous material with simultaneously negative electric permittivity ε and magnetic permeability μ, giving rise to a negative refractive index of the material, which therefore leads to the effect of flat lensing (Fig 1.27).

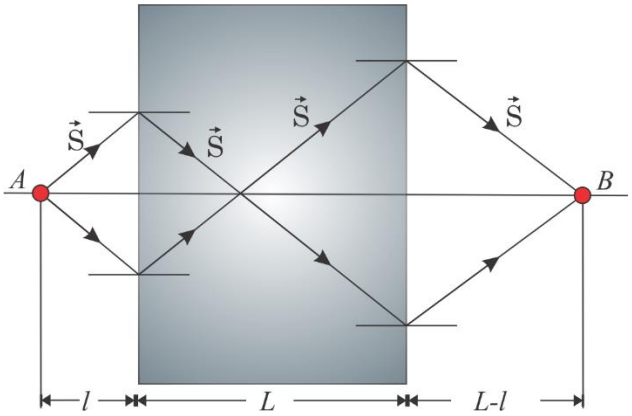

Figure 1.27. Illustration of the "Veselago lens", where gray area is marking the lens of length *L*. Point *A* is the source of radiation with the distance *l* from the lens. *B* is the image of the radiation source. The drawn rays show the passage of light undergoing negative refraction inside the structure with simultaneously negative electric permittivity ε and magnetic permeability μ. $\vec{S}$ is the Poynting vector.

In nature there are no materials which would have negative refractive index. Therefore, for many years, Veselago's idea was only at the theoretical level. However, at the end of the XX century, Pendry suggested a design of the material which consisted of periodically distributed metallic resonant structures, with the period much smaller than the wavelength, therefore the propagating wave would "see" such material as homogeneous with appropriately averaged simultaneously negative electric permittivity ε and magnetic permeability μ [Pen99, Pen00]. The kind of structure is the so-called metamaterial (metamaterials are considered to have a period at least ten times smaller as compared to the wavelength) and it has been experimentally fabricated [She01]. Moreover, focusing by flat metamaterials for microwave [Hou03, Iye03] and visible [Roc07] frequencies has been experimentally demonstrated. In addition, sub-wavelength imaging, with the resolution well below the diffraction limit (due to the enhancement and retrieval of evanescent wave components), for microwaves [Grb04, Lag04] and visible frequencies [Xio07, Smo07], has been shown. Although metamaterials can work as flat lenses, they are hard to fabricate, as they have to be structured on very small spatial scales, i.e., for visible frequency their size should be of the order

of several nanometers. Moreover, for visible frequencies it is not a very convenient material as it consists of metal and, therefore, a strong absorption is present and a lot of radiation energy is lost in propagation through the metamaterial.

Negative refraction in PhCs is not an identical effect and we should not consider its effective refractive index as negative. In PhCs, negative refraction appears only due to the bends of the iso-frequency contours for particular frequencies and both, its electric permittivity ε and magnetic permeability μ, are positive [Van14]. However, the effect is analogous, as the refraction of an incident wave appears at the same side of the normal. PhCs have an advantage over metamaterials, as their periods do not need to be much smaller than the wavelength of light, they are easily approachable from the fabrication point of view and, most important, PhCs can be built using only dielectric materials, so absorption of light can be considered as negligible.

1.3.3. **Negative diffraction and flat-lensing**

Although negative refraction in PhCs can be achieved and it can lead to flat lensing, the negative refraction theories based on sharp slopes of equi-frequency curves (and generally on Veselago proposal) are not consistent. In the example of Fig. 1.24, negative refraction can be obtained only manipulating plane waves within a particular narrow range of angles (directions), but for focusing we need to manipulate beams. Beams have a finite width Δx, and therefore a finite angular spectrum $\Delta\alpha = \Delta k_x/k_x$. To focus the whole beam, not the sharp slope of iso-frequency curve is important, but rather the curvature itself. In this way, the theory of negative refraction must be revised to give the adequate explanation of flat lensing for PhCs.

In the Fig. 1.28, the blue dashed circle corresponds to the spatial dispersion in an homogeneous material, while the solid blue circle corresponds to the spatial dispersion curve of the PhC (around the M symmetry point of the Brillouin zone). The way of finding the group velocity direction inside PhC is the same as explained for Fig. 1.24. However, in this case we can see that all the incident

wave vectors falling into the spatial dispersion curve of PhC would have negative refraction, therefore it can be called negative diffraction. For the negative diffraction effect to appear, the spatial dispersion curve has to have a convex shape, as illustrated in Fig. 1.28 (the appearance of only sharp corners (as illustrated in Fig. 1.24) is not sufficient for flat lensing with reasonably large numerical aperture).

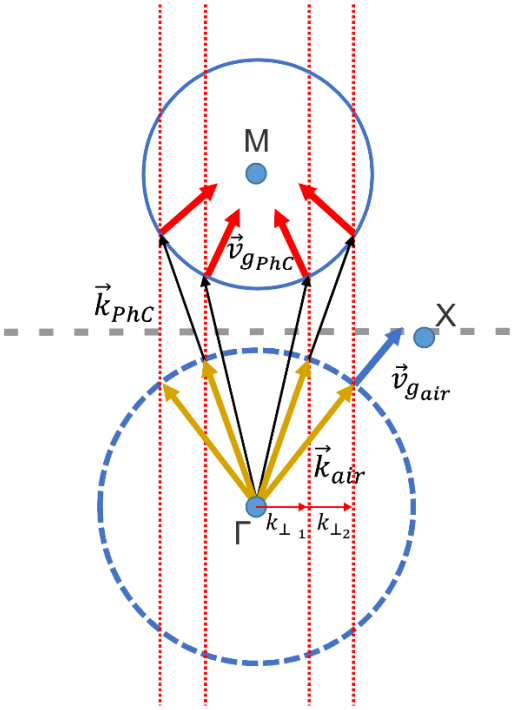

Figure 1.28. Schematic illustration of two iso-frequency curves for monochromatic source: (top) inside the PhC (only a part of iso-frequency contour around the symmetry point M is shown); (bottom) inside the homogenous material. The dotted thick gray line indicates the orientation of the interface between air and PhC.

Let us consider several examples on how diffraction, which is defined by the curvature of the dispersion, affects beam propagation. "Positive" diffraction or diffractive broadening of light beams in propagation is a fundamental phenomenon, which can be explained by equi-frequency curves. Consider a monochromatic beam of a finite width, which is decomposed into a set of plane

waves with particular directions. Those plane waves in propagation will acquire phase shifts depending on their propagation angles, consequently, this phase difference between the components results in a diffractive broadening of the beam.

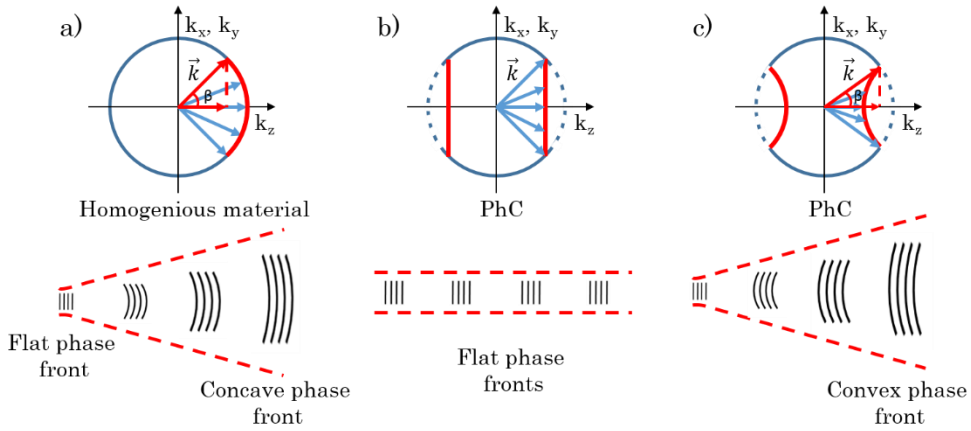

Figure 1.29. Geometrical interpretation of diffraction of the beam propagating along z axis: (a) (top) spatial dispersion for homogeneos materials, where due to the phase difference between $\vec{k}$ vectors, occurs positive diffraction of the beam (bottom); (b) (top) Modified spatisl dispersion (by PhC) where flat parts on the surface/curve appear. For the flat part of spatial dispaersion all $\vec{k}$ vectors propagate at the same velocity with respect to z axis, therefore self-collimation is obtained (bottom); (c) (top) modified spatial dispersion (by PhC), where convex chapes emerge, responsible for the appearnace of negative diffraction (bottom).

In Fig. 1.29(a) a schematic decomposition into of the set of plane waves, for a particular monochromatic beam which propagates in z direction, is shown (marked in blue arrows). Fig. 1.29(a) illustrates an iso-frequency contour for homogeneous isotropic material, which is a circle. The concave shape of the contour in the wave-vector domain $\vec{k} = (k_x, k_y, k_z)$ governs how the beam propagates in space, i. e. if we project all the $\vec{k}$ vectors (plane waves) of the beam to the coordinate of k_z we obtain the phase delay for each of the components compared to the central one (i.e. $k_{\parallel} = k_z = \left(|\vec{k}|^2 - |\vec{k}_{\perp}|^2\right)^{1/2}$, where $\vec{k}_{\parallel}$ is parallel to the central beam component and $\vec{k}_{\perp} = (k_x, k_y)$ is perpendicular). This phase delay

is responsible for the concave phase front formation of the beam and, therefore, is responsible for the normal or positive beam diffraction in real space, as illustrated in Fig 1.29(a) (bottom). The narrower is the beam in real space, the broader is its angular spectrum, the more $\vec{k}$ components it is going to have, the stronger will be the diffraction, and the faster will be the spreading of the beam (the spreading in angle is proportional to the wavelength divided by the beam width) [Joa08]. However, as it was clarified before, PhCs can strongly modify the iso-frequency contours and, thus, modify the behavior of diffraction. For example, in fig 1.29(b) spatial dispersion is modified (with a PhC) in a way that completely flat parts of dispersion appear. Consequently, if the projection for every $\vec{k}$ to the propagation axis is equal, the phase delay will not be obtained, so that, the phase fronts of the beam will stay flat in real space as shown in Fig 1.29(b) (bottom) and the beam will propagate without diffraction. It is a very peculiar effect, as the beam can propagate long distances without spreading, and there has been a lot of investigation on the topic. The non-diffractive propagation (as well called self-collimation) of light beams has been shown numerically [Kos99b, Chi03, Wit02, Aug05], analytically [Sta06], and experimentally [Ili04, Rak06, Lu06, Lom06] for 2D and 3D PhCs. In addition, self-collimation was demonstrated for Sonic Crystals [Per07, Esp07, Sol09] and the beams of plasmon polaritons [Lin12, Arm12]. With particular PhC configurations, the self-collimated beams can be bent and split and the effect can be used for beam steering or beam splitting devices [Yu03, Pra04, Kim07].

Finally, Fig. 1.29(c) shows the case where an iso-frequency contour in a PhC has a convex shape of the curvature (marked in red). In this case, the phase delay appears for the central $\vec{k}$, as the side components are experiencing smaller phase delay. Consequently, diffraction is still appearing for a propagating beam, but the phase fronts acquired in propagation of the beam are of convex shape. Therefore, such kind of diffraction is called anomalous or negative diffraction [Sta06, Per07]. The negative diffractive spreading of the beam is shown in Fig. 1.29(c) (bottom), which in principle looks the same as the beam with positive diffraction, except that wave fronts are of convex shape.

The flat lensing with a PhC can be explained by the combination of both positive and negative diffraction. It is schematically illustrated in Fig. 1.30.

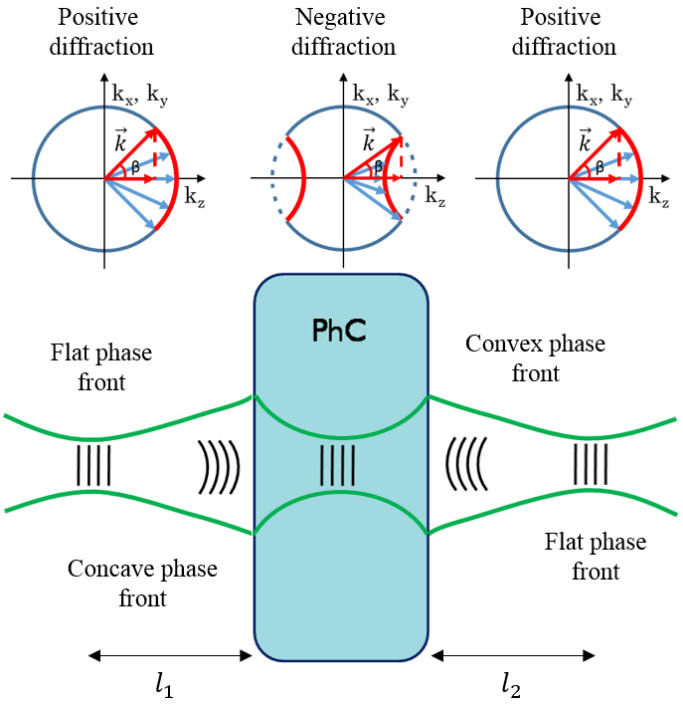

Figure 1.30. An illustration of a flat lensing by a PhC, where due to the compensation of positive and negative diffractions a focusing inside and outside the PhC is obtained.

The focused beam has a flat phase fronts in the focal point. However, propagating in a homogeneous material with concave iso-frequency curve, the beam is diffractively spreading and acquiring concave phase fronts. Then, when the beam enters into the PhC with the iso-frequency curve of convex shape, which provides negative diffraction, the already obtained concave phase fronts of the beam in the propagation in free space, start to flatten and inside the PhC become flat again. At the position of compensation, we have focusing inside the PhC. Nevertheless, in further propagation through the PhC, the beam starts to diffract negatively and acquires convexly shaped phase fronts. When the beam enters the

homogeneous material again, the following process is going to happen: due to the concave shape of dispersion in homogeneous material the acquired convex phase fronts of the beam will start to flatten and, at the certain distance, they will be flat again. Therefore, we will have focusing outside the structure. According to this principle, the flat lensing with PhCs can be achieved by compensation of positive and negative diffractions. As commented before, although the concept is different from the one that was proposed by Veselago, the outcome is very similar, as focusing is obtained both, inside and behind the structure.

It is interesting to notice that the relation between the object and the image distances for the PhC lens has a different form as compared to a conventional lens. The usual relation between the distance of the object and the lens, l_1, and the distance between the image and the lens, l_2, for conventional (or Fresnel lenses) is of the form: $\frac{1}{l_1}+\frac{1}{l_2}=\frac{1}{f}$, where f is a focal distance of the lens, while the relation for the PhC is given by :

$$l_1 + l_2 = f. \tag{1.61}$$

For a PhC lens, the parameter of the focal distance f depends on the strength of the convex spatial dispersion curvature inside the PhC. The stronger is the curvature (more convexly bent), the more significant is the "negative dephasing" between $\vec{k}$ vectors in propagation through the crystal and, therefore, the higher is the value of f and the beam can be focused at further distances in free space.

1.3.4. Equi-frequency contours: self-collimation, negative diffraction, spatial (angular) filtering

Positive diffraction, non-diffractive propagation, negative diffraction and spatial filtering can be found and explained by analyzing the iso-frequency contours of the PhC. Fig. 1.31 presents an example of iso-frequency contours of the first band for the structure already described in Fig. 1.23. In the first band of this particular

PhC, the effects of positive diffraction, non-diffractive propagation, negative diffraction and spatial filtering can be predicted. In Fig. 1.23(a) red arrows represent incident $\vec{k}$ vectors for $a/\lambda = 0.3041$ inside the PhC. It can be seen that for this frequency, the spatial dispersion contours in the PhC have concave curvature in all the directions, which means that a beam with this frequency will propagate with the normal-positive diffraction inside the structure. The thick blue arrows in Fig. 1.31(a) represent the incident $\vec{k}$ components for a frequency of $a/\lambda = 0.5068$. For these components at this frequency the dispersion surface is flat, which means that the beam composed from these particular $\vec{k}$ vectors will propagate without diffraction and will undergo self-collimation.

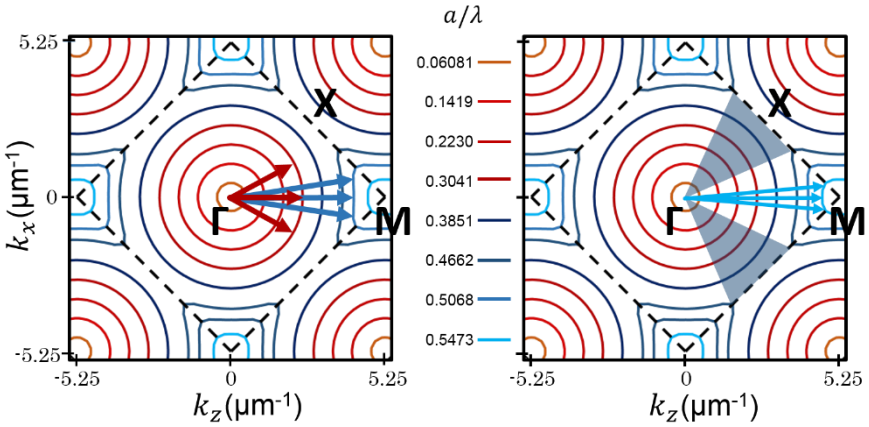

Figure 1.31. Iso-frequency contours of the first band, for the structure described in Fig. 1.23. (a) Red arrows mark $\vec{k}$ vectors (frequency $a/\lambda = 0.3041$) which undergo positive diffraction, blue arrows mark $\vec{k}$ vectors (frequency $a/\lambda = 0.5068$) which undergo self-collimation. (b) Bright blue arrows mark $\vec{k}$ vectors (frequency $a/\lambda = 0.5473$) which experience negative diffraction, while shaded blue areas denote angular BGs for $/\lambda = 0.4662$. The dashed black square marks a Brillouin zone.

The bright blue arrows in Fig. 1.31(b) stand for the incident $\vec{k}$ vectors at a frequency $a/\lambda = 0.5473$, where the iso-frequency curvature for this frequency and these components inside the PhC has a convex shape. This shape would lead to the negative diffraction effect, which could result in flat lensing outside the structure. In Fig. 1.31(b) two blue triangles can be observed. These triangles cover the region of $\vec{k}$ vectors for a frequency $a/\lambda = 0.4662$, for which spatial dispersion is undefined. That means that these $\vec{k}$ vectors (or angular components

of the beam) at these particular directions (angles) cannot propagate inside the structure and, therefore, they are scattered backwards and result in the opening of the spatial (angular) band gaps for this frequency at these particular directions. A more detailed analysis of the working principle and different mechanisms of spatial filtering, as well as numerical and experimental results obtained during the work of my PhD, are presented at the beginning of Chapter 2. The numerical and experimental results, obtained throughout my PhD, on the manipulation of positive, negative and non-diffraction effects in PhCs are presented in Chapter 3.

Chapter 2

Spatial filtering with Photonic Crystals

This chapter is structured into four main parts based on the three recently published papers by the author of the thesis [Mai10], [Pur13], [Pur14a] and one recently accepted [Pur14b], where we discuss theoretically, numerically and experimentally the basic results of the PhC structures for the spatial filtering of light beams. The last, not yet published work, is based on the numerical and experimental results of super-collimation obtained with axisymmetric micro structures.

Before presenting the results obtained throughout my PhD, a brief introduction of spatial filtering and different techniques to obtain it are shortly explained. Then, the mechanisms of spatial filtering with PhCs and SCs are introduced, and recent publications on the topic are reviewed.

In section 2.3, we present experimental evidence of spatial filtering of light

beams by 3D low-refractive-index-contrast PhCs. The PhCs were fabricated in a glass bulk, where the refractive index has been modulated using tightly focused femtosecond laser pulses. We observe filtered areas in the angular distributions of the transmitted radiation, and we interpret the observations by theoretical and numerical study of light propagation in index-modulated material in paraxial model. These results bring only the demonstrational character of the effect, as the efficiency of the reported spatial filtering is relatively low.

Therefore, in section 2.4 of the chapter, we propose the use of chirped low-refractive-index-contrast PhCs, where the longitudinal modulation period varies along the propagation direction. We show, theoretically and experimentally that these structures can provide a substantial spatial (angular) filtering of light beams and significantly improve the performance of the spatial filtering. Filtering efficiencies up to approximately 50% are experimentally demonstrated. The chirped PhCs were fabricated by the same method as the non-chirped PhCs – by modulating the refractive index in a glass bulk, with tightly focused femtosecond laser pulses.

In the part 2.5 of the chapter, we propose and advanced the geometry of the PhC to obtain the axisymmetric spatial (angular) filtering, as the previous configurations were not allowing to do that. We experimentally show spatial (angular) filtering of 2D light beams by axisymmetric 3D photonic microstructures. Such 3D microstructures were recorded in the same way as the previous ones and axisymmetric angular filtering of approximately 20 mrad is demonstrated experimentally. Analyzing the spatial filtering in axisymmetric PhCs, we came across the very unexpected and difficult-to-understand effect of super-collimation. Therefore, in the part 2.6, we propose a new mechanism of beam super-collimation by axisymmetric PhCs. The physical mechanism behind the effect is an inverse scattering cascade of different wave components back into on- and near-axis angular field components, resulting in substantial enhancement of these components. We explore the super-collimation by paraxial numerical calculations and prove it experimentally. We measure axial field enhancement up to 7 times in terms of intensity.

2.1. Introduction

Many applications in optics require beams of high spatial quality, as such beams diverge less and have smooth wavefronts, and consequently, can be focused more sharply (they have narrower beam waist in the focal region). Moreover, clean intense beams are more immune against nonlinear filamentations, self-focusing, etc. The highest spatial quality beams are of the Gaussian profile. Beams with profiles different from Gaussian would diverge more and would be focused to a larger spot size in the focal plane. Several definitions of beam spatial quality quantification are used [Sie93]. In the laser theory, spatial beam quality is commonly characterized by the ***beam parameter product*** (BPP). The BPP is defined as the product of a laser beam divergence angle (half-angle) and the radius of the beam at its narrowest point (the beam waist). The higher is the value of the BPP, the lower spatial quality the beam has. The diffraction-limited Gaussian beam has the lowest possible BPP, which is equal to λ/π, where λ is the wavelength of light. The ratio of the BPP of a particular beam to that of the Gaussian beam of the same wavelength is denoted as M^2 ("M squared"). This quality parameter does not depend on the wavelength and is also increasing when the beam quality is decreasing. A diffraction-limited Gaussian beam has an M^2 equal to 1 and physically it is not possible to achieve smaller M^2 value than this. Normally, the beams emitted by single transverse mode lasers and single-mode fiber lasers are of high spatial beam quality with $M^2 \approx 1$. However the beams emitted by optical devices like multi-transverse mode lasers, optical parametric oscillators, etc., are often of poor spatial quality ($M^2 > 1$). Moreover, if the beam is propagated through a laser amplifier, nonlinear material, scattering media or other optical component, usually the quality of such beam is reduced.

It is important to keep value of M^2 small, close to 1, as clean beams can be better focused; also for such beams modulation instability develops later. Therefore beams of M^2 higher than 1 have to be cleaned and their spatial quality is to be improved. Usually the beams are cleaned using a conventional spatial filter (Fig. 2.1).

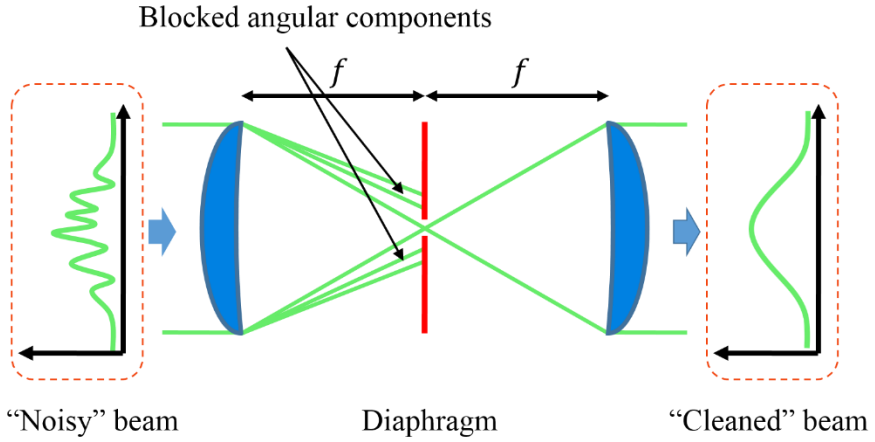

Figure 2.1. A scheme of conventional spatial filter, consisting of two focusing lenses in a confocal arrangement and a diaphragm located in the focal plane. The "dirty" entering beam profile is shown on the left side of the figure, while filtered out smooth beam profile is depicted on the right.

The conventional technique of spatial filtering consists of two focusing lenses in a confocal arrangement, where the far field image in focal plane is formed [Har96]. A diaphragm (which can be sharply edged, or sometimes apodized to enable Gaussian beam profile) of appropriate diameter located in the focal plane blocks the undesired angular components of the spatial spectrum. Therefore, after the propagation through such an arrangement only the central part of the beam is selected, and the spatial quality of the beam is improved. The main disadvantage of the conventional spatial filters is its relatively large size, as the distance between the focusing lenses is $2f$ (f being a focal distance, which is usually of length of centimeters). This technique is completely unsuitable for micro-lasers as well as for photonic circuits. As there is a need of compact spatial filters, there have been alternative proposals to spatially filter the light with interference patterns [Det84], multilayer stacks combined with a prism [Mor05], anisotropic media [Sch03], liquid-crystal cells [Kat96], metallic grids over a ground plane [Sid06], and resonant grating systems [Rab04].

In Chapter 2 we study an alternative method of spatial filtering – spatial filtering with the PhCs. The property of PhCs to have a photonic BG in frequency is very well known, as discussed in Chapter 1. Less known is the property of PhC

giving the possibility to provide the angular BGs. Angular BGs could be in principle used to obtain spatial filtering, therefore they can lead to the compact (10-100μm) and robust novel type of PhC spatial filter. In this chapter we explain in detail from numerical and experimental point of view this more recently proposed method.

2.2. Mechanism of spatial filtering

As we have already mentioned in Chapter 1, 1D PhCs can be in principle designed to spatially filter the light. However, any imprecision in fabrication, leads to a dramatic modification of the angular filtering properties [Don13] and thus, such a device is not of a practical use. The position and width of the angular BG can be much more effectively controlled in 2D or/and 3D PhCs, where the refractive index is modulated not only in longitudinal direction, but in transverse direction as well.

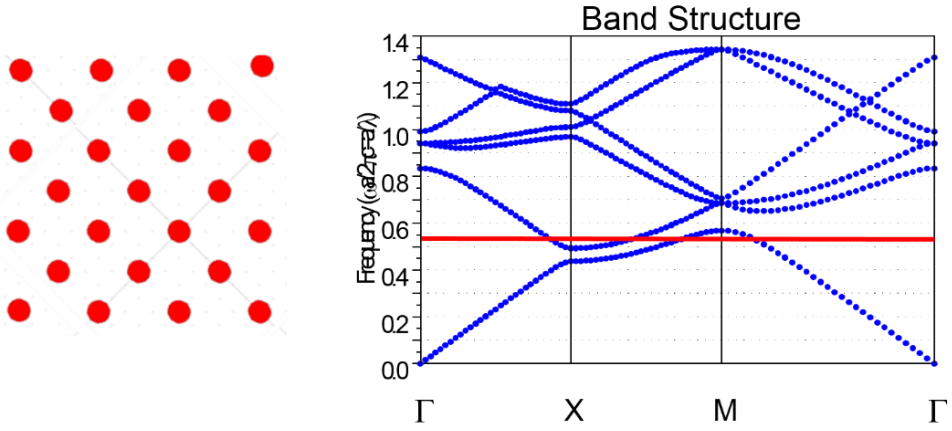

Figure 2.2. (a) The structure of the 2D PhC, (b) Band diagram.

Fig. 2.2(a) shows an example of a 2D PhC of a square geometry with the circular rods positioned at the lattice points. The lattice constant is $a = 0.6$ μm, the host medium is air, the rods of the radius $r = 0.2a$ are made from a material

with refractive index $n = 1.5$. Using the PWE method (with Software RSoft) we plot the band diagram of such structure for TE polarization (electric field is parallel to the rods) in Fig. 2.2(b). As can be seen, there is no complete frequency BG for the lowest bands, but only some partial BGs for some particular propagation directions. However, there appears an interesting region at normalized frequency of $a/\lambda = 0.55$, as it crosses the top part of the first band and bottom part of the second band. To explore more in detail the surroundings of this frequency region, we plot the iso-frequency contours of the spatial dispersion $\omega(k_x, k_y)$. The Fig. 2.3(a) represents iso-frequency contours of the first band, while Fig. 2.3(b) represents iso-frequency contours of the second band.

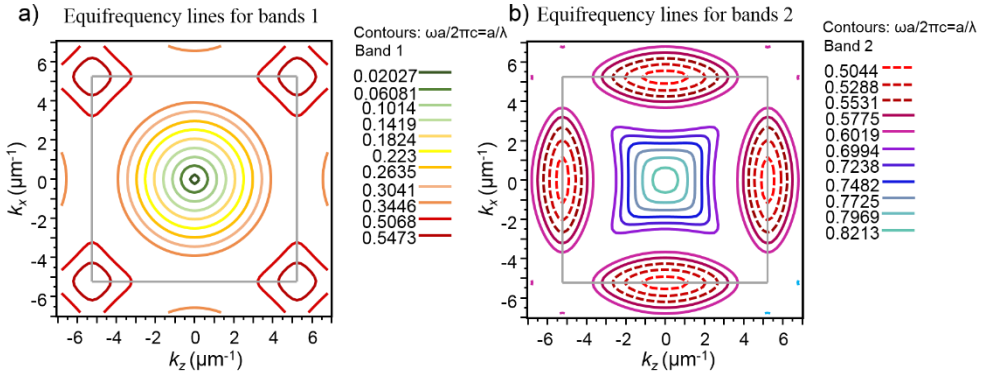

Figure 2.3. Iso-frequency contours of the first (a) and the second bands (b).

If we illuminate the PhC structure at frequency $a/\lambda = 0.55$, the Bloch modes lying on equifrequency lines will be excited for particular frequencies close to this value of a/λ, both in the first and the second bands (these particular equifrequency lines are marked in dark red in Fig. 2.3(a) and dashed dark red in Fig. 2.3(b). To have a more clear image we plot iso-lines for both bands in the same plot (Fig. 2.4).

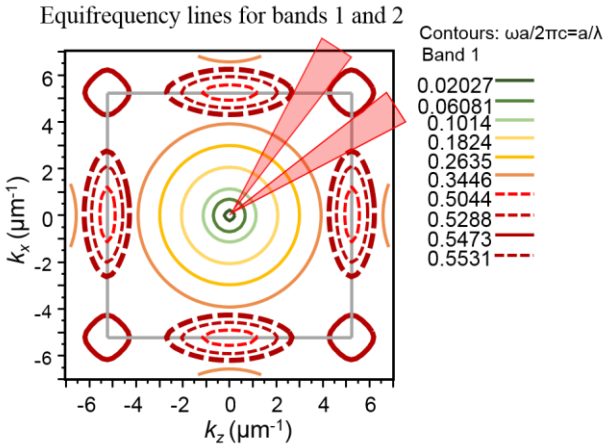

Figure 2.4. Iso frequency countours of both first and second bands shown in Fig. 2.3.

The appearance of the angular BG can be illustrated by simple terms, in Fig. 2.4. In the illustration of the effect, there are angles for the a/λ ~0.55 (marked in red triangles) corresponding to the Bloch waves for which the dispersion relation do not appear i.e. there is a BG in the angular domain. Therefore, the radiation corresponding to the plane wave components inside the angular band gap cannot propagate, being reflected back and consequently removed from the angular spectrum of forward propagating beam.

This kind of filtering was already proposed in optics [Col10, Tan07, Tan06, Ser09]. In Fig. 2.5(a) the numerical results from [Ser09] are presented, where the map on ($k_0 a$, angle) is shown for 2D square symmetry PhC. Here, wide range of angular band gap is obtained. With these results a spatial filter with steep switching between wide ranges of total transmission and total reflection can be obtained.

Fig. 2.5(b) demonstrates the numerical and experimental results for angular filtering from [Col10], where angular band-gap at the incident angles of 20-30º is obtained. Here, 2D square symmetry crystal with similar parameters to [Ser09] was used. The experiment was performed with a horn antenna of microwave wavelength.

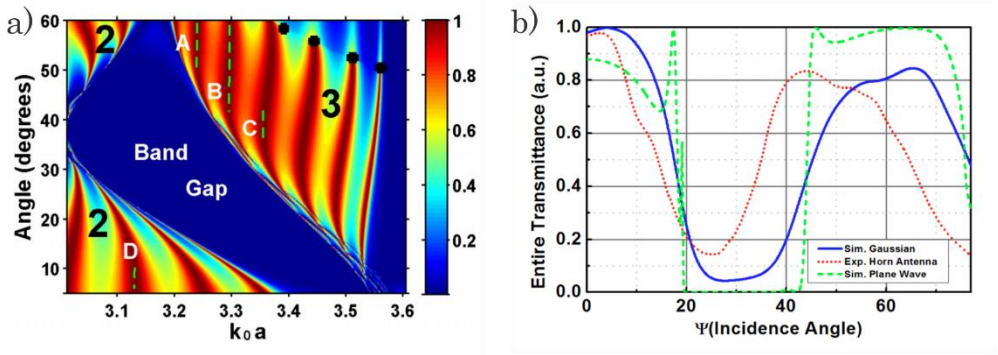

Figure 2.5. (a) Zero-order transmittance at varying $k_0 a$ and θ (Angle) for d/a=0.4, ε_r = 11.4, ε_h = 1 and N=8, where k_0 is wave vector of incident wave, a - lattice vector , d – diameter of rods, N – number of rod layers, ε_r and ε_h are permittivities of the rod and the host medium, correspondingly [Ser09]. (b) Transmittance for different source beams at frequency f = 21.763 GHz (a/λ = 0.5078) for Gaussian-beam excitation (solid blue line), horn-antenna excitation (dotted red line), and plane-wave excitation (dashed green line). The parameters of the crystal here is as follows: ε_r = 9.61, d = 3.1 mm, a = 7 mm, N=8. Both (a) and (b) are for square symmetry lattices.

Spatial filtering was also demonstrated in acoustics, for sonic crystals (SC) [Pic12]. Fig. 2.6(a) shows numerically simulated intensity distribution of a narrow acoustic beam, which passed through a 2D SC, in the far field, depending on frequency [Pic12]. It can be observed that the angular distribution of field experiences a significant narrowing in the region of 130 – 150 kHz and moreover, that filtering angles decrease with the increase of frequency. Figs. 2.6(b) and (c) demonstrate spatial filtering effect at particular frequency f = 140 kHz [Pic12]. Fig. 2.6(b) shows the beam propagation inside and behind the structure. The reflection of acoustic beam when entering the SC is clearly observed, which leads to the spatial filtering due to the angular BGs. Fig. 2.6(c) demonstrates the comparison between the far field profile of the beam which passed through SC (solid line) and the reference beam, which propagated only in water (dashed line). The beam which passed through the SC is evidently narrower in the far field domain compared to the reference beam, which confirms the spatial filtering effect.

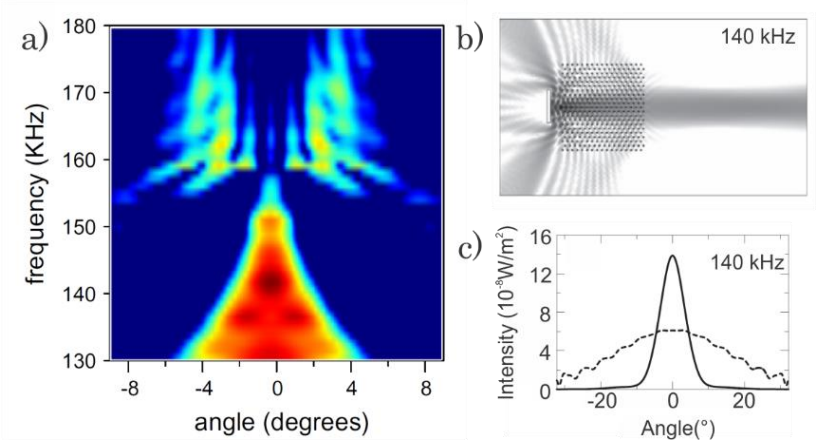

Figure 2.6. Numerical simulations with SC built from steel cylinders with $r = 0.6$ mm immersed in water. The crystal has a triangular symmetry, defined by lattice parameters $a = |\overrightarrow{a_1}| = |\overrightarrow{a_2}| = 6$ mm. Filling fraction is $f = 2\pi/\sqrt{3}(r/a)^2 = 0.03$. The material parameters are $\rho_h = 10^3$kg m^{-3} and $B_h = 2.2 \times 10^9$ N m^{-2} for the host medium (water) and $\rho_s = 7.8 \times 10^3$ kg m^{-3}, $B_s = 160 \times 10^9$N m^{-2}, with corresponding sound velocities $c_h = 1483$ m s^{-1} and $c_s = 4530$ m s^{-1}. The source is a Gaussian beam. (a) The far field (angular) distribution of the acoustic intensity transmitted through the crystal depending on the frequency in the configuration with angular band gaps. (b) a Gaussian beam propagating inside and behind SC for frequency of $f = 140$ kHz. (c) Far field (angular) distribution of the transmitted field shown in (b) (solid line) compared to propagation in free space (dashed line) [Pic12].

Moreover, in acoustics the spatial filtering with angular BGs was recently demonstrated experimentally [Pic13, Rom13]. Fig. 2.7 illustrates the experimentally obtained spatial filtering in propagation through the SC. It shows the angular sound field distribution at a distance R= 1 m behind the output face of the SC at the particular frequencies of 5158 Hz and 5543 Hz. The spatially filtered angular regions are shaded. The transmission through the crystal is compared with the free propagation (shown by dashed line), where clear spatial filtering at $\theta = 30^o$ in Fig. 2.7(a) and at $\theta = 15^o$ in Fig. 2.7(b) can be seen [Pic13].

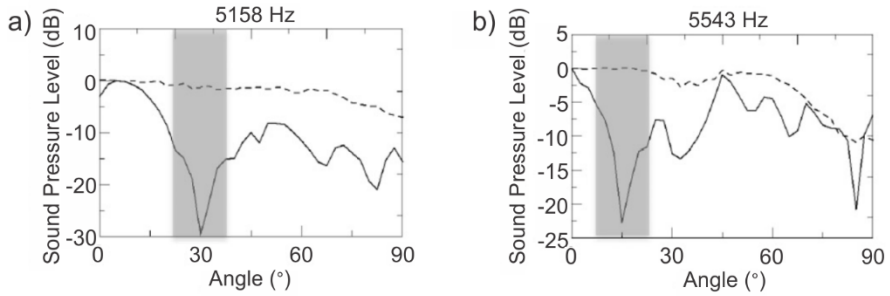

Figure 2.7. Experimental results evidencing the spatial filtering. The experiment was performed using SC of 9x10 matrix of cylindrical (methacrylate) scatterers of radius r = 1 cm, in square lattice with lattice constant a = 4.7 cm, surrounded by air. The filling fraction of the crystal $f = \pi(r/a)^2 = 0.14$. The emitter was broad band loudspeaker emitting white noise, a microphone was used as a receiver. (a) and (b) show the sound pressure level, with (continuous line) and without crystal (dashed line) for frequencies of f = 5158 Hz and f = 5543 Hz, correspondingly [Pic13].

In optics, for visible frequencies it is still a challenging technological task to realize such kind of spatial filtering experimentally, as the longitudinal period must be of the order of the wavelength. Even if technical problems were solved, the filtering with demonstrated angles $(20-30°)$ are hardly of technological interest. We were looking, therefore for alternatives of spatial filter with ~1°. It seems that such an alternative is spatial filtering in gapless configuration as suggested in [Sta09a]. During my PhD thesis work, we have experimentally proved these theoretical predictions, which are summarized in this chapter.

Fig. 2.8 illustrates iso-frequency curves combination for spatial filtering in both cases: Fig. 2.8(a) demonstrates spatial filtering with angular BGs, Fig. 2.8(b) – spatial filtering without angular BGs (gapless filtering). The dashed circles in Fig. 2.8 represent the dispersion curves (iso-frequency lines) for a beam propagating in an homogeneous medium, which obey $|k| = 2\pi/\lambda = const.$, the radius of these circles being proportional to the wavelength. In a periodic medium with negligibly low filling fraction (i.e. when the space occupied by the scatterers is much smaller than that occupied by the host medium) or, with negligibly low refractive index contrast, a periodic array of circles is formed in reciprocal space, where each circle is centered at each reciprocal lattice point (represented by black dots in Fig. 2.8).

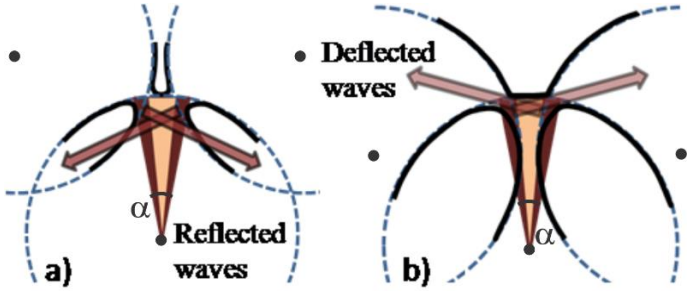

Figure 2.8. Illustration of the spatial filtering in a 2D PC, in spatial Fourier plane (k_x, k_y) (reciprocal space): with (a), and without (b) the angular bandgaps. Filtering occurs in both cases around the angles where the dispersion curves of the harmonic components for a particular frequency (dotted circles) cross. The spatial spectrum (far field) of the initial beam, consisting of the central (regular) part, and of the wings (the part to be removed, i.e. reflected in (a) or deflected in (b)), is illustrated with bright and dark triangles. The central dashed circle indicates the spatial dispersion of the homogeneous wave in homogeneous material, the lateral circles indicate the dispersion of the lowest harmonic components in the PhC.

In the periodic medium, where filling fraction or contrast of refractive index is non-negligible, dispersion lines follow approximately the shape of the circles, except that at the crossing points they mutually push, bend and distort the shape of the circle due to the mode interaction (distortion is shown by the thick lines in Fig. 2.8), avoiding the degeneracy of the solutions at the crossing points. Intersection between dispersion circles always lie at the corners of the Brillouin zone (at the symmetry points of reciprocal spaces). In Fig. 2.8, a total angular spectrum of the incident beam is denoted as α. Angular ranges marked by darker colour are the ones to be removed from the central angular spectrum by spatial filtering. In Fig. 2.8(a) these indicated angular ranges correspond to Bloch waves with the undefined dispersion relation. Bloch modes in the forward direction for these particular angular components do not exist, therefore plane wave components inside the angular BG cannot propagate, consequently they are back reflected (filtered out) from the angular distribution of the transmitted field. Therefore this region in reciprocal space is called an angular BG.

The idea of gapless filtering is that due to particular shapes of the spatial dispersion curve (in particular due to its strongly tilted segments), certain

angular components of the beam can be deflected at these tilted segments of the spatial dispersion curve. Fig. 2.8(b) illustrates the latter mechanism, which does not require the presence of the angular BG. Differently from the first mechanism, the angular components of the radiation do not reflect at the entrance of the PhC, but instead deflect into the first diffraction maxima along the propagation in the PhC. Therefore, there are no BGs in a strict sense in the latter case.

It is worth to remind that dispersion surfaces display a property that the group velocity vector for a given wavevector $\vec{k}$ coincides with the normal (which points to the direction of increasing frequency, as explained in Chapter 1) to the iso-frequency contour, i.e. $\overrightarrow{v_g} = \vec{\nabla}_{\vec{k}}\omega(\vec{k})$. The deflection mechanism of gapless filtering is directly related to this property: as illustrated in Fig. 2.8(b). The radiation at small angles, which corresponds on smooth segments of the dispersion curves, propagate without deflection, while the radiation at larger angles, which lies on strongly tilted segments, is deflected. Spatial filtering due to both mechanisms occurs at around the angles where the undistorted dispersion curves for a particular frequency mutually cross (having in mind that curves cross only if we neglect the filling fraction or refractive index contrast, otherwise, the curves mutually push and bend in the "cross location") .

We would like to mention, briefly, that there is an alternative way to interpret the spatial filtering effect, i.e. by the resonant interaction of modes lying on spatial dispersion curve. The appearance of the frequency BGs and the frequency filtering in 1D PhCs is related to the resonant back-scattering of the plane waves of particular frequencies. The spatial filtering, in the similar manner, can be explained by the resonant reflection or deflection of particular angular components of the light beam (Fig. 2.9).

First of all, the spatial dispersion curve for a monochromatic source of particular wavelength propagating in the homogeneous material has to be drawn in reciprocal space (In Fig. 2.9 dashed circle with the radius of $k = 2\pi/\lambda$). When the wave enters into PhC, the periodicity of the crystal starts playing the key role. The wave vector of refractive index modulation $\vec{q}$ (marked with blue arrows) couples forward propagating mode into backward propagating mode (first lying

on the top part of the circle, while the latter - on the bottom part). Therefore, due to this resonant coupling particular angular components surrounding the forward propagating mode are being backscattered and angular band gap in the forward direction appears. In Figs. 2.9(a) and (b) two examples of the described effect are demonstrated.

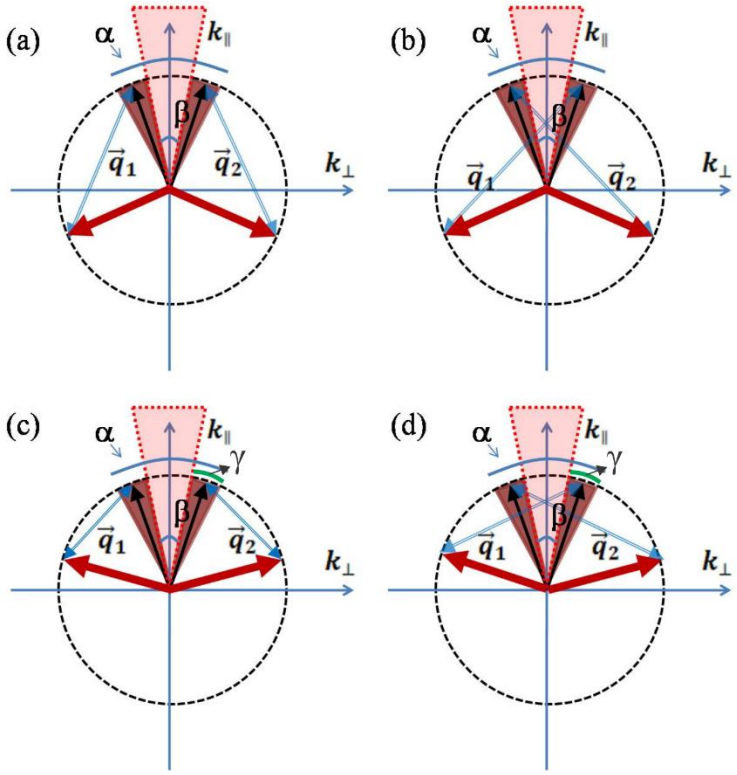

Figure 2.9. Illustration of the spatial filtering in a 2D PC, in spatial Fourier domain (k_x, k_y): with (a), (b) and without (c), (d) the angular bandgaps. Filtering occurs in both cases around the angles where particular $\vec{k}$ vectors (dark triangle zones) get into resonant condition with modulation wavevectors $\vec{q} = (q_x, q_z)$ (blue arrows) and are filtered out. Thick red arrows illustrate the direction of filtered out angular components of the angular spectrum. The spatial spectrum (far field) of the initial beam, consisting of the central (regular) part, and of the wings (the part to be removed, i.e. reflected in (a), (b) or deflected in (c), (d)), is illustrated with bright and dark triangles.

Here α marks the angular distribution of the beam, before entering the crystal. When the beam enters the crystal, some angular components of it fall into resonant condition determined by $\vec{q}$ (these particular components are marked as the dark triangles in Fig. 2.9), therefore, this angular region is

scattered into the backward propagating mode. The direction of the propagation of the scattered angles coincides with the direction of $\vec{k}$ vectors, marked in thick red arrows. The angular bandwidth that passes through the PhC without the resonant backscattering is marked with the bright triangle and indicated by angle β.

In Figs. 2.9(c) and (d) the gapless spatial filtering, and two cases of it, are illustrated. The description of the spatial dispersion diagrams in Figs. 2.9 (c), (d) is the same as in Figs. 2.9(a), (b) except of one important difference: there is no backscattering of the particular forward propagating angular beam components, but instead, occur their deflection, i.e. the resonant interaction creates two modes propagating in forward direction. The mode to which all the energy is scattered propagates at much higher angles (angle of the first diffraction maxima), but still in a forward direction, therefore, it cannot be called backscattering, but deflection instead. The central position of the angular band gap follows from geometrical considerations and corresponds to a resonant interaction between field harmonics [Pur13]. In paraxial approximation (appropriate for the gapless filtering) the expression for the filtering angle (marked in green angle in Figs. 2.9(c), (d)) is relatively simple (follows from simple geometrical considerations, see Fig. 9):

$$\sin(\gamma) = \frac{q_\perp}{2k_0}(Q-1) = \frac{\lambda}{2d_\perp}(Q-1). \tag{2.1}$$

Here $q_\perp = 2\pi/d_\perp$ is the transverse wavenumber of the index modulation, $k_0 = 2\pi/\lambda$ is the wavenumber of electromagnetic wave, $Q = 2d_\perp^2 n/(\lambda d_\parallel)$ is the geometry factor and n is the average refractive index. As (2.1) indicates the filtering angle γ depends, among others, on the longitudinal period of modulation (through the parameter Q).

To summarise, the basic parameters of the PhC, which determine the range of the wave components to be filtered out, are basically the longitudinal and transverse periods of the structure. The spatial filtering can be expected for the

transverse component of the modulation wavevector $q_\perp \leq k$ (equivalently $d_\perp \geq \lambda$). The longitudinal period of the modulation determines whether the filtered angular components of the beam reflect in the backward direction ($2k > q_\parallel > k$, equivalently $/2 < d_\parallel < \lambda$) or deflect in the forward direction ($q_\parallel < k$, equivalently $d_\parallel > \lambda$). As can be seen, the longitudinal periods for angular band gaps have to be smaller than the wavelength, therefore, for the visible frequencies, to fabricate such kind of structure is a complicated task. However, for the gapless filtering due to condition $d_\parallel > \lambda$, the fabrication becomes much less complex and PhC samples can be made. Hence, in the thesis, we consider the latter situation, which corresponds to the PhCs that are used for the experiments of spatial filtering in gapless configuration.

2.3. Signatures of light-beam spatial filtering in three-dimensional photonic crystals

2.3.1. **Numerical method**

We consider light propagation in a material with spatially modulated refractive index, as described by paraxial model:

$$(2ik_0\,\partial/\partial z + \nabla_\perp^2 + 2\Delta n(x,y,z)k_0^2)A(x,y,z) = 0. \qquad (2.2)$$

Here $A(x,y,z)$ is the slowly varying complex envelope of the electromagnetic field in 3D space $E(x,y,z,t) = A(x,y,z)e^{ik_0 z - i\omega_0 t} + c.c.$ propagating along the z-direction with the carrier wave-number $k_0 = n\,\omega_0/c$ (in a material with average refraction index n and carrier frequency ω_0), $\nabla_\perp^2 = \partial^2/\partial x^2 + \partial^2/\partial y^2$ is the Laplace operator in the space transverse to the propagation direction: $\vec{r}_\perp = (x,y)$ denotes the space perpendicular to the propagation direction, and $k_\perp = (k_x, k_y)$ denotes the transverse components of the propagation wavevector.

The profile of the refraction index, which is used in fabrication, is well approximated by a harmonic function:
$\Delta n(x,y,z) = \Delta n_o/4(\cos(q_x x) + \cos(q_y y))\cos(q_z z)$, where Δn_0 is the maximum amplitude of the variation of the refractive index (refractive index contrast). We expand the field into spatial harmonic components:

$$A(r_\perp, z) = \int e^{ik_\perp r_\perp}(A_0(k_\perp, z) + \sum_{m_x,m_y} A_{m_x,m_y}(k_\perp, z)e^{im_x q_x x + im_y q_y y - iq_z z})dk_\perp \qquad (2.3)$$

in the expansion we will consider only the most relevant diffracted components $A_{m_x,m_y}(k_\perp, z)$, $(m_x, m_y) = (0,-1),(0,+1),(-1,0),(+1,0))$, in addition to the zero component $A_0(k_\perp, z)$. This particular truncation is justified having in mind the smallness of the index modulation, and also from the experimental observations (described in the section 3.3.3), where only four diffraction maxima are dominating. Inserting Eq. (2.3) into Eq. (2.2) results:

$$\frac{d}{dz}A_0 = -\frac{ik_\perp^2}{2k_0}A_0 + \frac{i\Delta n_0 k_0}{16}\sum_{m_x,m_y} A_{m_x,m_y} \qquad (2.4.a)$$

$$\frac{d}{dz}A_{m_x,m_y} = \left(-\frac{i(k_x + m_x q_x)^2 + i\left(k_y + m_y q_y\right)^2}{2k_0} + iq_z\right)A_{m_x,m_y} + \frac{i\Delta n_0 k_0}{16}A_0 \qquad (2.4.b)$$

(2.4.b) describes a coherent transport of the radiation from the central component $k_\perp = (k_x, k_y)$ to the diffracted components $(k_x + m_x q_x,\ k_y + m_y q_y)$, and (2.4.a) describes an inverse process: the depletion of the zero component due to this scattering. The scattering and the depletion is most efficient for the angles $k_\perp$ corresponding to the resonant interaction between the zero component (2.4.a) and one or several of the diffracted components (2.4.b). The resonance condition reads:

$$(k_x + m_x q_x)^2 + (k_y + m_y q_y)^2 - 2q_z k_0 = k_x^2 + k_y^2 \qquad (2.5)$$

as follows from (2.4). This condition results in four crossing lines in $k_\perp$ space, each line corresponding to a particular set of (m_x, m_y), i.e. to the coupling with particular diffraction components. Physically speaking the radiation from each of the resonance lines is efficiently diffracted to their "own" diffraction components. The resonant lines are equivalent to the dark lines observed in experiment that we will present in the next section (Fig. 2.15 in the section 3.3.3). The pattern of the lines (the separation between the parallel lines) can be tuned by varying the parameters of the photonic structure for the same wavelength (or tuning the wavelength for the same structure as was done in experiment). For instance all four lines cross at the center $k_x = k_y = 0$ for $q_x^2 = q_y^2 = 2k_0 q_z$.

The resonance condition (2.5) allows calculating the angles of the dark lines with respect to the optical axis. In particular the resonance line $(m_x, m_y) = (+1,0)$ appears at the position $k_x/k_0 = q_z/q_x - q_x/(2k_0)$ in the angular space. This latter expression was used to design the PhCs described in section 3.3.2 and 3.3.3.

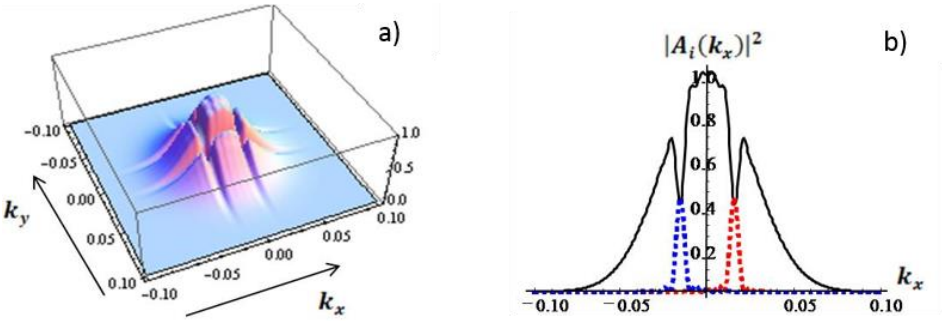

Figure 2.10. The 2D transmission profile (a) as well as the distribution on a horizontal cut (b), as obtained by numerical integration of (3) with the parameters: $m = 2 \cdot 10^{-4}$, $q_\perp = 0.25$, $q_\parallel = 0.035$, and for normalized propagation distance $z = 4 \cdot 10^3$. k_x and k_y are normalized into k_0.

The numerical integration of (2.4) shows the formation of the pattern in angular space (Fig. 2.10) which is analogous to that observed in experiment (Figs. 2.15 (a), (b) in the section 3.3.3). The amplitude of the modulation of refraction index $\Delta n_0 = 3 \cdot 10^{-3}$ has been chosen in numerical calculations in order to match

the configuration of the real samples that we were planning to use in the experiments. In fact the amplitude of refractive index modulation in PhC samples was estimated from the comparison of experimental and numerical spatial filtering profiles.

Figure 2.11 represents numerically calculated cases, analogous for the experimentally obtained results with $\lambda = 633$ nm (Fig. 2.15(b)), $\lambda = 570$ nm (Fig. 2.16(b)) and $\lambda = 532$ nm (Fig. 2.15(d)), respectively Figs. 2.11(a), (b) and (c). Moreover, the horizontal cross-sections are presented for each of the calculated cases (Figs. 2.11(d), (e), (f)). There is a very good agreement between the numerical calculations and experimental results.

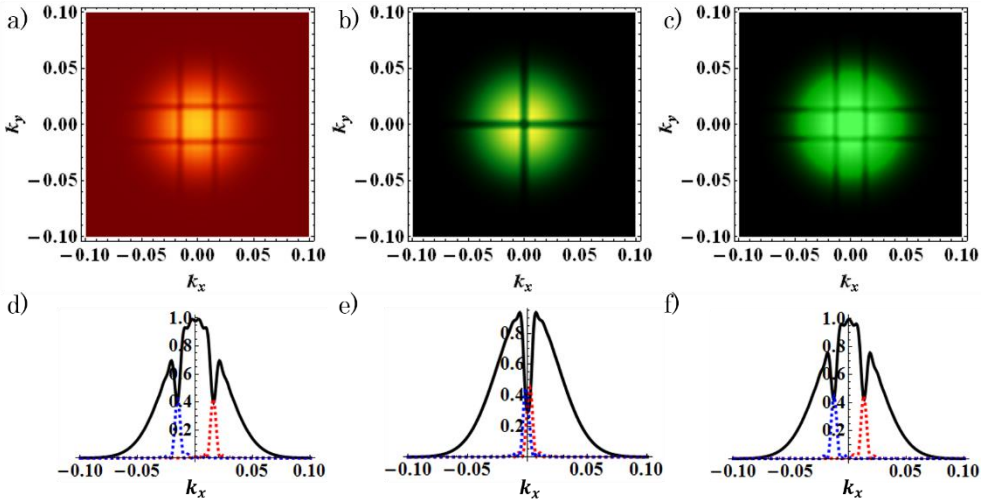

Figure 2.11. The 2D transmission profiles for the same parameters as described in Fig. 2.10, except $q_{\parallel}$. For (a) $q_{\parallel} = 0.035$ corresponding to experimental results with $\lambda = 633\ nm$, (b) $q_{\parallel} = 0.031$ corresponding to experimental results with $\lambda = 570\ nm$ and (c) $q_{\parallel} = 0.028$ corresponding to experimental results with $\lambda = 532\ nm$. Angular intensity distributions on the horizontal cross-sections (d), (e), (f), corresponding to the (a), (b) and (c). k_x and k_y are normalized into k_0.

In order to explore the formation of a particular, separately taken, dark line we simplify (2.4), by neglecting all the other resonances, except for a particular one (we consider the dark lines sufficiently separated). Considering the specific resonance line $(m_x, m_y) = (+1,0)$ the evolution of the field components on axis $k_y = 0$ follows:

$$\frac{d}{dz}A_0(k_x,z) = imA_{1,0}(k_x,z) \tag{2.6.a}$$

$$\frac{d}{dz}A_{1,0}(k_x,z) = i\Delta k_z(k_x)A_{1,0}(k_x,z) + imA_0(k_x,z) \tag{2.6.b}$$

where $\Delta k_z(k_x) = (2k_xq_x + q_x^2)/(2k_0) - q_z = \Delta k_x q_x/k_0$ is the off-resonance parameter for the interacting two waves (Δk_x is the transverse wavenumber with respect to the center of the dark line), and $m = \Delta n_0 k_0/16$ is the coupling parameter.

The solution of (2.6.a) is obtained analytically, which in terms of the field intensities reads:

$$\left|A_{1,0}(z)\right|^2 = \frac{|A_0(0)|^2\ \sin^2(zm\sqrt{1+\Delta k_z^2/(4m^2)})}{1+\Delta k_z^2/(4m^2)} \tag{2.7.a}$$

$$|A_0(z)|^2 = |A_0(0)|^2 - \left|A_{1,0}(z)\right|^2 \tag{2.7.b}$$

The evolution of the far field profile $|A_0(k_x,z)|^2$ along the propagation distance z is shown in Fig. 2.12. The dip in the central component increases, starts narrowing, and becomes maximally narrow at the full depletion. With increasing depth of the dip the oscillations on its fronts emerge. In particular the field components at the resonance $\Delta k_z = 0$ (i.e. on the center of the dark line) evolves with the propagation as: $|A_0(z)|^2 = |A_0(0)|^2\cos^2(mz) \approx |A_0(0)|^2(1 - m^2z^2/2)$. The half-width of the dark line decreases approximately as: $\Delta k_{z,1/2}^2 \approx 2(3 - m^2z^2/z^2)$ (at the level of ½ of intensity) as obtained by the series expansion of (2.6). The minimum width of the dark line at a distance of full depletion is: $\Delta k_{z,\,1/2,min} \approx m$. In terms of the variables of k_x, the half-width of the dark line evolves as: $\Delta k_{x,1/2}^2 \approx 2k_0^2(3 - m^2z^2)/(q_x^2z^2)$ down to the minimum width of $\Delta k_{x,1/2,min} \approx mk_0/q_x$.

The above estimations indicate that the overall effect of spatial filtering is linearly proportional to the depth of index modulation $m = \Delta n_0 k_0/16$ for a given geometry and for a fixed width of the PhC spatial filter.

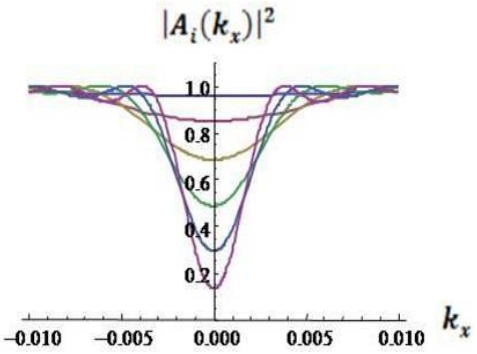

Figure 2.12. The evolution of the angular field profile around the resonance, as obtained from (2.7) along the propagation in PC. The parameters are: $m = 2 \cdot 10^{-4}$, $q_\perp = 0.25$, $q_\parallel = 0.04$, the lines show field profiles at equidistant propagation distances from $z = 0$ to $z = 6 \cdot 10^3$. k_x is normalized into k_0.

2.3.2. Fabrication of photonic crystal samples

Our PhCs were fabricated by selectively modifying the refractive index of fused silica glass bulk by tightly focused femtosecond laser pulses [Kam04, Gat08, Str02]. The magnitude of the refractive index change depends on the material and exposition conditions. It is generally considered that the index can be modified by 10^{-3} [Kam04, Gat08, Str02]. The micromachining system used operates with pulses of 300 fs duration pulses at $\lambda = 1030$ nm. Pulse energy $E_{imp} = 1$ μJ and the repetition rate of 200 kHz are used in fabrication process.

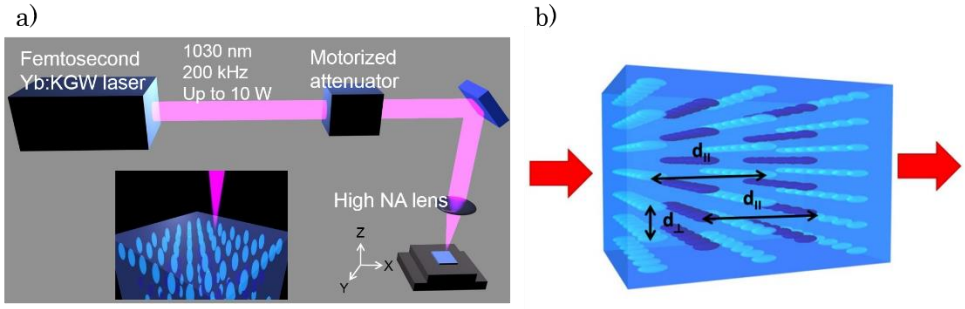

Figure 2.13. Schematic demonstration of fabrication setup and the fabricated crystal.

The glass sample was positioned, and moved by *XYZ* high precision linear motor driven stages. The laser beam was focused using aspheric lens with $f =$

4.07 mm focal length and with numerical aperture of $NA = 0.62$, which resulted in a spot of ellipsoid shape at the focal point of width $w_{\perp} \approx 1$ μm and of length $w_{\parallel} \approx 3$ μm.

The geometry of the PhC is illustrated in Fig. 2.13 where $d_{\perp} = 1.5$ μm and $d_{\parallel} = 11.6$ μm are the transverse and longitudinal periods respectively. Different colours of the ellipsoids indicate odd and even layers of photonic crystal which are half-period shifted one with respect to another in transverse plane. The total number of the longitudinal modulation periods is 25 and the square structure of the spots in each transverse layer is 500 by 500 points.

2.3.3. Experimental results and discussion

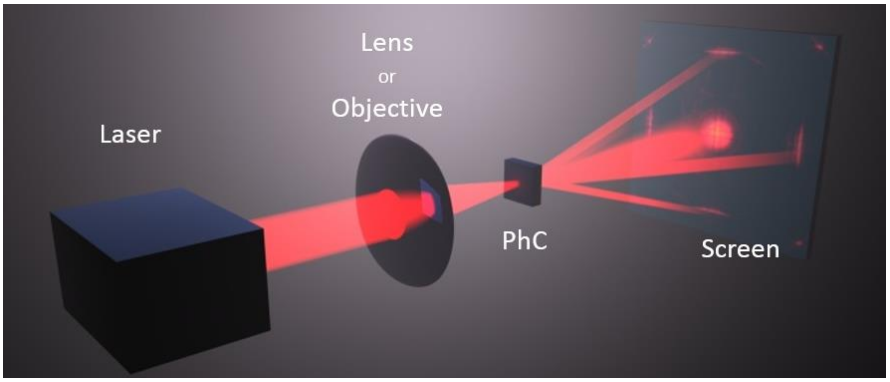

Figure 2.14. Experimental scheme consisting of a focused laser beam (10x objective), PhC sample at the focus, and a remote screen for observation of the far-field.

In order to observe the spatial filtering we illuminated the sample with a focussed CW laser beam of He-Ne laser of $\lambda = 633\ nm$ and the power up to 2 mW. The focussed beam fits well inside the PhC. The angular distribution of the intensity (distribution in the far field domain) of the beam transmitted through the PhC was observed on a screen and, moreover, was recorded by a CCD camera. A schematic representation of the setup is presented in Fig. 2.14.

The experimental measurements show clear presence of the first diffraction maxima (Figs. 2.15(a) and (c)) as well as the dark line structure in the central maximum (Figs. 2.15(b) and (d)), which correspond to the filtered out angular components.

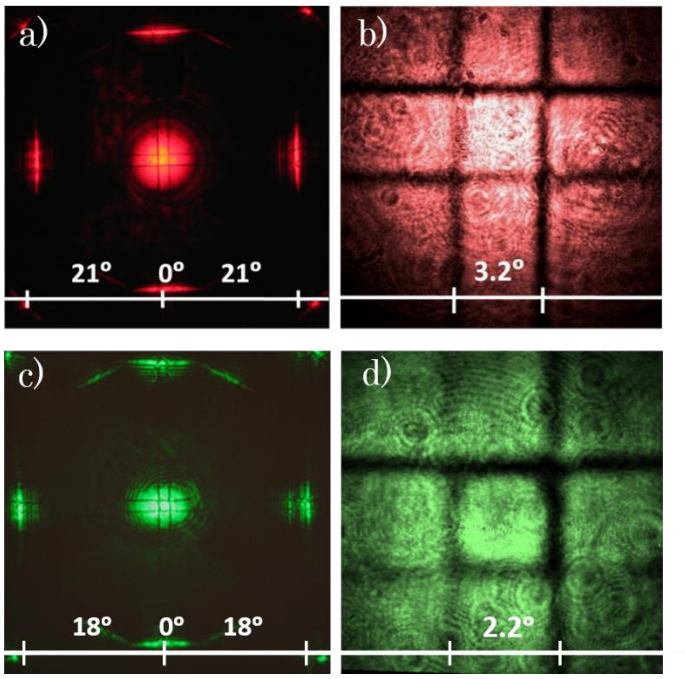

Figure 2.15. Experimental results: Image on a screen showing the central and first diffraction maxima for $\lambda = 633\ nm$ and $\lambda = 532\ nm$, correspondingly at (a),(c). CCD camera image of the central part of the beam with angular field components filtered out (dark lines crossing each other and making a square within the central maximum), for $\lambda = 633\ nm$ and $\lambda = 532\ nm$, corresponding to (b),(d).

The results are well reproducible and show the signatures of the expected effect of the spatial filtering. Additionally, have used a CW Nd:YAG laser of $\lambda = 532$ nm with a power up to 1 mW, for the same sample, and obtained the intensity distribution on a screen (Fig 2.15(c)). Intensity maxima are observed, as well as the dark line structure of filtered out components in Fig 2.15(d). The difference between the results obtained using He-Ne and Nd:YAG lasers, is in the diffraction maxima angles, as well as, the filtering angles in the central maximum of the beam, as both of them depend on the wavelength (dependence of the central part

filtering angle on wavelength is shown in (2.1)). According to the theory, there should be a region between $\lambda = 633$ nm and $\lambda = 532$ nm where dark lines in the central part of the beam cross each other. In order to check that (see Fig. 2.11(b)), we have used a Ti:Sapphire femtosecond laser that pumps on OPO to tune the wavelength from $\lambda = 577$ nm to $\lambda = 564$ nm and observe the effect. The most interesting results of the filtering regions are shown in Fig. 2.16, where a clear cross of the filtered out lines in the central part of the beam is observed. The pattern of the crossing for all three demonstrated cases is practically the same, except the cross point at $\lambda = 577$ nm is slightly brighter compared to the one of $\lambda = 568$ nm, which seems to be completely dark.

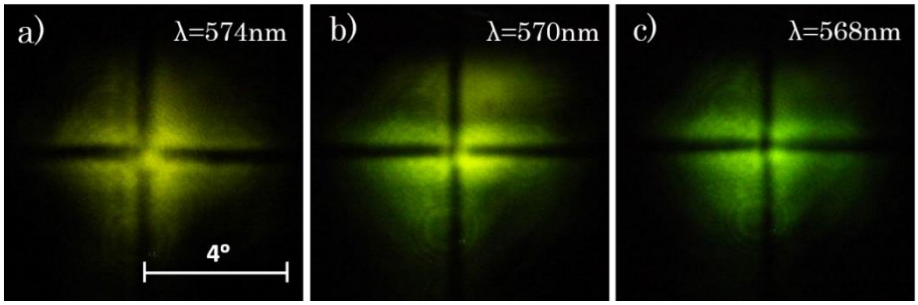

Figure 2.16. Far field distribution of the central part of the beam where the crossing of the filtering lines is observed: (a) at λ=574 nm, (b) at λ=570 nm and (c) at λ=568 nm.

Additionally, to the wavelength change for exploring filtering effect for the same sample, we have used several PhC samples fabricated under slightly different conditions and obtained similar results.

As discussed above the configuration of the dark lines shows the filtered out angular components of the spatial spectra. The structures of these dark lines within the central maximum correspond well to the structures of the bright lines observed in the first diffraction maxima, which is in a good correspondence with the theoretical expectations (see Fig. 2.17).

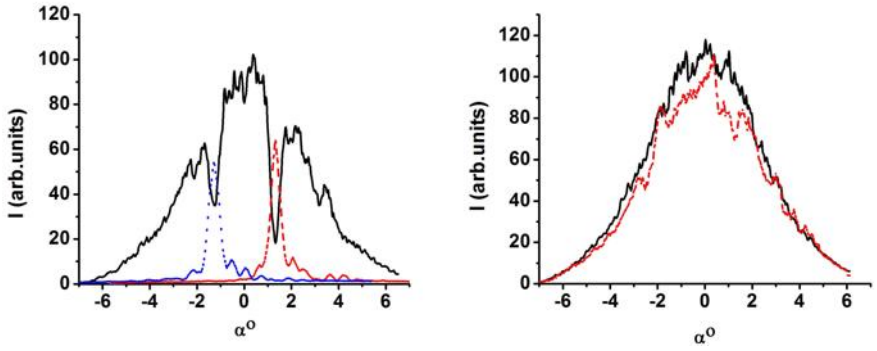

Figure 2.17. Intensity distributions well-behind the PC (in the far-field domain) along the horizontal cut crossing the center of the beam: (a) the field from central maximum (solid line) and from the first diffraction maxima (dashed, coloured lines). (b) full transmitted intensity distribution i.e. the central- and the first maxima added (dashed line) compared to the distribution without the crystal (solid line). α° - angle in a far field.

Fig. 2.17 summarizes a quantitative analysis of the spatial filtering effect for the case of 2.15(a), (b). From the evaluation of the field distributions follows that approximately 5% of the radiation energy was selectively removed from the central maximum, and deflected into the four diffraction maxima of the first order. The angular intensity distribution of the deflected radiation coincides well with the angular distribution of the "dips" in the central components, as the comparison in Fig. 2.17 indicates.

However, the above reported effect of spatial filtering is relatively weak, and carries a demonstrational character only, as the dark lines are relatively narrow. Approximately only 5% of the radiation is filtered out in the described PhC samples. The reason for the weak filtering is the relatively small amplitude of the refractive index modulation. In order to obtain a technologically utile spatial filter, which would filter out a substantial amount of the radiation, higher (but moderate) index contrast PhCs are necessary, which should be based on new materials and new fabrication technologies. Figure 2.18 represents four cases of PhC (the same geometry and the same width as the one discussed in this part of the chapter) with increasing refractive index contrast. We can observe that increasing the amplitude of contrast, the angular area of filtering (the "dip" in

the transmission spectrum) becomes broader. However, the broadening of the line is observed until some threshold value of the refractive index contrast amplitude, for the further increase of the contrast the splitting of the filtering line appears (Fig. 2.18(d)).

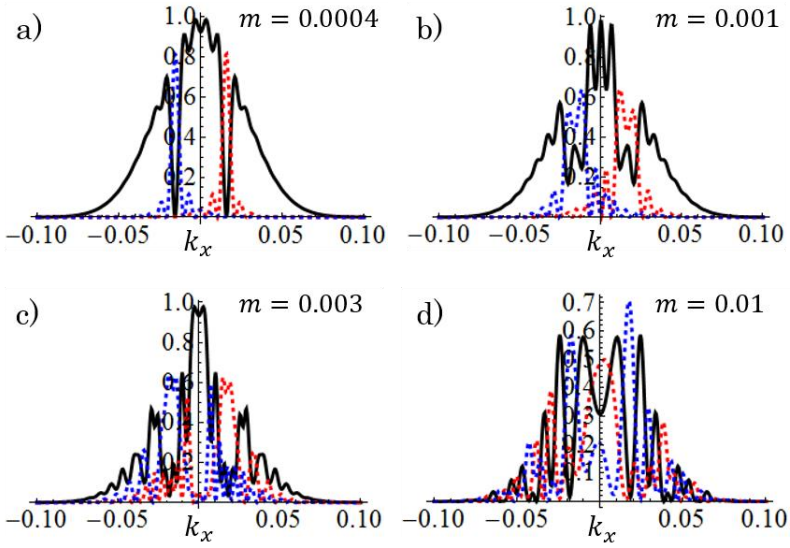

Figure 2.18. Series of numerical simulations of beam intensity distributions in far field of central and first diffraction components after propagation in PhC, with the same parameters described in Fig. 2.8, except varying the f parameter, which for (a) was $m = 0.0004$, for (b) $m = 0.001$, for (c) $m = 0.003$ and for (d) $m = 0.01$.

For a filtering relevant for applications, e.g. selectively removing approximately 50% of the radiation, the index modulation of order of $\Delta n_0 = 3 \cdot 10^{-2}$ would be ideal for the available geometry and periodicities of the PhC, that has been considered above.

However, the high index contrast PhCs are neither ideal for the spatial filtering, as for such crystals, the splitting of the dark lines occurs, according to the theoretical predictions (2.7) and numerical calculations in Fig 2.18(d). This, from the experimental viewpoint should lead to strong and unpredictable scattering of light by the PhC structure. Thus, the implementation of the high-index-contrast polymeric PhCs, such as woodpiles [Deu04, Miz04] or FCC-like PC structures [Che07] could be problematic. However, the above mentioned

polymeric structures [Deu04, Miz04, Che07] filled by the material with the refractive index similar to that of a polymer, could lead to the optimum refractive index contrast of $\Delta n_0 = 3 \cdot 10^{-2}$, and could thus result to optimally strong spatial filtering effect. Another way to improve spatial filtering effect is to add chirp to the structure, i.e. a linear increase of the longitudinal period along the PhC, without changing the contrast of refractive index. The effects of chirping are described in the next chapters.

2.4. Spatial filtering by chirped photonic crystals

As already explained in the previous section, we are using the filtering mechanism in a gapless configuration (Figs. 2.9(c), (d)). We recall that the fabrication of the gapless spatial filters is more convenient, as not so small longitudinal periods are required. On the other hand, the mechanism in gapless configuration restricts the efficiency of filtering, as the deflected wave components propagating in forward direction, can be scattered back into the modes of initial radiation. The process is summarized in Fig. 2.19, where the gapless filtering depending on the length of nonchirped PhC is shown. (We postpone the description of numeric as well as experiment in following sections). It is evident that initially the "dips" in the angular spectrum (the filtered out angular regions) increase in depth with the crystal length (Fig. 2.19, $n = 8, 14$).

However, when the area being filtered is depleted to zero, the reverse process starts, and the efficiency of the filtering decreases (Fig. 2.19, $n = 20, 22$). Moreover, the filtered out area appears to be not a smooth dip, as needed for applications, but develops oscillatory character. This is in strong contrast with the spatial filtering based on BGs, where the filtered out radiation propagates in backward direction (Fig. 2.20(b) all parameters for simulation are the same as 19.a, except of longitudinal period $d_{\parallel} = 0.35$ μm)) and, therefore, cannot be reversely scattered into forward propagating beam. As it is seen in Fig. 2.20(b) with the increase of the length of the PhC, the depth of the "dip" and the efficiency

of filtering is constantly increasing and no reverse scattering process is observed. In the figure, the red profiles mark the reflected angular components

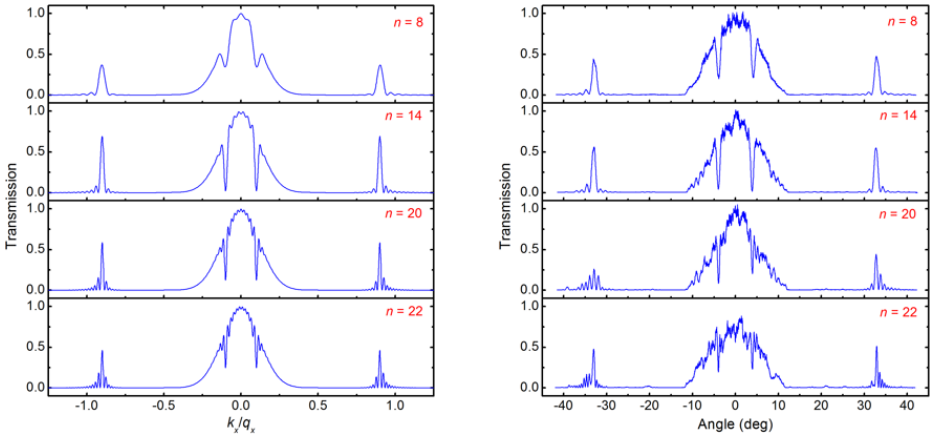

Figure 2.19. Angular profiles of filtered radiation depending on the length of the nonchirped PhCs (in terms of number of periods n). (a) Numerical and (b) experimental results. The transversal period of the crystal $d_{\perp} = 1\ \mu m$, the longitudinal period $d_{\parallel} = 6\ \mu m$, refractive index $n = 1.52$, refractive index contrast $\Delta n = 10^{-3}$, wavelength $\lambda = 633\ nm$.

In order to achieve efficient angular filtering in the gapless case, the reverse scattering process is to be suppressed, i.e. the interaction between modes is to be allowed for a limited propagation distance, and interrupted just at the distance when reverse process starts. For the parameters of Fig. 2.19, the optimum length providing maximum dip of filtered out components is approximately 14 periods. However, at the optimal distance the filtering dip is just of a limited width. As already mentioned, the other possibility to increase the efficiency of spatial filtering is to use the chirped structures [Sta09a], where the longitudinal period varies along the photonic structure. As the central angle of filtering depends on the geometry of the PhC, and among others on the longitudinal period, then the filtering angle will sweep along the chirped structure. As the result one can obtain simultaneously: 1) the angular range of filtered out components can be increased, i.e. is determined by the sweep of the instantaneous filtering angle along the full length of the crystal; 2) The reverse scattering process can be suppressed, as the efficient interaction length of the angular components is

limited by the velocity of the sweep.

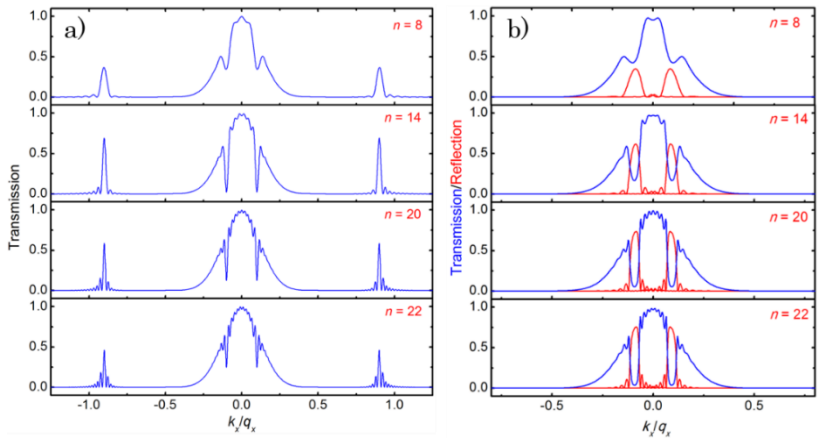

Figure 2.20. Numerical calculations of angular profiles of filtered radiation depending on the length of the PhCs (in terms of number of periods n). (a) in condition of gapless filtering, already described in Fig. 2.19(a), (b) in condition of filtering with angular BGs, where particular angular components are reflected back. Here blue colour marks transmission, while red – reflection.

The current section of the chapter is devoted to the experimental demonstration of the effect, and to the analysis of the efficiency of the angular filtering in presence of the chirp. It contains the description of fabrication and measurement of chirped PhC samples, as well as, the description of numerical calculations of the light propagation through the structure. The experimental results and numerical calculations are compared, discussed and summarized.

2.4.1. Numerical method

We use a simplified version of the transfer matrix method, where we consider only the forward propagating wave components. A similar technique was used to calculate the field evolution in resonators filled by PhCs [Pec09]. The transverse periodicity in lateral x direction imposes the corresponding transversal modulation of the field, therefore the field (at every longitudinal position z) can be expanded:

$$A(x,z) = e^{ik_{x,z}x}(a_0(z) + a_{-1}(z)e^{-iq_x x} + a_{+1}(z)e^{iq_x x} + a_{-2}(z)e^{-2iq_x x} + a_{+2}(z)e^{2iq_x x} + \cdots). \tag{2.8}$$

The amplitudes of Fourier coefficients of the field expansion (equivalently the amplitudes of angular components with transverse wave numbers $(k_x + mq_x)$ constitute a column vector:

$$\vec{A}(z) = (\ldots, a_{-2}, a_{-1}, a_0, a_{+1}, a_{+2}, \ldots)^T. \tag{2.9}$$

Next we list consecutive field transformations along one full longitudinal period of the modulation of photonic structure.

Scattering by one layer

The periodical modulation in transverse direction couples the angular components of the field vector (2.9). In particular the harmonic modulation couples only the neighbouring field harmonics. We introduce phenomenological coupling coefficient *s*, which can be linked to microscopic parameters of the modulation of refractive index. The scattering matrix is:

$$\hat{S} = Exp\begin{pmatrix} 0 & is & 0 & 0 & 0 \\ is & 0 & is & 0 & 0 \\ 0 & is & 0 & is & 0 \\ 0 & 0 & is & 0 & is \\ 0 & 0 & 0 & is & 0 \end{pmatrix}. \tag{2.10}$$

For simpler presentation we consider the scattering truncated to 5 harmonic components.

Free propagation

The free propagation between the scattering layers is considered by the paraxial propagation equation:

$$\partial_z A(x,z) = \frac{i}{2k_0}\frac{\partial^2}{\partial x^2}A(x,z). \tag{2.11}$$

Substitution of expansion (2.8) into (2.11) yields the equation system:

$$\partial_z a_m(z) = -\frac{i}{2k_0}(mq_x + k_x)^2 a_m(z). \tag{2.12}$$

The integration of (2.12) over the half of a longitudinal period results in diagonal field transformation matrix:

$$\hat{P} = Diag(\dots, e^{-iL(k_x-2q_x)^2}, e^{-iL(k_x-q_x)^2}, e^{-iLk_x^2}, e^{-iL(k_x+q_x)^2}, e^{-iL(k_x+2q_x)^2}, \dots) \tag{2.13}$$

Here $L = d_z/2\,k_0$ is the normalized longitudinal period.

Full period

The field transformation along the full longitudinal period is calculated by applying consecutively all the operators presented above:

$$\hat{T}_i = \hat{P}\hat{M}^{-1}\hat{S}\hat{M}\hat{P}\hat{S} \tag{2.14}$$

For the chirped crystal the parameters of one period transfer matrix depend on the lattice parameters in concrete period. The full transmission matrix is a matrix product of (2.14): $\hat{T} = \prod_i \hat{T}_i$. The transmission of the central component is given by the central element $T_{0,0}$ of the full transmission matrix $\hat{T}$. The scattering into sidebands harmonics is described by the corresponding off-diagonal column elements of the matrix, e.g. by elements $T_{-1,0}$ and $T_{+1,0}$ into the first diffraction components.

The coupling coefficient s depends on the modulation amplitude of refractive index, which is of order of $\Delta n \sim 10^{-3}$. We determined the concrete values of s by calibrating the experimental data with numerical calculations for light propagation through unchirped crystal (see Fig. 2.19). For our samples, the s has

been estimated $s \approx 0.05$, which means that approximately $s^2 = 0.25\%$ of radiation is scattered in propagation through each layer. We note, that this calibration allowed us to estimate the variation of refraction index of sample, which comes out to be approximately $\Delta n \approx 3 \cdot 10^{-3}$ for our samples fabricated with optimum parameters.

2.4.2. Fabrication of the photonic crystal samples

The PhCs were fabricated in standard microscope soda-lime glass slides (Carl Roth, $n_{ref} = 1.52$) by a point-by-point modification of refractive index by a tightly focused femtosecond laser beam. The method is widely used for inscription of various micro-optical and photonic components in glass, such as waveguides [Dav96, Nol03], Bragg gratings [Zha07], as well as vortex generators [Ber11]. The simplified scheme of the fabrication setup is depicted in Fig. 2.21(a).

Due to high intensity of focused light, the refractive index at the region of the focal point is locally modified, thus translation of sample results in a desired profile of modulation of refractive index in three dimensions. The change of refractive index and its spatial confinement depends on applied laser power. We used 300 fs pulse duration Yb:KGW laser providing 1030 nm wavelength radiation. The best results (the strongest refraction index modification) were obtained using 50 kHz repetition rate and 70 mW average power (before the objective, ~13% of the power after passing it), 2.5 mm/s scanning speed and 63x 1.4 NA objective. This corresponds to 0.2 μJ energy per pulse and 14 TW/cm^2 peak light intensity calculated as in [Mal11]. Assuming that voxel size is ~500 nm, the minimum transverse period of the photonic structure was 1 μm. Further increase of irradiation power did not provide any significant increase in refractive index contrast, but introduced scattering defects, caused by distortion and thermal damage of affected regions.

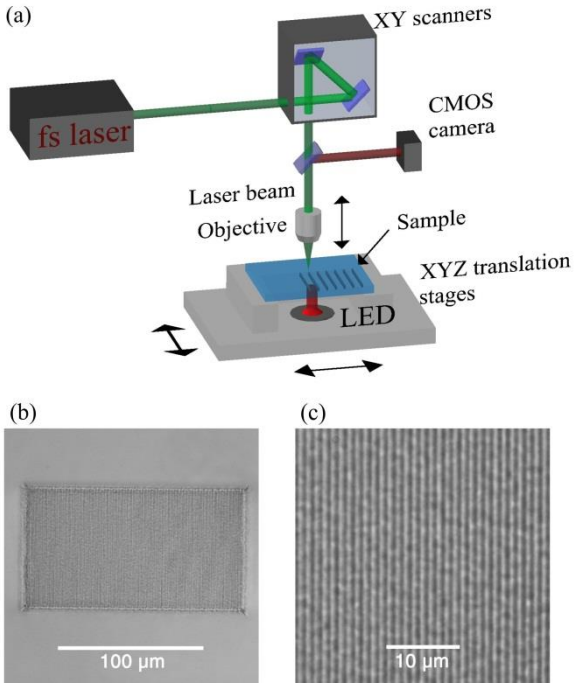

Figure 2.21. Illustration of fabrication setup and procedure (a). A sample of soda-lime glass is moved in respect to the tightly focused femtosecond laser beam inducing a point-by-point refractive index modification in the bulk of the glass. (b) The view of the produced structure. (c) The magnified view of the produced structure. Optical microscopy image.

PhCs were designed to be 150 µm × 80 µm size and have 100 layers of parallel, equally spaced rods with 1 µm transverse period (Fig 2.13(b), (c)). Every second layer was shifted by half of the transverse period with respect to the previous one, thus two layers result in one longitudinal period. For chirped crystals the longitudinal period d_z is linearly incrementing by Δd for every new period, $d_{z,j} = d_{z,B} + j \cdot \Delta d$, where j counts the periods $j = 1 \dots n$. The adimensional chirp parameter is defined $C = \Delta d / \overline{d_z}$, where $\overline{d_z} = (d_{z,Begin} + d_{z,End})/2$ is the average distance between layers. We chose $\overline{d_z}$ to be 6 µm and kept it constant in different samples, whereas the chirp parameter C was varied from sample to sample. Such fixed $\overline{d_z}$ corresponds to central filtering angle $\approx \pm 4^{\circ}$ degrees.

2.4.3. Experimental results and discussion

For measurements of the filtering performance we illuminated the samples by continuous 633 nm wavelength HeNe laser beam focused into PhC samples with 10x 0.2 NA objective (Fig. 2.22). Focusing provides a large angular range of radiation illuminating the PhC. By measuring the angular intensity profile at the output of the PhC we determine which components are filtered out. To register the output a CCD camera was placed 3 cm behind from the sample on a rotational stage, whose rotation axis coincided with the focal point of the objective. Intensity profiles were recorded at different camera positions and combined, resulting in an overall far-field distribution.

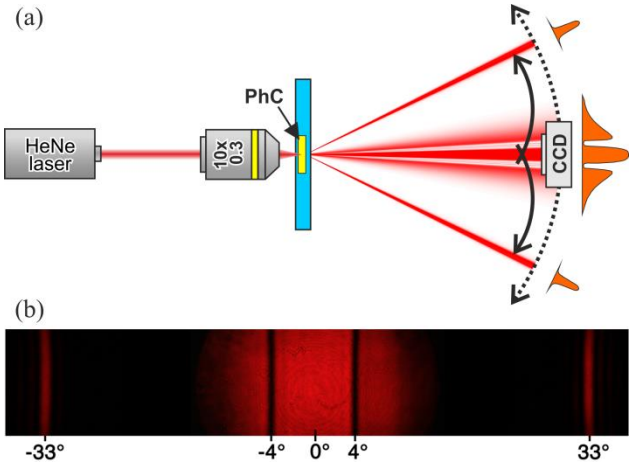

Figure 2.22. Illustration of experimental measurement (a). Focused HeNe laser beam provides a wide range of angular $\vec{k}$ components incident to the PhC. Some of the $\vec{k}$ components are deflected to the diffraction maxima and the rest passes through unaffected. A CCD camera placed on the rotational stage measures the angular intensity profiles. (b) CCD camera photograph of the beam after the PhC.

The main result of the study is presented in Fig. 2.23. The figure shows the constructive role of the chirp for spatial filtering performance. The angular range as well as the energy of filtered-out radiation increases with increasing chirp as expected. The experimental results correspond well to the numerical calculation results. Some discrepancy between the experimental measurements and numerical results is apparent, especially for large values of the chirp, which is

due to imperfections of fabrication of the samples. We note that the discrepancy increase with the length of the sample.

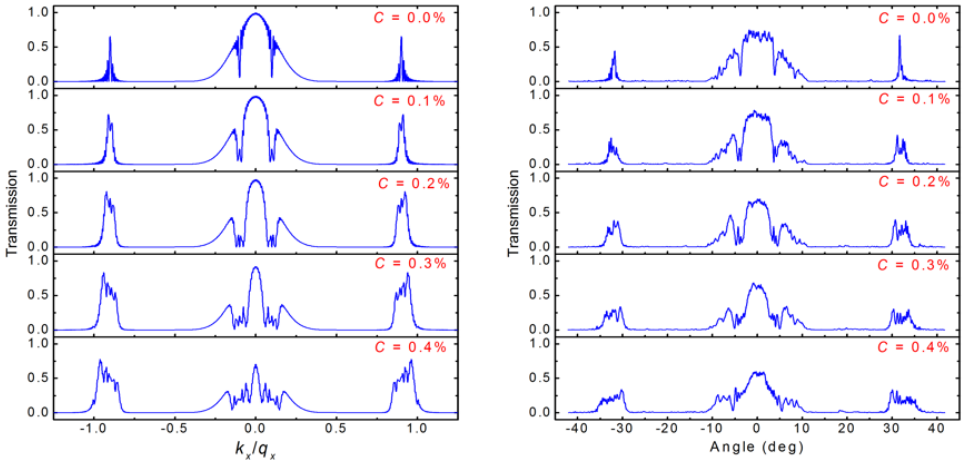

Figure 2.23. Angular transmission profiles for varying chirp parameter C for PhC sample with n = 50 periods. (a) Numerical and (b) experimental results. Transverse wave number kx is normalized to transverse wave number of refractive index modulation qx in (a).

Next we calculate quantitative data of the filtering performance. We define filtering performance by:

$$F = \frac{\int |\Delta I(k_x)| dk_x}{\int |I(k_x)| dk_x} \tag{2.15}$$

which is the depletion of energy normalized to the full energy. Here $\Delta I(k_x)$ is the depletion of $A(k_x)$ component.

Fig. 2.24(a) summarizes the dependence of the filtering performance on the chirp. If the filtering in unchirped PhC structures of increasing length saturates for short crystals ($n = 14$ periods). For chirped crystals the saturation begins for longer crystals and results to larger filtering performance values, correspondingly. Fig. 2.24(b) shows the dependence of filtering on the length of the sample for different chirp parameters C.

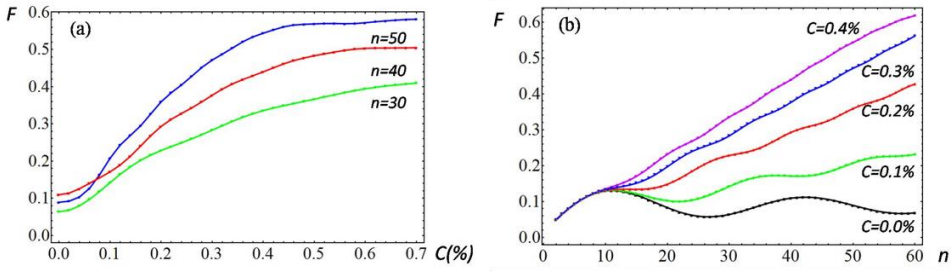

Figure 2.24. Quantitative study: (a) Dependences of filtering efficiency on chirp parameter for several crystals of different length (green plot for n = 30, red for n = 40, blue for n = 50); (b) Dependences of filtering efficiency on number of periods with different chirp parameters (black plot for C = 0.0%; green for C = 0.1%, red for C = 0.2%, blue for C = 0.3%, violet for C = 0.4%).

The above theoretical study is performed with the parameters corresponding to fabricated structures: the values of the coupling were $s = 0.05$ which correspond to the maximum achievable coupling for structures imprinted in glass. We also restricted to realistic length of the PhC, possible to write without large distortions, which is approximately $n = 60$. With the increasing length of the structure the imperfections of fabrication, as well as the losses and scattering of the structure increase. However even with these restrictions the filtering performance close to approximately *50%* has been demonstrated.

Looking into perspective, we analyzed the filtering performance of "hypothetical PhCs" with larger refractive index modulation (and also chirp), i.e. with corresponding larger coupling parameters s than those possible to obtain in reality. Examples of calculations for longer- and higher index contrast photonic structures are shown in Fig. 2.25. The both calculated cases show that the filtering performance can reach the values of *80%*, and could result in impressive enhancement of the beam quality by factor of 3.

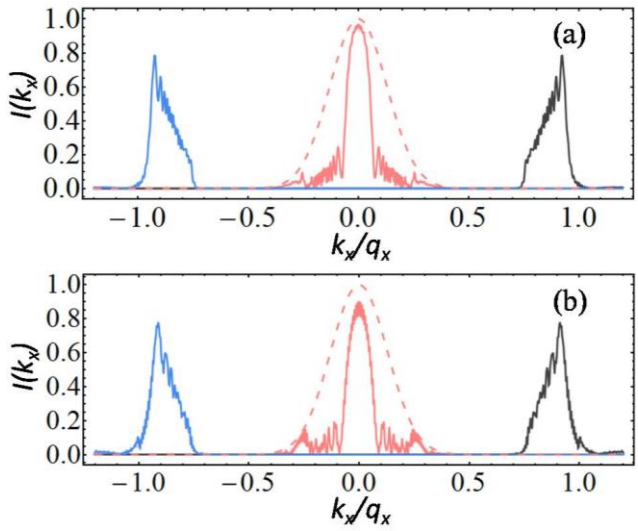

Figure 2.25. Numerically obtained field profiles for spatial filtering in chirped structures with higher number of periods (a) and for higher refraction index contrast (b). The parameters for (a): n = 120, s = 0.05, C = 0.24%, d_z = 7.44 μm.; for (b): s = 0.1, n = 50, C = 0.53%, d_z = 7.2 μm. The dashed line indicates angular profile of incident beam.

The filtering performance depending on parameters *s*, *n*, and *C* is summarized in Fig 2.26. As follows from Figs. 2.26(a), (c) the chirp parameter *C* has optimum values, which depends on the coupling parameter *s*: stronger coupling results in shorter filtering saturation length, therefore requires larger chirp for maximum filtering performances. The dependence of filtering performance on the length of PhC, as follows from Figs. 2.26(b) and (d), shows the monotonic increase of filtering efficiency with eventual saturation.

In spite of relatively weak index modulation (small scattering by one row) a substantial part of the radiation was shown to be filtered out. In order to obtain a technologically utile spatial filter the higher (but moderate) index contrast PhCs are necessary, which are to be based on novel materials and new fabrication technologies. A technologically relevant spatial filtering, allowing to improve the beam quality parameter by the factor of 2-3, requires the refractive index modulation of order of approximately $\Delta n_0 = 10^{-2}$.

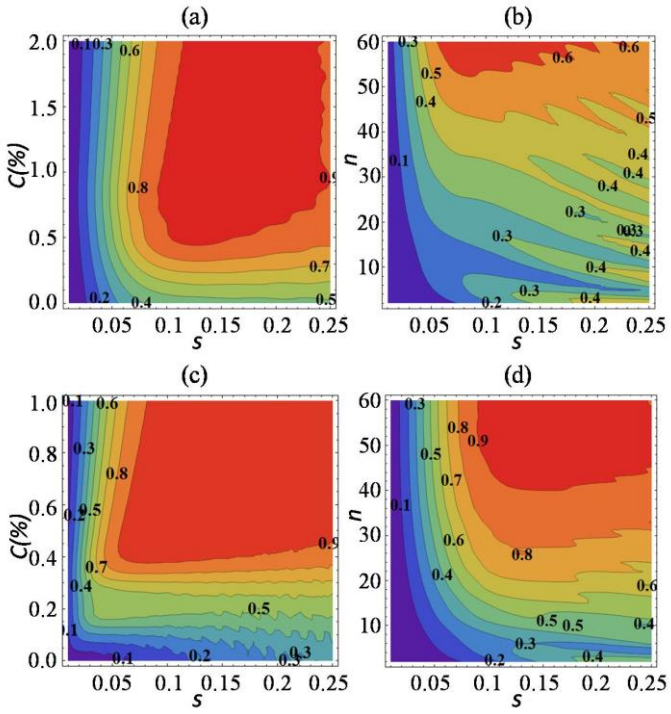

Figure 2.26. The filtering efficiency, represented by isolines and by different colors, depending on sets of parameters. (a), (c) show dependences on C and s; (b), (d) show dependences on n and s Parameters: (a) n = 50, (c) n = 120. (b) C = 0.3% and (d) C = 1%.

2.5. Spatial filtering by axisymmetric photonic microstructures

In the previous sections, the angular filtering has been considered for 2D and 3D PhCs, where the refractive index is modulated in longitudinal as well as in transverse direction. Moreover, for the 2D PhC the strongly positive effect of chirp for improving the spatial filtering efficiency has been demonstrated [Pur13].

2D PhCs can provide only 1D spatial filtering, which can be used for specific applications, where the beam is spatially random along only one quadrature. The schematic illustration of 2D PhC and its resulting 1D spatial filtering is shown in Figs. 2.27(a) and (b) correspondingly.

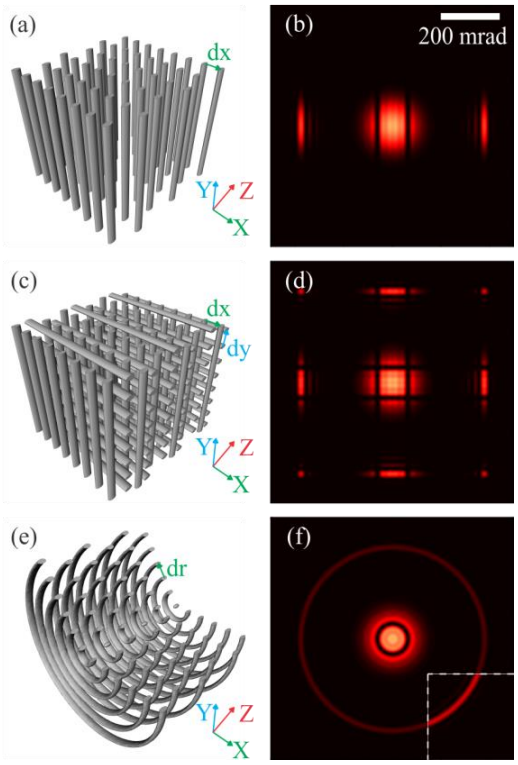

Figure 2.27. The geometries (a, c, e) of the photonic structures, and their corresponding far field filtering distributions obtained by numerical calculations (b, d, f). (a, b) 2D case as considered in [Pur13]; (c, d) square symmetry case in transverse plane case as considered in [Mai10]; (e, f) spatial filtering in axisymmetric structures. The inset in (f) shows 5 times enhanced field intensity for visualization of the outer ring. The parameters for simulations are given below in the main text.

In order to form axisymmetric beams of a high spatial quality a 2D filtering is required. Therefore, this should be performed by 3D PhC. The shape of the filtering window, however, depends strongly on the geometry of the 3D crystal. In the section 3.3.2 we have described 3D PhC, which had a square symmetry in transversal plane and it resulted in the square filtering window (check Fig. 2.13(b) for geometry and Fig. 2.15 for filtering). In Fig. 2.27(c) the 3D PhC with square symmetry in transversal plane is demonstrated, and the intensity distribution in the far field of the beam which passed through such crystal is demonstrated in Fig. 2.27(d) where filtering window is of a square shape.

Therefore, as the filtering window depends on the geometry of the transverse plane of PhC, it is natural to expect that the axisymmetric filtering requires axisymmetric shape of the PhC. The axisymmetric PhC is schematically shown in Fig. 2.27(e) and its resulting spatial filtering window in Fig. 2.27(f).

A demonstration and analysis of such axisymmetric spatial filter, in axisymmetric PhCs is the object of the present section of the chapter. First we provide numerical integrations of the light beam propagation through (and behind) such structure. Subsequently, based on the numerical calculation results we fabricated the crystal by femtosecond pulse writing in a bulk of glass (the same fabrication conditions as in previous section), and demonstrate the effect experimentally. In summary, among others, the scaling laws are discussed, enabling to extend the obtained results to different materials (different refractive index modulation amplitudes) and different practical needs (different angular resolutions of spatial filtering).

2.5.1. Numerical method

For numerical study a split step technique was used, which is a proper model for paraxial light propagation in the low index contrast structures, where each layer scatters a small portion of radiation. In one step the scattering by one modulated layer was calculated by applying the phase modulation for the propagating wave in one layer: $\Delta\psi(x,y) = \Delta n(x,y)k_0\Delta l_{\parallel}$, where $\Delta n(x,y)$ is the modulation profile of the refractive index in the inscribed structure, and $\Delta l_{\parallel}$ is the voxel size along the structure. In the next step the paraxial propagation between the layers is calculated by applying the paraxial propagation operator: $-d_{\parallel}(k_x^2 + k_y^2)/(4k_0)$ in the Fourier space (propagation over a half of longitudinal period is considered; we note that $d_{\parallel}$ is the full longitudinal period).

Next the scattering by reciprocal layer was calculated, and then once more the propagation of half period, which completes the full longitudinal period of the PhC. The modulation index change was estimated approximately $\Delta n \approx 10^{-3}$ for our samples fabricated with the optimum parameters. More convenient, however, is to use the scattering coefficient by one layer: $s = \pi\Delta n d l_{\parallel}/(2\lambda)$. The convenience

of the use of s is that the filtering efficiency depends on this parameter and on number of longitudinal periods only for the arbitrary spatial periods of the modulation.

The scattering coefficient of one layer was estimated from the above expression $s \approx 0.15$, which means that approximately $s^2 \approx 2\%$ of radiation energy is deflected by each layer. This estimation was checked a posteriori from the comparison between the experimental results and the results of numerical analysis with different s.

Fig. 2.28 represents numerically calculated cases with slightly different PhC parameters (varying Q (described in (2.1))).

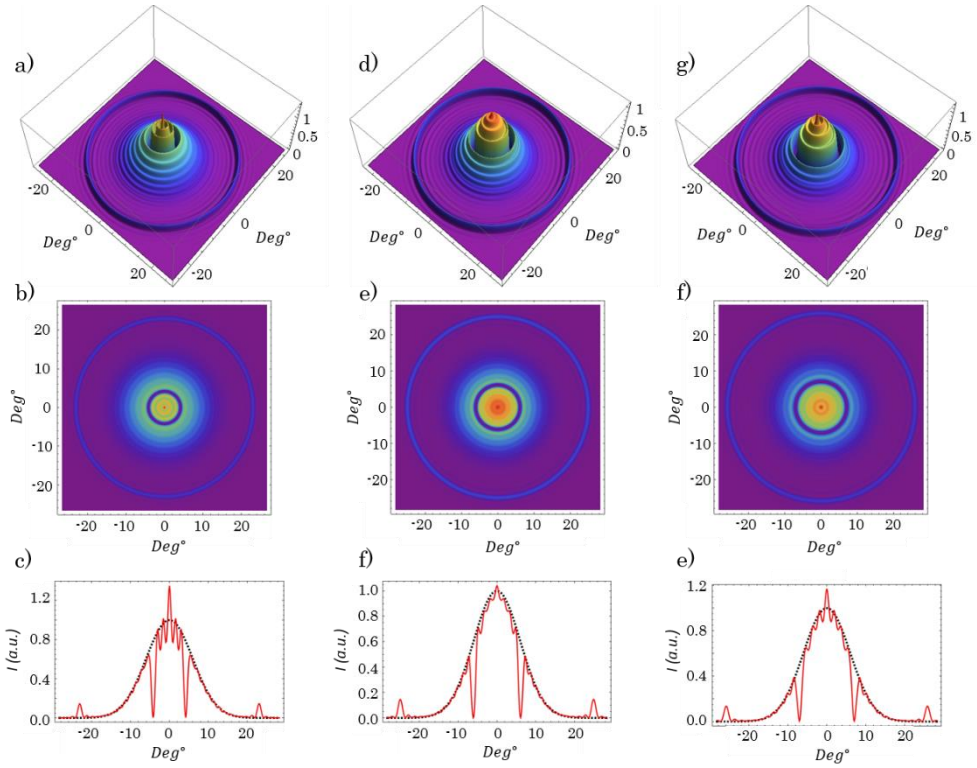

Figure 2.28. Series of numerical simulations with crystal parameters described above, only varying the parameter Q. The intensity distribution shown in 3D image for Q=1.45 (a), for Q=1.65 (d), for Q=1.75 (g), then follows the intensity distribution shown in 2D image for the same parameters correspondingly (b), (e), (f). Then it is followed by the intensity distribution in the horizontal cross section in the middle of the distribution of the beam, for the same parameters as in previous cases, correspondingly: (c), (f) and (e).

For better visualization of the spatial filtering effect three different representations (for the same parameters) of the intensity distribution behind the PhC in the far field are shown: 3D intensity distribution (Figs. 28(a), (d), (g)), 2D intensity distribution (Figs. 28(b), (e), (f)) and horizontal cross-section of the central part of the distribution (Figs. 28(c), (f), (e)). When the Q parameter is being increased, the radius of the filtering ring is increasing, too, therefore as already has been shown in the section 3 of the chapter, by changing the Q parameter of the sample, we can tune the radius of the filtering ring in the center. The other possibility is to keep the Q parameter fixed, but to change the wavelength to obtain the same result.

2.5.2. Fabrication of photonic crystal samples

The layers of the axisymmetric structure were designed to have 100 concentric circles with 2 μm separation between the rings in a layer. In every second layer the structure of rings was reciprocal, i.e. the radii with refractive index maxima correspond to radii with index minima in the next layer. We chose the longitudinal period to be $d_{\parallel} = 13.4$ μm, guided by the expression (2.1). The chosen longitudinal period corresponds to central filtering angle of ≈68 mrad.

Photonic structures of such geometry were fabricated in standard microscope soda-lime glass slides ($n = 1.52$) by a point-by-point modification of the refractive index using tightly focused femtosecond laser beam. The fabrication set-up is similar to the one shown in the Fig. 2.21(a). We used the Yb:KGW laser of 300 fs pulse duration at 1030 nm radiation and focused it onto the sample with a 40x 0.95 NA microscope objective. Repetition rate of the laser pulses was 1 kHz and marking speed was of 800 μm/s. For such configuration optimal laser power was 0.6 mW (after the objective), resulting in voxel length ~6.5 μm and width of ~1 μm. Such fabrication condition results in maximum diffraction efficiency from one layer (and the performance of spatial filtering in general).

2.5.3. Experimental results and discussion

For characterization of filtering performance we have illuminated the samples by continuous 633 nm wavelength HeNe laser beam focused into PhC samples with a 0.3 NA objective. The beam half-width at waist was 2 μm which corresponded to angular divergence of 180 mrad. To explore the spatial filtering we recorded the beam far field profiles by CCD camera positioned at ≈10 mm distance behind the PhC.

The experimentally recorded far field distributions of radiation behind the axisymmetric filter are shown in Fig. 2.29.

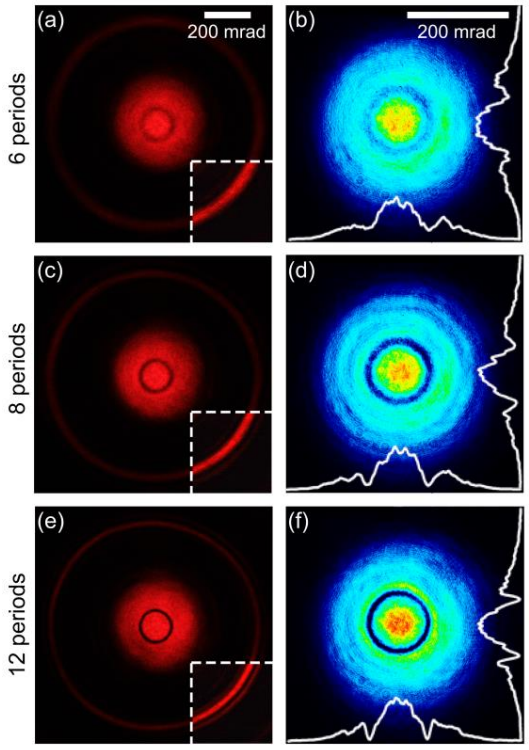

Figure 2.29. Experimentally recorded far field distributions behind the axisymmetric structure for N=6, 8, and 12 longitudinal periods of the structure. (a, c, e) show the large scale distributions, (b, d, f) show the small scale distributions together their vertical cross-sections crossing the center of the beam. The radii of dark inner and light outer circles are 65 mrad and 396 mrad respectively. The insets in (b, d, f) shows 5 times enhanced field intensity for visualization of the outer ring.

We observe the appearance of a dark ring in the central part of the far field. For this particular geometry of photonic structure the radius of dark ring was 65 mrad, in correspondence with (2.1) (note that the angle was 69 mrad according to eq. (2.1) derived in paraxial limit). The radiation from the dark ring is deflected to the bright ring (radius 396 mrad) in consistence with the theory of diffraction of 1D grating. The increasing number of periods leads to the more pronounced dark ring, i.e. more energy is filtered to the outer bright ring.

Next we perform a systematic study of the efficiency of the spatial filtering, depending on the crystal length (on the number of longitudinal periods). We estimated the width and depth of the filtering line and plotted its dependence on the crystal length in Fig. 2.30.

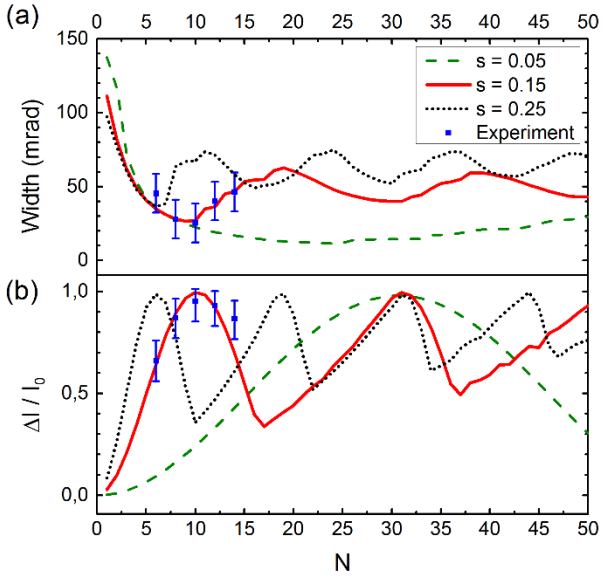

Figure 2.30. (a) Numerically calculated width and (b) depth of the filtering line, depending on the length of the crystal for three different s parameter values: 0.05, 0.15 and 0.25. The data from experimental measurements are shown by points with error bars. The red solid line corresponds to experimental values of s.

As the profiles of the dark rings generally have irregular shape, the width of filtered rings was calculated as the distance between 10% and 90% intensity levels in integrated angular spectrum, using the well-established knife edge

method. We performed numerical calculations not only for the values corresponding to the experimental $s = 0.15$, but also smaller $s = 0.05$ and larger $s = 0.25$ scattering coefficients corresponding to the different refractive index modulation amplitudes.

According to Fig. 2.30, an optimum crystal length exists for a given amplitude of the refractive index modulation. The angular range of filtering decreases and the depth increases with increasing length of the structure, and the maximally narrow line is obtained corresponding to 100% filtering at the center of the angular filtering range. For longer structure the filtering line splits due to the back scattering (from outer bright ring to inner dark ring), typical to the gapless configuration, similarly to 1D gapless filtering in [Pur13].

The numerical analysis for the different amplitudes of refractive index modulation shows the perspective of the filtering for the PhC fabricated from crystals with the larger and smaller index contrast. In fact the simple analysis leads to the following scaling relations: the 100% filtering is obtained under the condition $s \cdot N \approx 1$, or equivalently $\Delta n \cdot l \approx 1$, where $l = d_z N$ is the length of the structure and N is the number of the periods of the structure. The minimum width of the filtering line (which occurs at 100% filtering at $s \cdot N \approx 1$) scales as $\Delta\varphi_{min} \approx \Delta n$.

Despite the fact that the refractive index modulation of the structure was relatively low, a substantial part of the radiation was filtered out. The angular range of the filtering line was around 25 mrad. This means that the spatial filters based on the considered structure could be used to substantially improve the spatial quality of the beams of around 50 mrad divergence.

One way to improve the filtering performance, as already described in detail in the previous chapter, is by adding a chirp to the structure. Two numerically calculated examples with different chirp parameter in axisymmetric PhCs are shown in the Fig. 2.31 (both examples are represented in three different ways: 3D intensity distribution, 2D intensity distribution and 1D cross-section profile in the center of the distribution). As it is seen from the figure, adding a chirp parameter enhances the spatial filtering effect. Moreover, increasing the chirp

parameter (the length of the crystal was increased as well to n=50), the filtering performance has improved significantly, as can be seen from the figures 2.31. (d), (e) and (f).

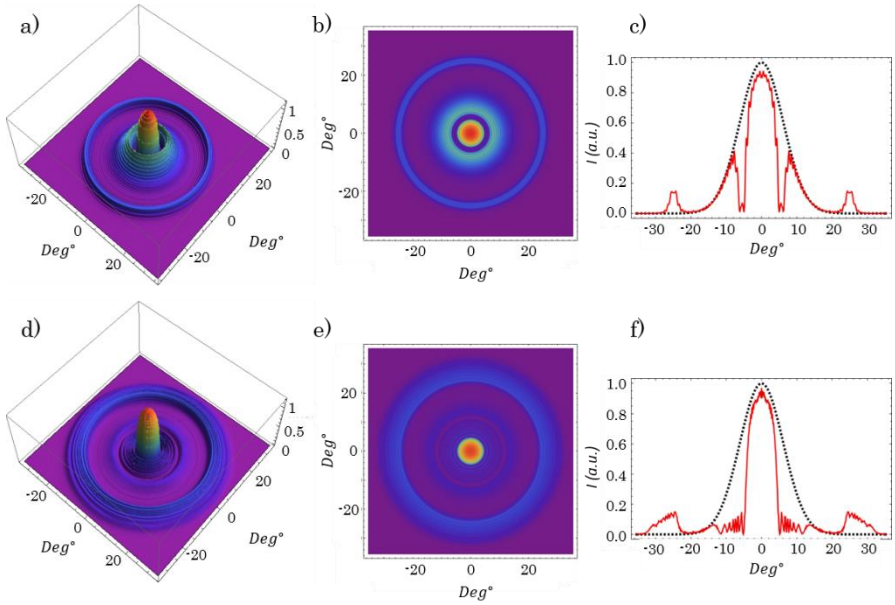

Figure 2.31. Two cases of numerically simulated axisymmetric PhCs the same crystal parameters described in this section, only adding chirp parameter and varying Q. (a) The intensity distribution shown in 3D image for chirp linearly increasing from Q=1.45 to Q=1.75, (b) intensity distribution shown in 2D image for the same parameters and (c) the intensity distribution in the horizontal cross section; for Q linearly varying from 1.45 to 2.39 the intensity distribution visualized with 3D image corresponds to (d), intensity distribution for the same parameters visualized in 2D image is shown in (e) and the intensity distribution in the horizontal cross section (f).

In addition, the scaling discussed above suggests the materials and conditions for spatial filter for the different needs. In particular, to improve the spatial quality of beams in solid state lasers, where the typical divergence is several mrads, the amplitude of refractive index must be of the order of $\Delta n \approx 10^{-3}$. The structures, however, must be relatively long ($N \approx 80$ periods) to provide the 100% filtering. On the contrary, to improve the beam structure of semiconductor microlasers with typical divergence of the beams of approximately >100 mrad, the amplitude of refractive index modulations must be of order of $\Delta n \approx 0.1$. The latter is hardly possible using inorganic glasses, but presumably can be done in polymers [Tru11] or dichromated gelatin films [Dai12].

2.6. Super-collimation by axisymmetric PhCs

Due to the angular band-gaps a range of the angular components of the beams can be blocked, i.e. reflected in backward direction [Luo09, Col10], or deflected at large angles in forward direction [Mai10]), therefore the angular distributions of the transmitted field can be modified as illustrated in Fig. 2.32(a). Some angular areas of the far field components of transmitted field can be thus attenuated (see the dips in Fig. 2.32(a)), but, evidently, no angular components can be amplified.

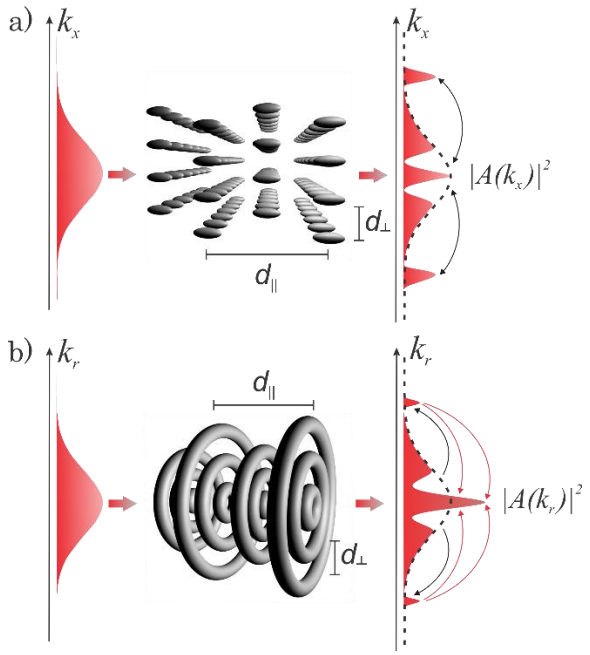

Figure 2.32. Illustration of the spatial filtering in periodic 2D PhC (a) and of the super-collimation in axisymmetric PhC (b). Dashed lines indicate the far field profile without the structure. Arrows indicate diffractive scattering of the field components in forward direction (angular filtering), and in backward direction.

We present an unexpected phenomenon observed in an axisymmetric PhCs, while investigating the filtering effects, that some on- or around-axis field components can be strongly amplified. The structure which we consider consists of periodic planes of concentric rings, as illustrated in Fig. 2.32(b). The

axisymmetric deflection of the angular components is possible, resulting in axisymmetric diffraction, and angular filtering as described in the previous section of the chapter. However, unexpectedly, the reverse cascade of diffraction can enhance strongly the axial and near-axial components of the transmitted radiation, see Fig. 2.32(b). This, speaking in advance, occurs for a precise matching between the longitudinal and transverse periods of the photonic structure. This results in a spectacular enhancement of the field in the centeral area of the far field: as detalized below the numerically simulated enhancement was up to 25 times (for the PhC parameters that can be fabricated); this also results in a clean, well collimated beam.

This section is devoted to numerically and experimentally study the predicted phenomenon. Before moving to details, we note, that the effect is possible only in the case of axisymmetric PhCs. No far field enhancement is possible in purely periodic conventional PhCs, what also follows from the Bloch-mode expansion analysis.

2.6.1. Structures

The layers of the axisymmetric microstructures were designed to contain 30 concentric circles with 2 μm separation between the rings in a layer. In every second layer the structure of rings was reciprocal, i.e. the radii with refractive index maxima correspond to radii with index minima in the next layer. The longitudinal period of the structure was calculated following the spatial filtering theory [Mai10, Pur14a], where the angle of the filtered out components can be calculated from geometric considerations with the expression (2.1).

In order to achieve maximum super-collimation effect we intended to work at very small filtering angles $\alpha \approx 0$, therefore the Q parameter according to (2.1) was very close to 1 for the 633 nm wavelength to observe the super-collimation. Here we demonstrate several numerically simulated intensity distributions (the numerical method used, is the same already described in 3.5.1), where the clear intensity peak in the central part of the distribution appear (Fig. 2.33).

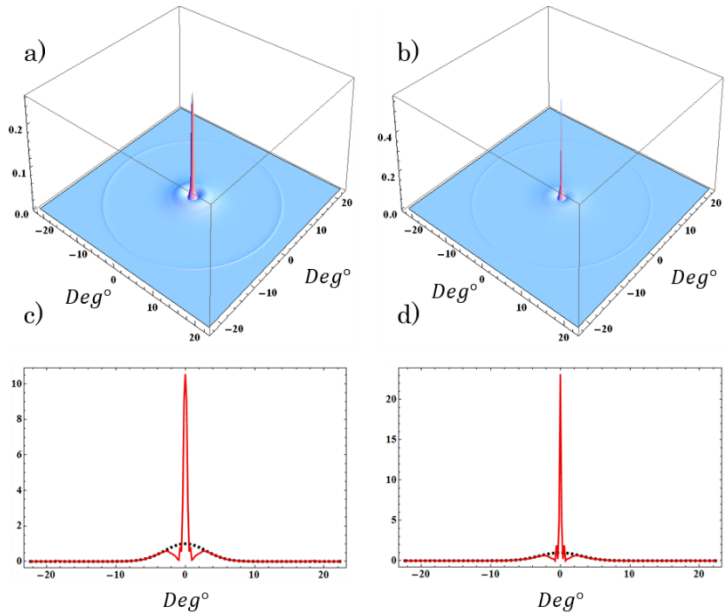

Figure 2.33. Intensity distribution of the beam in a far field after propagation in axisymmetric crystal, with parameters of n=21, initial beam width 2μm, s=0.15 in 3D beam representation (a) with Q=0.97, (b) with Q=0.98. (c) and (d) represents horizontal cross section of intensity distribution for the corresponding cases.

2.6.2. Interpretation

Fig. 2.34 is devoted to the qualitative interpretation of the effect we observe. Let us consider first the perfectly periodic structure, with transverse period q. Then the arbitrary plane wave component, with transverse $k_\perp$ ($k_\perp^2 + k_\parallel^2 = k_0^2$) can be scattered into $k_\perp + q_\perp n$. The set of waves for each $k_\perp$ form the so called Bloch mode in modulated structure. Important is that different Bloch modes (with different $k_\perp$) do not mix in propagation, i.e. propagate independently one from another. The character of the propagation of the Bloch mode depends on the longitudinal periodicity. At the resonance condition the coupling between the plane waves in the Bloch mode is strong, so the angular filtering is obtained.

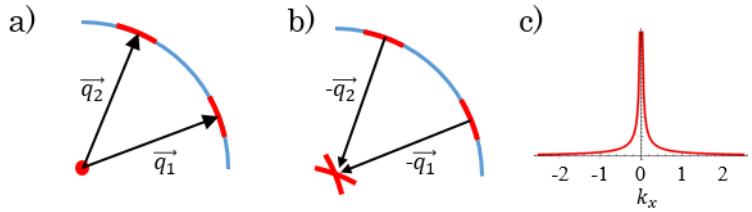

Figure 2.34. Illustration of (a) the formation of Bloch modes for regular PhC (absence of mixing between different Bloch modes), and (b) of superdiffusion of wave-components in axisymmetric PhCs. (c) the profile of back-scattered radiation (for the case of (b)). k_x is normalized into q_x.

In case of axisymmetric PhCs the ring of waves with $k_\perp = const.$ are scattered not into two rings with $q_\perp \pm k_\perp$ but rather fill the area between these rings, as illustrated in Fig. 2.34(b). Therefore the diffraction rings are broadened (for nonzero $k_\perp$) the reverse scattering is even more sophisticated: the manifold of the lattice vavevectors scatter the radiation not back to the initial ring, but rather to a diffused spot centered around the optical axis. As a Fig. 2.34(c) shows the profile of the back scattered radiation is not uniform, but follows approximately a $1/|k_\perp|$ law. This means, that the forward-backward scattering cascade introduces an axisymmetric diffusion. Usual diffusion tends to smoothen the intensity distribution – the super-diffusion tends to smoothen the distribution too, but not the intensity distribution, however the distribution of $I(k_\perp)k_\perp$. The last conclusion can be viewed as the diffusion of the radial density of the energy $E(k_\perp) = I(k_\perp)k_\perp$. As a result the smooth radial energy density profiles $E(k_\perp) = const.$ means the sharp intensity distribution profiles $I(k_\perp) = const/k_\perp$.

2.6.3. Numerics and quantitative study

This interpretation has been checked by a series of numerical integration. For the numerical study a split step technique was used, the same one, already described in 3.5.1.

The numerical results for optimum condition are shown by a sequence of far field distributions in propagation along the structure (Fig. 2.35 left side).

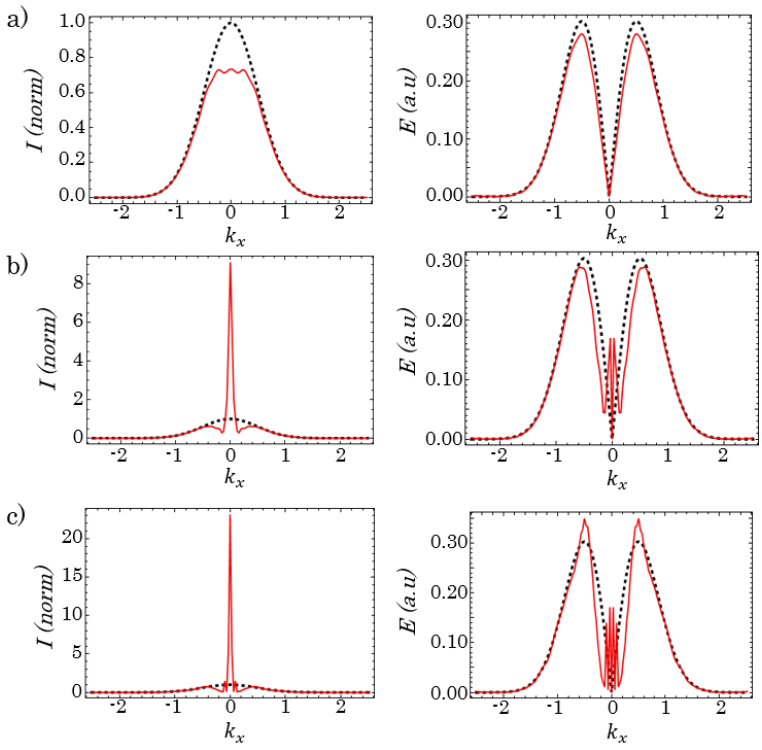

Figure 2.35. The evolution of radial distribution of the far-field along the crystal at three different lengths of the crystal: (a) at n=6; (b) at n=12 and (c) at n=20. At the left side of the figure the evolution of intensity profile (with increasing length of the crystal) is showing formation of sharp peak; At the right side of the figure the evolution of radial density of the energy ($E(k_\perp) = I(k_\perp)k_\perp$ is showing diffusion like smoothing, with increasing length of the crystal (and the appearance of the intensity peak). k_x is normalized into q_x.

In correspondence to above interpretation, the diffusion of fields in terms of radial energy density is observed (Fig. 2.35 sequence on the right side): the distribution with initially hole in the middle (due to factor $k_\perp$ in $E(k_\perp) = I(k_\perp)k_\perp$ become smoother under the action of diffusion. The radial distribution of the field intensity develop correspondingly a singularity centered on optical axis. However, the detailed mechanism of the super-collimation remains unclear.

Quantitative study. The effect of super-collimation, strongly depends on the parameters, most critically on the geometry parameters. Fig. 2.36 summarizes that dependence: the maximum intensity of the super-collimated beam has been

plotted in 2D parameter space of (Q,n(length)). The area of optimum super-collimation is clearly seen at around Q=0.98. In fact, another area of high collimation is visible at Q=1.02. The map was performed for a fixed s=0.15 and for fixed width of the beam (2 μm). Note also that the length of the structure has an optimum value. Longer structures do not improve, but rather decrease the super-collimation.

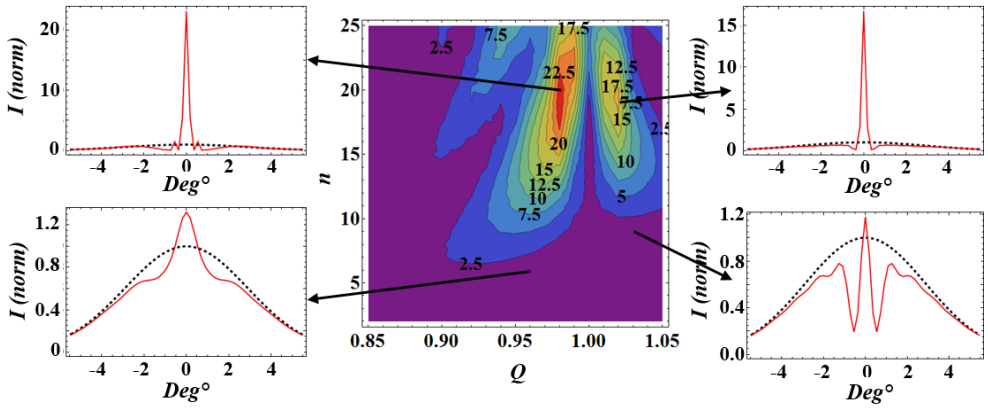

Figure 2.36. Map of on-axis intensity enhancement in the parameter plane of (Q,n), showing the optimum geometry and the optimum length of the structure calculated numerically. Insets show typical cases for different parameters.

2.6.4. Experimental results and discussion

Fabrication

The fabrication technique for the samples is the same as already described in section 3.5.2. The resolution of the inscribed structure (the voxel size) was ~9 μm in longitudinal, and ~1 μm in transverse direction. The change of refractive index of irradiated areas was estimated to be $\Delta n \approx 8 \cdot 10^{-3}$. The layers of the axisymmetric microstructures contain 30 concentric circles at 2 μm increment of radii of rings in a layer. In every second layer the structure of rings is reciprocal, i.e. the radii with refractive index maxima correspond to radii with index minima in the next layer.

Experimental results

The characteristic experimental observation results are summarized in Fig. 2.37.

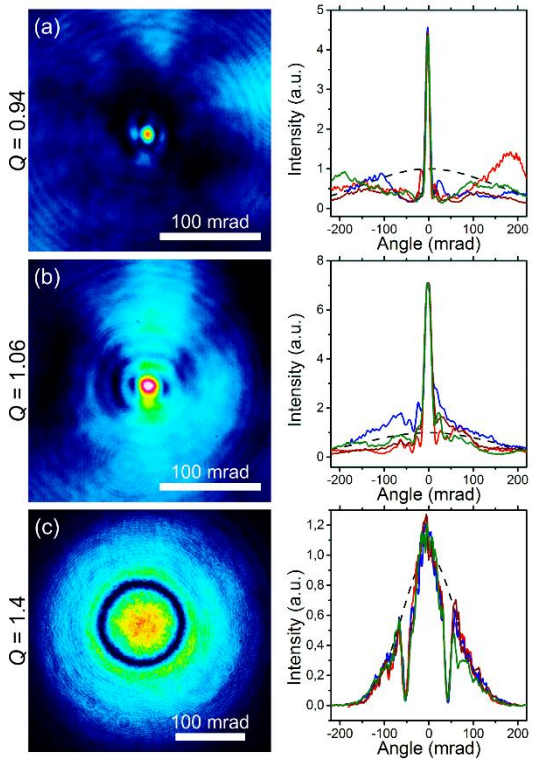

Figure 2.37. The 2D far field intensity profiles together with their axial (vertical, horizontal and both diagonal) cross-sections for the parameters corresponding to super-collimation (a) and (b), and deviated from the self-collimation regime (c). (a) and (b) contains 20 periods of 20.4 μm and 18.1 μm respectively, corresponding to the close to optimum parameters from the map calculated in Fig. 2.35; (c) has 12 periods of 13.7 μm.

The laser beam was focused just in front of the PhC sample with a 0.3 NA objective. The beam half-width at waist was 2 μm which corresponded to angular divergence of 180 mrad. We recorded the far field profiles of the beam by CCD camera positioned at approximately 10 mm distance behind the sample. Fig. 2.37(a), and (b) shows the far field distributions (together with their axial cross-sections taken at each 45 degree angle) at optimum geometry for the super-collimation. The far-fields at different propagation length (different length of the

structure in experiments) show the formation of the super-collimated beam. For comparison the beam propagation at a geometry of PhC designed for spatial filtering (Fig. 2.37(c)) shows no super-collimation effects (for the identic fabrication conditions of the structure, except for the different longitudinal periods, i.e. different geometry parameter and lower number of periods $N = 12$). The latter distribution shows spatial filtering, similarly to reported in [Pur14a] for this geometry, but no super-collimation.

In our experiments the maximum enhancement of the intensity was around 7 times and the angular distribution of super-collimated beam was around 20 mrads. In the numerical simulations, where crystals were modelled according to realistic parameters of previously fabricated axisymmetric PhC crystals, the maximum enhancement of the intensity is more than 20 times, where around 30% of energy was within the super-collimated beam.

The experimental deviation from numerical results is most likely caused by spherical aberrations during fabrication process which decreased the quality of our rather high (~350 μm height) structures. Such aberrations could in principle be compensated with a spatial light modulator [Cum11] or other techniques.

In addition it is worth to note that the super-collimated beam depends very weakly on the position of focusing in front (or behind) the crystal. The position could be varied by appr. ± 0.5 mm without a substantial influence on super-collimation. In usual (or in Fresnel) lensing, the divergence of the collimated beam would be very sensitive to the position of the focus (of source) along the axis. Moreover, the demonstrated technique could be well utilized outside the optics, to other fields of wave dynamics. Recently the spatial filtering has been shown for acoustic beams [Pic13] – the idea can be well utilized, for formation of supercollimated beams in acoustics. The technique could also be applied for cooling of the atomic ensembles, or finite temperature Bose-condensates, where also a spatial filtering (removal of particular velocity components) was recently proposed by modulated media [Sta11].

2.7. Conclusions

We have experimentally proved the effect of the spatial filtering of light beams by 3D PhCs with low refractive index contrast in the gapless configuration. The angular spectra of the propagating beams was modified by the PhC, in the way that particular angular components, selected by the geometry factor of the structure, were removed from the central part of the beam and were deflected into the first order diffraction maxima. Moreover, our theoretical-numerical analysis reproduces well the experimental observations and interprets the observed effect as the spatial filtering in the gapless configuration.

However, the above reported effect of spatial filtering is relatively weak, as the dark lines were relatively narrow, and therefore, it carried a demonstrational character only. The reason for the weak filtering is the relatively small amplitude of the modulation of refractive index. In order to improve the spatial filtering performance, we have introduced chirp into the structure and studied its effect on the radiation. As a consequence, we have theoretically calculated and experimentally proved the effect of chirping of photonic crystal on the efficiency of spatial filtering. Our theoretical-numerical analysis reproduces well the experimental observations. In spite of relatively weak index modulation (small scattering by one row) a substantial part of the radiation was shown to be filtered out. In order to obtain a technologically utile spatial filter the higher (but moderate) index contrast PhCs are necessary, which are to be based on novel materials and new fabrication technologies. A technologically relevant spatial filtering, allowing to improve the beam quality parameter by the factor of 2-3, requires the refractive index modulation of order of approximately $\Delta n_0 = 10^{-2}$.

Moreover, the axisymmetric spatial filtering effect by axisymmetric microstructures (analogs of PhCs) have been studied. We have theoretically calculated and experimentally proved the axisymmetric spatial filtering in axisymmetric photonic microstructures. Our theoretical-numerical analysis is in good correspondence with experimental observations.

While analyzing the effect of axisymmetric spatial filtering by axisymmetric photonic microstructures, the new effect of super-collimation of the beam in the

far field has been discovered. We have predicted and experimentally demonstrated the super-collimation effect in axisymmetric photonic structures. We interpret the effect in terms of axisymmetric character of diffusion, which tends to smoothen the radial energy density. It was numerically found that the intensity in the central part of the beam can raise more than 20 times compared to the reference beam. The experimentally obtained enhancement of intensity was around 7 times (due to experimental deviation from numerical results, most likely caused by spherical aberrations during fabrication process) and the angular distribution of super-collimated beam was around 20 mrads.

To conclude, we highlight the advantage of the novel method of filtering demonstrated in the Chapter 2. The main advantages (comparing with the conventional pinhole spatial filter) are: 1) extremely small thickness (hundreds of microns) of the filter enabling the integration of such a filter into micro-optical devices or into micro resonators of small lasers; 2) translational invariance of the PhC spatial filter (insensitivity to the lateral shift of PhC-structure) simplifying its utilization (however this advantage is no longer valid for the axisymmetric crystal case); 3) possibility to combine (to add) the filtering functionality to some other, already existing, functionalities (amplification, nonlinearities) in bulk material, by additional modulation of refractive index of the (amplifying or nonlinear) material.

Chapter 3

Negative diffraction effects in Photonic Crystals

This chapter is devoted to the study of the light beam propagation in PhCs possessing negative diffraction properties. The chapter is mainly divided in five sections.

In the first one, we make a short overview of the state of the art in the topic of flat lensing with PhCs.

In the second one, we consider a 2D PhC (rhombic array of dielectric cylinders surrounded by air) and we investigate its properties to tailor spatial propagation of light beams. We show that the structure supports negative (anomalous) diffraction, which leads to focusing and collimation of beams behind the PhCs. We demonstrate the self-collimated propagation inside the PhC.

In the third part of the chapter, we demonstrate full 2D focalization (imaging) of light beams at visible frequencies by a 3D polymer woodpile PhC [Mai13]. We experimentally show flat lensing with focal distances of the order of

50-70 micrometers. These experimental results are compared with numerical calculations and interpreted by mode expansion theoretical studies.

In the fourth section, we experimentally observe formation of narrow laser beams behind the woodpile PhC, when the beam remains well collimated in free space propagation behind the crystal. We show that the collimation depends on the input laser beam's focusing conditions, and we interpret theoretically the observed effect by calculating the spatial dispersion of propagation eigenmodes and by numerically solving the paraxial propagation model.

In the fifth part of the chapter, we study the light beam propagation in metallic photonic crystals (MPhCs). All the previous studies presented in the thesis were done in conservative systems, i.e. dielectric PhCs. However, the presented ideas can be exported to similar lossy systems, as we show with numerical simulations in non-conservative system of MPhC. In particular, we consider a 2D rhombic array of metallic cylinders embedded in air and we explore its ability to tailor spatial propagation of light beams. We show that the structure supports self-collimated propagation and negative (anomalous) diffraction. In this later case, flat lensing is observed, leading to the focusing of beams behind the MPhCs. Moreover, the anisotropic attenuation of light provided by the structure enables spatial filtering of noisy beams.

3.1. Introduction

As described in the last part of the Chapter 1, recent investigation of spatial dispersion relation of PhCs led to the discovery of novel spatial propagation effects like: self-collimation due to the flattening of the curvature of spatial dispersion [Kos99b, Wit02, Chi03, Aug05, Sta06, Lu06, Lom06]; spatial filtering due to the angular gaps in dispersion curves, or strongly tilted segments [Sta09a, Mai10] (as described in Chapter 2); focalization and imaging behind a PhC [Luo02a, Luo02b, Li03, Luo03, Wan04, Fab06, Ren07] due to the convexly curved segments of the spatial dispersion. Full 2D flat lens focusing has been experimentally shown for microwaves ($f = 16.4$ GHz point source, for a body centered cubic PhC, with lattice constant $a = 6.35$ mm, and dielectric material of $\varepsilon = 25$, which was embedded in air (Fig. 3.1(a), (b))) [Lu05b] and for sound waves [Ceb12].

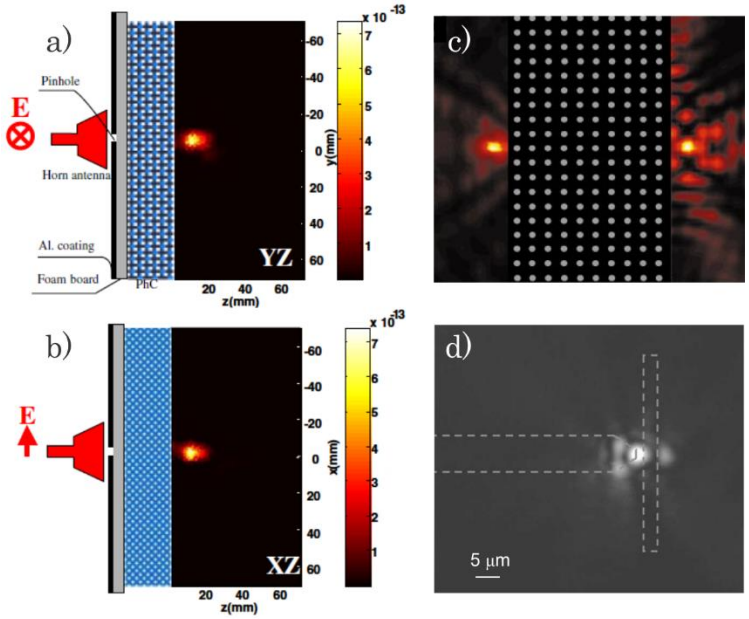

Figure 3.1. Experimentally measured intensity distributions for 3D PhC [Lu05b]: (a) in the vertical plane, (b) in the horizontal plane; Experimentally measured electric field intensity map on a cross sectional view of the 2D source- image (left-right) system for a flat lens: (c) in microwave regime, where the dimensions of the panel are 37.5 × 30.0 *cm* [Par03], and (d) in the IR regime [Sch06].

1D focusing/imaging by PhC slabs has been experimentally demonstrated in the microwaves (f = 9.3 GHz, for 2D PhC from a square array of alumina rods embedded in air (Fig. 3.1(c))) [Par03] and near-IR frequency range (with incident wavelength of 1562 nm from a point-like source, into the triangular lattice of air holes in silicon, with the lattice constant of a = 540 nm (Fig 3.1(d))) [Sch06].

It is a hard technological task to demonstrate flat lensing in the visible regime, as periods have to be of the order of wavelength. In this chapter we demonstrate 2D flat lensing in visible regime in high order bands [Mai13], as will be explained in section (3.3).

We would like to remind, that, for the usual conventional lens, the focal length f is given by:

$$\frac{1}{l_1}+\frac{1}{l_2}=\frac{1}{f}. \tag{3.1}$$

where l_1 is the distance from the object plane to the lens and l_2 is a distance from the image plane to the lens. It is clear that with a lens which holds the relation (3.1), one can focus and image at any distance without restriction. This includes also the imaging to infinity (far field area).

Inside the PhC lens, the electromagnetic field is highly modulated and simple ray diagrams applicable in homogeneous media, can not be used. PhCs hold a different relation for the focal length:

$$f = l_1 + l_2 \tag{3.2}$$

where the distance from the PhC lens to an image plane is limited by the size of the focal length and it would not be able to image infinitely far away. Therefore, we can say that a PhC lens can focus or image only in a “near” field and we call the effect as ***flat lens focusing***. Fig. 3.2 schematically demonstrates such kind of flat lens.

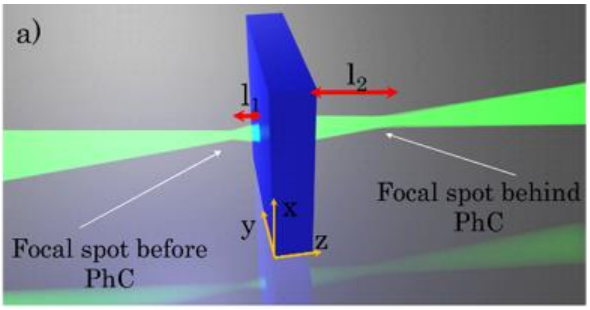

Figure 3.2. Flat PhC lensing scheme.

In the existing literature about the flat lensing with PhCs, the relation (3.2) is rarely taken into account [Lu05c], although it is usually shown that for a single frequency, a point source at one side of the PhC results in a point image on the other side of the PhC (as demonstrated in Fig. 3.3(a), (b)). However, no consistent study about focal length dependence on frequency has been done for PhCs [Luo02a, Li03, Luo03, Wan04, Mou05, Lu05a, Fab06].

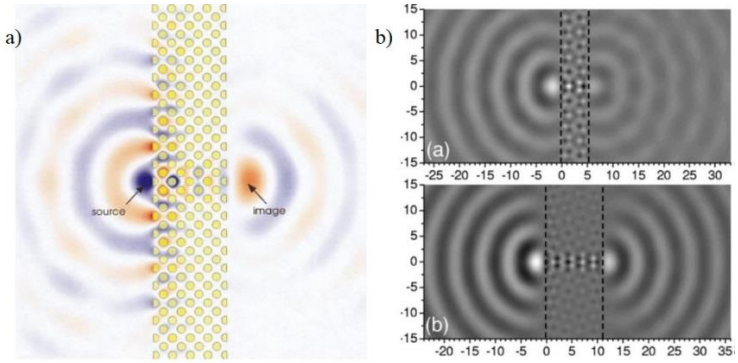

Figure 3.3. (a) Field of a pion source and its image across a PhC [Luo02a], (b) Field pattern of the point source, behind and after the crystal [Li03].

Contrarily, in the field of acoustics, an accurate study of lensing using sonic crystals (SC) has been done [San09]. Fig. 3.4 by Ref [San09] shows the summary of focusing behavior depending on frequency, calculated numerically and

analytically. In Ref [San09] the analytical estimation for the focal distance behind the SC is derived and it takes the form:

$$z_f = L\frac{f^2}{\Delta\Omega^3}, \tag{3.3}$$

where L is the length of the SC, $\Delta\Omega = (\Omega_g - \Omega)/\Omega_g$ with $\Omega_g = \omega_g a/2\pi c_h$ being the normalized Bragg frequency, and c_h being the speed of sound of the host medium, f is the filling fraction $f = V_s/V_{uc}$, where V_s and V_{uc} are the volume occupied by the scatterer and the unit cell, respectively. It is important to mention that this analytical estimation of z_f is valid for small f.

Fig 3.4(a) shows the focal distance behavior depending on the frequency of sound waves, while Fig 3.4(b) shows the beam width at the focal position depending on frequency. These results show that the increase of frequency would lead to the increase of the focal distance, as well as increase of beam width at the focal position [San09]. The structure for which the calculations were done is a 2D SC of a square geometry, where the steel cylinders of radius $r = 0.8$ mm are position in lattice points. The lattice constant is $a = 5.25$ mm and the host material is water.

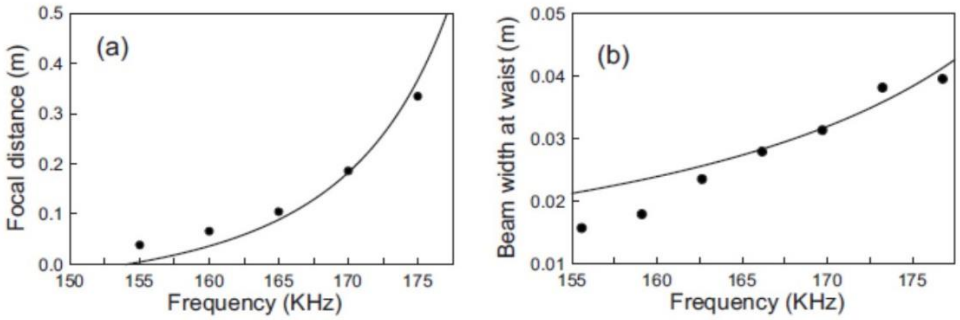

Figure 3.4. (a) Focal distance for the SC lens for increasing frequencies evaluated from the analytical expression Eq. (3.3) (solid line) and by numerical simulation using the FDTD method [San09]; (b) Beamwidth at the focal distance, analytical (solid line) and numerical (symbols) results [San09].

These results were followed by the experimental work in Ref [Ceb12], where sound beams focusing behavior behind a 3D woodpile like SC was proved. The SC consists of steel cylinders of a radius $r = 0.8$ mm and the lattice constant $a = 5.25$ mm. The host medium is water. Fig 3.5(a) summarizes the intensity values of the sound beam behind the crystal on z-axis depending on the frequency. The green solid line represents the analytical fit (derived in Ref [San09]) of the focal distance depending on frequency, which is in good agreement with the experimental results. According to this fit, one can tell that when the frequency of sound is increasing, the position of the focal point is shifting to further distances. This means that the focal position can be tuned by changing the frequency. Figs 3.5(b)-(d) show focusing behavior around the optimum distance (most intense focusing spot obtained), which is marked with a white horizontal line in Fig. 3.5(a).

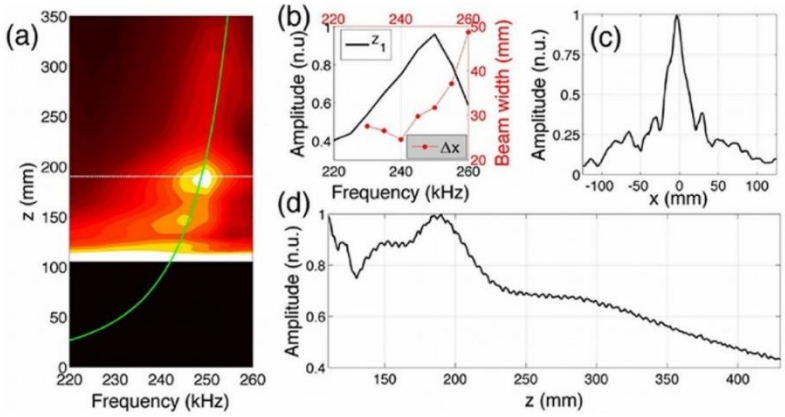

Figure 3.5. (a) Measurements of the on-axis intensity distribution on the frequency-z plane [Ceb12]. The continuous green line corresponds to analytical fit Eq (3.3). The black area represents the space occupied by the SC. The white dashed line represents the point z_1. (b) The continuous line represents the measured beam amplitude in normalized units at point z_1 and red dotted line represents the measured beam width. (c) Experimental profiles in the x-axis of the beam at z_1 point and (d) measured amplitude in normalized units on the z-axis at 250 kHz [Ceb12].

Regarding flat lensing effects we should mention that, recently, interesting numerical results on dual-negative refraction in triangular PhC have been presented [Don11]. It is claimed that with dual-negative refraction effect one can

obtain double imaging focusing effect behind the PhC. The principle of the idea is based on the fact that for the same frequency and polarization of light there are two available different photonic bands (Fig. 3.6(a) (second and third bands)). This means that double negative refraction could occur for the same polarization state of a monochromatic wave and different wave vectors (Fig. 3.6(b)).

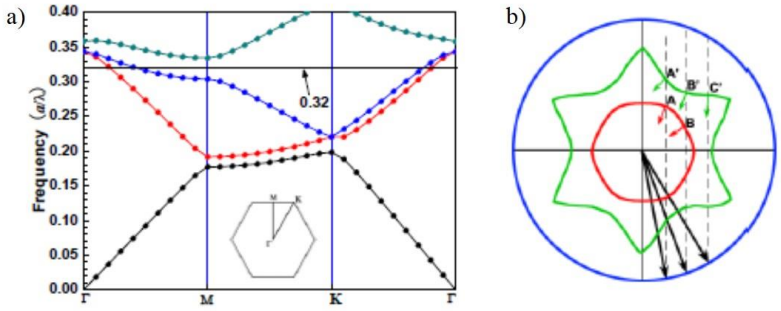

Figure 3.6. (a) Lowest four bands of the PhC for TM polarization (electric field parallel to the rods); (b) wave vector diagram for the second (red curve), third (green curve) bands and air (blue curve) for the frequency of 0.32 [Don11].

In Fig. 3.6(a) a band diagram [Don11] for the triangular PhC structure with hexagonal dielectric rods in air is shown with dielectric constant $\varepsilon = 11.56$, where a is the lattice constant. In Fig. 3.6(a) it is seen that in the frequency region of 0.22 to 0.34 the second and the third bands overlap for the different wave vectors. This means that two refractions at the same frequency with different phase and group velocities may occur. Fig. 3.6(b) shows the dispersion contours at the frequency of 0.32 for the second band (red contour), for the third bans (green contour) and for air (blue contour). The vertical dashed lines are the construction lines of the parallel components for the wave vectors. The black long arrows indicate incident wave vectors with different angles. We can see that the construction lines 1 and 2, both intersect with the second and third bands. The small coloured arrows at these intersections are directions of group velocities, which indicate that the refraction for those particular incident $\vec{k}$ vectors is negative. This means that for the incident wave of the frequency of 0.32 at particular angles shown in Fig. 3.6(b) (marked 1 and 2) two negative refracted

waves with the different refractive angles and different eigenmodes are excited synchronously (Fig. 3.7(a), (b)). Dual negative refraction can lead to the double focusing/imaging (Fig. 3.7(c)) [Don11]. Based on the same effect, numerical and experimental results of double imaging focusing were presented in acoustics [Lu07].

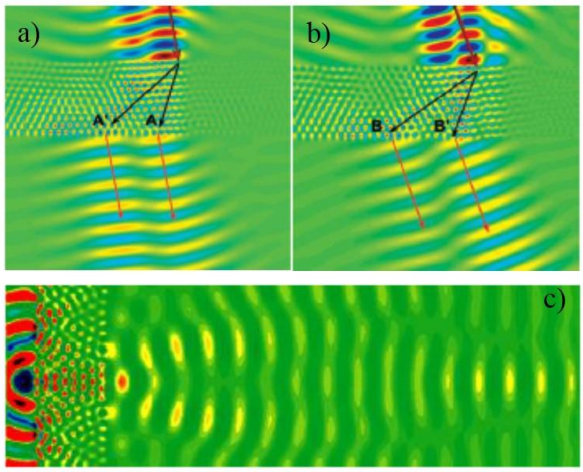

Figure 3.7. The FDTD simulations of electric field distributions with different incident angles of (a) $\theta = 10°$; (b) $\theta = 20°$ at the frequency of 0.32; (c) electric field pattern of double focusing imaging [Don11].

3.2. Focusing and collimation effects in a 2D PhC

In this section we present numerical calculations of the flat lensing effect in a rhombic PhC, as well as the double focusing effect due to double convex curvatures of iso-lines for monochromatic beams of the same polarization. In addition, self-collimation in the structure will be analysed.

3.2.1. Spatial propagation effects behind the PhC

Simulations

We consider a PhC structure which consists of 2D rhombic array (Fig. 3.8) of dielectric rods with refractive index $n = 1.5$ embedded in air. The lattice constant is equal to $a = 0.87$ μm, radius $R = 0.32 \times a$ and the angle between the lattice vectors $\alpha = 72°$. Thus, the longitudinal period of the structure is $d_{\parallel} =$ 1.4 μm and transversal period is $d_{\perp} = 1.02$ μm . The total width of the structure is $L_{\parallel} = 7 \times d_{\parallel}$ (~9.8 μm) and transversal length $L_{\perp} = 40 \times d_{\perp}$ (~40.8 μm).

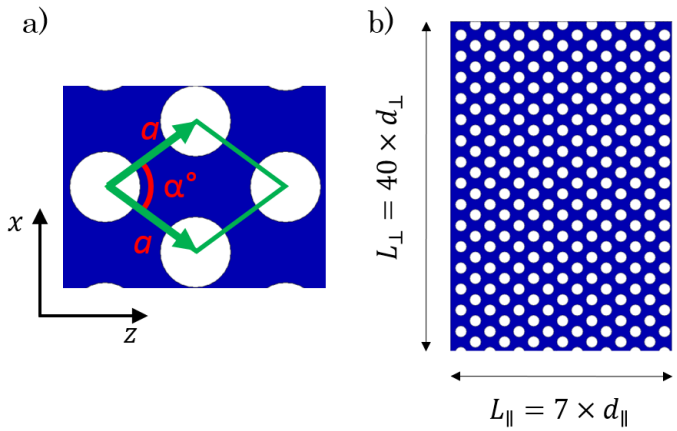

Figure 3.8. (a) Schematic representation of the simulated PhC geometry, where lattice constant $a = 0.87\ \mu m$, angle between the lattice vectors $\alpha = 72°$, the radius of the rods $R = 0.32 \times a$. The direction of the propagation of the beam is along z axis. (b) The periodic structure, which in z direction contains 7 longitudinal periods, while in x direction it contains 40 transversal periods.

In order to study the propagation properties of light through the crystal, we calculate the band diagram and spatial dispersion (iso-frequency surfaces) for the first 8 bands of the structure. The calculation is based on the PWE method and it was done using the commercial Crystal Wave software (Fig. 3.9).

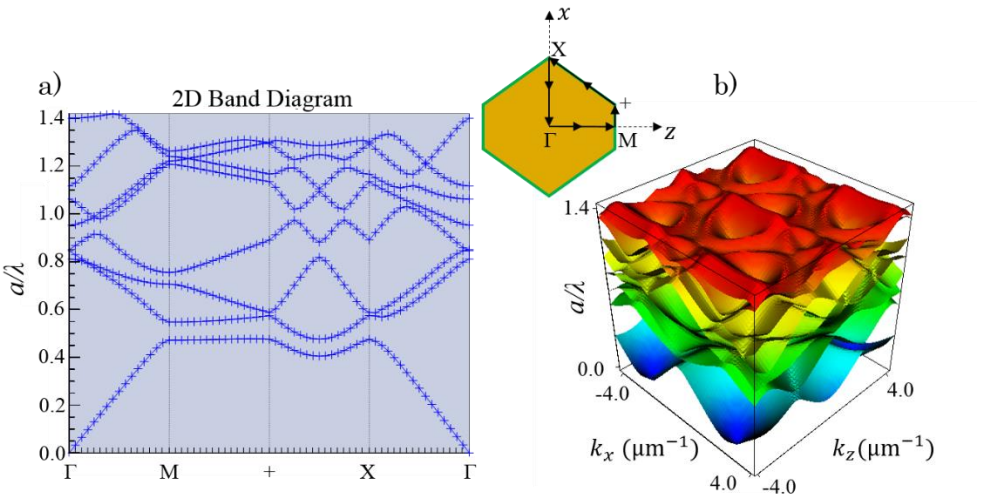

Figure 3.9. (a) Band diagram of the structure described in Fig. 1, for the first eight propagation bands. The orange inset shows the irreducible Brillouin Zone. (b) the 3D plot of the iso-frequency surfaces for the first eight bands of the structure.

The band diagram for the TM polarization (electric field is parallel to the rods) reveals the frequencies that are allowed and the frequencies that are forbidden to propagate in the structure. The band diagram (Fig. 3.9(a)) shows that there is no full frequency BG. However, taking a look only to the ΓM direction, in which we will propagate the beam and which, it is seen that the BG appears at two frequency regions a/λ: 0.47-0.55 and a/λ: 0.92-0.95. The inset of the Fig. 3.9 shows the irreducible Brillouin Zone with the propagation directions.

To understand beam shaping effects spatial dispersion surfaces are calculated (Fig. 3.9(b)). From the calculated iso-frequency curvatures we expect interesting results in beam shaping, such as: focusing, double-focusing, self-collimation and filtering.

The finite difference time domain (FDTD) method with Crystal Wave software was used to launch a beam into the above described PhC structure along the ΓM direction to scan different frequencies. The input source is the monochromatic Gaussian beam with a beam width of 3.5μm, normally incident

on the structure. The Gaussian beam is located just at the surface of the PhC and is centered to be just in the middle of the structure. An example of the intensity distribution of the beam along and behind the crystal, for a particular frequency of a/λ=0.608, is shown in Fig. 3.10(a).

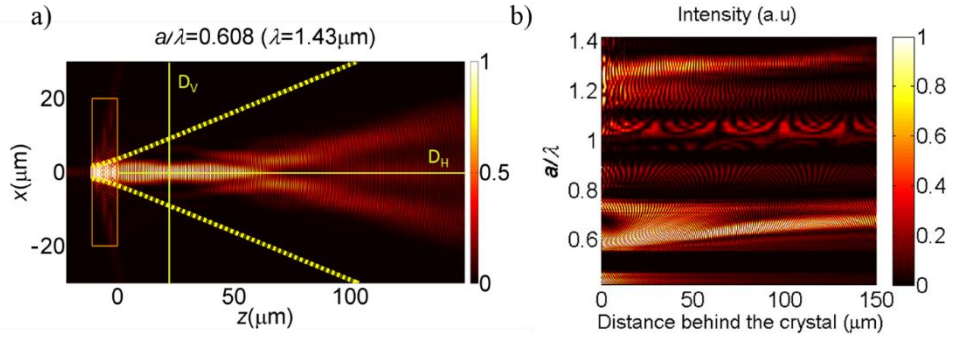

Figure 3.10. (a) An example of field intensity distribution at a/λ=0.608, when beam passes through the PhC. The orange rectangle marks the borders of the PhC structure. The 3.5 μm width Gaussian beam is placed just at the surface of the PhC and beam shaping behavior can be observed when the beam goes out from the structure. (b) Intensity distribution along the horizontal axis, z, at x=0 μm (just where the detector D_H is located), depending on frequency.

The shape of orange rectangle marks the boundaries of PhC. The total length of the structure is 9.8μm, whereas the total width is 40.8 μm. The thick yellow dashed line corresponds to the contour of the reference diffractive beam propagated in air. The solid yellow lines in the figure represent the detectors, which can be set at the positions of interest to obtain intensity, amplitude and phase data of the beam. The horizontal line represents the detector D_H which is always set in the center of the x plane (at x=0). It records the data of beam intensity distribution in its central part (according to propagation direction). The vertical yellow line in Fig. 3.10(a) represents detector D_V which contains information of transversal distribution of the field (in this particular example at the distance of z=20μm). We do not keep detector D_V at fixed position z, but we can move it to any z position to obtain the data of interest. The map of Fig 3.10(b) was done taking the intensity distribution data from detector D_H for scanned frequencies (from a/λ of 0.42 to 1.4). This map confirms the BG prediction from

the 2D band diagram where forbidden frequency regions appear at a/λ: 0.47-0.55 and a/λ: 0.92-0.95. Moreover, the map shows focusing and collimation effects at particular frequencies. There are two focusing regions, where first region occurs at a/λ: 0.58-0.74 (this frequency region belongs to the second and third bands), the second focusing region occurs at a/λ: 1.17-1.32 (frequency region belongs to the seventh and eighth bands). There are two collimation regions: a/λ: 0.85-0.89 (fourth band) and a/λ: 1.02-1.06 (fifth and sixth bands).

As these effects are of particular interest we are going to look at them more in the detail and explain them using spatial dispersion (iso-frequency) diagrams. We have calculated iso-frequency surfaces for the first eight bands of the structure, the examples of the first three band surfaces are shown in the figure 3.11.

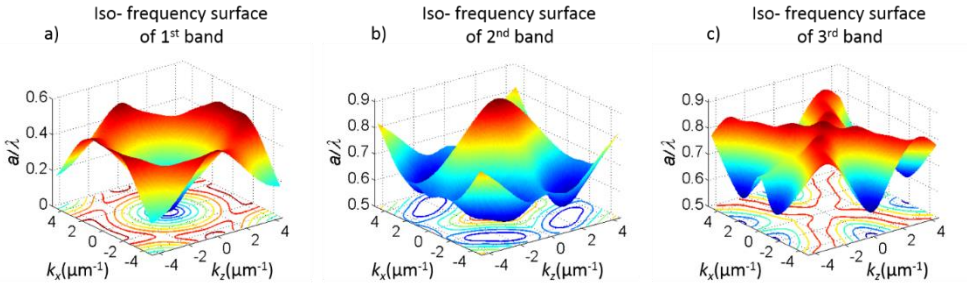

Figure 3.11. (a), (b), (c) Represent the 3D plots of spatial dispersion surfaces consequently for the first, second and third order bands. The lines at the bottom of the images represent the 2D iso-frequency contours. The frequency is increasing when color is changing from the blue to red.

Although 3D band surfaces are nice for visualization, to analyze the results it is more convenient to use the iso-frequency contours, which are obtained projecting 3D iso-frequency into a plane (as shown in the bottom part of the Fig. 3.11). Therefore, in the following figures we are going to present only iso-frequency contours.

Double focusing

We will start studying the iso-frequency contours of the first three bands (Fig. 3.12). Fig. 3.12(a), (c) represent iso-frequency contours of first band. The black arrows stand for the $\vec{k}$ vectors with different directions, which all emerge from the center of the first iso-frequency contour diagram, to the direction of the higher frequencies. Different lengths of $\vec{k}$ vectors stand for different frequencies, while different angles – for different angles of propagation in the crystal.

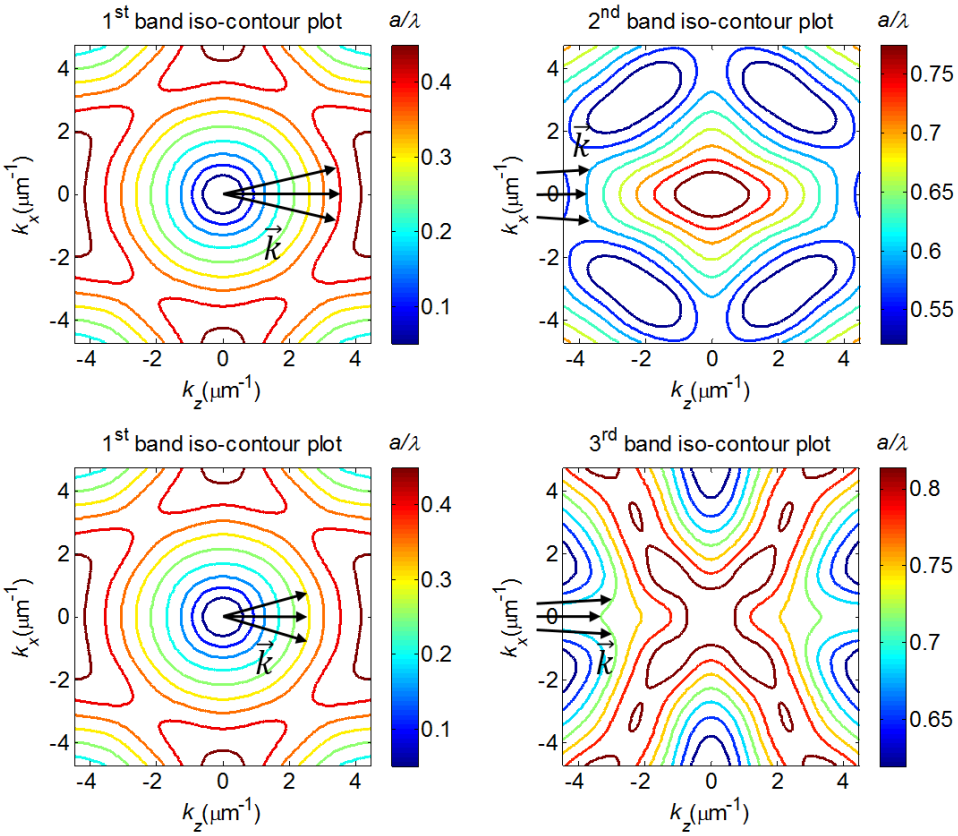

Figure 3.12. Iso-frequency contours. (a), (c) for the first order band, (b) for the second band, (d) for the third band. Black arrows represent $\vec{k}$ vectors emerging from the center of the first band and pointing to the direction of higher frequencies.

With respect to the ΓM direction it is seen that all the iso-frequency contours for the first band are concave, which means that they correspond to positive

diffraction, therefore at these frequencies the beam spreads. However, when the $\vec{k}$ vector reaches the second band, the flat segments at the frequency of a/λ: 0.58 appear and they stand for the non-diffractive propagation of the beam inside the PhC. As we continue to higher frequencies we observe that the iso-frequency contours become more and more convex. Therefore, at these frequencies, negative diffraction and focusing effect are expected. Different curvatures of the iso-frequency contours determine the focal distance of the beam behind the crystal. The more convexly shaped is the contour, the further will be the focal position of the PhC. Almost all the second band iso-frequency lines are curved convexly in the ΓM direction, therefore a large focusing region is expected.

Moreover, from the diagrams of the third band (Fig 3.12(d)), we observe that some frequencies are overlapping with the second band. As Fig. 3.12(d) demonstrates, for particular $\vec{k}$ vectors close to the region of a/λ: ~0.73 it has a convex curvature as well. This is very interesting, as it means that for the same region of frequencies close to a/λ: ~0.73 there exist two different convex curvatures for the same frequency and polarization of beam. Therefore, we expect that different portions of the radiation for the same frequency will project to these two different curvatures, which will result in two different focal positions for a monochromatic beam.

Proceeding with the assumptions which were determined by the iso-frequency contours, we have scanned the frequency region belonging to the second and third bands, as well as the part of the first band (a/λ: 0.42 – 0.82). The numerical results are summarized in Fig. 3.13, the intensity distribution along horizontal axis, z (at position x=0), depending on the frequency is shown. A clear dependence of the intensity profile on the frequency along the longitudinal plane is shown. As predicted, the existence of intensity maxima is evident for frequencies corresponding to the negative diffraction range. Moreover, from a/λ ~ 0.58 to a/λ ~ 0.75, we see a clear intensity maximum shifting to the right, which means that with the increasing frequency the focal distance behind the PhC increases.

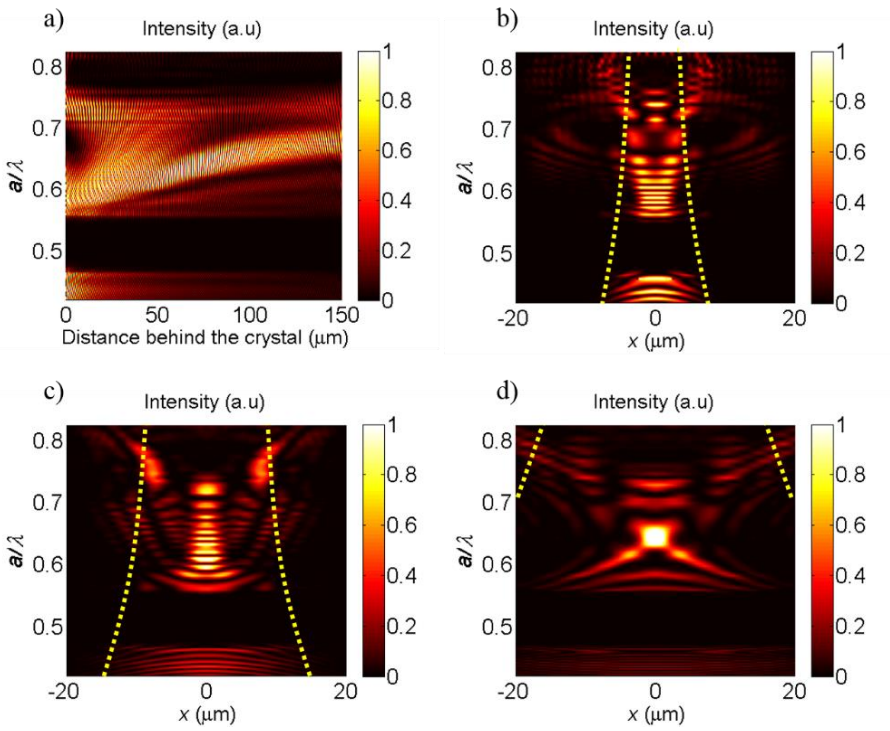

Figure 3.13. (a) Intensity distribution along the horizontal axis, z, at x=0 μm, depending on frequency (for a/λ: 0.42 – 0.82). (b), (c) and (d) intensity distributions along the transversal axis *x*, depending on frequency at the corresponding positions of z = 5, 30 and 75 μm. The yellow thick dashed line correspond to the reference beam in free space propagation.

All these results can be explained with figure 3.12(b) (the iso-frequency contours of the second band), where for increasing frequencies there are stronger spatial dispersion curvatures of convex type which provides longer focal distances.

What is clearly seen from the map (Fig. 3.13(a)) is that, at around $a/\lambda \sim 0.63$, a splitting of the intensity maximum appears, and from $a/\lambda \sim 0.63$ to $a/\lambda \sim 0.75$ we have two intensity maxima regions for the same frequencies, which correspond to the double focusing effect. As explained previously, second and third bands intersect and in the third band some iso-frequency contours (Fig. 3.12(d)) are convex, therefore we have frequency regions where radiation projects on two iso-frequency lines, with different convex curvatures. Consequently, two different focal positions for the same frequencies are obtained. The curvatures of

the second band are more pronounced and they are broader compared to the ones of the third band. Therefore, the second band is responsible for the further focal position and more clear focusing effect. As the convex curvatures of the third band are less pronounced, the focal positions belonging to the third band are closer to the PhC. Moreover, the convex curvatures for the third band are narrower, therefore only narrow $\vec{k}$ vector spectrum can be projected into it and consequently, the focus itself is not as strong as in the second band case.

To observe the effect in more detail, we have plotted the intensity maps along three different vertical planes at z=5 µm, z=30 µm and z=75 µm (using the information from non-fixed vertical detector Dv which is illustrated in Fig. 3.10(a)), corresponding to figures 3.13(b), 3.13(c) and 3.13(d). Here, the horizontal axis is the transversal plane x, while the vertical axis is the frequency. The dashed yellow line stands for the reference beam contour in the free space. Fig. 3.13(b) demonstrates how the transversal beam profile looks like, when the beam goes out from the crystal. At the position of z=30 µm (Fig. 3.13(c)), the beam focusing compared to the reference beam is clearly seen for the frequency range of a/λ: 0.58 – 0.75. Fig. 3.13(d) demonstrates the exixtance of strongly pronounced region of focusing at $a/\lambda \sim 0.65$. Here (at the distance of z=75 µm) the focusing region has a narrower interval of frequencies. This happens due to the strong shift of focal position depending on frequency, which is determined by the convex iso-frequency curvatures of the second band. At the position of $z < 75$ µm, the intensity maximum (as well as the narrowest beam-width region in the map) would appear for lower frequencies, while at position of $z > 75$ µm, for higher frequencies.

Finally, a very clear BG at a/λ: 0.47-0.55 can be seen in all plots of Fig. 3.13, as already predicted from the band diagram in the Fig. 3.9(a) taking into account all the beam propagation effects described above, which are determined by the geometry of the PhC and its iso-frequency contours. The clear sequence of the behavior of beam propagation for our studied case can be summarized as follows: firstly, with increasing frequencies, the BG appears, afterwards a self-collimation

region inside the PhC emerges, which later with increasing frequencies is followed by the focusing effects.

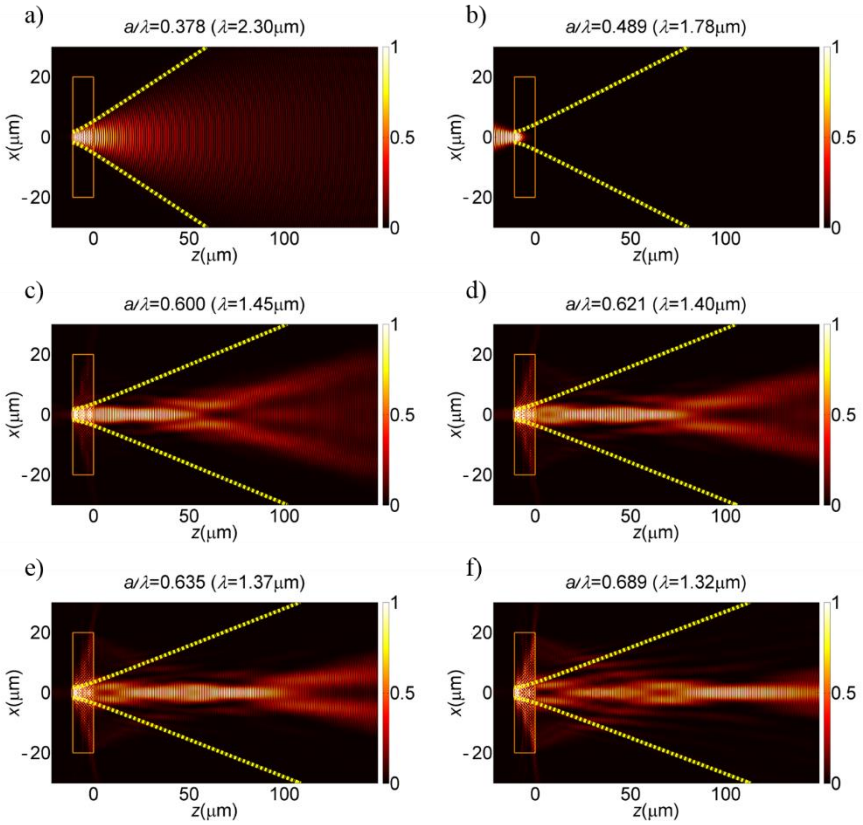

Figure 3.14. Intensity distribution behind the crystal, for different frequencies of the first three bands. (a) for a/λ=0.378, where beam spreads. (b) for band-gap frequency a/λ=0.489, (c) for a/λ=0.600, where focus appears, (d) for a/λ=0.621, where shifting of the focus is observed, (e) for a/λ=0.635, where double focusing is seen, (f) for a/λ=0.689, where distance between two focal positions is increased. The yellow dashed line in all the figures represents the reference beam in free propagation.

In Fig. 3.14 some full intensity profiles of particular frequencies of first, second and third bands are shown. The dashed yellow lines stand for the reference beam contour in the free space propagation. Fig 3.14(a) shows the frequency a/λ=0.378 which belongs to the first band and therefore, as for this frequency the iso-contour has a usual shape, we have the expected spreading of the beam. The frequency a/λ=0.489 of Fig 3.14(b) falls into the band gap, therefore we see only the reflection of the beam from the PhC structure. Fig 3.14(c) stands

for the frequency of a/λ=0.600, where the clear focusing at the distance of $z\approx$20 μm appears, which is due to the convex curvature of the second band. In Fig. 3.14(d) we see the slight shifting of the focal position to the right (now the focal position is at $z\approx$60 μm), as well as the appearance of the second focal point at $z\approx$30 μm, determined by the convex curvature of the third band for this frequency. In Fig. 3.14(e), at the frequency of a/λ=0.635, the clearer separation of the two focal positions is observed, where the first focus is determined by the curvature of second band and is shifted towards $z\approx$75 μm, while the second focus stays close to $z\approx$30 μm. The differences between the shapes of convex curvatures for the third band is not so pronounced, consequently, the focal positions for this band move only very slightly. Finally Fig. 3.14(f) demonstrates a clear move of the first focus to the position of $z\approx$100 μm, while the second focus moves to $z\approx$40 μm. The second focus is less intense for this frequency.

Collimation

Fig 3.15(a) demonstrates the iso-frequency contours of fourth band. We observe that there exists the self-collimation region close to $a/\lambda\approx$0.87, where the iso-frequency contour flattens. Fig. 3.15(b) represents the intensity distribution along horizontal axis, z (at position x=0), depending on the frequency. The plot demonstrates that in the region a/λ: 0.85-0.9 the intensity along the horizontal axis decays very slowly. This is probably due to the self-collimation affect at this region. Figures 3.15(c), (d) and (f) represent intensity maps along three different vertical planes, correspondingly, at z=5 μm, z=20 μm and z=85 μm. In these plots vertical axis is frequency, while horizontal axis is transversal beam distribution. From these three figures we see that at the region $a/\lambda\approx$0.87 the beam intensity is kept over longer distances.

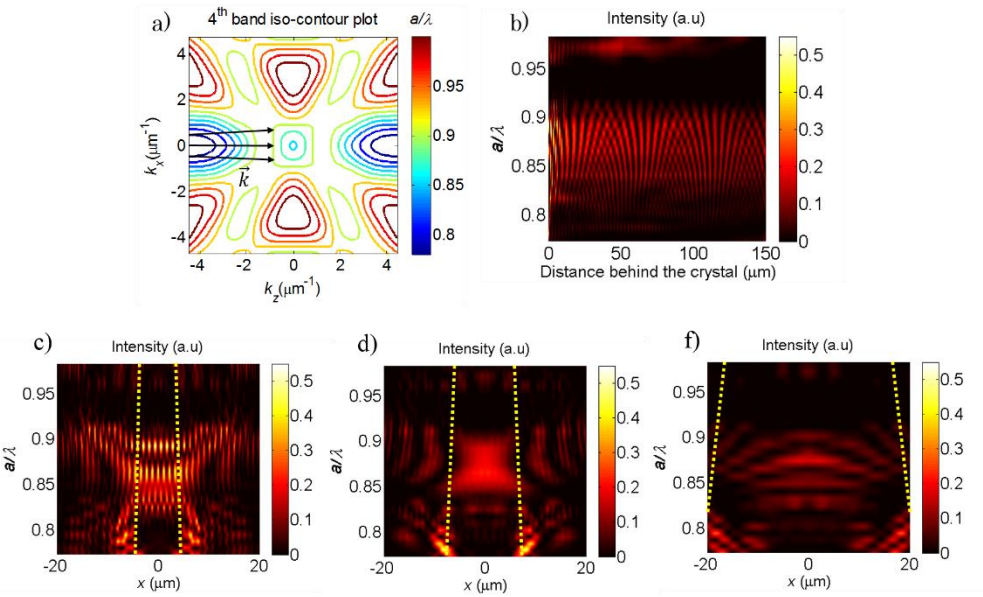

Figure 3.15. (a) The iso-frequency contour of fourth band, (b) intensity distribution along the horizontal axis, z, at x=0 μm, depending on frequency (for the frequencies of fourth band). (c), (d), (f) intensity distributions along the transversal axis x, depending on frequency (frequency range belonging to the fourth band) at the corresponding positions of z = 5, 20 and 85 μm. The yellow thick dashed line correspond to the reference beam in free space propagation.

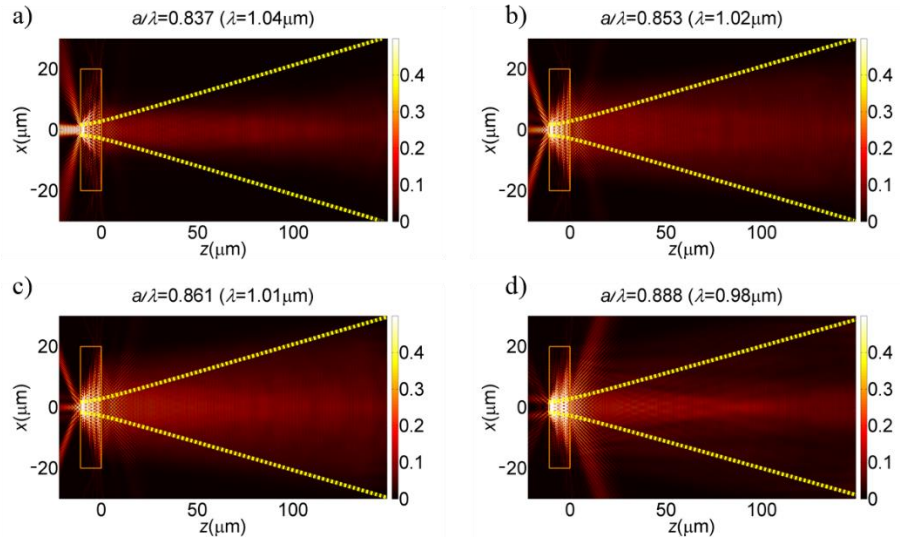

Figure 3.16. Intensity distribution behind the crystal, for different frequencies of the fourth band. (a) for a/λ=0.837, (b) a/λ=0.853, (c) for a/λ=0.861, (d) for a/λ=0.888. The yellow thick dashed line correspond to the reference beam in free space propagation.

In Fig. 3.16 we have plotted, intensity distributions of the beam for several frequencies of a/λ=0.837, a/λ=0.853, a/λ=0.861, a/λ=0.888, which correspondingly are shown in Fig. 3.16(a), (b), (c) and (d). From these figures it can be noticed that, indeed, the intensity distribution in propagation is more homogeneous compared to the contours of the reference beam. Moreover, although the beam waist is broad, the beam remains collimated along the propagation for these frequencies, which is probably be due to the existence of the self-collimation effect close to these frequencies.

Focusing

To investigate the behavior of higher bands, we draw iso-frequency contours for the fifth, sixth, seventh and eight bands (correspondingly, Fig. 3.17(a), (b), (c) and (d)).

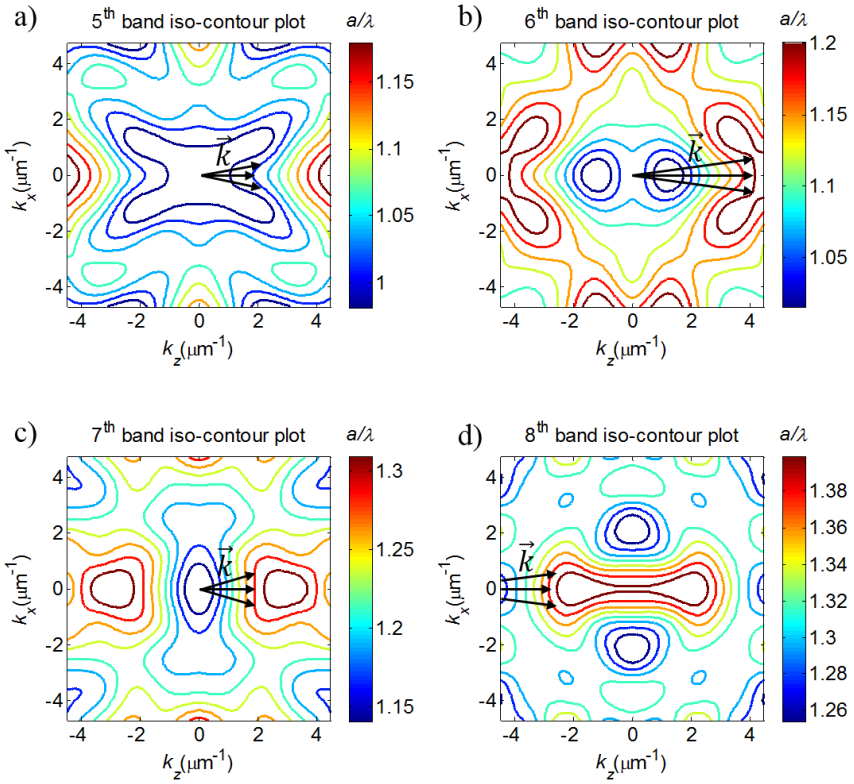

Figure 3.17. Iso-frequency contours. (a) for the fifth order band, (b) for the sixth order band, (c) for the seventh order band, (d) for the eight order band. Black arrows represent $\vec{k}$ vectors pointing to the direction of higher frequencies.

Fifth and sixth bands overlap, however, the behavior for the same frequencies at these different bands is opposite, i.e. all the contours of the fifth band has a convex curvature, therefore, it indicates negative diffraction. However, the curvatures of the sixth band are concave and they account for the positive diffraction and normal spreading of the beam and, therefore, it is hard to predict beam behavior for the overlapping iso-frequency contours of fifth and sixth band.

Moving to the seventh band there are clear flattish segments of iso-frequency contours from $a/\lambda \approx 1.20$ to $a/\lambda \approx 1.28$, where the self-collimation inside PhC should appear. Moreover, around $a/\lambda \approx 1.30$ appears a convex dispersion line segment, which should lead to the negative diffraction effect. Seventh band (Fig. 3.17(c)) is intersecting with the eight band (Fig. 3.17(d)). For the eight band the convex shape curvatures start with frequency $a/\lambda \approx 1.29$ and finishes at $a/\lambda \approx 1.40$. At these frequencies the negative diffraction should occur. Moreover, double focusing for $a/\lambda \approx 1.30$ is expected as around this frequency both seventh and eighth bands have convex curvatures. To check all these predictions we proceed with the intensity distribution along horizontal axis, z (at position $x=0$) for different frequencies (Fig. 3.18(a)), as well as with intensity distributions along transversal planes of the beam at three different positions of $z=5$ µm, $z=20$ µm and $z=85$ µm for different frequencies (Figs. 3.18(b), (c), (d)).

Fig. 3.18(a) shows a very weak focusing-collimation effect starting from the lower bands within a/λ: 0.95 – 1.1, as intensity at this region drops very slowly along the propagation direction. This effect can be accounted to the convex iso-frequency contours of the fifth band. However, the focusing effect is most likely not very pronounced due to the overlap of the sixth band which has only concave iso-frequency curves, and as the radiation of the beam splits to both bands, we have no clear focusing, however some weak collimation effect is obtained. As well, this statement is confirmed with the plots of 3.18(b), (c), (d), where we see that for this frequency region, the transversal profile of the beam is spreading along propagation much less compared to the reference beam.

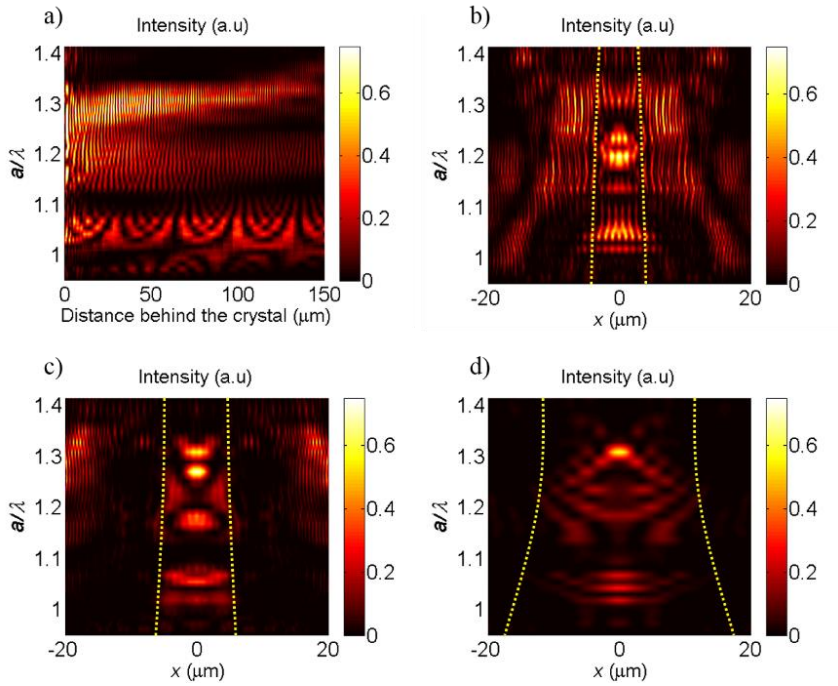

Figure 3.18. (a) Intensity distribution along the horizontal axis, z, at x=0 μm, depending on frequency (for a/λ: 0.95 – 1.4). (b), (c), (d) intensity distributions along the transversal axis x, depending on frequency at the corresponding positions of z = 5, 20 and 85 μm. The yellow thick dashed line correspond to the reference beam in free space propagation.

When we move to the higher bands we notice that there is some pronounced intensity region close to the crystal surface at $a/\lambda \approx 1.2$, which is most likely due to the flattish dispersion curve segments at seventh band for these frequencies.

For even higher frequencies, we notice more pronounced intensity region at $a/\lambda \approx 1.28$, which is shifting to the right with increasing frequency up to $a/\lambda \approx 1.38$. Therefore, the scenario repeats as it happened in the second and third bands, where the focal position was moving away from the crystal when the frequency was being increased. However, for the higher bands it appears for the much smaller frequency range. Although it is not clearly seen in Fig. 3.18(a), it can be observed in Figs. 3.18(b), (c) and (d) that there is a double focusing at $a/\lambda \approx 1.31$. At this frequency in the Fig. 3.18(c) (which represents distance behind the crystal

at z=20 μm), a narrow beam profile with increased intensity is observed. What is more, in Fig. 3.18(d) (distance behind crystal z=85 μm), the narrow and intense beam profile is seen again close to the same frequency region. Therefore, we have a double focusing around the frequency $a/\lambda \approx 1.31$. Indeed, if we look at the iso-frequency contour of seventh band for this frequency, we will notice that the curve is of convex shape, corresponding to the negative diffraction, as well as the eight band has a convexly shaped dispersion curve for this frequency. The contours are of the different strength of the convex shape, and focusing appears at two different distances, as the different portions of radiation projects into both of the dispersion curves.

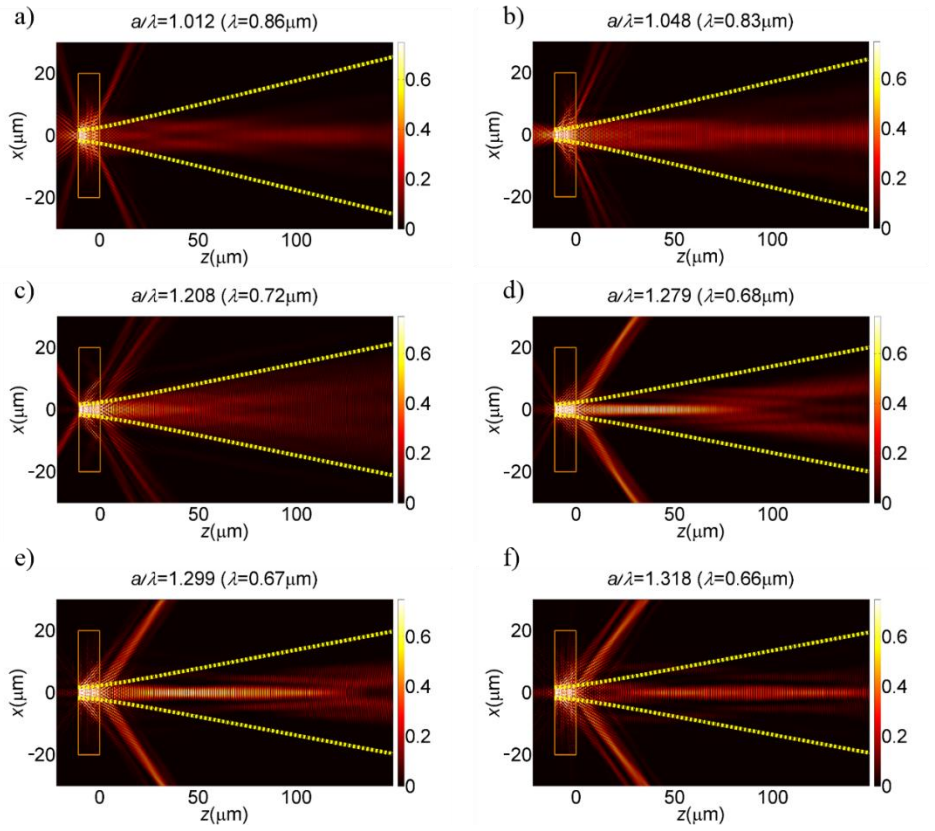

Figure 3.19. Intensity distribution behind the crystal, for different frequencies of the 5th, 6th, 7th and 8th bands. (a) for a/λ=1.012, (b) for a/λ=1.048, (c) for a/λ=1.208, (d) for a/λ=1.279, (e) for a/λ=1.299, (f) for a/λ=1.318. The yellow thick dashed line correspond to the reference beam in free space propagation.

To demonstrate all these effects, we have plotted intensity distributions for separate frequencies (Fig. 3.19). In Fig. 3.19(a) and (b) we have frequencies a/λ=1.012 and a/λ=1.048 from fifth and sixth bands and as mentioned previously, it is seen some weak focusing-collimation effect. Fig. 3.19(c) at frequency a/λ=1.208 demonstrates some higher intensity just at the output of the crystal, but no clear focusing is observed, while in Fig. 3.19(d) a very pronounced focusing at around z=40 μm is seen, which appears due to the convex curvature of dispersion curve in the 8th band. If we continue increasing the frequency until a/λ=1.299, in Fig. 3.19(e) we notice that first focus has shifted by several microns and as well a second one appeared at the distance of z≈85 μm. The second focus appeared due to the convex segment for this frequency in the 7th band. In Fig. 3.19(f) we see double focusing due to the simultaneously convex curvatures at both seventh and eighth bands for the frequency of a/λ=1.318.

Summarizing, we observe that beam propagation behavior with increasing frequency evolves in this manner as for lower bands: firstly, appears a BG, then we can observe self-collimation, which afterwards is followed by focusing effect. The focal position tends to shift away from the PhC with increasing frequency. A similar tendency should remain moving to even higher order bands.

3.2.2. Non-diffractive propagation inside the PhC

To observe the self-collimation effect we have increased the transversal size of the crystal up to 80 μm and the longitudinal size up to 70 μm and performed FDTD simulations. The results are demonstrated in Fig. 3.20.

Fig. 3.20(a) demonstrates a very clear self-collimation effect as expected for the flat segment of the second band iso-frequency contour at a/λ≈0.58. The yellow dashed line represents the contour of the reference beam propagating in free space. It is obviously seen that in PhC beam stays confined compared to the reference beam. Fig. 3.20(b) demonstrates the intensity drop while beam is propagating in PhC, from which we can tell that the drop is stronger at the

beginning, but later is not so significant. The intensity drop of reference beam is much stronger compared to the beam inside the structure. Fig. 3.20(c) demonstrates intensity profiles of the beam inside the crystal at three different distances (black line - 0 μm, red - 20 μm, green - 40 μm), from which we can tell that the beam width along the distance stays stable.

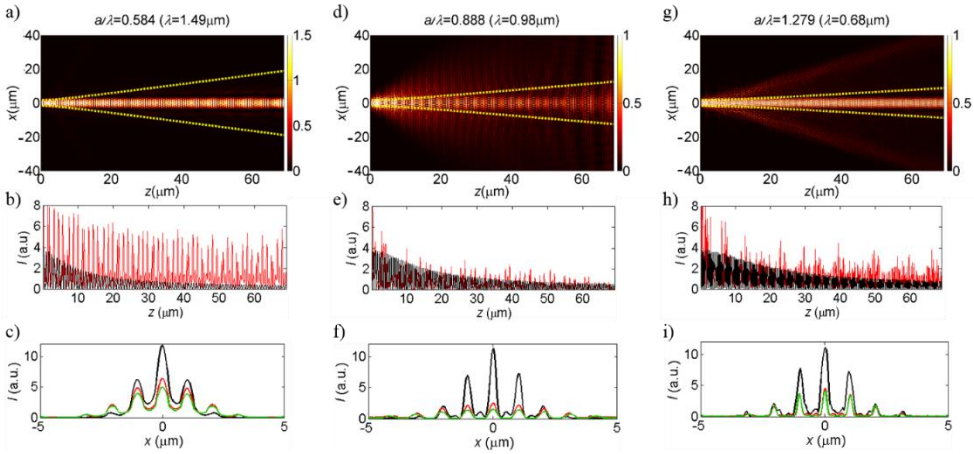

Figure 3.20. (a), (d), (g) Intensity distribution of the non-diffractive propagation inside the infinite PhC for the corresponding frequencies of a/λ=0.584, a/λ=0.888 and a/λ=1.279. The yellow thick dashed line correspond to the reference beam in free space propagation. (b), (e), (h) horizontal cross-section intensity profile at x=0 of the propagated beam in a length of 70 μm, for the corresponding frequencies of a/λ=0.584, a/λ=0.888 and a/λ=1.279, marked with the red color, while black color stands for the beam with the same conditions propagating in a free space. (c), (f), (i) transverse cross section intensity profiles at different propagation distances: black line z=0 μm, red line z=20 μm, green line z=40 μm, for the corresponding frequencies of a/λ=0.584, a/λ=0.888 and a/λ=1.279.

Fig. 3.20(d) demonstrates a not so strongly confined self-focusing effect, but still a clear region of higher intensity "tunnel" is observed for $a/\lambda \approx 0.88$. It can be explained with the fourth band's flattened iso-frequency contour, which is not that broad. Therefore, not all k vectors project into the flat part of the segment and as a consequence, we have not so strongly confined beam propagation and we observe some spreading of it. Fig. 3.20(e) shows the intensity drop in logarithmic scale for $a/\lambda \approx 0.88$ while the beam propagates along the structure. This time the drop is more significant compared to Fig. 3.20(b), but still stays more intense compared to the reference beam. Figs. 3.20(g), (h), (i) demonstrate

clear self-collimation at a region of $a/\lambda \approx 1.28$, which belongs to the flat segment of the dispersion curve belonging to the seventh band.

3.2.3. Discussion

The results obtained with the crystal parameters of Fig. 3.2 demonstrate clear focusing and even double focusing effect behind the PhC for different frequency ranges. However, to fabricate this kind of structure is still a big technological challenge, as the longitudinal period is very small ($d_{\parallel} = 1.4\ \mu m$). Fortunately, as we have noticed, focusing effect appears not only in the first bands of the structure, but, also, it repeats for the higher bands. This is a plausible property of the PhCs, which can be used for the modeling of the structure with longer longitudinal periods, nevertheless, still enabling to observe the focusing in higher order bands (higher frequencies, lower wavelengths). Therefore, we can solve the technological problem of fabrication, by enlarging the longitudinal periods and consequently observing focusing effect in visible frequency regime experimentally. This, on the one hand, simplifies the fabrication of the samples, but on the other hand, makes the observation and interpretation of the focalization effect more complex, since the harmonic expansion techniques become very complicated in high order propagation bands.

3.3. Experimental demonstration of flat lensing behind the woodpile PhC

In this section we experimentally demonstrate full 2D focusing by a polymer based 3D woodpile PhC. As discussed in section 3.1, full 2D flat lens focusing has been experimentally shown for microwaves [Lu05b] and for sound waves [Ceb12]. Even the 1D focusing/imaging by PhC slabs has been so far experimentally

demonstrated only in the near-infrared frequency range [Sch06]. Most of the theoretical studies on the flat PhC lensing or self-collimation effect consider modulation periods of the order of the wavelength. Therefore, in such case, focusing effects occur in the first order bands.

In particular, for PhCs with square symmetry, the corner of the Brillouin Zone is given by the simple condition $\lambda = d_0\bar{n}$ (λ is the wavelength, $\bar{n}$ is the effective refractive index of the PhC, and d_0 is the lattice period). The self-collimation (the flattening of the spatial dispersion lines), as well as focusing effects, occur at frequencies below the corner of BZ, i.e. at $\lambda > d_0\bar{n}$. The experimental demonstration of these effects in visible range is, therefore, a difficult task due to technological limitations of fabrication of PhCs at this scale. To avoid this problem we use an alternative approach by considering PhCs with larger modulation periods, but searching the focusing effects in higher order bands. In particular, we consider woodpile PhCs (Fig. 3.23(a)). Since the usual harmonic expansion becomes inconvenient for the interpretation of the results in this regime, we adapted the simplified paraxial theory for the design of our structure and interpretation of the results.

In this section, firstly, we analytically (applying paraxial model and mode expansion) show that in high order bands exist spatial dispersion with the convex curvatures. Then we have perform numerical FDTD simulations (with Crystal Wave software) to prove the predicted results and finally according to the numerics we perform an experiment with which we obtain flat lensing effect in visible frequency range.

3.3.1. Paraxial model

The paraxial wave equation used to describe light propagation in an inhomogeneous medium is given by:

$$\left(\frac{2ik_0\partial}{\partial z} + \nabla_\perp^2 + 2\Delta n(x,y,z)k_0^2\right)A(x,y,z) = 0. \qquad (3.4)$$

Here $A(x,y,z)$ is the complex envelope of the electromagnetic field $E(x,y,z,t) = A(x,y,z)e^{ik_0z-i\omega_0t} + c.c.$ propagating along the z-direction with the wave-number $k_0 = n\omega_0/c$, $\nabla_\perp = \partial^2/\partial x^2 + \partial^2/\partial y^2$ is the Laplace operator in the transverse to propagation space. Relatively large spatial periods of the index variation (comparing with the wavelength) justifies Eq. (3.4) as an acceptable approximation.

As the woodpile structure (Fig. 3.23(a)) consists of bars directed along x and y directions in alternating order, the 3D refractive index profile can be expressed as a sum of 2D profiles:

$$\Delta n(x,y,z) = \Delta n_x(x,z) + \Delta n_y(y,z). \tag{3.5}$$

The reduced 2D index profiles are of rhombic symmetry, and light propagation is parallel to the long diagonals of the rhombus. This particular symmetry allows the factorization of the 3D wave envelopes,

$$A(x,y,z) = A_x(x,z) \cdot A_y(y,z), \tag{3.6}$$

where both field quadratures propagate independently one from another. This factorization, allows to apply the 2D calculations for simulation of the beam propagation through full 3D crystal, in the way that $A(x,y,z)$, inserted into Eq. (3.4) allows to separate the factorized components:

$$\left(2ik_0\frac{\partial}{\partial z} + \frac{\partial^2}{\partial x_i^2} + 2\Delta n_{x_i}(x_i,z)k_0^2\right)A_{x_i}(x_i,z) = 0. \tag{3.7}$$

Here $x_i = x,y$. Eq. (3.7) is used for harmonic expansion of the fields.

Mode expansion:

In order to calculate the spatial dispersion curves in 2D (and eventually the dispersion surfaces in 3D because of factorization), the harmonic expansion can be applied to each ($x_i = x,y$) of factorized components:

$$A_x(x,z) = \iint_{BZ} e^{ik_z z} e^{ik_x x}\Big(A_0(k_x,k_y) + \sum_{m_x,m_z} A_{m_x,m_z}(k_x,k_z)\, e^{im_x q_x x - im_z q_z z}\Big)\, dk_x dk_z. \tag{3.8}$$

Eq. (3.8) is in fact the Fourier integral, where, however the integration is performed in each Brillouin zone separately, and the integrals are added. We consider only three most relevant Brillouin zones: $(m_x, m_z) = (0,0)$, which is the central Brillouin zone, and $(m_x, m_z) = (-1,+1), (+1,+1)$, which are the nearest neighbors to the central Brillouin zone. Speaking differently, the above truncation to three Brillouin zones, or, equivalently to three harmonic components means that the spatial modulation of the field in the Bloch-mode is harmonic (i.e. the higher modulation harmonics are irrelevant). Inserting Eq. (3.8) into Eq. (3.7) results into three coupled equations for the above field components:

$$K_z A_{m_x,m_z} = \left(-\frac{(K_x + m_x Q_x)^2}{2} + m_z Q_z \right) A_{m_x,m_z} + \Delta n_0 f \sum_{l_x,l_z \neq m_x,m_z} A_{l_x,l_z}, \tag{3.9}$$

here Δn_0 is the refraction index contrast, and f is the filing factor, i.e. the area of the polymer bar with respect to the area of the 2D cell (in experiment $f \approx 0.1$). $K_{x,z} = k_{x,z}/k_0$ and $Q_{x,z} = q_{x,z}/k_0$ are normalized wavevector components. The coordinates are correspondingly normalized to $\lambda\!\!\!^{-} = \lambda/2\pi$.

The coupling between all three harmonic components is most efficient at the resonance

$$Q_x^2 - 2Q_z = 0, \tag{3.10}$$

as follows from Eq. (3.9), which means that all three dispersion lines cross at $K_x = 0$ point (the dashed lines in Fig. 3.21(a)). The resonance point in paraxial model corresponds to the corner of a particular Brillouin zone in the full model. At the

cross-point the lines deform due to the mode coupling, and the convexly curved segments appear evidencing the negative diffraction of corresponding Bloch modes (Fig. 3.21(a)).

The eigenvalues of Eq. (3.9) have simple expression exactly at the resonance point $\Delta Q = Q_z - Q_x^2/2 = 0$ (the corner of the Brillouin zone):

$$K_z = \left\{ -\frac{K_x^2}{2},\ \sqrt{2(\Delta n_0 f)^2 + (K_x Q_x)^2} - \frac{K_x^2}{2},\ -\sqrt{2(\Delta n_0 f)^2 + (K_x Q_x)^2} - \frac{K_x^2}{2} \right\} \tag{3.11}$$

For the formation of flat lensing the upper branch (second eigenvalue of Eq. (3.11)) is important. This branch corresponds to the Bloch mode with the convexly curvature (anomalous spatial dispersion). The Taylor series expansion of the corresponding branch for small K_x reads:

$$K_z = \sqrt{2}(\Delta n_0 f) + \frac{K_x^2}{2}\left(\frac{\sqrt{2}}{2}\frac{Q_x^2}{\Delta n_0 f} - 1\right) + \cdots \tag{3.12}$$

This means that the PhC imposes an anomalous spatial dispersion (convex curvature) which can compensate the normal spatial dispersion (concave curvature) of the homogeneous space if $Q_x^2 \geq \sqrt{2}\Delta n_0 f$. Eq. (3.12) is calculated exactly at the resonance point. In reality the curvatures of the dispersion curves of the Bloch mode depend strongly on detuning (i.e. on the distance from the corner of Brillouin zone), as it is shown in Fig. 3.21.

Another important part of the problem is the projection of the incoming plane wave into the Bloch modes. Some part of the incoming wave projects into one Bloch mode and is focused, some part projects into another mode, and is defocused. The projections are calculated from the eigenvectors of Bloch modes (simply speaking from the plane wave composition of particular Bloch mode). The full solution of Eq. (3.9) for let us say the mode is:

$$A_{0,0}(z) = \sum_{j=1,2,3} a_{0,j} exp\left(iK_{z,j} z\right), \tag{3.13}$$

i.e. it is composed from three Bloch modes propagating with their own wavenumbers $K_{z,j}$. The coefficients $a_{0,j}$ are mode projection coefficients and indicate how much the particular Bloch mode is excited by a plane wave. The analytic expression of projection coefficients is complicated even in resonant case, and we again used series expansion.

$$a_0 = \frac{1}{2}\left(1 - \frac{1}{2}\frac{K_x^2 Q_x^2}{(\Delta n_0 f)^2}\right), \tag{3.14}$$

which allows to estimate the angular half width of the projection profile (in term of intensities): $\Delta K_x = \Delta n_0 f/\sqrt{2}Q_x$. The dispersion curves, as well as projection curves are plotted in Fig. 3.21.

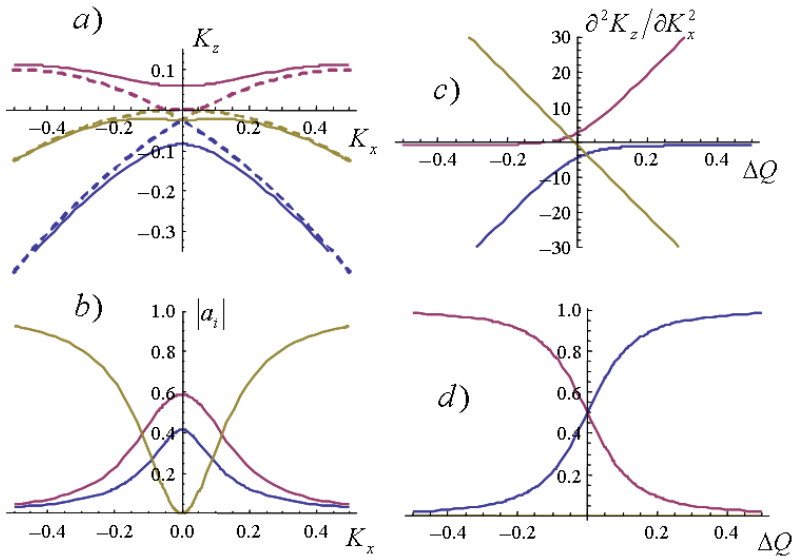

Figure 3.21. (a) Dispersion curves (by dashed lines are shown dispersion curves of noninteracting modes); (b) amplitudes of the Bloch modes; (c) curvatures of dispersion curves $\partial^2 K_z/\partial K_x^2$ (corresponding to focusing distances) and (d) amplitudes of Bloch modes depending on detuning at $K_x = 0$. Parameters: $\Delta n_0 f = 0.05$ in all cases; detuning $\Delta Q = -0.025$ in (a) and (b).

In Fig. 3.21(a) three dispersion branches are shown, where the upper one has a convex curvature (negative diffraction), and the field projected on it can be focused. The focal distance is given by the curvature (Fig. 3.21(c)) of dispersion curve. For increasing detuning from resonance the curvature of dispersion

increases, however the projection into focusing Bloch mode decreases (Fig. 3.21(d)). The best performance of the flat lensing is given by compromise between curvature and projection, and is expected at around $\Delta Q \approx 0$.

Moreover, three spatial dispersion curvatures in Fig. 3.21(a) mean that for a given frequency three propagation bands overlap. In fact when we do not obtain a complete BG (the situation quite frequent in 2D) some frequencies overlap. If, beside a convex-curved segment of spatial dispersion curve (used for focusing) appear other segments, the radiation can be additionally focused-defocused on these segments, and can interfere with focusing.

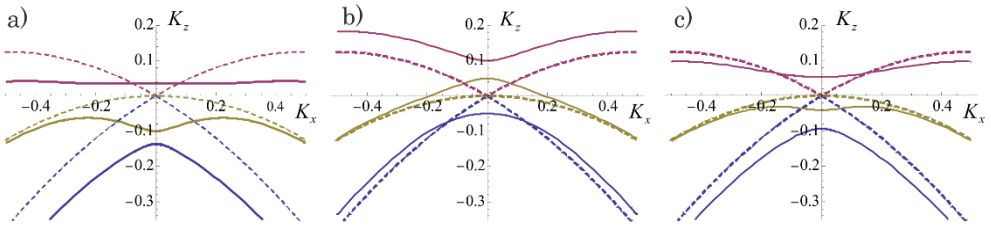

Figure 3.22. Spatial dispersion curves for the parameters around the edge of Brillouin zone with $\Delta n_0 f = 0.05$ in all cases; (a) detuning $\Delta Q = -0.1$, (b) $\Delta Q = -0.04$, (c) $\Delta Q = 0.05$.

Fig. 3.22 shows spatial dispersion curves, for slightly different parameters, but all close to the corner of the Brillouin Zone. It is seen that in all the cases appear three branches (for a single frequency). The radiation can project onto all three Bloch branches (dispersion curves). Each branch is responsible for focalization (or imaging) of its "own" radiation independently from other branches. The focalization distances are proportional to the curvatures of these branches. Therefore each convex branch is expected to focus its "own" radiation at corresponding distances behind the PhC, and several image planes can form.

The dashed curves in Fig. 3.22 correspond to noninteracting modes around their crossing point (at the corner of Brillouin Zone) and the three modified spatial dispersion curves arise from the splitting and deformation of these modes due to the refractive index contrast (sufficient for the interaction).

It is seen that in all the simulated cases in Fig. 3.22, the lower spatial dispersion branch is concave, therefore, it corresponds to positive beam

diffraction and no lensing for it is expected. The shapes of the middle and the upper branches strongly depend on off-resonance detuning. In Fig. 3.22(a) the upper branch corresponds to the self-collimation, while the middle one for negative diffraction. In Fig. 3.22(b), beam negatively diffracts only in the upper branch. For some parameter sets two dispersion curves can display convex segments (Fig. 3.22(c)), where the upper and the middle curves due to negative diffraction, both can lead to flat lensing effect. The magnitudes of the curvatures are generally different, therefore focal distances corresponding to them are different. These results confirm the ones already obtained in the section 3.2, where double focusing has been numerically demonstrated.

However, for high order bands it is hard to observe double focusing, due to multiple mode interactions numerically, and especially to prove it experimentally. Therefore, in following work we consider a PhC designed to obtain single focusing effect, which is clearly pronounced.

3.3.2. Structure and simulations

As mentioned above, the woodpile structure (Fig. 3.23(a)) is very convenient from the calculation point of view, as the 3D index profile can be simplified to a 2D index profile. The reduced 2D index profile (Fig. 3.23(b)) consists of elliptically shaped rods of refractive index n = 1.5 (the same as of the polymer) embedded in air. FDTD calculations were performed for such a simplified (Fig. 3.23(b)) 2D PhC structure. The parameters of the simulated PhC are: longitudinal period $d_{\parallel}$ = 6 μm and transverse period of $d_{\perp}$ = 0.9 μm (filling factor f = 70%), which from fabrication point of view, are technologically approachable. The transverse size of the crystal was 80 μm, and length was L ~ 30 μm (5 longitudinal periods). The Gaussian beam with the focal spot width in the range of 1.6 – 3.0 μm was focused just at the front face of the PhC into the structure and launched looking for focusing in the visible regime.

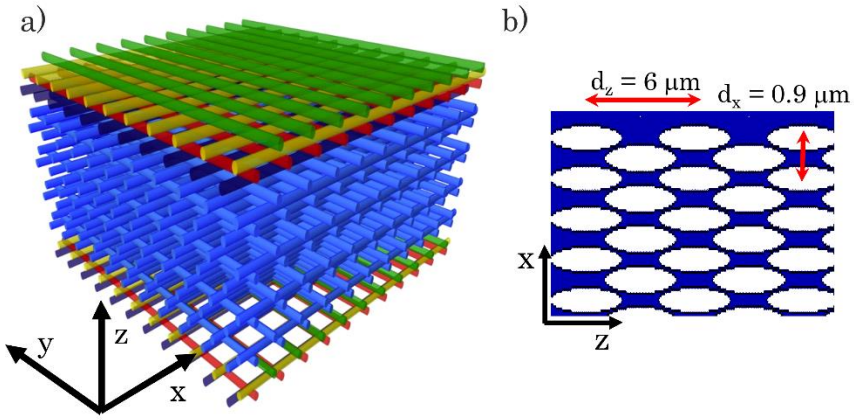

Figure 3.23. (a) Schematic representation of the woodpile structure. (b) 2D PhC profile used for FDTD simulation.

Following the above described paraxial model and mode expansion (Section 3.3.1) the resonant interaction between the harmonic field components spanned by $\vec{q}_{1,2} = (\pm q_x, -q_z)$ is given by the condition $2q_z k_0 \bar{n}/q_x^2 \equiv 2d_x^2 \bar{n}/(d_z \lambda) = 1$ (derived from Eq. (3.10)). This defines the wavelength corresponding to the edge of BZ: $\lambda_{BZ} = 2d_x^2/d_z$ (which in our described case is estimated at $\lambda_{BZ} = 370$ nm). The self-collimation regime is obtained for the frequencies below the resonance $\lambda_{SC} > \lambda_{BZ}$, depending on the amplitude of index modulation. For frequencies between those of self-collimation and the edge of BZ $\lambda_{BZ} < \lambda < \lambda_{SC}$ the spatial dispersion curves become convex, and the flat lens focusing can be expected.

Therefore, firstly we identified the self-collimation wavelength, by propagating the narrow beam inside the elongated woodpile structure (20 longitudinal periods), and we found it at around $\lambda_{SC} = 610$ nm. We concentrated, consequently, on the range $370\text{ nm} < \lambda < 610\text{ nm}$, according to the previous analysis. The results are summarized in Fig. 3.26. The beam of 532 nm wavelength focuses at a distance of around 40 μm, while the 570 nm beam has a smallest width at a distance around 70 μm behind the PhC. For the wavelength of 780 nm (Fig. 3.26(e)), which is already in the normal spatial dispersion regime according to the estimation above, no focusing was obtained.

3.3.3. Experimental results and discussion

Woodpile PhC samples, with the parameters used in the above FDTD calculations, were fabricated by laser direct writing technique [Deu04]. A hybrid organic inorganic sol-gel photopolymer prepared as in ref. [Ovs08] was used, except the molar ratio of MAPTMS to ZPO that was chosen 5:3, and thioxanthen-9-one was used as photo-initiator. PhCs were written employing point-by-point irradiation of the sample by femtosecond laser pulses (300 fs pulse duration, 515 nm wavelength, 200 kHz repetition rate). A sample translation speed of 500 μm/s and laser power of 40 μW (after the objective) were chosen. The beam was tightly focused by a 63x 1.4 NA lens. An example of resulting PhC structure is shown in Fig. 3.24.

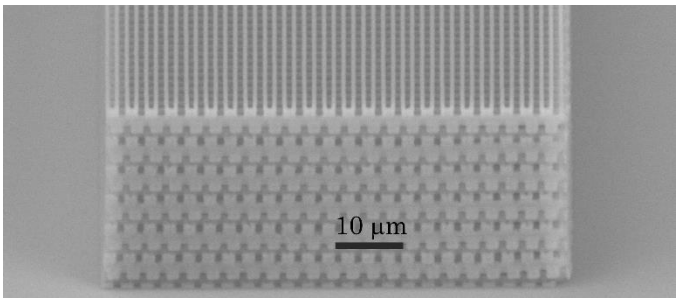

Figure 3.24. Fabricated woodpile PhC sample by direct laser writing technique.

For the experimental measurements a supercontinuum source pumped by a 800 nm Ti:Saphire laser was used (Fig. 3.25). The particular wavelengths of 532 nm, 570 nm and 700 nm were selected by a monochromator. The beams were focused using a 20x 0.4 NA microscope objective onto the front face of the PhC, which for different frequencies resulted in widths of the waist varying from 1.6 to 3 μm. The beam profiles at different distances behind the crystal were recorded with a CCD camera mounted, together with the imaging system, on a translational stage. The width of the beam behind the PhC was calculated applying a Gaussian fit to the CCD images. The experimental results are

summarized and compared with the FDTD calculation results in Fig. 3.26. Quantitative correspondence between the experimental and numerical data is not perfect, but the qualitative tendencies are the same.

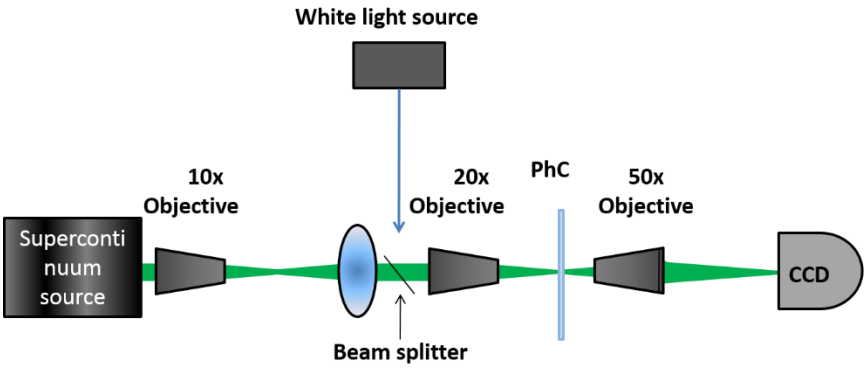

Figure 3.25. Schematic representation of the experimental set-up.

The smallest beam diameter is found at particular distances (around 50 μm) behind the PhC, at 532 nm and 570 nm while monotonous spreading is observed at 700 nm. However, even in the latter case the divergence was slightly less than that of the reference beam, due to the spatial filtering of the beam. The minimum widths of the beam behind the PhC were around 2.1 μm and 3.4 μm at 570 nm and 532 nm, respectively. This result gives a rough estimation of the numerical aperture of the flat lens: NA ≈ 0.1.

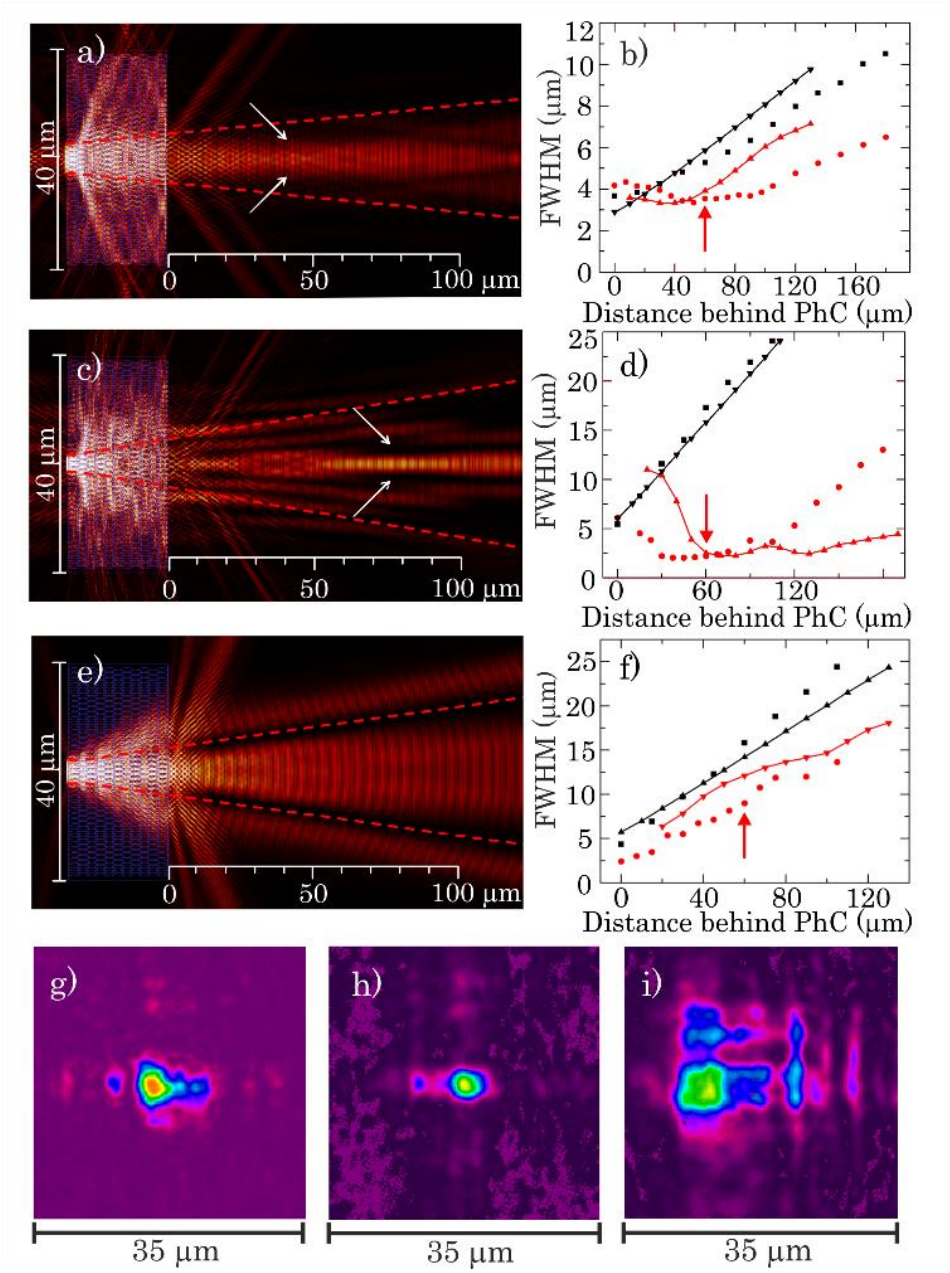

Figure 3.26. (a), (c), (e) Field intensity distributions at 532 nm, 570 nm and 780 nm, inside and behind the PhC calculated by 2D FDTD. (b), (d), (f) show the beam width depending on distance behind the crystal (red colour) compared to the width of the reference beam (black colour); dots – experimental results, lines – numerical results. (g), (h), (i) 2D distributions of the beams at the plane of 60 µm behind the PhC taken with the CCD camera for the corresponding wavelengths of 532 nm, 570 nm and 700 nm (correspondingly positions are marked by arrows in panels (b), (d), (f)).

We note, that we could not observe the beam focalization continuously in all expected wavelength range $\lambda_{BZ} < \lambda < \lambda_{SC}$, however just in several distinct areas of this range. Fig. 3.27 shows the focalization performance calculated by FDTD (the beam diameter at the focus as well the focal length depending on the wavelength). The reason for that is that we work at very high order propagation bands: although the character of the iso-frequency lines is globally defined by the first harmonic of the index modulation, the higher harmonics interfere, and distort the isoline picture. The higher is the propagation band, the more harmonics come into play, resulting in a stronger distortion of the isoline picture.

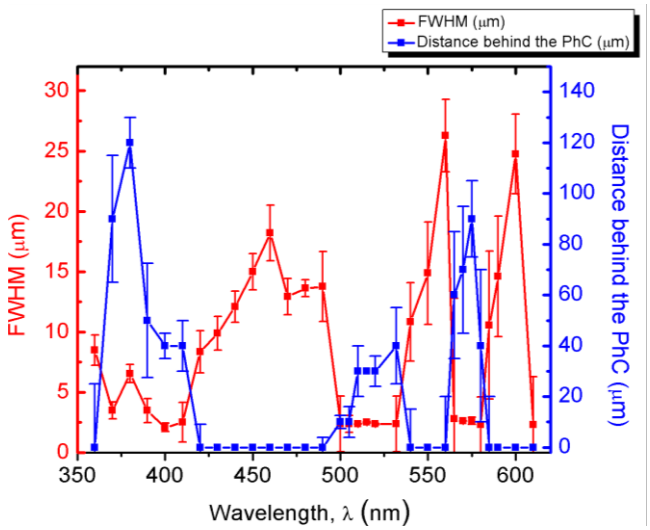

Figure 3.27. Minimum diameter of the beam behind the PhC (red), and the focal distance (blue) versus wavelength calculated by FDTD. Two insets represent iso-frequency lines where the spanning harmonics (see main text) are highlighted by red colour and global trends of iso-frequency lines highlighted by blue. Left inset is at the frequency of flat lensing (at 570 nm), the right one – at self-collimation (at 610 nm).

As seen from the Fig. 3.28, although the isoline picture (calculated by the PWE method using the MIT Photonic-Bands program) is quite disordered, the global trends can still be traced (highlighted by blue color) indicating the appearance of flat segments (for self-collimation (Fig. 3.28(a), (b)) as well as convexly curved segments (for flat lensing (Fig. 3.28(c), (d)). The spanning

harmonics are highlighted by red colour (obtained from calculations with very small index contrast).

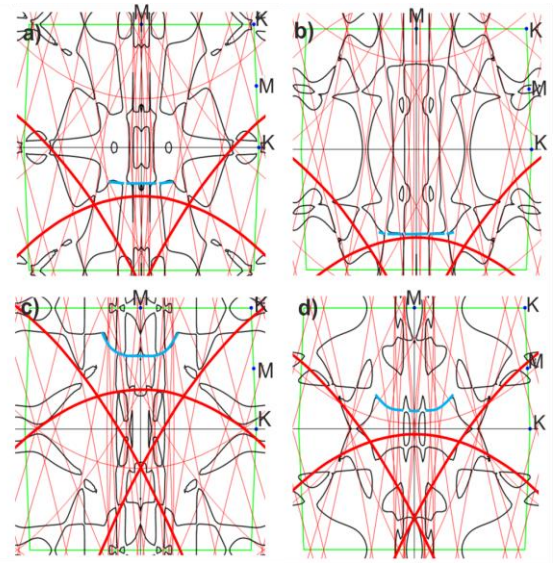

Figure 3.28. Iso-frequency lines corresponding to SC at around λ≈610 nm (a,b) and flat lensing at λ≈520 nm and λ≈575 nm correspondingly for (c,d). The dispersion lines of spanning harmonics are highlighted by red colour. The trends in isoline are highlighted by blue.

Summarizing the results for the woodpile PhC structure, we have reported the first experimental confirmation of the beam focusing by a flat 3D woodpile PhC at visible frequencies. The results show a convincing flat lensing with focal distances of around 50-70 μm behind the crystal. No focusing appears at other wavelengths, excluding all possible geometrical focusing effects (e.g. due to possibly curved surfaces of the woodpile). The observations are in good correspondence with the 2D FDTD simulations.

3.4. Formation of collimated beams behind the woodpile PhC

In this section, we report an experimental observation of a well-collimated beam formation behind a 3D woodpile PhC. We also theoretically interpret the results by expansions in plane wave components and by a numerical study based on the paraxial wave propagation model in modulated media.

3.4.1. Structure and fabrication

We used the photopolymer PhC of the woodpile type, as shown in Fig. 3.29. The photopolymer was a hybrid organic-inorganic Zr containing SZ2080, ensuring high resolution and low geometrical distortions [Mal10]. We used two types of samples: (i) moderate-contrast refractive index sample, where the index varies from 1.5 in polymer to 1 in air voids, and (ii) low-contrast sample, where the voids were filled by another polymer (polyethylene glycol) diacrylate (average $Mn \sim 258$) with the refractive index of 1.45. The transverse period was 1 μm in all samples; the longitudinal periods were 9 and 8 μm for the low- and moderate-contrast samples respectively, resulting in approximately the same optical length for both kinds of samples. The PhCs contain 12 longitudinal periods (i.e., consist of 48 woodpile layers on a glass substrate) and have transverse dimensions of 80 μm. The longitudinal modulation period is around one decade larger than the halfwavelength; therefore the corresponding propagation band is of a very high order (~100 in this case). We work, in this way, around a corner of a high-order Brillouin zone.

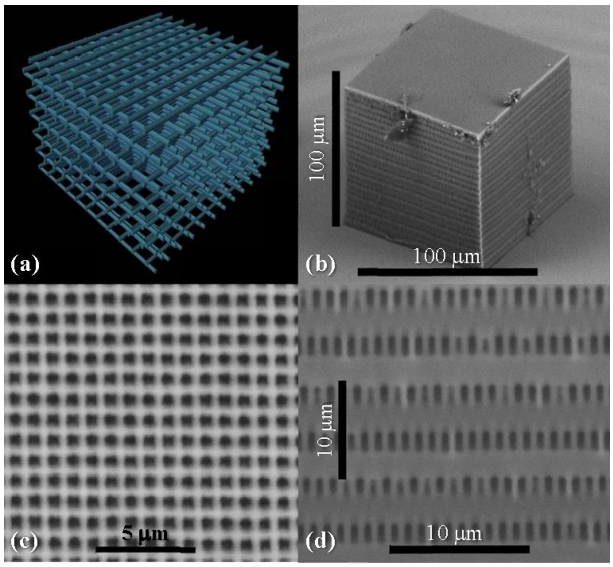

Figure 3.29. The woodpile PhC sample. Every second layer of piles of the same orientation is half-period shifted: (a) illustration and (b)–(d) micrographs by an electronic microscope showing the top (c) and side (d) views.

3.4.2. Experimental scheme and results

The experimental scheme and the reported experimental observation are illustrated in Fig. 3.30: a continuous wave laser beam at 532 nm is focused by a ×10 objective lens to a beam waist of $w_0 = 2\,\mu\text{m}$, and the woodpile PhC is positioned at some distance (on the order of millimeters) behind the focal plane. The PhC scatters the light, and therefore a shadow of the PhC contours is visible. At the middle of the shadow, a relatively round spot was observed, which is the key result presented in the section. The shape and the intensity of the spot depend on the distance between the focal plane and the crystal but do not depend on the distance to the observation plane.

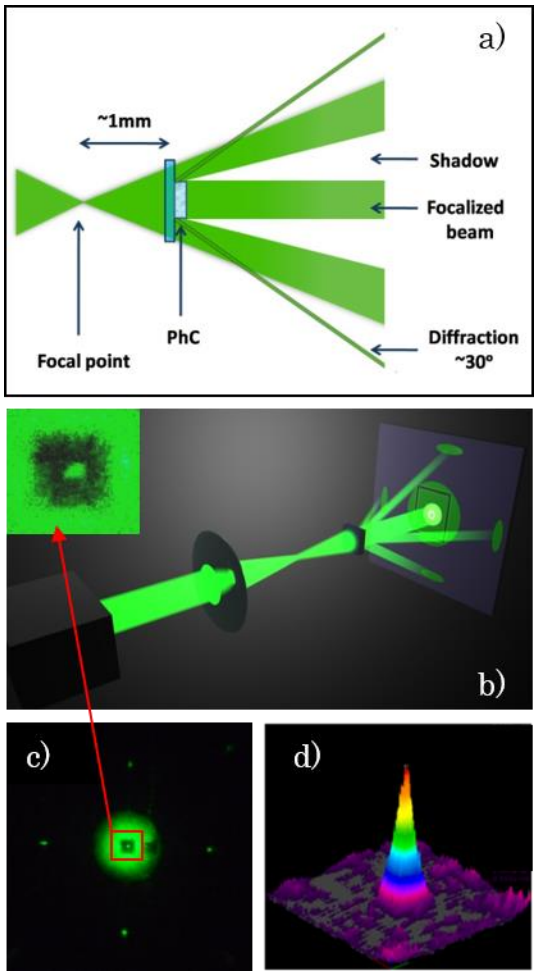

Figure 3.30. (a) The experimental setup to observe the formation of a well-collimated beam. The laser beam (532 nm) is focused (with a ×10 microscope objective), and the woodpile-like PhC is positioned at some distance (on order of millimeters) behind the focal plane. Behind the crystal, in the far-field area, the "shadow" of the PhC sample occurs, at the middle of which a narrow spot is observed, indicating formation of a well-collimated beam. (b), (c) The snapshots of typical observed transmitted field distribution on large (c) and small (d) spatial scales. The shown domain in (d) corresponds to the *"shadow" of the PhC.*

The remote screen, or camera located at approximately 5 cm behind the PhC, records the far-field distributions. When the spot (i.e., the well-collimated beam) is obtained, the four first order diffraction maxima appear too, as shown in Fig. 3.30(b). The diffraction angles (34 and 31 deg between the central and the first

maxima for moderate- and low-contrast samples, respectively) fit well with those calculated from the transverse period of the PhC.

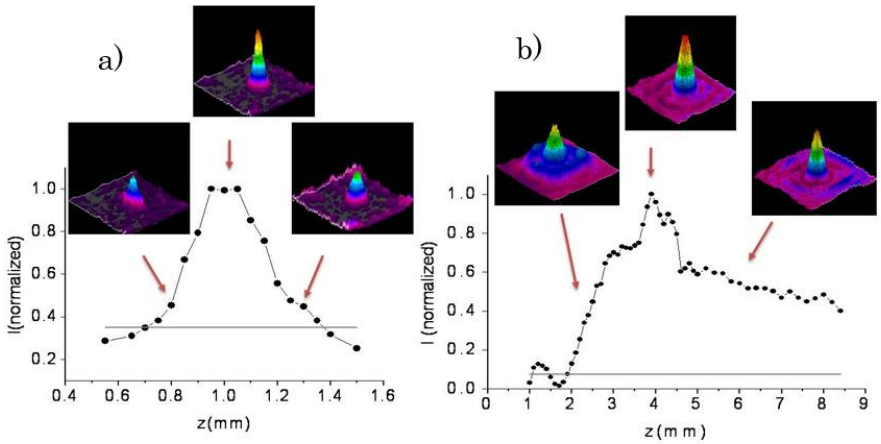

Figure 3.31. Top intensity of the collimated beam depending on the distance between the focal plane and the PhC for moderate contrast (a) and low-contrast (b) sample. Insets show typical shapes of the beam for different positions of the PhC. Thin horizontal lines mark the intensity of the light without the crystal. The shown domains in the inset corresponds to the "shadow" of the PhC.

The quantitative results of observation for both types of samples are summarized in Fig. 3.31, which evidences the existence of the optimum distance between the focal plane and the PhC sample (1 mm and 4 mm for the moderate- and low-contrast samples, respectively) for the optimum beam collimation. The top intensities of the spot significantly exceeded the irradiation intensity (by approximately 4 and 14 times for the moderate- and low-contrast samples). The width of the beam was 0,12 and 0.2 relative to the width of the shadow of the sample for the moderate- and low-contrast samples, respectively, and did not depend on the distance between the PhC and the screen. This means that approximately 2% and 22% of the shadowed radiation are transferred to the well-collimated beam in moderate- and low-contrast samples, respectively.

An important observation was that the bright spot remains at the middle of the shadow by slightly tilting the PhC sample (within approximately 2 deg). This excludes all possible interpretations of the effect by the reflections from the

surfaces of the sample or by a light guiding along the lateral facets or possible defect lines along the PhC.

3.4.3. Interpretation and discussion

Although the observed picture seems to be reminiscent of geometrical lensing, the observations cannot be interpreted by ray optics: optical thickness of the used PhC samples is constant over their transverse size; therefore the geometrical lensing due to the spherically varying thickness of the sample is excluded. Moreover, the width of the collimated beam is almost independent of the distance between PhC and the focal plane, which would not be the case for geometrical lensing. The character of collimation does not depend on the lateral dimensions of the PhC sample. Also, the beam propagates in a well collimated fashion over long distances behind the PhC samples and does not exhibit a sharp focus along its path.

We interpret the beam focalization by a negative diffraction (anomalous spatial dispersion) of the Bloch modes in the bulk of the PhC. The beam front acquires a positive curvature of the wave front (due to normal spatial dispersion) in the propagation before the PhC, and the anomalous spatial dispersion inside the PhC compensates for it. The wave front of the beam therefore becomes flat or nearly flat at the back face of the PhC, which results in a well-collimated propagation behind the PhC (see Chapter 1, Fig. 1.29).

In order to support this interpretation, applying the mode expansion method explained in Section 3.3.1, we calculate spatial dispersion curves (Fig. 3.32), with the parameters of the fabricated samples (parameters are close to the resonance condition Eq. (3.10)).

It can be seen that the upper spatial dispersion branch always, in all the simulated cases of Fig. 3.32, has a convexly shaped curvature, which stands for the negative diffraction. This anomalous spatial dispersion inside the PhC plays a key role in the formation of the collimated beams: Diffractive broadening of the beam accumulated in a propagation from the focal plane to the PhC is

compensated by the anomalous diffraction in propagation through the PhC. Therefore, the optimum distance between the PhC and the focal plane is determined basically by the crystal bulk parameters, that is, eventually by the curvature of the spatial dispersion curves. The curvatures of the dispersion curves of the Bloch modes depend strongly on the detuning from the corner of the Brillouin zone, as shown in Figs. 3.32(a), (b), (c), and can be varied by fine-tuning the geometry parameters of the PhC $\Delta Q_z = (Q_z - Q_x^2/2) = 0$. The shape of the 3D dispersion surface follow straightforwardly (due to factorization (see section 3.3.1)) from the 2D dispersion curves calculated above and is shown in Fig. 3.32(d).

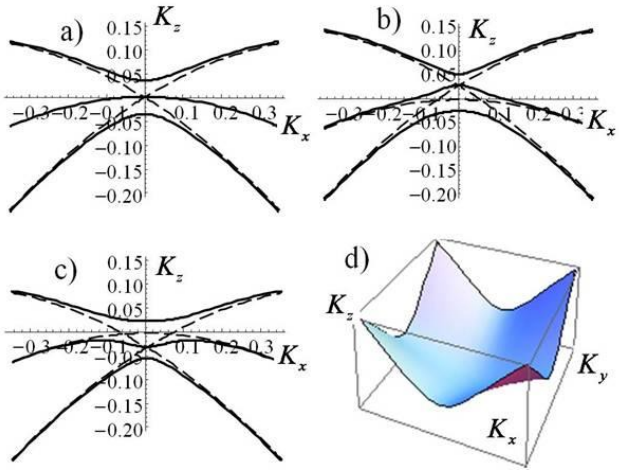

Figure 3.32. Spatial dispersion curves as calculated by diagonalization of Eq. (3.9) in 2D (a,b,c) and obtained (by factorization) in 3D (d). Parameters are: $Q_x = 0.5$ and $\Delta n_0 f = 0.025$. The difference between the calculated cases is off-resonance detuning: $\Delta Q_z = (Q_z - Q_x^2/2) = 0$ for (a,d), $\Delta Q_z = 0.03$ for (b), and $\Delta Q_z = -0.03$ for (c). The site of square domain in plot (d) corresponds to coordinate range in (a).

Finally, a series of numerical simulation of the paraxial model Eq. (3.7) were performed in order to justify the above interpretation of the beam collimation by the dispersion curves and surfaces. Well-collimated beams in the 2D case as well as beams of relatively good rotational symmetry in 3D have been found (Fig. 3.33). The parameters in calculations (the size of PC sample, modulation periods)

correspond to both experimental samples used, and the modulation depth ($\Delta n_0 f = 0.025$) is close to that of the estimated value of the high-contrast sample.

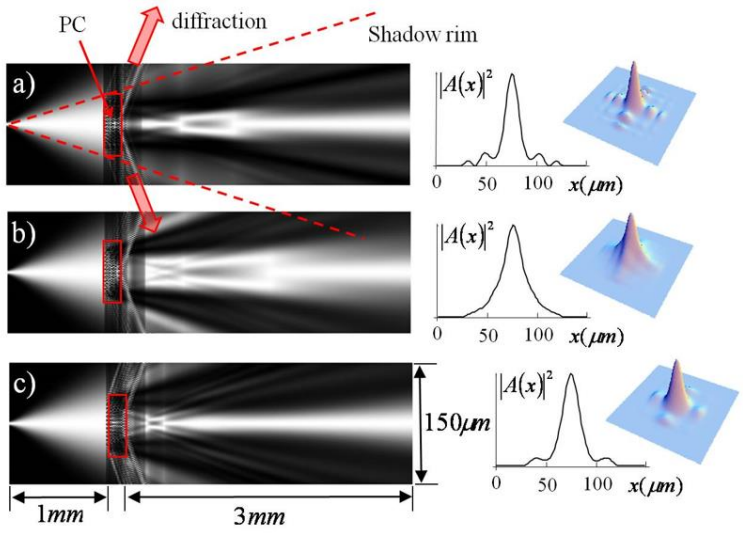

Figure 3.33. Beam propagation inside and behind the PhC as obtained by numerical integration of the paraxial model Eq. (3.7) in 2D. The one-dimensional (1D) profile of beam in the far-field domain and the 2D profile in the far-field domain (as obtained by factorization) are shown on the right. The site of square 2D domain corresponds to the coordinate range in 1D plots. The parameters for (a)–(c) cases correspond to these in Fig. 3.31.

3.5. Beam shaping in 2D metallic Photonic Crystals

The previously described spatial effects such as flat lensing, self-collimation, spatial filtering, etc, can be found not only in dielectric PhCs, but also in Gain or Loss Modulated Materials (GLMM). In such materials only the imaginary part of the complex dielectric constant is modulated, providing additional spatial dispersion properties to the material [Sta09b, Bot10, Kum12, Kum13]. Purely GLMM present sharp peaks or dips in the imaginary part of the spatial dispersion relations, close to the edges of the Brillouin Zone, which cause anisotropic gain or losses [Sta09b, Kum12]. Such anisotropy of the

amplification/attenuation leads to the narrowing of the angular spectrum of propagating radiation with wavevectors close to the edges of the first Brillouin Zone which in turn results in spatial filtering effects.

The most simple approach to the propagation of light beams is a paraxial approximation of the Maxwell Equations, which may be used either for PhCs or GLMMs with low contrast (when the back-reflections are negligible). Hence, the first reported studies on beam shaping effects in GLMM were based on such a paraxial beam propagation model, thereby helping to understand and characterize the effects [Sta06, Sta09b]. More recent analysis have shown the dependence of directional gain and spatial modulation effects on the beam propagation in Loss Modulated Materials (LMM) [Kum12, Kum13].

It has to be taken into account that both PhCs, and GLMMs, are two limiting cases. In general, periodically structured materials show both refractive index and gain/loss variations, since they both are intrinsically related via the Kramers-Kronig relations. Pure index modulations may only occur in the limit when the resonant frequencies of a given material are distant from the considered frequencies whereas purely gain/loss modulations are barely possible exactly at resonance. In actual materials, such extreme cases are never achieved.

The present section is devoted to a detailed analysis of light beam propagation in Metallic Photonic Crystals (MPhCs), consisting of gold cylinders embedded in air, where the modulations of both losses and refractive index are present. We predict that the structure supports non-diffractive (self-collimated) propagation associated to zero diffraction. In this case, the lack of phase shift among transverse modes maintains the beam profile unchanged along the crystal. We also predict flat lensing associated to negative diffraction. In the latter case, the anomalous phase-shifts accumulated within the structure, when compensated by normal diffraction behind the structure, lead to a significant focalization of light beams. While negative diffraction was previously considered in MPhCs [Kal08, Swi11] we note that the purpose here showing its effect on beam propagation, providing a significant focalization. In addition, we numerically demonstrate one more effect: the spatial filtering of noisy beams on

the due to the anisotropic attenuation of light. All predictions are accounted by the spatial dispersion relations and demonstrated by numerical integration of the full set of Maxwell's equations using FDTD method.

3.5.1. MPhC simulations

We consider a 2D periodic structure made of gold cylinders in air as schematically shown in Fig. 3.34(a). The geometry of the structure is defined by the lattice constant a, the angle between two lattice vectors θ, and the radius of the cylinders R, see Fig. 3.34(a). The dielectric constant of gold for frequencies larger than the plasma frequency, ω_p, is estimated by the Drude model, therefore following the expression: $\varepsilon(\omega) = 1 - \omega_p^2/(\omega(\omega - i\gamma))$, where ω is the frequency of light, and γ stands for the collision frequency of gold.

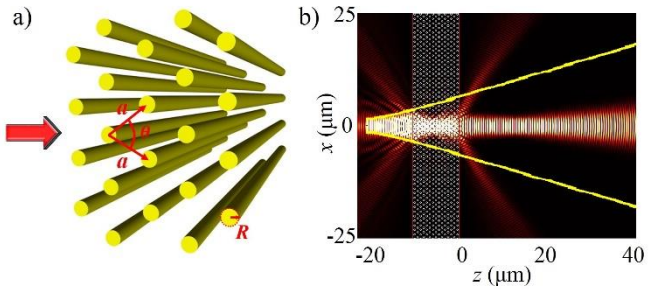

Figure 3.34. (a) Schematic representation of a 2D rhombic periodic array of metallic (gold, ω_p = 12229.7 THz, γ = 139.7 THz) rods in a lattice constant a = 0.83 μm, angle between the lattice vectors $\theta = 75°$ and radius of the rods R = 0.2*a. The red arrow indicates the direction of propagation of the beam. (b) Comparison between a 3 μm-wide Gaussian beam, generated at a distance of 5 μm from the left facet of the structure, and propagated through a MPhC to free space propagation of the same beam (thick yellow curve). The considered MPhC structure has 7-periods in the longitudinal direction z, which corresponds to approximately 10 μm. The frequency of the propagated beam is f = 307 THz, corresponding to a/λ = 0.85.

The input source is a monochromatic Gaussian beam, normally incident on the structure. An example of the field intensity distribution through the crystal and behind it is shown in Fig. 3.34(b), where the yellow curve corresponds to the

contour of reference beam propagated trough air. Therefore, in comparison, a significant focalization of the beam behind the MPhC (at a distance of around 35 μm, in this particular case) can be clearly observed in the figure. The intensity distribution behind the crystal is calculated using paraxial beam propagation to optimize the calculation time. The recorded data (amplitudes and phases) just behind the MPhC (as calculated by FDTD) were used as an input source for the paraxial beam propagation. In the particular case of Fig. 3.34(b), 37% of the input energy reaches the focal point while 15% goes to the sidebands. We choose such a rhombic LMM structure and propagation along the long diagonal, for the strong spatial effects observed, being stronger than for a square geometry.

The expected propagation effects may be explained by the shapes of the spatial dispersion curves (iso-frequency contours). The calculated band diagram and the spatial dispersion for the structure above described are shown in Fig. 3.35. Note that propagation is along the ΓM direction, and that resonance in this direction is around $a/\lambda = 0.83$. Figure 3.35(b) and 3.35(c) shows iso-frequency contours of the bands below and above the band gap, respectively. In Fig. 3.35(b) a flattening of the dispersion isofrequency contours can be observed for $a/\lambda = 0.68$, indicating a non- diffractive propagation inside the MPhC. For higher frequencies, $0.68 < a/\lambda < 0.74$, the dispersion curve becomes convex, which causes the beam to undergo negative diffraction within the MPhC, and focusing behind it. It is interesting to note, that for higher frequencies both scenarios repeat: another zero-diffraction regime and another focusing regime are observed for $a/\lambda > 0.84$. The negative diffraction area in Fig. 3.35(c) is more pronounced and the convex iso-frequency curve covers a larger angular spectrum, indicating a stronger negative diffraction. Note also that a stronger curvature is expected to provide a longer focal distance. However, the second zero-diffraction regime is less visible in simulations due to its narrow angular spectrum. In following, we analyze in detail the most interesting frequency regions of non-diffractive propagation and negative diffraction.

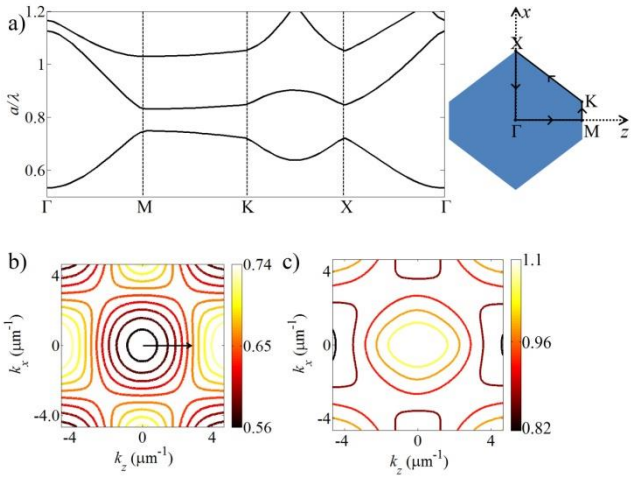

Figure 3.35. (a) Band diagram of the structure described in Fig. 3.33, for the frequency range a/λ = 0.5-1.2. The inset shows the irreducible BZ of the structure. Iso-frequency contours for two consecutive bands (4th and 5th bands): (b) band below the band gap, (c) band above the band gap. The side bar indicates frequency in a/λ units. Propagation is considered in the ΓM direction.

3.5.2. Non-diffractive propagation inside MPhC

Non-diffractive beam propagation inside a MPhC occurs due to in-phase propagation of the involved angular components of the beam. Hence, it is accounted by flat segments of the dispersion curves. The phases of most angular beam components propagate with equal phase velocity, preserving the spatial shape of the beam.

Figures 3.36(a) and (b) show the propagation of two beams within an infinite MPhC, with the same previously considered parameters, for two different frequencies of $a/\lambda = 0.68$ ($f = 246$ THz) –first self-collimation frequency–, and $a/\lambda = 0.79$ ($f = 286$ THz) –close to the second self-collimation frequency–. The intensity is normalized at each cross-section (vertical cross section, $z =$ const.) for a better visualization of the effect since, due to losses and reflections, the beam intensity exponentially decreases in propagation along the structure. Figures 3.36(c) and (d) depict such on-axis beam intensity (horizontal cross section at $x = 0$) in logarithmic scale, for both cases. Finally, in Figs. 3.36(e) and (f), the vertical cross section profiles, at different z positions, confirm that the beam

approximately keeps its width in propagation, exhibiting either no or weak diffraction broadening. The beam profile small variations along the crystal may be attributed to phase shifts of higher spatial harmonics and the slight narrowing along propagation (in Fig. 3.36(a)) to a negative diffusion inside the structured material; also, a slight diffusive broadening is appreciated in Fig. 3.36(b).

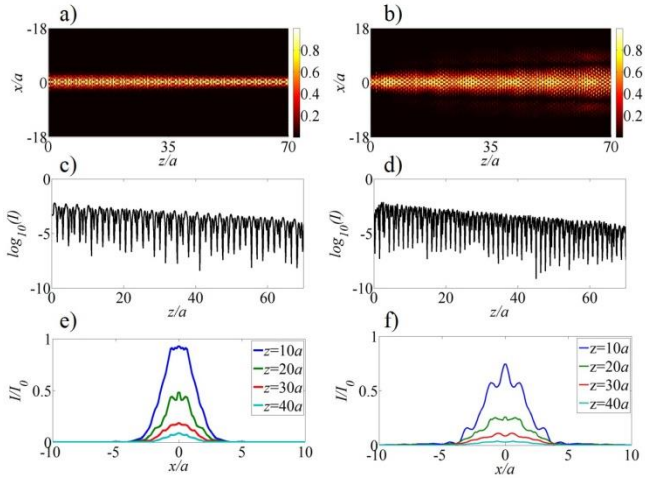

Figure 3.36. Non-diffractive propagation inside an infinite MPhC with the same structural parameters of Fig. 3.33: (a) Normalized intensity profile of the propagated beam in a length of 70a considering an initial beam of width 2.5a. at a./λ = 0.68 and (b) at a./λ = 0.79. Horizontal cross section intensity profile corresponding to x /a = 0 for; (c) a./λ = 0.68, and (d) a./λ = 0.79. (e) Transverse cross section intensity profiles at different propagation distances: z = 10a, 20a, 30 a and 40 a , normalized to the initial intensity, for: (e) a./λ = 0.68 and (f) a./λ = 0.79.

3.5.3. Focusing behind the MPhCs

Next, we analyze Gaussian beams transmitted through a finite MPhC slab. Fig. 3.37 summarizes the focusing properties of the MPhC depending on frequency –for the negative diffraction range within the structure, namely for frequencies slightly above resonance. We clearly observe focalization of the transmitted beams after free propagation in air. Negative diffraction accumulated within the structure by negative spatial dispersion (anomalous or convex curvature of the spatial dispersion) is compensated by positive diffraction

in free space (with normal concave curvature), leading to focalization behind the structure. The focal point corresponds precisely to the position where negative diffraction is compensated by the positive one, and all angular components of the beam are in phase. That is to say, the position of the focal point as well as intensity at this focal point are determined by the curvature of the spatial dispersion, which is strongly frequency dependent, as shown in Figs. 3.37(a) to 3.37(f). The more curved the dispersion segment, the more distant the focal point.

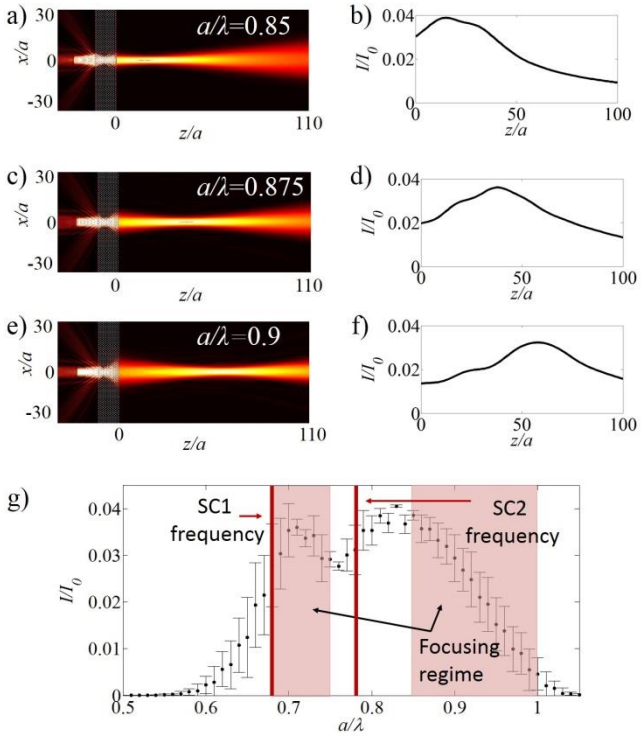

Figure 3.37. Focusing behind MPhC with the same parameters as in Fig. 3.33, for a monochromatic Gaussian beam at different frequencies; a./Λ = 0.85, 0.875, and 0.9 (f = 307, 316, and 325 THz). (a)/(b) –(c)/(d), (e)/(f)– Display the field intensity profile corresponding on-axis intensity (horizontal cross section) in free space propagation behind the structure at the position x = 0, for the first –second and third– frequencies. (g) Maximum intensity (on the right facet or at the focal point) behind the MPhC depending on frequency.

A larger negative diffraction accumulated within the structure, requires a longer propagation distance to compensate it by positive diffraction in a homogeneous material. The convexly curved spatial dispersion segments and corresponding frequencies can be determined from the calculation of the spatial dispersion curves (Fig. 3.35). As expected, FDTD calculations confirm that focalization is observed precisely at frequencies for which negative diffraction occurs in the structure, which are frequencies close to resonance. The focal position in Figs. 3.37(a), (c) and (e) can be clearly identified with the maximum of the on-axis horizontal cross section of the corresponding beam intensity behind the structure, depicted in Figs. 3.37(b), (d) and (f), normalized to the intensity of the initial beam. As expected in this case, higher frequencies correspond to larger focal distances as the curvature of dispersion line increases.

The maximum intensity of the transmitted beam,–calculated either at the focal point or just on the right facet of the MPhC slab, as a function of frequency, is summarized in Fig. 3.37(g) – normalized to the intensity of the incident beam. The highest intensities obtained around $a/\lambda = 0.7$ and at $a/\lambda = 0.85$ can be attributed to two different situations. On one hand, $a/\lambda = 0.68$ the non-diffractive, non-spreading, propagation along the crystal (Fig. 3.36(a)) provides a high transmission just at the crystal output. Hence, since below $a/\lambda = 0.68$, the beam rapidly spreads in air due to normal diffraction the maximum intensity is found just at the output. On the other hand, for $a/\lambda = 0.85$ a focusing regime is found and intensity at focus reduces as frequency increasing due to the width of isofrequency contours which limits focusing to a few angular beam components. Finally, in the ranges $0.68 < a/\lambda < 0.74$ another negative diffraction regime occurs.

In order to analyze in detail the focusing performance of the MPhC structure, we scan the frequencies ranging from 0.5 to 1.2 (frequency is normalized to a/λ, corresponding to 181 to 434 THz). The numerical results are summarized in Figs. 3.38(a) and 3.38(b). The clear dependence on frequency of the output intensity profile along the longitudinal plane is demonstrated in Fig. 3.38(a). As predicted, the existence of intensity maxima is evident for frequencies corresponding to the negative diffraction range (a/λ=0.6-1.0) Moreover, such

intensity maxima, determining the focal position of the beam, move away from the structure when frequency increases. This dependence of the focal distance on frequency, is correctly predicted by the different curvatures of spatial dispersion curves for every given frequency (Fig. 3.35). Additionally, Fig. 3.38(b) shows the position of the minimum beam width depending on frequency.

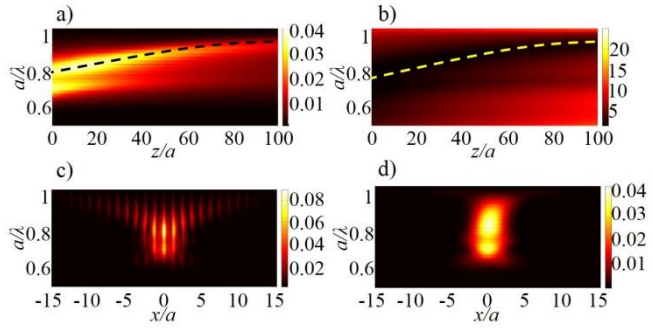

Figure 3.38. (a) Normalized intensity distribution along the horizontal axis, z, depending on frequency. The focal distance from the MPhC is indicated by a dark dashed line, for a/λ >0.8. (b) Beam width depending on frequency along z, normalized to the incident beam width W_0 (where W_0 = 3.6a, being a the lattice constant). The bright dashed line indicates the position of the smallest beam width. The normalized intensity maps at z/a = 0, i.e at the exit face of the device and at the focal plane depending on frequency is depicted in (c) and (d).

Inspecting in more detail Figs 3.38(a) and (b) we again appreciate the two key frequency ranges. One, around *a*/λ=0.68 which corresponds to a collimated propagation of the beam inside the structure. Another, ranging from *a*/λ=0.85 (just above resonance) above where a frequency band gap is obtained (Fig. 3.35(a)), although not clearly observed from these maps. Figures 3.38(c) and (d) supply supplementary information; Fig. 3.38(c) represents the intensity profile in the transversal plane and depending on frequency, just at the output of the crystal, while Fig. 3.38(d) corresponds to the same intensity profile at the minimum beam width position, behind the crystal and normalized to the profile obtained in Fig. 3.38(c). This last figure, exhibits again the focusing frequency ranges (*a*/λ =0.68-0.74 and *a*/λ = 0.85-1.0).

Finally, to deeper analyze these results we determine the normalized beam widths behind the MPhC for different frequencies, at planes with the narrowest profile (Fig. 3.39(a)). We study the MPhC performance by varying initial beam widths. Fig. 3.39(b) indicates the positions of the smallest beam widths behind the PhC depending on frequency. From these two plots the behavior of focusing can be interpreted in the region of a/λ=0.85-1.0, i.e., the beam profile at the focal point has a similar beam width as the initial beam and the focus moves away when frequency increases.

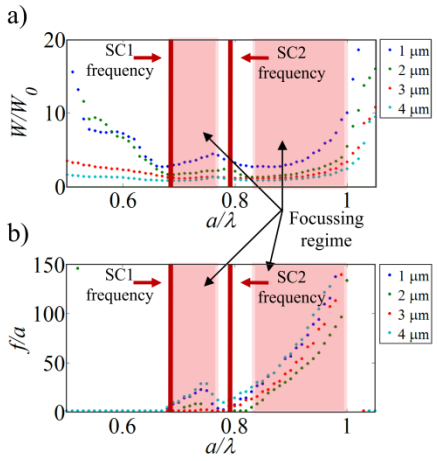

Figure 3.39. Cross sectional widths of the beams at the plane of minimum width along propagation plotted as a function of frequency for different initial beam widths, as indicated in the legend. (a) Beam width normalized to the initial beam and (b) focal distance. All normalized to the lattice constant, a.

3.5.4. Spatial filtering using MPhCs

As above discussed, the curvature of the iso-frequency curves defines the focal distance. Besides, the size of the isofrequency contour itself is also important: the smaller it is, the smaller the angular range of beams components is affected. Hence less beam components can be focused or, eventually, propagated through the structure. In other words, the size of the isofrequency curves determines the spatial (angular) filtering of the structure. Therefore,

either narrow or noisy beams exhibiting an angular spectrum broader than the corresponding contour, will be spatially (angularly) filtered while propagating trough the structure.

Indeed, Fig. 3.39(a) indicates that the focusing performance of narrower beams is weaker than for broader ones. This can be seen as a signature of spatial filtering in a MPhC. The narrower is the beam, the broader is the angular range of spatial components which are filtered out, and hence the focal width of the transmitted beam is broader.

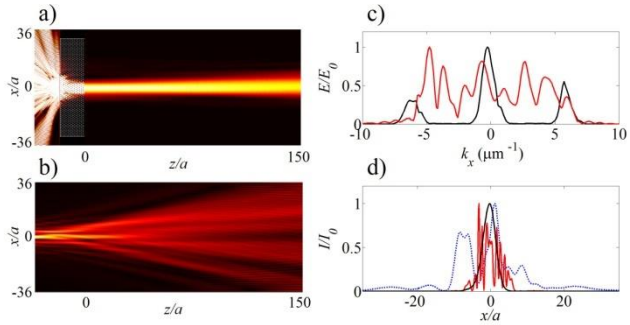

Figure 3.40. (a) Propagation of a random input beam in a MPhC and behind it with frequency a/λ = 0.76. (b) The propagation of the same random input beam in free space without the MPhC structure. (c) Fourier spectra of the input beam (red, solid) and the Fourier spectra of the beam after propagation through a MPhC (black, solid). The normalized intensity profiles of the same are denoted in (d). The dotted blue curve denotes the intensity profile of the beam in the absence of MPhC.

To show the functionality of spatial filtering we analyze the transmission of noisy beams by a MPhC. The noise is introduced by propagation of Gaussian beams through random diffusers. Fig. 3.40(a) and (b) show the transmission of such a randomized beam compared to its free space propagation. It is clear that after propagation trough the structure the spatial quality of the beam increases significantly. Actually, it is evident from the Fourier spectra of the input and output beams, shown in Fig. 3.40(c). The spatial Fourier spectrum of the filtered beam is narrower with shifted sidebands depending on the crystal periodicity. The filtered beam displays a smooth shape after propagation trough the MPhC,

as shown in Fig. 3.40(c). Finally, the intensity width profile of the filtered beam is comparable to the input noisy beam, while the reference free propagated beam becomes broader.

3.6. Conclusions

We investigated beam shaping effects by a rhombic 2D PhC made of dielectric rods embedded in air. For given frequencies, we observe a clear focalization of the beams behind a thin flat PhC slab. It is shown that the focalization is accounted by negative diffraction propagation inside the crystals, with convex spatial dispersion segments, and then compensated in free space up to focus. Moreover, we prove that the dependence of the focal position on frequency is clearly explained by the curvature of the spatial dispersion segments. In addition, we observe a clear double focusing effect for several ranges of frequencies in the first and higher order bands. It is shown, that the double focusing effect arises due to the overlap of photonic bands (for a single frequency), which mutually display convex shapes of spatial dispersion with different curvatures. We proved that this leads to the appearance of two focuses with different focal distances. Additionally, non-diffractive propagation through the structure is demonstrated; the spatial shape of the beams remains constant while propagation within the structure due to flat segments of the spatial dispersion curve. We would like to notice as well that, for the studied case, beam propagation behavior with increasing frequency evolves in the same manner both for lower and higher order bands: for frequencies beyond the corner of the Brillouin Zone we find the self-collimation region, which afterwards is followed by the focusing effect. The focal position tends to shift away from the PhC with increasing frequency.

We have also reported the first (to our knowledge) experimental confirmation of beam focusing at visible frequencies by a flat 3D woodpile PhC, which was fabricated by direct femtosecond laser writing technique. The results show a convincing flat lensing with focal distances of around 50–70 μm behind the crystal. No focusing appears at other wavelengths, excluding all possible geometrical focusing effects (e.g., due to possibly curved surfaces of the woodpile). The observations are in good correspondence with the 2D FDTD simulations and the flat lensing effect is successfully explained by convex spatial dispersion curvatures, which were predicted by analytical results of mode expansion and calculated by the PWE method.

Additionally, we have reported experimental evidence of the formation of well-collimated optical beams from initially diverging beams by a 3D PhC at visible wavelengths. The collimation was achieved using a low-refractive-index modulation PhC structure facilitated by direct femtosecond laser writing technique. We have interpreted the results by the theoretical analysis which indicates that origin of the observed collimation is anomalous spatial dispersion (convexly curved spatial dispersion). The theoretical model was validated by good qualitative agreement between the results of numerical simulations based on the integration of a paraxial model and the experimental data. It is important to achieve near resonance condition $|\Delta Q_z| \ll 0$ (close to the Brillouin zone boundary), where collimation can occur for both negative $(Q_z < 0)$ and positive $(Q_z > 0)$ detuning. However, even small variations of these parameters lead to complicated and not fully understandable variation of the collimated beam quality. A better theoretical understanding and experimental optimization of the beam collimation will require careful theoretical and numerical studies in the future.

Furthermore, we have investigated beam shaping effects by a rhombic 2D periodic structure made of gold cylinders embedded in air. For given frequencies, we have observed a clear focalization of the beams behind a thin flat MPhC slab. It has been shown that the focalization is accounted by negative diffraction propagation inside the crystals, which is then compensated in free space up to

focus. In addition, we have proven that the dependence of the focal position on frequency is clearly explained by the convex curvature of the spatial dispersion segments. Moreover, non-diffractive propagation through the structure has been demonstrated. Finally, we have investigated on the spatial filtering performance with this same structure. We have shown that high spatial Fourier harmonics of a noisy beam are removed by propagation through the MPhC, leading to an improvement of its spatial quality. The focusing performance of narrower beams is weaker than for broader ones. While the drawback of metal structures are losses, as part of light is absorbed, we point out that they provide new perspectives in light manipulation on the micrometer scale. MPhCs are miniaturized devices which give spatial control over beam propagation and their study may be important either from fundamental point of view as well as for applications.

Finally, we note that physical mechanisms of beam formation outlined in the studies in this chapter are quite general and thus are applicable to a broader class of waves in periodic structures, such as acoustic waves in sonic crystals, or exciton and surface polariton wave beams. These principles may contribute to the development of new types of compact, misalignment-tolerant beam collimators and shapers.

Chapter 4

General conclusions and outlook

In this last chapter, we will briefly summarize the main results that we have presented in this PhD thesis, remarking possible future perspectives.

In this thesis several beam shaping effects that may appear when light propagates within different PhC structures have been studied, both experimentally and theoretically: including spatial filtering in gapless configuration, improvement of spatial filtering by adding chirp, flat lensing in high order bands, double focusing, collimation, super-collimation, etc. The majority of the studied phenomena can be explained by the anomalous shapes and bends of spatial dispersion curves, and most of them have been proved by experimental results, which fit well with the analytical and numerical predictions.

Before describing in detail each of the studied effects, in Chapter 1 we have presented an overview of the general properties of PhCs (starting with the analogy between PhCs and crystalline solids, also showing the presence of PhCs in nature). We have introduced basic concepts such as dimensionality, lattice or

band gap. We have also presented Maxwell's equations for the propagation of waves in periodic materials, followed by the explanation of the PWE method, which is broadly used to calculate temporal and spatial dispersions. Indeed, this chapter was significantly devoted to explain and distinguish the concepts of temporal and spatial dispersion. Thus, examples of temporal dispersion phenomena such as frequency BGs are described, while introducing the concepts of linear defects and chirp. On the other hand, spatial-dispersion-related effects are explained: negative refraction, super-prism, flat lensing, super-lensing, negative diffraction, self-collimation, spatial filtering, etc. These phenomena directly lead to the understanding of the effects studied in this thesis. We give an overview on the coupled-mode and the scattering matrix methods, used to find the transmission and reflection spectra of PhCs.

In Chapter 2 we have studied the effect of spatial filtering in gapless PhCs. Firstly, the definition, importance and usage of traditional spatial filtering have been explained. The common techniques to obtain spatial filtering have been described and, alternative methods have been mentioned. One of these alternative methods is spatial filtering with PhCs. In Section 2.1 we have presented the mechanisms of spatial filtering with PhCs and overviewed the state of the art in the field.

In Section 2.2 we have experimentally proved the effect of the spatial filtering of light beams in the gapless configuration of a PhC, which was firstly theoretically predicted in [Sta09]. We have applied our theoretical-numerical analysis to obtain realistic parameters of the system to result in spatial filtering effect. The simulated PhC was fabricated applying tight femtosecond laser pulses to periodically change refractive index in fused silica glass. The structure used for measurement resulted in a 3D PhC with low refractive index contrast $\Delta n \sim 10^{-3}$. The proof of the effect consisted in the modification of angular spectrum of the beam through the propagation inside the PhC. It resulted in the way that particular angular components, selected by the geometry factor of the structure, were removed from the central part of the beam and were deflected into the first

order diffraction maximum. Experimental observations were in a good agreement with the theoretical-numerical predictions.

The reported effect of spatial filtering is relatively weak and carries a demonstrational character only. Therefore, we have proceeded with theoretical-numerical studies looking for the possible ways to enhance it. We found that the increase of the refractive index contrast (of the order of $\Delta n \sim 10^{-2}$) significantly improves spatial filtering. Moreover, we noticed that introduction of chirp into the structure with the same refractive index contrast of PhC reported in Section 2.2, contributes to the enhancement of the effect. Therefore, we have studied the chirp influence on the performance of spatial filtering. The results are presented in Section 2.3. The analysis consists of numerical simulations of the structure with realistic parameters for which the optimum filtering has been found. The 2D PhCs, according to simulated parameters, were fabricated applying the same method as described in Section 2.2, which resulted in the same refractive index contrast. The experimental demonstration of the constructive role of the chirp for improvement of spatial filtering was convincingly shown.

In Section 2.4 we have advanced the PhC geometry into axisymmetric micro structure, which consists of concentric circles in every of its layer. We have predicted that, with such kind of structure, it is possible to obtain axisymmetric spatial filtering (which was not possible with the geometries of the structures described in Section 2.2. and Section 2.3). The fabrication process and obtained refractive index contrast was the same as described in previous sections of Chapter 2. The geometry parameters were designed according to the optimum numerical simulation results. The effect was proved experimentally and results were in good correspondence with our theoretical-numerical predictions. In addition, we have numerically study the influence of chirping of the axisymmetric microstructure on the spatial filtering efficiency, which proved to be significantly positive. In the future plans, we consider fabricating chirped axisymmetric structures and prove its influence to achieve efficient axisymmetric spatial filtering.

In Section 2.5 we have presented the super-collimation effect obtained by axisymmetric micro structures. While numerically analyzing axisymmetric spatial filtering effect, we have noticed that, for particular parameters of the structure, the intensity of the central part of the beam in the far field domain can raise significantly. The raise of intensity compared to the reference beam for some parameter range is more than 20 times. We have fabricated axisymmetric structures (the same process as in Section 2.4) and proved super-collimation effect experimentally. The experimentally obtained enhancement of intensity was around 7 times (due to experimental deviation from numerical results, most likely caused by spherical aberrations during fabrication process) and the angular distribution of super-collimated beam was around 20 mrads. We interpret the effect in terms of diffusion of the radiation in the far field domain, during the forward-backward diffractive scattering cascade.

We want to highlight the advantage of the novel method of filtering demonstrated in the Chapter 2. The main advantages, comparing with the conventional pinhole spatial filer, are: 1) extremely small thickness (hundreds of microns) enabling the integration of such a filter into micro-optical devices or into micro resonators of small lasers; 2) translational invariance of the PhC spatial filter (insensitivity to the lateral shift of PhC-structure) simplifying its utilization (however this advantage is no longer valid for the axisymmetric crystal case); 3) possibility to combine (to add) the filtering functionality to some other, already existing, functionalities (amplification, nonlinearities) in the bulk material, by additional modulation of the refractive index of the (amplifying or nonlinear) material.

In Chapter 3 we have studied beam shaping effects by PhCs due to the anomalous spatial dispersion. In particular, we have concentrated on the effect of flat lensing behind the PhC, which we proved to arise due negative diffraction inside the structure which is governed by the convex shape of spatial dispersion. In the Section 3.1, we have overviewed the state of the art of the flat lensing effects (the working principle was explained in Chapter 1).

In Section 3.2 we have considered a 2D PhC of a rhombic lattice, which is made from dielectric rods embedded in air. We have proceeded with numerical simulations, where for given frequencies, we observed a clear focalization of the beams behind the structure. We have shown that the effect arise due to the convex spatial dispersion segments. In addition we have demonstrated that the focal position behind the structure depends on frequency. This dependence was accounted due to the different strengths of the curvatures for distinct frequencies. We have identified that, the focal position tends to shift away from the PhC with increasing frequency. Furthermore, the clear double focusing effect has been observed for particular ranges of frequencies. It has been shown that the double focusing effect arises due to the overlap of photonic bands (for a single frequency), which mutually display convex shapes of spatial dispersion with different curvatures, leading to the different focal distances for the same frequency. Moreover, we have demonstrated the non-diffractive propagation through the structure. A particular behavior of the beam propagation has been observed: for frequencies beyond the corner of the Brillouin Zone, firstly appears the self-collimation region, which afterwards, with increasing frequencies is followed by the focusing effects. The tendency repeats for higher order bands.

In Section 3.3., we have studied the flat lensing effect in high order bands of the PhC. We have applied the mode expansion analysis with realistic parameters of the structure, which predicted focusing behind a flat PhC. The prediction was based on the obtained convex shapes of spatial dispersion, which cause negative diffraction of the beam that, due to the compensation of positive and negative diffraction effects, leads to focusing behind the PhC. The convexly shaped spatial dispersion curves were, for particular cases, verified by the PWE method. The structure considered in simulations was a 3D woodpile, which due to its geometry was simplified to 2D profiles. The analytical predictions were obtained using the PWE method, as well as, numerical simulations performed by the FDTD method. The FDTD simulations have shown a clear focusing effect in visible frequencies. According to these results, a 3D polymer based woodpile PhC (refractive index contrast of the structure $\Delta n = 0.5$) has been fabricated by direct laser writing

technique. The experimental results have confirmed the existence beam focusing at visible regime and they were in good correspondence the 2D FDTD simulations. The reported focal distances were of around 50–70 μm behind the structure. No focusing appears at other wavelengths, excluding all possible geometrical focusing effects (e.g., due to possibly curved surfaces of the woodpile). To the best of our knowledge, this is the first confirmation of flat lensing by PhCs in the visible regime.

In Section 3.4, we have studied the beam collimation effect behind the 3D polymer based woodpile PhC at visible wavelengths. We have experimentally recorded the formation of well-collimated optical beams from initially diverging beams, for moderate and low-refractive index contrasts of the structure. The PhC was fabricated by the direct femtosecond laser writing technique. The experimental results have been interpreted by the theoretical mode expansion analysis, which indicates that origin of the observed collimation is anomalous spatial dispersion (convexly curved segments). Numerical simulations based on the integration of a paraxial model have proven the beam collimation effect behind the structure with the parameters predicted in the theoretical model. However, even small variations of these parameters lead to complicated and not fully understandable variation of the collimated beam quality. Therefore, for the future studies a better theoretical understanding and experimental optimization of the beam collimation effect is needed.

In the Section 3.5, we study light beam propagation in MPhCs, which is different from the previous studies because it is a non-conservative system. We numerically (by the FDTD method) proved that the ideas implemented for dielectric PhCs can be exported to similar lossy systems as MPhCs. In particular, we have investigated beam shaping effects by a rhombic 2D periodic structure made of gold cylinders embedded in air. We have observed a clear focalization of the beams behind the structure, which we have shown to appear due to the convex curvature of spatial dispersion. Moreover, we have demonstrated the dependence of the focal point position on the frequency, which was accounted due to the different strengths of the convex curvatures of spatial dispersion for

different frequencies. In addition, we have analyzed non-diffractive propagation inside the MPhC, where it was accounted due to the flat segments of dispersion. Finally, the investigation of spatial filtering performance by the structure have been done. The substantial improvement of the beam spatial quality has been demonstrated due to the removal of the spatial Fourier harmonics of a noisy beam through the propagation in the MPhC. While the drawback of metal structures are losses, as part of light is absorbed, we point out that they provide new perspectives in light manipulation on the micrometer scale. MPhCs are miniaturized devices which give spatial control over beam propagation and their study may be important either from fundamental point of view as well as for applications.

Future work

In order to obtain a technologically useful spatial filter, higher (but moderate) index contrast PhCs are necessary. These PhCs can be constructed using new materials and fabrication technologies. A technologically relevant spatial filtering, allowing us to improve the beam quality parameter by the factor of 2–3, requires the refractive index modulation of order of approximately $\Delta n_0 \approx 10^{-2}$. Therefore, materials like polymers or gels are planned to be investigated for improvement of the effect.

Moreover, the periodic modulation to obtain spatial filtering effect can be applied not only in dielectric materials, but in amplifying media as well. A particularly interesting case is broad emission lasers, which are compact, energetically efficient devices, but with very low spatial beam quality. Periodic modulation of amplifying media of broad emission lasers could lead to significantly improved spatial beam quality.

Additionally, we have numerically demonstrated double focusing effect in 2D PhC in near the IR regime. The effect has never yet been shown experimentally at frequencies around visible regime. Therefore, we are planning

to fabricate samples corresponding to presented numerical parameters and we expect to show the effect experimentally.

Another perspective of the future work is possibility to add nonlinearities in PhCs, for example, by filling air gaps of woodpile structure with liquid crystals. By doing this, the effects of spatial filtering or flat lensing could be tunable. For example, due to nonlinearities the refractive index contrast of the PhC can be tuned due to variation of beam intensity, or voltage, etc., consequently, the change of refractive index contrast would modify the spatial filtering properties of the PhC. In addition, it could tune the focal position behind the structure. These are very interesting effects, and the studies are planned for the future.

Finally, we note that physical mechanisms of beam formation outlined in the thesis are quite general and thus are applicable to a broader class of waves in periodic structures, such as acoustic waves in sonic crystals, or exciton and surface polariton wave beams. These principles may contribute to the development of new types of compact, misalignment-tolerant beam collimators and shapers.

Bibliography

[Arm12] S. Armstrong. *Plasmonics: diffraction-free surface waves*. Nature Photonics **6**, 720 (2012).

[Asa04] T. Asano, K. Kiyota, D. Kumamoto, B.-S. Song, and S. Noda. *Time-domain measurement of picosecond light-pulse propagation in a two-dimensional photonic crystal-slab waveguide*. Applied Physics Letters **84**, 4690 (2004).

[Ash76] N. W. Ashcroft and N. D. Mermin. *Solid state physics*. (Cengage Learning, 1976).

[Aug05] M. Augustin, R. Iliew, C. Etrich, D. Schelle, H.-J. Fuchs, U. Peschel, S. Nolte, E.-B. Kley, F. Lederer, and A. Tünnermann. *Self-guiding of infrared and visible light in photonic crystal slabs*. Applied Physics B **81**, 313 (2005).

[Bab04] T. Baba, D. Mori, K. Inoshita, and Y. Kuroki. *Light localizations in photonic crystal line defect waveguides*. IEEE Journal of Selected Topics in Quantum Electronics **10**, 484 (2004).

[Bab08] T. Baba. *Slow light in photonic crystals*. Nature Photonics **2**, 465 (2008).

[Ber04] A. Berrier, M. Mulot, M. Swillo, M. Qiu, L. Thylén, A. Talneau, and S. Anand. *Negative refraction at infrared wavelengths in a two-dimensional photonic crystal*. Physical Review Letters **93**, 073902 (2004).

[Ber11] M. Beresna, M. Gecevičius, P. G. Kazansky, and T. Gertus. *Radially polarized optical vortex converter created by femtosecond laser nanostructuring of glass*. Applied Physics Letters **98**, 201101 (2011).

[Bot10] M. Botey, R. Herrero, and K. Staliunas. *Light in materials with periodic gain-loss modulation on a wavelength scale*. Physical Review A **82**, 013828 (2010).

[Bra10] P. Brady and M. Cummings. *Differential response to circularly polarized light by the jewel scarab beetle chrysina gloriosa*. The American Naturalist **175**, 614 (2010).

[Bro99] J. Broeng, D. Mogilevstev, S. E. Barkou, and A. Bjarklev. *Photonic*

crystal fibers: A new class of optical waveguides. Optical Fiber Technology **5**, 305 (1999).

[Cas14] M. Castellanos Muñoz, A. Y. Petrov, L. O'Faolain, J. Li, T. F. Krauss, and M. Eich. *Optically induced indirect photonic transitions in a slow light photonic crystal waveguide*. Physical Review Letters **112**, 053904 (2014).

[Ceb12] A. Cebrecos, V. Romero-Garcia, R. Pico, I. Perez-Arjona, V. Espinosa, V. J. Sanchez-Morcillo, and K. Staliunas. *Formation of collimated sound beams by three-dimensional sonic crystals*. Journal of Applied Physics **111**, 104910 (2012).

[Che04] L.-S. Chen, C.-H. Kuo, and Z. Ye. *Acoustic imaging and collimating by slabs of sonic crystalsmade from arrays of rigid cylinders in air*. Applied Physics Letters **85**, 1072 (2004).

[Che07] J. Chen, W. Jiang, X. Chen, L. Wang, S. Zhang, and R. T. Chen. *Holographic three-dimensional polymeric photonic crystals operating in the 1550 nm window*. Applied Physics Letters **90**, 093102 (2007).

[Chi03] D. Chigrin, S. Enoch, C. Sotomayor Torres, and G. Tayeb. *Self-guiding in two-dimensional photonic crystals*. Optics Express **11**, 1203 (2003).

[Col01] V. L. Colvin. *From opals to optics: Colloidal photonic crystals*. MRS Bulletin **26**, 637 (2001).

[Col10] E. Colak, A. O. Cakmak, A. E. Serebryannikov, and E. Ozbay. *Spatial filtering using dielectric photonic crystals at beam-type excitation*. Journal of Applied Physics **108**, 113106 (2010).

[Cre99] R. F. Cregan, B. J. Mangan, J. C. Knight, T. A. Birks, P. S. J. Russell, P. J. Roberts, and D. C. Allan. *Single-mode photonic band gap guidance of light in air*. Science **285**, 1537 (1999).

[Cub03] E. Cubukcu, K. Aydin, E. Ozbay, S. Foteinopoulou, and C. M. Soukoulis. *Electromagnetic waves: Negative refraction by photonic crystals*. Nature **423**, 604 (2003).

[Cum11] B. P. Cumming, A. Jesacher, M. J. Booth, T. Wilson, and M. Gu. *Adaptive aberration compensation for three-dimensional micro-fabrication of photonic crystals in lithium niobate*. Optics Express **19**, 9419 (2011).

[Dai12] R. Dai, S. Chen, Z. Ren, Z. Wang, and D. Liu. *Defect modes in silver-doped photonic crystals made by holography using dichromated gelatin*. Applied Physics B **109**, 15 (2012).

[Dav96] K. M. Davis, K. Miura, N. Sugimoto, and K. Hirao. *Writing waveguides in glass with a femtosecond laser*. Optics Letters **21**, 1729 (1996).

[Den71] E. Denton. *Reflectors in fishes*. Scientific American **224**, 64 (1971).

[Det84] L. Dettwiller and P. Chavel. *Optical spatial frequency filtering using interferences*. Journal of the Optical Society of America A **1**, 18 (1984).

[Deu04] M. Deubel, G. von Freymann, M. Wegener, S. Pereira, K. Busch, and C. M. Soukoulis. *Direct laser writing of three-dimensional photonic-crystal templates for telecommunications*. Nature Materials **3**, 444

(2004).

[Don11] G. Y. Dong, J. Zhou, X. L. Yang, and L. Z. Cai. *Dual-negative refraction in photonic crystals with hexagonal lattices*. Optics Express **19**, 12119 (2011).

[Dow94] J. P. Dowling and C. M. Bowden. *Anomalous index of refraction in photonic bandgap materials*. Journal of Modern Optics **41**, 345 (1994).

[Esp07] V. Espinosa, V. J. Sánchez-Morcillo, K. Staliunas, I. Pérez-Arjona and J. Redondo. *Subdiffractive propagation of ultrasound in sonic crystals*. Physical Review B **76**, 140302 (2007).

[Fab06] N. Fabre, S. Fasquel, C. Legrand, X. Mélique, M. Muller, M. François, O. Vanbésien and D. Lippens. *Towards focusing using photonic crystal flat lens*. Opto-Electronics Review **14**, 225 (2006).

[Fei05] M. W. Feise, I. V. Shardrivov, and Y. Kivshar. *Bistable diode action in left-handed periodic structures*. Physical Review E **71**, 037602 (2005).

[Fer95] M. E. Fermann, K. Sugden, and I. Bennion. *High-power soliton fiber laser based on pulse width control with chirped fiber bragg gratings*. Optics Letters **20**, 172 (1995).

[Fin06] C. E. Finlayson, F. Cattaneo, N. M. B. Perney, J. J. Baumberg, M. C. Netti, M. E. Zoorob, M. D. B. Charlton, and G. J. Parker. *Slow light and chromatic temporal dispersion in photonic crystal waveguides using femtosecond time of flight*. Physical Review E **73**, 016619 (2006).

[Fot03] S. Foteinopoulou, E. N. Economou, and C. M. Soukoulis. *Refraction in media with a negative refractive index*. Physical Review Letters **90**, 107402 (2003).

[Fro13] A. Frölich, J. Fischer, T. Zebrowski, K. Busch, and M. Wegener. *Titania woodpiles with complete three-dimensional photonic bandgaps in the visible*. Advanced Materials **25**, 3588 (2013).

[Gal10] J. W. Galusha, L. R. Richey, M. R. Jorgensen, J. S. Gardner, and M. H. Bartl. *Study of natural photonic crystals in beetle scales and their conversion into inorganic structures via a sol-gel bio-templating route*. Journal of Materials Chemistry **20**, 1277 (2010).

[Gat08] R. R. Gattass and E. Mazur. *Femtosecond laser micromachining in transparent materials*. Nature Photonics **2**, 219 (2008).

[Ger05] H. Gersen, T. J. Karle, R. J. P. Engelen, W. Bogaerts, J. P. Korterik, N. F. van Hulst, T. F. Krauss, and L. Kuipers. *Real-space observation of ultraslow light in photonic crystal waveguides*. Physical Review Letters **94**, 073903 (2005).

[Grb04] A. Grbic and G. V. Eleftheriades. *Overcoming the diffraction limit with a planar left-handed transmission-line lens*. Physical Review Letters **92**, 117403 (2004).

[Gru96] U. Grüning, V. Lehmann, S. Ottow, and K. Busch. *Macroporous silicon with a complete two-dimensional photonic band gap centered at 5 μm*. Applied Physics Letters **68**, 747 (1996).

[Har96] P. Hariharan. *Optical holography: Principles, techniques and*

applications. (Cambridge University Press, 1996).

[Hau83] H. Haus and L. Molter-Orr. *Coupled multiple waveguide systems*. IEEE Journal of Quantum Electronics **19**, 840 (1983).

[Hil94] K. O. Hill, K. Takiguchi, F. Bilodeau, B. Malo, T. Kitagawa, S. Thériault, D. C. Johnson, and J. Albert. *Chirped in-fiber bragg gratings for compensation of optical-fiber dispersion*. Optics Letters **19**, 1314 (1994).

[Ho90] K. M. Ho, C. T. Chan, and C. M. Soukoulis. *Existence of a photonic gap in periodic dielectric structures*. Physical Review Letters **65**, 3152 (1990).

[Hou03] A. A. Houck, J. B. Brock, and I. L. Chuang. *Experimental observations of a left-handed material that obeys snell's law*. Physical Review Letters **90**, 137401 (2003).

[Ili04] R. Iliew, C. Etrich, U. Peschel, F. Lederer, M. Augustin, H.-J. Fuchs, D. Schelle, E.-B. Kley, S. Nolte, and A. Tünnermann. *Diffractionless propagation of light in a low-index photonic-crystal film*. Applied Physics Letters **85**, 5854 (2004).

[Ino02] K. Inoue, N. Kawai, Y. Sugimoto, N. Carlsson, N. Ikeda, and K. Asakawa. *Observation of small group velocity in two-dimensional algaas-based photonic crystal slabs*. Physical Review B **65**, 121308 (2002).

[Iye03] A. Iyer, P. Kremer, and G. Eleftheriades. *Experimental and theoretical verification of focusing in a large, periodically loaded transmission line negative refractive index metamaterial*. Optics Express **11**, 696 (2003).

[Jia05] S. Jiang, Y. Liu, G. Liang, and H. Wang. *Design and fabrication of narrow-frequency sharp angular filters*. Applied Optics **44**, 6353 (2005).

[Jia06] S. Jiang, J. Li, J. Tang, and H. Wang. *Multi-channel and sharp angular spatial filters based on one-dimensional photonic crystals*. Chiese Optics Letters **04**, 605 (2006).

[Joa08] J. D. Joannopoulos. *Photonic crystals: Molding the flow of light*. (Princeton University Press, 2008).

[Joh87] S. John. *Strong localization of photons in certain disordered dielectric superlattices*. Physical Review Letters **58**, 2486 (1987).

[Juo11] S. Juodkazis, L. Rosa, S. Bauerdick, L. Peto, R. El-Ganainy, and S. John. *Sculpturing of photonic crystals by ion beam lithography: Towards complete photonic bandgap at visible wavelengths*. Optics Express **19**, 5802 (2011).

[Kal08] M. A. Kaliteevski, S. Brand, J. Garvie-Cook, R. A. Abram, and J. M. Chamberlain. *Terahertz filter based on refractive properties of metallic photonic crystal*. Optics Express **16**, 7330 (2008).

[Kam04] M. Kamata and M. Obara. *Control of the refractive index change in fused silica glasses induced by a loosely focused femtosecond laser*. Applied Physics A **78**, 85 (2004).

[Kat96] J. Kato, I. Yamaguchi, and H. Tanaka. *Nonlinear spatial filtering with a dye-doped liquid-crystal cell*. Optics letters **21**, 767 (1996).

[Ke05] M. Ke, Z. Liu, C. Qiu, W. Wang, J. Shi, W. Wen, and P. Sheng. *Negative-refraction imaging with two-dimensional phononic crystals*. Physical Review B **72**, 064306 (2005).

[Kim07] M.-W. Kim, S.-G. Lee, T.-T. Kim, J.-E. Kim, H. Y. Park, and C.-S. Kee. *Experimental demonstration of bending and splitting of self-collimated beams in two-dimensional photonic crystals*. Applied Physics Letters **90**, 113121 (2007).

[Kni98] J. C. Knight, J. Broeng, T. A. Birks, and P. S. J. Russell. *Photonic band gap guidance in optical fibers*. Science **282**, 1476 (1998).

[Koe03] A. F. Koenderink and W. L. Vos. *Light exiting from real photonic band gap crystals is diffuse and strongly directional*. Physical Review Letters **91**, 213902 (2003).

[Kos98] H. Kosaka, T. Kawashima, A. Tomita, M. Notomi, T. Tamamura, T. Sato, and S. Kawakami. *Superprism phenomena in photonic crystals*. Physical Review B **58**, R10096 (1998).

[Kos99a] H. Kosaka, T. Kawashima, A. Tomita, M. Notomi, T. Tamamura, T. Sato, and S. Kawakami. *Photonic crystals for micro lightwave circuits using wavelength-dependent angular beam steering*. Applied Physics Letters **74**, 1370 (1999).

[Kos99b] H. Kosaka, T. Kawashima, A. Tomita, M. Notomi, T. Tamamura, T. Sato, and S. Kawakami. *Self-collimating phenomena in photonic crystals*. Applied Physics Letters **74**, 1212 (1999).

[Kra07] T. F. Krauss. *Slow light in photonic crystal waveguides*. Journal of Physics D: Applied Physics **40**, 2666 (2007).

[Kra14] C. Kraeh, A. Popsecu, M. Schieber, H. Hedler, T. Bieniek, G. Wielgoszewski, M. Moczała, and J. Finley. *Fabrication of high aspect ratio microtube arrays for 2D photonic crystals*. Materials Research Express **1**, 026201 (2014).

[Kum12] N. Kumar, M. Botey, R. Herrero, Y. Loiko, and K. Staliunas. *High-directional wave propagation in periodic loss modulated materials*. Photonics and Nanostructures - Fundamentals and Applications **10**, 644 (2012).

[Kum13] N. Kumar, R. Herrero, M. Botey, and K. Staliunas. *Flat lensing by periodic loss-modulated materials*. Journal of the Optical Society of America B **30**, 2684 (2013).

[Kum14] N. Kumar, L. Maigyte, M. Botey, R. Herrero, and K. Staliunas. *Beam shaping in two-dimensional metallic photonic crystals*. Journal of the Optical Society of America B **31**, 686 (2014).

[Lag04] A. N. Lagarkov and V. N. Kissel. *Near-perfect imaging in a focusing system based on a left-handed-material plate*. Physical Review Letters **92**, 077401 (2004).

[Lee91] D. W. Lee. *Ultrastructural basis and function of iridescent blue colour of fruits in elaeocarpus*. Nature **349**, 260 (1991).

[Lee97] D. W. Lee. *Iridescent blue plants*. American Scientist **85**, 56 (1997).

[Let01] X. Letartre, C. Seassal, C. Grillet, P. Rojo-Romeo, P. Viktorovitch, M. L. V. d' Yerville, D. Cassagne, and C. Jouanin. *Group velocity and propagation losses measurement in a single-line photonic-crystal*

waveguide on InP membranes. Applied Physics Letters **79**, 2312 (2001).

[Li03] Z.-Y. Li and L.-L. Lin. *Evaluation of lensing in photonic crystal slabs exhibiting negative refraction*. Physical Review B **68**, 245110 (2003).

[Li13] Y. Li and R. M. Almeida. *Adjustable YAG : Ce $^{3+}$ photoluminescence from photonic crystal microcavity*. Journal of Physics D: Applied Physics **46**, 165102 (2013).

[Lin96] S.-Y. Lin, V. M. Hietala, L. Wang, and E. D. Jones. *Highly dispersive photonic band-gap prism*. Optics Letters **21**, 1771 (1996).

[Lin12] J. Lin, J. Dellinger, P. Genevet, B. Cluzel, F. de Fornel, and F. Capasso. *Cosine-Gauss plasmon beam: a localized long-range nondiffracting surface wave*. Physical Review Letters **109**, 093904 (2012).

[Liu11] J. Liu, P. Han, G. Qiao, and J.Yang. *Properties of pc filters in one-dimensional photonic crystals containing defects*. Journal of Intense Pulsed Lasers and Applications in Advanced Physics **1**, 69 (2011).

[Lom06] B. Lombardet, L. A. Dunbar, R. Ferrini, R. Houdré and F. Robin. *A quantitative analysis of self-collimation effects in planar photonic crystals*. Journal of Applied Physics **99**, 096108 (2006).

[Lou05] V. Lousse and S. Fan. *Tunable terahertz bloch oscillations in chirped photonic crystals*. Physical Review B **72**, 075119 (2005).

[Lu05a] Z. Lu, C. Chen, C. A. Schuetz, S. Shi, J. A. Murakowski, G. J. Schneider, and D. W. Prather. *Subwavelength imaging by a flat cylindrical lens using optimized negative refraction*. Applied Physics Letters **87**, 091907 (2005).

[Lu05b] Z. Lu, J. A. Murakowski, C. A. Schuetz, S. Shi, G. J. Schneider, and D. W. Prather. *Three-dimensional subwavelength imaging by a photonic-crystal flat lens using negative refraction at microwave frequencies*. Physical Review Letters **95**, 153901 (2005).

[Lu05c] W. T. Lu and S. Sridhar. *Flat lens without optical axis: Theory of imaging*. Optics Express **13**, 10673 (2005).

[Lu06] Z. Lu, S. Shi, J. A. Murakowski, G. J. Schneider, C. A. Schuetz, and D. W. Prather. *Experimental demonstration of self-collimation inside a three-dimensional photonic crystal*. Physical Review Letters **96**, 173902 (2006).

[Lu07] M.-H. Lu, C. Zhang, L. Feng, J. Zhao, Y.-F. Chen, Y.-W. Mao, J. Zi, Y.-Y. Zhu, S.-N. Zhu, and N.-B. Ming. *Negative birefraction of acoustic waves in a sonic crystal*. Nature Materials **6**, 744 (2007).

[Luo02a] C. Luo, S. G. Johnson, J. D. Joannopoulos, and J. B. Pendry. *All-angle negative refraction without negative effective index*. Physical Review B **65**, 201104 (2002).

[Luo02b] C. Luo, S. G. Johnson, and J. D. Joannopoulos, *All-angle negative refraction in a three-dimensionally periodic photonic crystal*, Applied Physics Letters **81**, 2352 (2002).

[Luo03] C. Luo, S. G. Johnson, J. D. Joannopoulos, and J. B. Pendry. *Subwavelength imaging in photonic crystals*. Physical Review B **68**, 045115 (2003).

[Luo09] Z. Luo, Z. Tang, Y. Xiang, H. Luo, S. Wen. *Polarization-independent low-pass spatial filters based on one-dimensional photonic crystals containing negative-index materials.* Applied Physics B **94**, 641 (2009).

[Mai10] L. Maigyte, T. Gertus, M. Peckus, J. Trull, C. Cojocaru, V. Sirutkaitis, and K. Staliunas. *Signatures of light-beam spatial filtering in a three-dimensional photonic crystal*. Physical Review A **82**, 043819 (2010).

[Mai13] L. Maigyte V. Purlys, J. Trull, M. Peckus, C. Cojocaru, D. Gailevičius, M. Malinauskas, and K. Staliunas. *Flat lensing in the visible frequency range by woodpile photonic crystals*. Optics Letters **38**, 2376 (2013).

[Mal10] M. Malinauskas, A. Žukauskas, G. Bičkauskaitė, R. Gadonas, and S. Juodkazis. *Mechanisms of three-dimensional structuring of photo-polymers by tightly focussed femtosecond laser pulses*. Optics Express **18**, 10209 (2010).

[Mal11] M. Malinauskas, P. Danilevičius, and S. Juodkazis. *Three-dimensional micro-/nano-structuring via direct write polymerization with picosecond laser pulses*. Optics Express **19**, 5602 (2011).

[Mat07] L. M. Mäthger and R. T. Hanlon. *Malleable skin coloration in cephalopods: Selective reflectance, transmission and absorbance of light by chromatophores and iridophores*. Cell and tissue research **329**, 179 (2007).

[McC91] S. L. McCall, P. M. Platzman, R. Dalichaouch, D. Smith and S. Schultz. *Microwave propagation in two-dimensional dielectric lattices*. Physical Review Letters **67**, 2017 (1991).

[Mea92] R. D. Meade, K. D. Brommer, A. M. Rappe, and J. D. Joannopoulos. *Existence of a photonic band gap in two dimensions*. Applied Physics Letters **61**, 495 (1992).

[Miz04] V. Mizeikis, K. K. Seet, S. Juodkazis, and H. Misawa. *Three-dimensional woodpile photonic crystal templates for the infrared spectral range*. Optics Letters **29**, 2061 (2004).

[Mor05] I. Moreno, J. J. Araiza, and M. Avendano-Alejo. *Thin-film spatial filters*. Optics Letters **30**, 914 (2005).

[Mou05] R. Moussa, S. Foteinopoulou, L. Zhang, G. Tuttle, K. Guven, E. Ozbay, and C. M. Soukoulis. *Negative refraction and superlens behavior in a two-dimensional photonic crystal*. Physical Review B **71**, 085106 (2005).

[Nak12] H. Nakamura. *Nonadiabatic Transition: Concepts, Basic Theories and Applications*. (World Scientific, 2012).

[Nod99] S. Noda, N. Yamamoto, H. Kobayashi, M. Okano, and K. Tomoda. *Optical properties of three-dimensional photonic crystals based on III–V semiconductors at infrared to near-infrared wavelengths*. Applied Physics Letters **75**, 905 (1999).

[Nod00] S. Noda, K. Tomoda, N. Yamamoto, and A. Chutinan. *Full three-dimensional photonic bandgap crystals at near-infrared wavelengths*. Science **289**, 604 (2000).

[Nol03] S. Nolte, M. Will, J. Burghoff, and A. Tuennermann. *Femtosecond waveguide writing: A new avenue to three-dimensional integrated optics*. Applied Physics A **77**, 109 (2003).

[Not00] M. Notomi. *Theory of light propagation in strongly modulated photonic crystals: Refractionlike behavior in the vicinity of the photonic band gap*. Physical Review B **62**, 10696 (2000).

[Not01] M. Notomi, K. Yamada, A. Shinya, J. Takahashi, C. Takahashi, and I. Yokohama. *Extremely large group-velocity dispersion of line-defect waveguides in photonic crystal slabs*. Physical Review Letters **87**, 253902 (2001).

[Not02] M. Notomi. *Negative refraction in photonic crystals*. Optical and Quantum Electronics **34**, 133 (2002).

[Oue87] F. Ouellette. *Dispersion cancellation using linearly chirped bragg grating filters in optical waveguides*. Optics Letters **12**, 847 (1987).

[Ovs08] A. Ovsianikov, J. Viertl, B. Chichkov, M. Oubaha, B. MacCraith, I. Sakellari, A. Giakoumaki, D. Gray, M. Vamvakaki, M. Farsari, and C. Fotakis. *Ultra-low shrinkage hybrid photosensitive material for two-photon polymerization microfabrication*. ACS Nano **2**, 2257 (2008).

[Par03] P. V. Parimi, W. T. Lu, P. Vodo, and S. Sridhar. *Photonic crystals: Imaging by flat lens using negative refraction*. Nature **426**, 404 (2003).

[Par04] P. V. Parimi, W. T. Lu, P. Vodo, J. Sokoloff, J. S. Derov, and S. Sridhar. *Negative refraction and left-handed electromagnetism in microwave photonic crystals*. Physical Review Letters **92**, 127401 (2004).

[Pec09] M. Peckus, R. Rogalskis, M. Andrulevicius, T. Tamulevicius, A. Guobiene, V. Jarutis, V. Sirutkaitis, and K. Staliunas. *Resonators with manipulated diffraction due to two- and three-dimensional intracavity photonic crystals*. Physical Review A **79**, 033806 (2009).

[Pen99] J. B. Pendry, A. J. Holden, D. J. Robbins, and W. J. Stewart. *Magnetism from conductors and enhanced nonlinear phenomena*. IEEE Transactions on Microwave Theory and Techniques **47**, 2075 (1999).

[Pen00] J. B. Pendry. *Negative refraction makes a perfect lens*. Physical Review Letters **85**, 3966 (2000).

[Per07] I. Pérez-Arjona, V. J. Sánchez-Morcillo, J. Redondo, V. Espinosa, and K. Staliunas. *Theoretical prediction of the nondiffractive propagation of sonic waves through periodic acoustic media*. Physical Review B **75**, 014304 (2007).

[Pic12] R. Picó, V. J. Sánchez-Morcillo, I. Pérez-Arjona, and K. Staliunas. *Spatial filtering of sound beams by sonic crystals*. Applied Acoustics **73**, 302 (2012).

[Pic13] R. Picó, I. Pérez-Arjona, V. J. Sánchez-Morcillo, and K. Staliunas. *Evidences of spatial (angular) filtering of sound beams by sonic crystals*. Applied Acoustics **74**, 945 (2013).

[Pli91a] M. Plihal, A. Shambrook, A. A. Maradudin, and P. Sheng. *Two-*

dimensional photonic band structures. Optics Communications **80**, 199 (1991).

[Pli91b] M. Plihal and A. A. Maradudin. *Photonic band structure of two-dimensional systems: The triangular lattice*. Physical Review B **44**, 8565 (1991).

[Pra04] D. W. Prather, S. Shi, D. M. Pustai, C. Chen, S. Venkataraman, A. Sharkawy, G. Schneider, and J. Murakowski. *Dispersion-based optical routing in photonic crystals*. Optics Letters **29**, 50 (2004).

[Pur13] V. Purlys, L. Maigyte, D. Gailevičius, M. Peckus, M. Malinauskas, and K. Staliunas. *Spatial filtering by chirped photonic crystals*. Physical Review A **87**, 033805 (2013).

[Pur14a] V. Purlys, L. Maigyte, D. Gailevičius, M. Peckus, M. Malinauskas, R. Gadonas, and K. Staliunas. *Spatial filtering by axisymmetric photonic microstructures*. Optics letters **39**, 929 (2014).

[Pur14b] V. Purlys, L. Maigyte, D. Gailevičius, M. Peckus, R. Gadonas, and K. Staliunas. *Super-collimation by axisymmetric photonic crystals*. Accepted in Applied Physics Letters (2014).

[Qiu05] C. Qiu, X. Zhang, and Z. Liu. *Far-field imaging of acoustic waves by a two-dimensional sonic crystal*. Physical Review B **71**, 054302 (2005).

[Qiu99] M. Qiu and S. He. *Large complete band gap in two-dimensional photonic crystals with elliptic air holes*. Physical Review B **60**, 10610 (1999).

[Rab04] R. Rabady and I. Avrutsky. *Experimental characterization of simultaneous spatial and spectral filtering by an optical resonant filter*. Optics letters **29**, 605 (2004).

[Rak06] P. T. Rakich, M. S. Dahlem, S. Tandon, M. Ibanescu, M. Soljačić, G. S. Petrich, J. D. Joannopoulos, and E. P. Ippen. *Achieving centimetre-scale supercollimation in a large-area two-dimensional photonic crystal*. Nature Materials **5**, 93 (2006).

[Ren07] K. Ren, Z.-Y. Li, X. Ren, S. Feng, B. Cheng, and D. Zhang. *Three-dimensional light focusing in inverse opal photonic crystals*. Physical Review B **75**, 115108 (2007).

[Rin08] S. A. Rinne, F. García-Santamaría, and P. V. Braun. *Embedded cavities and waveguides in three-dimensional silicon photonic crystals*. Nature Photonics **2**, 52 (2008).

[Rob92] W. M. Robertson, G. Arjavalingam, R. D. Meade, K. D. Brommer, A. M. Rappe, and J. D. Joannopoulos. *Measurement of photonic band structure in a two-dimensional periodic dielectric array*. Physical Review Letters **68**, 2023 (1992).

[Roc07] C. Rockstuhl, F. Lederer, C. Etrich, T. Pertsch, and T. Scharf. *Design of an artificial three-dimensional composite metamaterial with magnetic resonances in the visible range of the electromagnetic spectrum*. Physical Review Letters **99**, 017401 (2007).

[Rom13] V. Romero-García, R. Picó, A. Cebrecos, K. Staliunas, and V. J. Sánchez-Morcillo. *Angular band gaps in sonic crystals: evanescent waves and spatial complex dispersion relation*. Journal of Vibration and Acoustics **135**, 041012 (2013).

[Sab11] M. Saba, M. Thiel, M. D. Turner, S. T. Hyde, M. Gu, K. Grosse-Brauckmann, D. N. Neshev, K. Mecke, and G. E. Schröder-Turk. *Circular dichroism in biological photonic crystals and cubic chiral nets*. Physical Review Letters **106**, 103902 (2011).

[Sak04] K. Sakoda. *Optical properties of photonic crystals*. (Springer, 2004).

[Sal07] B. E. A. Saleh and M. C. Teich. *Fundamentals of photonics*. (Wiley-Interscience, 2007).

[San04] H. Sang, Z. Y. Li, and B.Y. Gu. *Stack-sequence dependent defect modes in one-dimensional photonic crystals*. Physics Letters A **331**, 414 (2004).

[San09] V. J. Sánchez-Morcillo, K. Staliunas, V. Espinosa, I. Pérez-Arjona, J. Redondo, and E. Soliveres. *Propagation of sound beams behind sonic crystals*. Physical Review B **80**, 134303 (2009).

[Sch03] D. Schurig and D. R. Smith. *Spatial filtering using media with indefinite permittivity and permeability tensors*. Applied Physics Letters **82**, 2215 (2003).

[Sch06] E. Schonbrun, T. Yamashita, W. Park, and C. J. Summers. *Negative-index imaging by an index-matched photonic crystal slab*. Physical Review B **73**, 195117 (2006).

[Ser06] J. Serbin and M. Gu. *Experimental evidence for superprism effects in three-dimensional polymer photonic crystals*. Advanced Materials **18**, 221 (2006).

[Ser09] A. E. Serebryannikov, A. Y. Petrov, and Ekmel Ozbay. *Toward photonic crystal based spatial filters with wide angle ranges of total transmission.* Applied Physics Letters **94**, 181101 (2009).

[She01] R. A. Shelby, D. R. Smith, and S. Schultz. *Experimental verification of a negative index of refraction*. Science **292**, 77 (2001).

[Sid06] O. F. Siddiqui and G. V. Eleftheriades. *Resonant modes in continuous metallic grids over ground and related spatial-filtering applications*. Journal of Applied Physics **99**, 083102 (2006).

[Sie93] A. E. Siegman. *Defining, measuring, and optimizing laser beam quality*. Proc. SPIE **1868**, Laser Resonators and Coherent Optics: Modeling, Technology, and Applications, 2 (1993).

[Smi93] D. R. Smith, R. Dalichaouch, N. Kroll, S. Schultz, S. L. McCall, and P. M. Platzman. *Photonic band structure and defects in one and two dimensions*. Journal of the Optical Society of America B **10**, 314 (1993).

[Smo07] I. I. Smolyaninov, Y.-J. Hung, and C. C. Davis. *Magnifying superlens in the visible frequency range*. Science **315**, 1699 (2007).

[Sol09] E. Soliveres, V. Espinosa, I. Pérez-Arjona, V. J. Sánchez-Morcillo, and K. Staliunas. *Self collimation of ultrasound in a three-dimensional sonic crystal*. Applied Physics Letters **94**, 164101 (2009).

[Son05] B.-S. Song, T. Asano, Y. Akahane, Y. Tanaka, and S. Noda. *Multichannel add-drop filter based on in-plane hetero photonic crystals*. Journal of Lightwave Technology **23**, 1449 (2005).

[Son13] D. Son, Z. Tang, L. Zhao, Z. Sui, S. Wen, and D. Fan. *Experimental demonstration of a low-pass spatial filter based on a one-dimensional*

photonic crystal with a defect layer. Chinese Physics Letters **30**, 044206 (2013).

[Sou96] C. M. Soukoulis. *Photonic band gap materials: The "Semiconductors" of the future?*. Physica Scripta **1996**, 146 (1996).

[Sta06] K. Staliunas and R. Herrero. *Nondiffractive propagation of light in photonic crystals*. Physical Review E **73**, 016601 (2006).

[Sta09a] K. Staliunas and V. J. Sánchez-Morcillo. *Spatial filtering of light by chirped photonic crystals*. Physical Review A **79**, 053807 (2009).

[Sta09b] K. Staliunas, R. Herrero, and R. Vilaseca. *Subdiffraction and spatial filtering due to periodic spatial modulation of the gain-loss profile*. Physical Review A **80**, 013821 (2009).

[Sta11] K. Staliunas. *Removal of excitations of bose-einstein condensates by space- and time-modulated potentials*. Physical Review A **84**, 013626 (2011).

[Str02] A. M. Streltsov and N. F. Borrelli. *Study of femtosecond-laser-written waveguides in glasses*. Journal of the Optical Society of America B **19**, 2496 (2002).

[Suk08] A. Sukhovich, L. Jing, and J. H. Page. *Negative refraction and focusing of ultrasound in two-dimensional phononic crystals*. Physical Review B **77**, 014301 (2008).

[Sun06] G. Sun, A. S. Jugessur, and A. G. Kirk. *Imaging properties of dielectric photonic crystal slabs for large object distances*. Optics Express **14**, 6755 (2006).

[Swi11] G. P. Swift, A. J. Gallant, N. Kaliteevskaya, M. A. Kaliteevski, S. Brand, D. Dai, A. J. Baragwanath, I. Iorsh, R. A. Abram, and J. M. Chamberlain. *Negative refraction and the spectral filtering of terahertz radiation by a photonic crystal prism*. Optics Letters **36**, 1641 (2011).

[Tan04] T. Tan, D. Wong, and P. Lee. *Iridescence of a shell of mollusk haliotis glabra*. Optics express **12**, 4847 (2004).

[Tan06] Z. Tang, H. Zhang, Y. Ye, C. Zhao, S. Wen, and D. Fan. *Low-pass spatial filtering using optically thinner left-handed photonic crystals*. International Symposium on Biophotonics, Nanophotonics and Metamaterials 2006, 488 (2006).

[Tan07] Z. Tang, D. Fan, S. Wen, Y. Ye, and C. Zhao. *Low-pass spatial filtering using a two-dimensional self-collimating photonic crystal*. Chinese Optics Letters **5**, S211 (2007).

[Tan11] A. Tandaechanurat, S. Ishida, D. Guimard, M. Nomura, S. Iwamoto, and Y. Arakawa. *Lasing oscillation in a three-dimensional photonic crystal nanocavity with a complete bandgap*. Nature Photonics **5**, 91 (2011).

[Tru11] J. Trull, L. Maigyte, V. Mizeikis, M. Malinauskas, S. Juodkazis, C. Cojocaru, M. Rutkauskas, M. Peckus, V. Sirutkaitis, and K. Staliunas. *Formation of collimated beams behind the woodpile photonic crystal*. Physical Review A **84**, 033812 (2011).

[Van14] O. Vanbésien and E. Centeno. *Dispersion Engineering for Integrated Nanophotonics*. (Wiley-ISTE, 2014).

[Ves68] V. G. Veselago. *The electrodynamics of substances with simultaneously negative values of ε and μ*. Soviet Physics Uspekhi **10**, 509 (1968).

[Vig06] J. P. Vigneron, J.-F. Colomer, M. Rassart, A. L. Ingram, and V. Lousse. *Structural origin of the colored reflections from the black-billed magpie feathers*. Physical Review E **73**, 021914 (2006).

[Vil92] P. R. Villeneuve and M. Piche´. *Photonic band gaps in two-dimensional square and hexagonal lattices*. Physical Review B **46**, 4969 (1992).

[Vla05] Y. A. Vlasov, M. O'Boyle, H. F. Hamann, and S. J. McNab. *Active control of slow light on a chip with photonic crystal waveguides*. Nature **438**, 65 (2005).

[Vuk03] P. Vukusic and J. R. Sambles. *Photonic structures in biology*. Nature **424**, 852 (2003).

[Wan04] X. Wang, Z. Ren, and K. Kempa. *Unrestricted superlensing in a triangular two dimensional photonic crystal*. Optics Express **12**, 2919 (2004).

[Wan97] R. Wang, J. Dong, and D. Y. Xing. *Defect studies in a one-dimensional photonic band gap structure*. physica status solidi (b) **200**, 529 (1997).

[Wit02] J. Witzens, M. Loncar, and A. Scherer. *Self-collimation in planar photonic crystals*. IEEE Journal of Selected Topics in Quantum Electronics **8**, 1246 (2002).

[Wu10a] C.-J. Wu, J.-J. Liao, and T.-W. Chang. *Tunable multilayer Fabry-Perot resonator using electro-optical defect layer*. Journal of Electromagnetic Waves and Applications **24**, 531 (2010).

[Wu10b] C.-J. Wu, Y.-N. Rau, and W.-H. Han. *Enhancement of photonic band gap in a disordered quarter-wave dielectric photonic crystal*. Progress In Electromagnetics Research **100**, 27 (2010).

[Xio07] Y. Xiong, Z. Liu, C. Sun, and X. Zhang. *Two-dimensional imaging by far-field superlens at visible wavelengths*. Nano Letters **7**, 3360 (2007).

[Yab87] E. Yablonovitch. *Inhibited spontaneous emission in solid-state physics and electronics*. Physical Review Letters **58**, 2059 (1987).

[Yab91a] E. Yablonovitch, T. J. Gmitter, and K. M. Leung. *Photonic band structure: The face-centered-cubic case employing nonspherical atoms*. Physical Review Letters **67**, 2295 (1991).

[Yab91b] E. Yablonovitch, T. J. Gmitter, R. D. Meade, A. M. Rappe, K. D. Brommer, and J. D. Joannopoulos. *Donor and acceptor modes in photonic band structure*. Physical Review Letters **67**, 3380 (1991).

[Yab93] E. Yablonovitch. *Photonic band-gap structures*. Journal of the Optical Society of America B **10**, 283 (1993).

[Yab01] E. Yablonovitch. *Photonic crystals: Semiconductors of light*. Scientific American **285**, 47, 54 (2001).

[Yam98] N. Yamamoto, S. Noda, and A. Chutinan. *Development of one period of a three-dimensional photonic crystal in the 5–10 μm wavelength region by wafer fusion and laser beam diffraction pattern observation*

techniques. Japanese Journal of Applied Physics **37**, L1052 (1998).

[Yan04a] C.-R. Yang, Y.-S. Hsieh, G.-Y. Hwang, and Y.-D. Lee. *Photoablation characteristics of novel polyimides synthesized for high-aspect-ratio excimer laser liga process*. Journal of Micromechanics and Microengineering **14**, 480 (2004).

[Yan04b] S. Yang, J. H. Page, Z. Liu, M. L. Cowan, C. T. Chan, and P. Sheng. *Focusing of sound in a 3D phononic crystal*. Physical Review Letters **93**, 024301 (2004).

[Yar02] A. Yariv and P. Yeh. *Optical Waves in Crystals: Propagation and Control of Laser Radiation*. (Wiley-Interscience, 2002).

[Yin12] H. Yin, B. Dong, X. Liu, T. Zhan, L. Shi, J. Zi, and E. Yablonovitch. *Amorphous diamond-structured photonic crystal in the feather barbs of the scarlet macaw*. Proceedings of the National Academy of Sciences of the United States of America **109**, 10798 (2012).

[Yu03] X. Yu and S. Fan. *Bends and splitters for self-collimated beams in photonic crystals*. Applied Physics Letters **83**, 3251 (2003).

[Zha07] H. Zhang, S. M. Eaton, and P. R. Herman. *Single-step writing of bragg grating waveguides in fused silica with an externally modulated femtosecond fiber laser*. Optics Letters **32**, 2559 (2007).

[Zho01] W. D. Zhou, J. Sabarinathan, P. Bhattacharya, B. Kochman, E. W. Berg, P.-C. Yu, and S. W. Pang. *Characteristics of a photonic bandgap single defect microcavity electroluminescent device*. IEEE Journal of Quantum Electronics **37**, 1153 (2001).

[Zhu09] Q. Zhu and Y. Zhang. *Defect modes and wavelength tuning of one-dimensional photonic crystal with lithium niobate*. Optik - International Journal for Light and Electron Optics **120**, 195 (2009).

[Zi03] J. Zi, X. Yu, Y. Li, X. Hu, C. Xu, X. Wang, X. Liu, and R. Fu. *Coloration strategies in peacock feathers*. Proceedings of the National Academy of Sciences **100**, 12576 (2003).

List of publications

In this thesis we reported completely original work. Testimony to this is the fact that summaries of this work have been published in peer-reviewed journals and presented to international conferences.

Publications

[1] **L. Maigyte**, T. Gertus, M. Peckus, J. Trull, C. Cojocaru, V. Sirutkaitis, and K. Staliunas. *Signatures of light-beam spatial filtering in a three-dimensional photonic crystal*. **Physical Review A 82**, 043819 (2010).

[2] J. Trull, **L. Maigyte**, V. Mizeikis, M. Malinauskas, S. Juodkazis, C. Cojocaru, M. Rutkauskas, M. Peckus, V. Sirutkaitis, and K. Staliunas. *Formation of collimated beams behind the woodpile photonic crystal*. **Physical Review A 84**, 033812 (2011).

[3] V. Purlys, **L. Maigyte**, D. Gailevičius, M. Peckus, M. Malinauskas, and K. Staliunas. *Spatial filtering by chirped photonic crystals*. **Physical Review A 87**, 033805 (2013).

[4] **L. Maigyte**, V. Purlys, J. Trull, M. Peckus, C. Cojocaru, D. Gailevičius, M. Malinauskas, and K. Staliunas. *Flat lensing in the visible frequency range by woodpile photonic crystals*. **Optics Letters 38**, 2376 (2013).

[5] V. Purlys, **L. Maigyte**, D. Gailevičius, M. Peckus, M. Malinauskas, R. Gadonas, and K. Staliunas. *Spatial filtering by axisymmetric photonic microstructures*. **Optics letters 39**, 929 (2014).

[6] N. Kumar, **L. Maigyte**, M. Botey, R. Herrero, and K. Staliunas. *Beam shaping in two-dimensional metallic photonic crystals*. Journal of the Optical Society of America B **31**, 686 (2014).

Accepted papers

[7] V. Purlys, **L. Maigyte**, D. Gailevičius, M. Peckus, R.Gadonas, and K. Staliunas, *Super-collimation by axisymmetric photonic crystals*. **Applied Physics Letters** (2014)